EFFECTS OF NANOPARTICLES ON THE WEAR RESISTANCE OF
POLYTETRAFLUOROETHYLENE

By

DAVID LAWRENCE BURRIS

A DISSERTATION PRESENTED TO THE GRADUATE SCHOOL
OF THE UNIVERSITY OF FLORIDA IN PARTIAL FULFILLMENT
OF THE REQUIREMENTS FOR THE DEGREE OF
DOCTOR OF PHILOSOPHY

UNIVERSITY OF FLORIDA

2007

This document is dedicated to my parents, Karen and Larry Burris, who encouraged me to find my own path

ACKNOWLEDGMENTS

TABLE OF CONTENTS

LIST OF TABLES

8

LIST OF FIGURES

11

12

Abstract of Dissertation Presented to the Graduate School
of the University of Florida in Partial Fulfillment of the
Requirements for the Degree of Doctor of Philosophy

EFFECTS OF NANOPARTICLES ON THE WEAR RESISTANCE OF
POLYTETRAFLUOROETHYLENE

By

David L. Burris

December 2007

Chair: W. Gregory Sawyer
Major: Mechanical Engineering

Solid lubricants comprise an important class of materials and find use in applications

where the use of more traditional lubrication techniques is undesirable or precluded.

Polytetrafluoroethylene (PTFE) is reputed as having the lowest friction of any bulk polymer and

is used to lubricate a wide variety of systems from armor piercing bullets to frying pans, but high

wear rates limit its application. The use of nanofillers has proven to be an effective means for

reducing the wear of PTFE without introducing detrimental effects on its other beneficial

properties; microfillers often increase abrasion and friction, and reduce mechanical integrity and

chemical resistance. Past studies have been used to identify several potential wear resistance

mechanisms of PTFE nanocomposites: 1) bonding and strength at the filler/matrix interface, 2)

dispersion and mechanical effects of load support and crack deflection, 3) morphological effects

of nanoparticles on the matrix and 4) fibrillation and toughening, 5) transfer film coverage, 6)

transfer film orientation and 7) chemical degradation.   It is found that for wear resistance to

increase by more than two orders of magnitude at trace nanoparticle loadings, the filler must

activate a synergism of wear resistance mechanisms. These studies suggest that the nanofillers

interact with the PTFE and possibly lead to a finer scale lamellar structure. The resulting

mechanical properties preclude easy crack propagation through the material, which results in the regulation of debris size. The small size of the debris makes removal from the interface difficult and as a result, the debris are transferred to both the counterface and pin. The transferred debris deform, and over time, form protective transfer films. These thin and protective transfer films are largely responsible for the additional 100X in wear resistance over traditional PTFE composites.

CHAPTER 1
INTRODUCTION

Lubrication in Mechanical Design

Tribology is the study of surfaces in relative motion, and lubrication is one of the most critical and underestimated aspects of mechanical design. Nearly all moving mechanical systems rely on lubrication for motion. In the best case, a poor understanding of tribology leads to inefficiency; in the worst case, it leads to catastrophic system failure. Materials do not have intrinsic friction coefficients or wear rates. These parameters are system dependent and can be strongly affected by speed, pressure, temperature and environmental pressure and composition. Modern designs are subject to increasingly dynamic and harsh environments with space tribology being a classic example. The engineer must not only design tribological systems that can endure such harsh environments, but forecast the system response to extreme changes in the operating environment.

Engineers often regard materials in terms of bulk properties. In tribology, surfaces dominate the phenomena under study. Atoms in the bulk of a material are surrounded by and bonded to neighboring atoms, and as a result, they are in a low energy state. At the surface, atoms are exposed and in a higher energy state. Macroscopically, this is manifested as surface energy. When two clean surfaces come into contact, there is a strong tendency of the system to enter a lower energy state by forming bonds at the contacting surface protuberances or asperities [1]. Thus, one of, if not the major challenge in tribology is to keep solid surfaces separated. This is traditionally achieved through the use of a lubricant whose primary objective is to separate solid surfaces, preventing direct asperity contact and reducing the likelihood for seizure. In fluid lubricated systems, surfaces can be separated by a hydrodynamic film. In grease lubricated systems, the grease has low surface energy relative to the surface and a boundary layer

naturally forms to reduce direct contact of the surfaces. Because sliding in these systems occurs through shearing of low strength films, friction coefficients and wear rates are characteristically low [2].

Introduction to Tribometry

Friction coefficients and wear rates are the most commonly discussed and quantified parameters in tribology. Friction coefficients can dictate required motor torques and loads, and wear can lead to debris generation, binding, slop and limited life. Because of the important role of each in design, they are the primary metrics of performance in tribological systems.

A friction coefficient, μ, is defined as a ratio of the force that resists sliding to the normal force. A tribometer is a device used to measure friction coefficients. While there is no standard tribometry test, experimental setups generally utilize similar design philosophies. In its simplest form, a flat sample is slid against the flat surface of a much larger and harder block of material called the counterface. This results in an approximately uniform pressure distribution within the sample. In many cases, the counterface material and surface finish are important factors in system performance. Upon sliding, the frictional and normal forces are measured or inferred at the specimen simultaneously. A detailed uncertainty analysis of the measurement of friction coefficient on a similar pin-on-flat tribometer was performed by Schmitz *et al.*[3], and illustrates the metrology challenges associated with such a seemingly simple measurement.

Wear rate, k, is defined as the volume of material removed per unit of normal load per unit distance of sliding, with typical units being $mm^3/(Nm)$. Values of wear rates can vary by many orders of magnitude depending on the bearing materials, environment and lubricant. Since volumetric measurements can not practically cover this range, the test length often becomes a function of the wear rate being measured (loads are usually held constant). Reporting the

experimental uncertainty is necessary to indicate the quality of measurement, and it is especially important when wear rates are low. Calculations of normal load and sliding distance with associated uncertainties are fairly straightforward, but measurements of volume loss often require more careful consideration. For materials that do not uptake or outgas, material mass measurements are typically made because dimensional distortions due to elasticity, plasticity, creep and thermal fluctuations can confound dimensional measurements of wear. Density can be calculated by making an initial sample mass measurement with dimensional measurements or with another direct measurement of volume. Schmitz *et al.*[4] performed a detailed uncertainty analysis of wear rate measurement for a pin-on-flat tribometer.

Solid Lubricants

In an increasing number of applications the use of traditional fluid or boundary lubricants is undesirable or even precluded; these applications often necessitate the use of solid lubricants. A solid lubricant is typically a low strength material that promotes low friction sliding without the requirement of an external lubricant. In many cases, a solid lubricant is used as a low cost, environmentally friendly alternative to fluid and grease based systems, eliminating the need for fluids, reservoirs, pumps, filters and maintenance [2]. In some cases, solid lubricants play a supplementary role. Thin, solid lubricant films are used on foil air bearings and engine valve trains to protect the components during start-up and shut-down when speeds are insufficient for aero- or hydrodynamic lubrication. Fluid and grease lubricated systems are highly sensitive to contamination, and many rely on solid lubricant seals to keep dirt, debris and other contamination out of the tribological interface. In areas like the food industry, solid lubricants are used for conveyor bushings to prevent contamination of the product by the lubricant. In the integrated circuits industry, very chemically resistant solid lubricants (*e.g.* PTFE) must be used

for valve seats and bushings in the transport of caustic etchants. Many aerospace applications require solid lubricants to endure an extreme range of harsh environmental conditions [5-7]. These environmental challenges can include salt spray, sand, radiation, vacuum and cryogenic temperatures.

Polymeric Composites

Polymeric solid lubricants comprise an important segment of the lubrication field, providing robust lubrication under a wide range of conditions, but with poor performance relative to fluid and grease lubricants. Figure 1 is a graph of wear rate plotted versus friction coefficient for various unfilled polymers, polymer blends, and polymer composites used in tribology studies [8-19]. While tribological performance does not have a single unique definition, broadly speaking, solid lubricants with low wear rates and low friction coefficients are desirable. For practical purposes a designer might include constant performance guidelines (Figure 1 illustrates how such guidelines might be used) whose slopes depend on the relative importance of friction coefficient and wear rate for a specific application (note: wear rates are on a log scale). High performance engineering polymers like Polyetheretherketone (PEEK) and Polyimide (PI) have good wear resistance but high friction coefficients, while low friction materials like Polytetrafluoroethylene (PTFE) usually have prohibitively high wear rates. In general, neat polymers lack the tribological performance required for most applications; there are many examples of polymer composites in tribology.
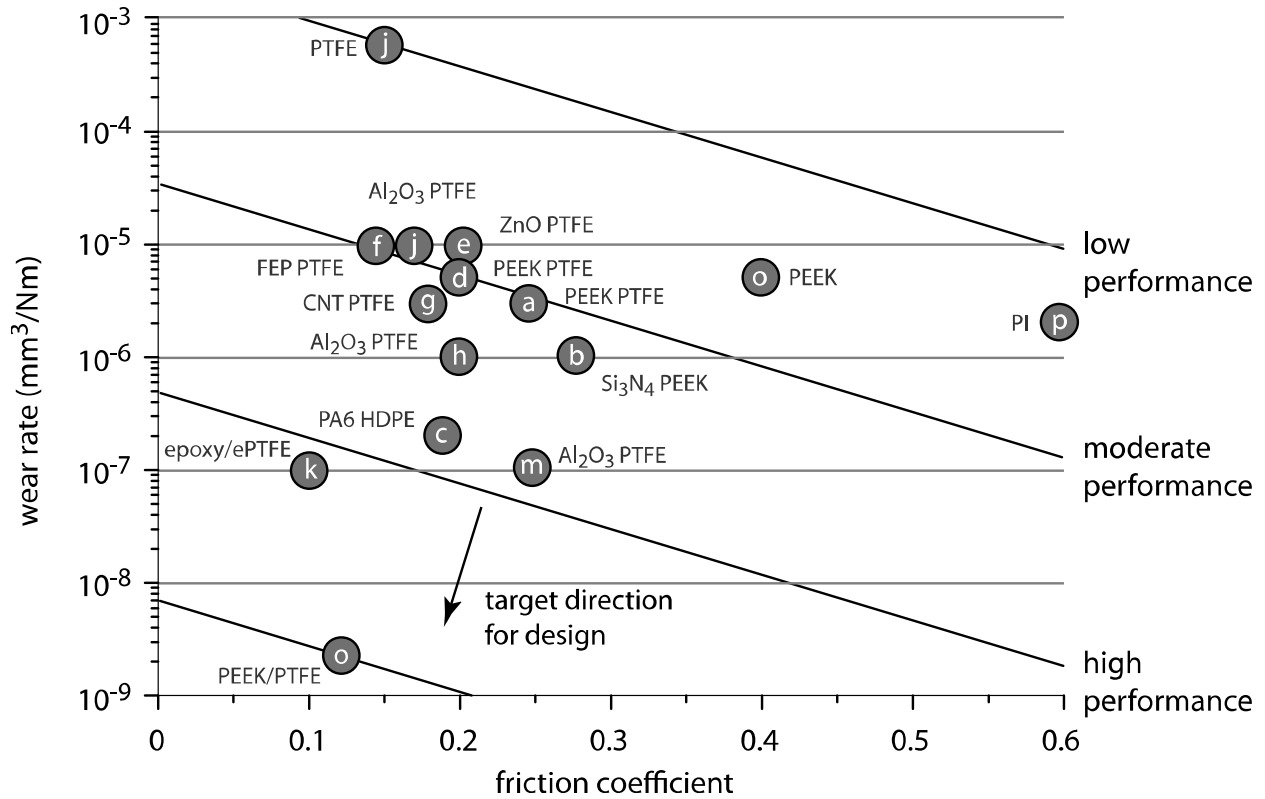
Figure 1-1. Wear rate plotted versus friction coefficient for various solid lubricating polymeric composites, unfilled polymers, and polymer blends. The target region is the lower left hand corner, a region of ultra low wear rate and friction coefficient. The data points are labeled with the constituents and listed as a-p: a) PTFE/PEEK composite Lu *et al.*1995, b) Si$_3$N$_4$/PEEK nanocomposite Wang *et al.*1996, c) PA6/HDPE blend Palabiyik *et al.*2000, d) PTFE/PEEK composite Wang *et al.*2000, e) ZnO/PTFE nanocomposite Li *et al.*2001, f) FEP/PTFE composite Menzel *et al.*2002, g) CNT/PTFE nanocomposite Chen *et al.*2003, h) Al$_2$O$_3$/PTFE nanocomposite Sawyer *et al.*2003, j) Al$_2$O$_3$/PTFE nanocomposite and unfilled PTFE Burris and Sawyer 2005, k) epoxy/ePTFE composite McCook *et al.*2005, m) Al2O3/PTFE nanocomposite Burris and Sawyer 2006, o) PEEK/PTFE composite and unfilled PEEK Burris and Sawyer 2006, p) unfilled PI unpublished, V = 50.8 mm/s, P = 6.25 MPa, reciprocating pin-on-disk tribometer.

One philosophy of material design in tribology is to improve the frictional behavior of a wear resistant polymer. For example, additions of PTFE to PEEK have been found to significantly reduce friction coefficients; this often results in reduced wear. In this particular composite a soft PTFE film is preferentially drawn from the composite to separate the surfaces, protecting the relatively soft polymeric material from direct asperity contact, and providing a low

shear friction reducing film to accommodate the sliding motion; this is called a transfer film. Transfer films are exceedingly important to the success of a solid lubricant, both protecting the bulk and reducing the sliding forces at the interface [20].

The opposite method is also employed where hard particle and fiber fillers are used to reduce the wear of a low friction high wear material like PTFE, often at the expense of friction coefficient. There are significant efforts dedicated to the research and development of low friction, low wear solid lubricants with traditional particle and fiber fillers, many of which have successfully transferred to application. Friedrich *et al.*[21] and Zhang [22] reviewed the state of the art of polymer composites in tribology in 1995 and 1998, respectively.

Polymeric Nanocomposites

In tribology, one of the drawbacks of the traditional hard micron-sized particle and fiber fillers frequently used to reinforce polymers is that they tend to abrade the counterface. Abrasion prevents the formation of a protective transfer film, increases the friction coefficient and counterface roughness, and leads to third body wear of the composite. Nanoparticles (defined as particles with a characteristic dimension less than 100 nm) have the potential to reduce the abrasion that leads to these cascading and problematic events. Because nanoparticles are of the same size scale as counterface asperities, they may polish the highest asperities and promote the development of tribologically favorable transfer films. Once formed, transfer films shield the composite from direct asperity contact and damage [20].

Another benefit of nanoparticles is that at low loadings (<5%), nanocomposites can have tremendous particle number densities and interfacial surface areas. Consequently, nanoparticles have great potential for impacting a number of physical properties at low filler loadings. Siegel *et al.*[23] found that with about 2% (volume) alumina nanoparticles, the tensile strain to failure

of PMMA improved by 400%, and Ng *et al.*[24] found the scratch resistance of a TiO_2-Epoxy nanocomposite to be superior to both unfilled and micro-filled Epoxy. During strain dependent Raman spectroscopy measurements of multi-walled carbon-nanotube (MWCNT) filled Lexan polycarbonate, Eitan *et al.*[25] found that load was transferred to the nanotubes. They also found that an epoxide surface treatment of the nanotubes improved the load transfer through the interface, highlighting the role of the interface on mechanical properties. Nanofillers can not only improve material properties through mechanical transfer, but they can also influence the crystallization and morphology of the polymeric matrix which can further alter physical properties. Many authors have observed the direct effects of the nanoparticles on the matrix through changes in the glass transition and degradation temperatures of the polymer matrices [26-29]. Clearly, nanoparticles can influence the crystallinity, morphology and behavior of the polymer itself and the potential for multifunctionality in these nanostructured materials is substantial. Detailed studies of matrix properties are needed but generally lacking in the tribology literature.

Within the past decade there have been a number of tribological studies conducted to investigate the role of nanoparticles in polymer nanocomposites [8, 10, 11, 16-19, 30-34]. Early studies by Wang *et al.*[17] used nanoparticles in a PEEK matrix. The nanoparticles were dispersed in the PEEK powder by ultrasonication in an alcohol bath. In an initial study, <50 nm Si_3N_4 was found to be effective in reducing the wear rate and friction coefficient of PEEK. The improvements in tribological performance were mostly attributed to the vast improvements observed in the quality of the transfer films. A follow-up study looked directly at the effects of particle size and shape on the tribological behavior of the composite [34]. Micron-scale whiskers, microparticles and nanoparticles of SiC were used with 5% loading in PEEK. The

whiskers were effective in reducing the wear of PEEK (~33%) but friction was only reduced ~8%. The microparticles were effective in reducing the friction coefficient (~33%) but wear rate was only reduced by ~9%. The nanoparticles effectively reduced both with a reduction in wear rate of ~44% and a reduction in friction coefficient of ~50%. In a later size study involving nanometer ZrO_2 from 10 nm to 100 nm in a PEEK matrix, it was found that for approximately 2% loading, both friction coefficient and wear rate increased monotonically with increased filler size (improved performance of PEEK with various loadings of SiO_2 nanoparticles was also found) [32, 33]. In each of these studies, thin uniform transfer films accompanied reduced wear rates and friction coefficients.

In 2000, Schwartz and Bahadur published a study that examined the influence of alumina nanoparticles on the tribological behavior of polyphenylene sulfide (PPS) [31]. Powders were dispersed with what is described as an electric mixer. A 2X reduction of wear was observed for a 2% filled nanocomposite. They found good correlation between the bond strength of the transfer film and the wear rate of the composite and concluded that the role of the filler was to anchor the transfer film. They attributed the increased wear rates at loadings above 2% to abrasion of the transfer film by nanoparticle aggregates.

CHAPTER 2
POLYTETRAFLUOROETHYLENE AS A SOLID LUBRICANT

Neat Polytetrafluoroethylene

Tribology in extreme environments is one of the primary driving forces for the development of novel solid lubricants with improved performance. In space environments, for example, the tribological components are subjected to near perfect vacuum, intense radiation, atomic oxygen and a wide thermal range. Properties like vapor pressure, chemical inertness and thermal stability are critical in these applications and preclude the use of traditional fluid and grease lubricants. Polytetrafluoroethylene (PTFE) is a unique polymer; not only is it widely regarded to have the lowest friction coefficients of any bulk polymer, but it also has a low vapor pressure, is chemically inert and has one of the largest operational thermal ranges of any bulk polymer. It is uniquely suitable for a variety of extreme environment tribological applications, and is the solid lubricant matrix material under investigation in this study.

PTFE typically consists of 20,000-200,000 mers, or repeating units, of tetrafluoroethylene (C_2F_4) in a helix configuration. The carbon-fluorine bond is very strong, and although the carbon backbone is only single bonded, it is located within a fluorine encasement, which effectively shields it from chemical attack. The unique physical properties of PTFE are derived from high chemical stability and smooth linear morphology of the PTFE molecule.

The tribological properties of PTFE have been studied for more than 50 years. McLaren and Tabor found that the friction of PTFE behaved as if governed by viscoelastic effects, increasing with increased speed and decreased temperature [35]. Makinson and Tabor found that thin transfer films were developed on the counterface during sliding with PTFE [36]. In addition, they found evidence that the film was strongly adhered to the counterface contrary to the conventional wisdom that low friction of PTFE was the result of poor adhesion. From these

results, it was concluded that the tribological interface consisted of self-mated PTFE surfaces. This conclusion led to the hypothesis that motion occurred through the shearing of crystallites past one another in a lamellar fashion similar to the shearing of a deck of cards. Pooley and Tabor found frictional anisotropy with high friction against the chain direction and low friction with the chain direction and concluded that low friction was due to the smooth molecular profile with high radial stiffness and low axial resistance to sliding [37].

Despite the beneficial frictional characteristics of PTFE for tribological application, its wear rate is significantly higher than many other polymers; this high rate of wear has prohibited its use in many applications and is largely responsible for the limited PTFE research in the area of solid lubrication. During low speed sliding (< 10mm/s), PTFE has a low friction coefficient (between $\mu=0.03$ and $\mu=0.1$) and moderate wear resistance (10^{-5} mm^3/Nm). Makinson and Tabor [36] found that as the sliding speed increased to above 10 mm/s at room temperature, a transition from mild to severe wear (10^{-5} mm^3/Nm to 10^{-3} mm^3/Nm) accompanied increased friction. As speed is increased from an original condition of low friction and moderate wear, they conjectured that the stresses required for sliding exceeded the stress required to cause failure at boundaries between crystalline domains in the sintered material; this leads to larger debris and increased wear rates. Tanaka proposed a similar model with failure occurring at boundaries of the characteristic 'banded' structure of PTFE [38]. Blanchet and Kennedy [39] studied this severe wear transition at several temperatures and found an increase in the transition speed to accompany increased temperature. When the wear rate, k, was plotted versus the friction coefficient, μ, the transition to severe wear occurred at $\mu = 0.1$ in each case. These results are consistent with the proposed transition mechanism of Makinson and Tabor [36] and suggest that the severe wear transition is a response to the stress state and thus the friction coefficient, while

26

the friction coefficient is a function of both speed and temperature. Recent studies suggest that the temperature dependence of the friction coefficient may be due to thermally activated barriers to sliding.

Several samples from the studies of Blanchet and Kennedy were microtomed perpendicular to the wear surface in the direction of sliding after mild and severe wear had taken place. Cracks were found to propagate in the direction of sliding beneath a layer of worked material at subsurface depths consistent with observed debris thicknesses for severe wear samples. No such cracks were found in mild wear samples. They believed that defects in the sintered material acted as initiated cracks. When speeds are low, the kinetic friction coefficient at the tribological interface is low, and the static friction coefficient between internal crack faces is sufficient to fully support the surface tractions. However, when the kinetic coefficient of friction at the tribological interface increases with increased sliding speed and exceeds the static coefficient of friction ($\mu \sim 0.1$) at internal PTFE/PTFE interfaces, the crack tips must support shear. This leads to a progressive delamination wear process similar to that described in Suh's delamination theory of wear [40].

PTFE Composites

For decades, fillers have been successfully used to reduce the wear of PTFE. In Figure 2-1, wear rate is plotted versus filler wt% for testing of some representative PTFE composites found in the literature [12, 14, 41-43]. Despite being tested with varying configurations, testers, methods, pressures, speeds and fillers, there is a systematic trend of decreased wear rate with increased loading up to 50 wt%.
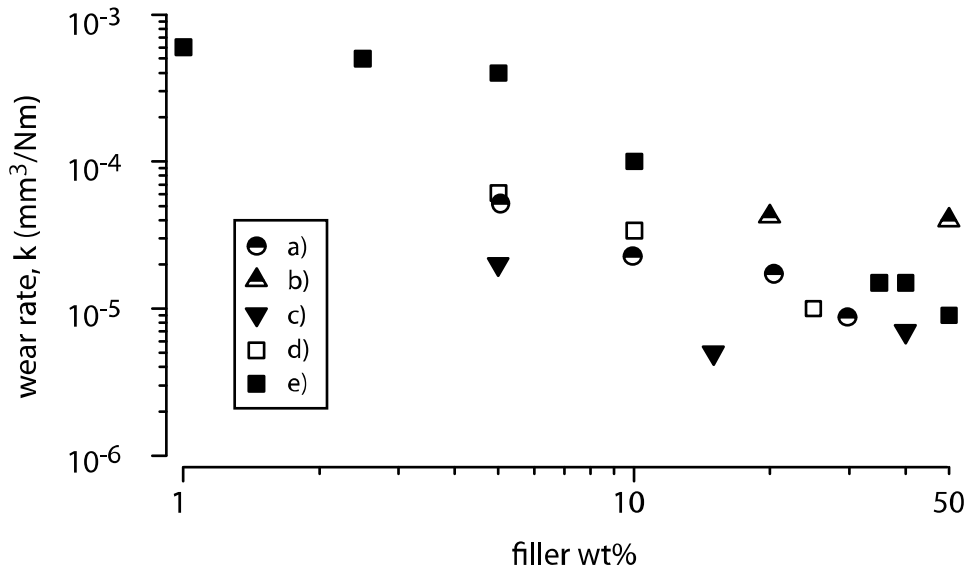
Figure 2-1. Wear rate versus filler loading for some of the PTFE based microcomposite systems found in the tribology literature: a) Li *et al.*2000 - graphite b) Bahadur and Gong 1992 – graphite c) Lu *et al.*1995 - PEEK d) Burroughs *et al.*1999 – B_2O_3 e) Menzel and Blanchet 2002 – irradiated FEP. Neat PTFE has a high wear rate (k~10^{-3} mm³/Nm) at speeds above 10 mm/s, while composites typically approach a moderate wear rate (k~10^{-5} mm³/Nm) as filler loading increases above 10 wt%.

The wear reducing mechanism of fillers in PTFE based composites remains a topic of debate. Lancaster [44] proposed that the hard wear-resistant fillers, especially those with a high aspect ratio, preferentially support the load and reduce the wear of PTFE in the composite. Sung and Suh [45] found that vertically oriented fibers were most effective in reducing wear, but suggested that the critical role of the filler was to arrest crack propagation, rather than to support the load. Tanaka *et al.*[46] suggested that the filler prevented the initial transfer of the PTFE to the counterface, and thus prevented transfer wear. Briscoe [47] noted the formation of a thin, well adhered transfer film for a high density polyethylene composite and hypothesized that fillers provide augmented transfer film adhesion, and thus reduced transfer wear by slowing transfer film removal and the requisite replenishment. Using X-Ray photoelectron spectroscopy (XPS), Gong *et al.*[48] found that the wear rate of PTFE was independent of chemical bonding with the

counterface, and concluded that cohesive failure within the PTFE must govern its wear rate. Blanchet *et al.*[49] had similar findings with XPS analysis of PTFE and PTFE composites in dry sliding, and concluded that the wear reducing role of the filler is to slow primary removal of material from the bulk by arresting crack propagation rather than slowing secondary removal of material from the counterface via increased transfer film adhesion. Bahadur and Tabor [50] and Blanchet and Kennedy [39] saw direct relationships between wear rate, debris size and the ease with which debris are expelled from the contact, and concluded that the fillers interrupt the formation of the larger debris that form during severe wear of PTFE.

PTFE Tribological Nanocomposites

Various fiber and particle fillers have successfully reduced the wear of PTFE by several orders of magnitude, but they also increase friction coefficients and abrade favorable transfer films and the counterface, both of which limit the effectiveness of the filler. Additionally, the high filler loadings (~20%) needed for significant wear reductions have detrimental effects on the beneficial frictional, thermal and chemical properties that make PTFE so attractive to designers.

The use of nanoparticles has the potential to eliminate many of the limitations of traditional fillers in a PTFE matrix. Low loadings of nanoparticles have imparted impressive improvements in mechanical properties such as strength, modulus and strain to failure to other polymeric matrices. They have also been found to reduce abrasion and promote transfer film development.

Despite the success of micro-fillers in abating severe wear of PTFE and the demonstrated benefits of nanoparticles on the properties of other polymer matrices, there was a sentiment in the field that nanoscopic fillers were ineffective in reducing the wear of PTFE. This was

primarily based on a study by Tanaka and Kawakami [46] that showed inferior wear performance of sub-micron TiO_2-PTFE composites to PTFE composites with larger sized fillers of other materials. As a result of these findings, it remains widely accepted that nanofillers cannot provide improvements in the wear resistance of PTFE because they are readily swept away within the matrix as debris by relatively large asperities.

In 2001, Li *et al.*[11] filled PTFE with 15 wt% nano-scale ZnO, and found a two order of magnitude reduction in wear while retaining a low coefficient of friction. This study not only established that nanofillers could be as effective as microparticles in reducing the wear of PTFE at lower loadings, but it also demonstrated that low friction coefficients could be retained upon loading. Uniform, well-adhered transfer films were observed for low wear composites and no signs of abrasion to the counterface were observed. Chen *et al.*[10] created a PTFE nanocomposite with single-walled carbon-nanotubes and found that friction coefficient was reduced slightly and wear resistance was improved by more than two orders of magnitude over unfilled PTFE. Sawyer *et al.*[16] made nanocomposites of PTFE with 38 nm Al_2O_3 and found a 600x reduction in wear with 20 wt% filler concentration. Wear was reduced monotonically as filler concentration was increased to 20 wt%. The most important result from these initial exploratory PTFE nanocomposite studies was a 10X improvement in wear resistance at 0.4 wt% nanoparticle loading; in the microcomposites literature, negligible reductions in wear are observed with less than 5 wt% microparticle loading. Initial rules of mixtures and preferential load support models of wear resistance were inadequate to predict the success of nanofillers at low loadings, resulting in an impetus to formulate new models for wear resistance in these unique materials to facilitate future material design.

Early investigations of the dominant wear reduction mechanisms in PTFE nanocomposites focused on strengthening and toughening of the matrix and the transfer films. Li *et al.*[11] used secondary electron microscopy (SEM) to study cross sections of unfilled and nanofilled PTFE. The neat PTFE had many fibers drawn from the bulk while the nanocomposite did not. They suggested that the nanoparticles effectively prevented the destruction of the banded structure. They also found thick, patchy transfer films formed by unfilled PTFE, while thin, tenacious transfer films were formed by the wear resistant nanocomposite. It was offered that the nanoparticles help bond the transfer film to the counterface which promotes low wear by protecting the soft composite from direct asperity damage. Chen *et al.*[10] also found evidence to suggest that the nanotubes prevented destruction of the crystalline structure of the PTFE. The high aspect ratio fillers were thought to reinforce the matrix by intertwining with PTFE crystals. In addition, they hypothesized that the nanotubes may provide additional self lubrication after breaking off from the composite during wear. In the study by Sawyer *et al.*[16], SEM revealed that the PTFE particles were decorated by the nanoscopic alumina during a powder blending process that preceded compression molding. The resulting structure after molding was cellular with thin regions of highly concentrated alumina rich material surrounding micrometer sized domains of nominally unfilled PTFE. These concentrated regions were hypothesized to act as barriers to crack propagation, reducing the delamination wear of PTFE. Further, it was offered that with increasing filler concentration, the number, size and possibly strength of the compartmentalizing regions increased.

In 2006, Burris proposed a simple, delamination-based wear model for PTFE nanocomposites that assumed that the severe wear mode of PTFE is one in which cracks pre-exist or initiate and propagate to failure [51]. Once these cracks encounter resistance (filler),

they are arrested or are turned toward the surface to generate a wear particle. Fillers were therefore assumed to play a crack arresting role that was described as damage compartmentalization. For simplification, it was assumed that the rate of initiation is constant so that each wear particle represents an initiation point. Therefore, the smaller the wear particle at each initiation point, the lower the rate of wear (this is the basis of the wear model presented by Bahadur and Tabor [50].

A few things should be kept in mind with this model: 1) the rate of initiation is probably faster in a filled system due to the addition of imperfections at the particle/matrix interfaces, 2) only cracks at depths of the same order of magnitude as the compartmentalized length can effectively be liberated as debris because of the surrounding material, and 3) the wear volume scales by R^3, where R is the characteristic compartment (matrix particle) radius. Point 2) likely counteracts the false assumption that the initiation rate is constant, and point 3) suggests that small matrix particles are desirable for reducing wear.

The PTFE used during processing was a granular compression molding resin and it was presumed that cracks are arrested most efficiently when each matrix particle is compartmentalized by a monolayer of filler; this corresponds to the least amount of filler required to effectively arrest a crack propagating through any matrix particle. At filler loadings less than the critical loading, the probability of arresting each crack is diminished. At loadings much greater than the critical loading, there is insufficient matrix available to effectively bind all of the particles and the mechanical properties of the composite rapidly deteriorate with loading. The model system is shown schematically in Figure 2-2.

monolayer coverage by filler

D_m

model system

filler

centerline sphere

D_c

matrix

$\theta^* = 0.907$
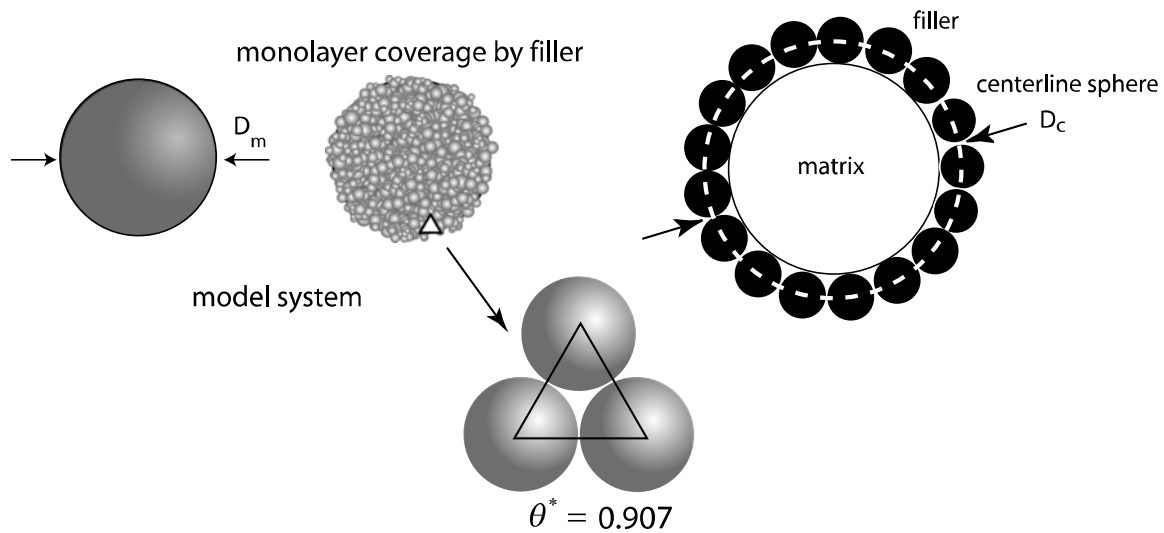
Figure 2-2. Representation of the matrix and filler particles used in compartmentalization modeling. The model matrix particle and filler particles are treated as spheres. The volume fraction for complete coverage of the matrix by filler is solved for using various simplifying assumptions.

v_f

D_f/D_m
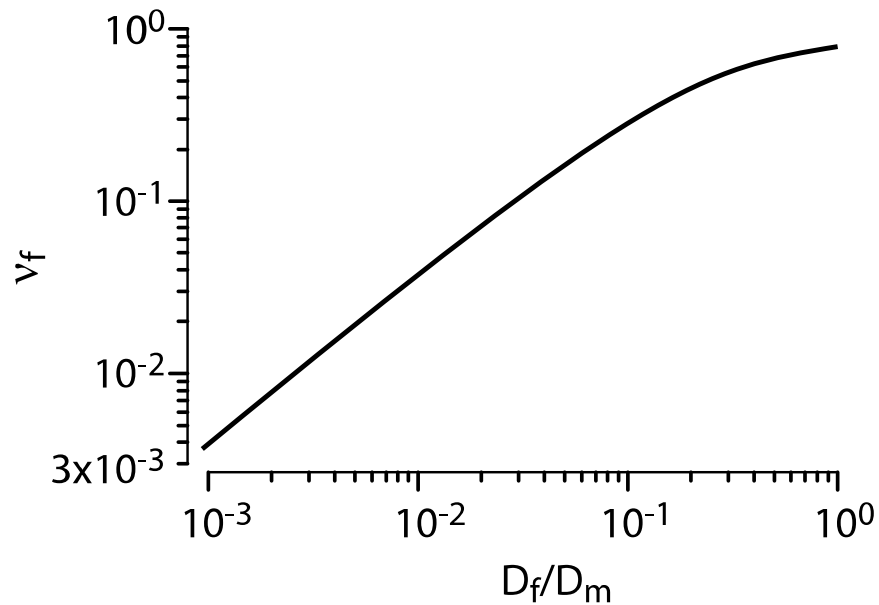
Figure 2-3. Plot of required filler volume fraction plotted vs. the dimensionless diameter. Nearly an order of magnitude reduction in required filler content is achieved by an order of magnitude reduction in filler diameter.

Figure 2-3 shows the volume fraction of filler required for complete damage

compartmentalization as a function of the relative size of filler to matrix particles. This graph

can be used as a simple tool for composite design, and is instructive in considering the

advantages of nanocomposites over microcomposites; by reducing the filler diameter by an order

of magnitude, the required filler content is also reduced by an order of magnitude. If the matrix

and filler particles are of the same size (D*=1), the simplified model gives a required 80 vol%

filler (this is underestimated by 15% due to the assumption that the filler is much smaller than

the matrix). If the filler is 1/100 the size of the matrix (D*=0.01), the model predicts a required

3.8 vol% filler (1.9% underestimated). For D* = 0.001, as is typical for nanocomposites, 0.4

vol% filler is required for monolayer coverage. Hence, very effective damage

compartmentalization in PTFE should be possible at very low filler volume fractions. Though

the model is oversimplified, it has the potential to capture a wide range of effects not accounted

for using rules of mixtures, including mechanical crack deflection, morphological and

crystallization effects in the matrix due to the presence of the nanoparticles.

In 2005, Burris and Sawyer used a highly energetic jet-mill dispersion technique to create

PTFE nanocomposites with 80 nm particles of alpha phase alumina [8]. The nanocomposites

were about an order of magnitude more wear resistant than the state of the art of the time, but

most striking was the fact that the 3000X improvement in wear resistance occurred with only

0.5% alumina loading; prior to this study, wear reductions were on the order of 100X and were

only found at nanoparticle loadings above 5 wt%.

In 2006, McElwain directly studied the effects of size on the tribological properties of 5

wt% PTFE composites using the same alpha phase alumina [52]. Particles were dispersed using

a high speed dry powder shear mixing technique. They found that 40 and 80 nm nanocomposites

were on the order of 10^4 more wear resistant, while 1, 2, 5 and 20 μm composites were on the

order of 10^2 more wear resistant than neat PTFE. These results suggested a transition in

behavior from the nanoscale to the microscale as opposed to the continuous behavior predicted

by the damage compartmentalization model. Interestingly, despite the similarity in performance of nanocomposites at 5 wt%, McElwain found negligible improvements at 1 wt%, while Burris and Sawyer retained high wear resistance. This result implicated the powder blending (jet-milling) as a crucial part of the processing.

Following McElwain's size study, additional experiments were conducted to study the cause of the reduced microcomposite wear resistance. They created hybrid composites with nanoparticles and microparticles and found that the presence of the microparticles in the composite disabled low wear sliding of the nanocomposites by providing an additional wear pathway that was otherwise unavailable. The microparticles abraded the transfer film and led to the abrasion and transfer wear process typical of microcomposites.

CHAPTER 3
IDENTIFICATION OF WEAR RESISTANCE MECHANISMS: MOTIVATION FOR
CURRENT STUDIES

In general, the results from the PTFE nanocomposites tribology literature are striking.

Contrary to early suggestions that nanoparticles would be ineffective fillers in reducing wear of

PTFE, the use of nanoparticles in PTFE has been very successful with 1,000X improvements in

wear resistance occurring with as little as 1wt% (0.5% by volume) nanoscale filler. There is

however, a clear lack of understanding of the fundamental mechanisms of wear and wear

resistance in these materials, which makes PTFE nanocomposite design an exercise of trial and

error.

It has been demonstrated that the presence of micron-scale abrasives can increase wear

rates by orders of magnitude due to a disruption of transfer film development [52]. However,

studies showing impressive improvements at low nanoparticle loadings are contrasted by studies

demonstrating equally unimpressive improvements; significant differences in the tribological

properties of nanocomposites in the literature occur with seemingly subtle differences in the

materials and processing methods. Many undefined variables arise from study to study, and too

often, only qualitative descriptors of transfer films, debris morphology, mechanical properties

and most importantly, nanoparticle dispersion are used. To date, it is unclear whether the key

factors driving the physical properties of PTFE nanocomposites have been identified. Previous

studies suggest that the wear rates of these systems are complex and coupled, possibly involving

crack deflection, filler/matrix interactions, regulation of debris size and debris/counterface

interactions, but there is a current need for more quantitative measurements to enable

identification of relevant wear resistance mechanisms. Given the scope of this area, a broad

exploratory effort was necessary to direct the current research initiative.

Transfer films have been shown to be a critical part of the solid lubricant tribo-system, providing a low shear interface for sliding and forming a protective layer over counterface asperities. In the material science literature, it is well understood that the filler/matrix interface can have a dramatic influence on a number of critical properties [25, 53-60]. In nanocomposites, the number and area of these interfaces are inherently large, and these regions can have far-field effects on matrix crystallinity, phase and morphology. These three areas were systematically studied by Burris *et al.*[61]; the results are outlined in the following sections. The first quantitatively examine the morphological, tribological, compositional and chemical properties of the transfer films and address their influences on the tribo-system. The following section examines the nature of the matrix/filler interface and its effect on the tribology of the system. The final section discusses the phase and morphology changes in the PTFE that occur as a result of nanoparticle inclusion, and the effects of these changes on the wear resistance of the nanocomposite.

Investigations of Transfer Films

Contrary to early suggestions that nanoparticles could not appreciably improve the wear resistance of PTFE, it has been shown that nanofillers can be far superior to microfillers with a transition in the dominant wear reduction mechanism likely occurring at a particle size on the order of 100 nm. Preliminary evidence suggests that reduced counterface abrasion, reduced third body wear and retention of protective transfer films are primarily responsible for the improvements in wear resistance. Thin, uniform transfer films consistently accompany wear resistance in the tribological nanocomposites literature [8, 9, 11, 17, 19, 30-33, 51], but quantitative measurements of these films are lacking. Some authors suggest that wear resistance is due to the transfer film protecting the composite while others offer that the films are formed as a consequence of low wear. It is currently unclear why and how these films form, how they

facilitate wear resistance, if they are composed primarily of the PTFE, the filler or the composite, and if chemical reactions are involved.

Burris and Sawyer [8] conducted a study with 5 wt% α phase and Δ:Γ phase alumina-PTFE nanocomposites against various rough counterfaces to study the effect of asperity size on the transfer and wear of different PTFE nanocomposites. The surfaces were made using different standard finishing techniques and interferometry measurements of these surfaces are shown in Figure 3-1.
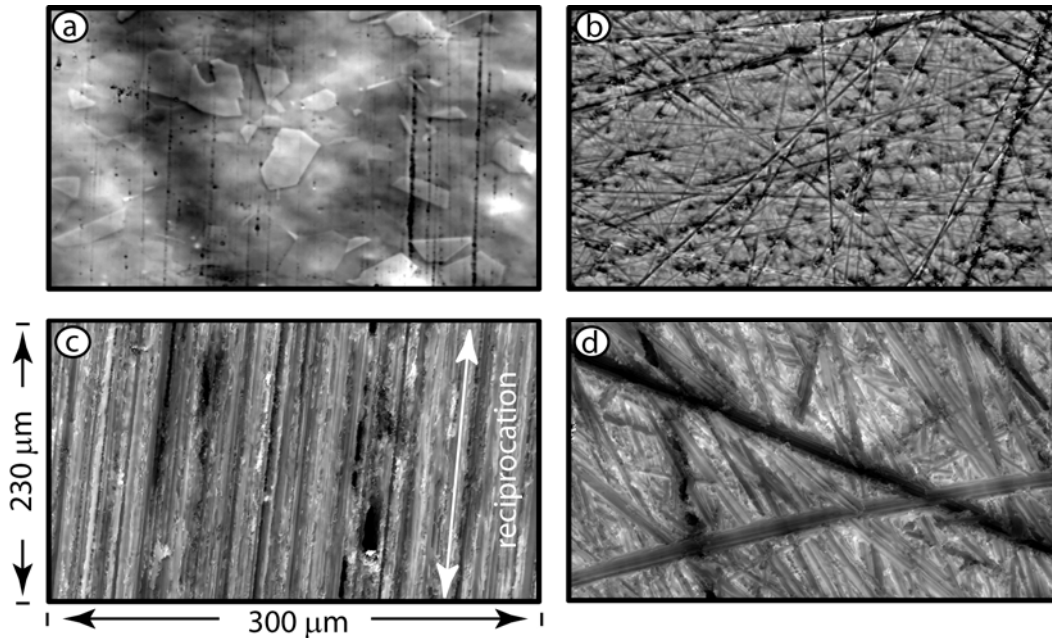
Figure 3-1. Surfaces used to study roughness effects on PTFE nanocomposite transfer and wear: a) electro-polished – Rq (root mean squared roughness) = 80nm, b) lapped – Rq = 160nm, c) wet-sanded – Rq = 390nm, d) dry-sanded – Rq = 580nm. Note that the lay of the wet-sanded surface is oriented in the direction of sliding; it is smoother in the direction of sliding than against it.
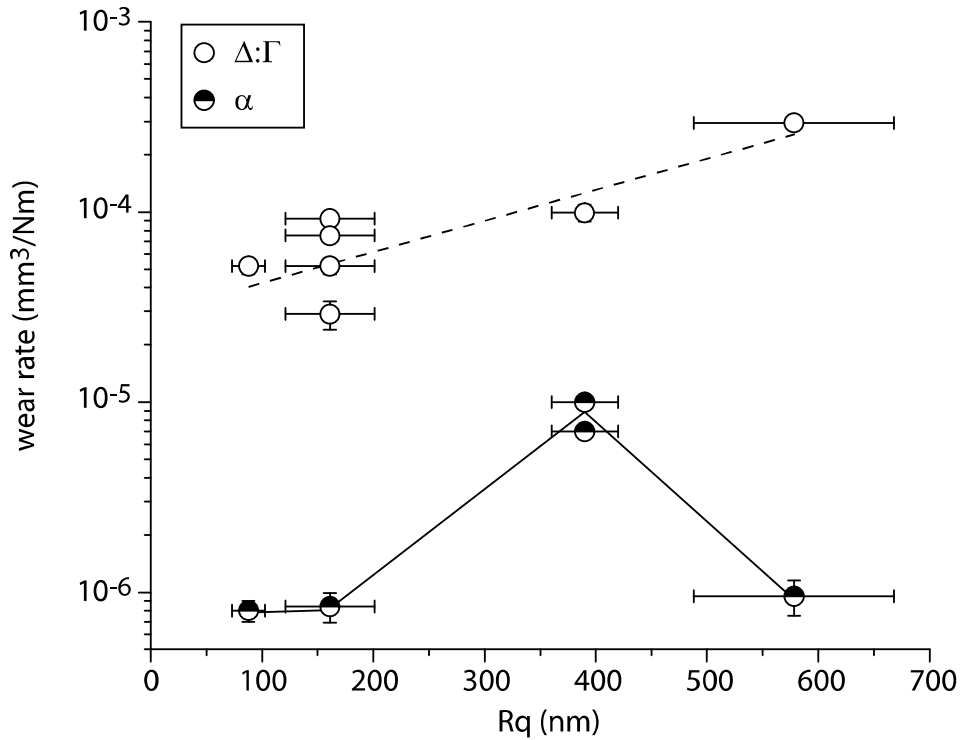
Figure 3-2. Wear rate plotted versus counterface surface roughness, Rq for 5 wt% 40 nm Δ:Γ phase and 80 nm α phase alumina-PTFE nanocomposites. The two phases of alumina filler produce wear rates that differ by 100X on average with different surface sensitivities.

Wear rates for these composites are plotted versus counterface roughness R_q in Figure 3-2. The different phases of alumina were found to result in widely different tribological properties despite identical processing and testing. Wear rates of Δ:Γ alumina nanocomposites increased monotonically from 50-300x10^{-6} mm^3/Nm with increased surface roughness. Additionally, wear debris were relatively large and transfer films thick and discontinuous. Wear rates of α alumina nanocomposites did not correlate with roughness and were significantly lower than those of the Δ:Γ nanocomposites ranging from 0.8-10x10^{-6} mm^3/Nm. Wear rates from tests conducted on counterfaces without predominant orientation were equivalently low despite roughness ranging from 80 – 580 nm R_q. Transfer films on these surfaces were all thin and uniform. Testing against the oriented wet-sanded surface on the other hand increased the wear rate of the

nanocomposites by an order-of-magnitude. A repeat at this condition confirmed the validity of the result. Transfer films on the wet-sanded surface were incomplete, thick and banded in the direction of sliding.

Transfer Film Morphology

An examination of the data collected throughout the test reveals an additional key difference between $\Delta{:}\Gamma$ and α phase alumina nanocomposites. The $\Delta{:}\Gamma$ nanocomposites reached steady state almost immediately, while the α nanocomposites had a significant transient period of moderate wear followed by a transition to a lower steady state wear rate. Despite the relative insensitivity of steady state wear rates to counterface roughness for α nanocomposites, the transient wear rate (during transfer film development) increased monotonically with increased roughness. Additionally, the total volume removed during the transient portion of the test increases with increased roughness. These results suggest that as material is removed from the sample and deposited onto the counterface, more of the asperities become covered by a transfer film and the wear rate is reduced. Larger asperities require more material to transfer before steady state is reached, but at steady state, abrasion is insignificant and wear rate is independent of roughness. The orientation of the wet-sanded surface likely disrupted the formation of a stable transfer film, resulting in comparable transient and steady state wear rates. It can be concluded that the presence of a protective transfer film is necessary for low wear of PTFE nanocomposites. It is also interesting to note that when neither composite was sufficiently protected by transfer films, either during the transient region or against the wet-sanded surface, the α alumina nanocomposites outperformed the $\Delta{:}\Gamma$ nanocomposites. This suggests a difference in the wear mechanisms, which likely governs the ability of the composite to form

protective films during sliding. Qualitatively, transfer films were found to increase in thickness and discontinuity with increasing wear rate.

Thin, uniform transfer films and fine debris consistently accompany wear resistance in these studies and in the nanocomposites tribology literature. Global relationships between wear rates and transfer films were studied by quantitatively measuring transfer films of widely varying PTFE-based tribo-systems using either scanning white-light interferometry or mapping stylus profilometry. These systems include 5 wt% alumina-PTFE composites with α and Δ:Γ particle phases, 40 nm, 80 nm and 0.5 μm particle sizes, and counterfaces of polished, lapped, wet-sanded and dry-sanded surface finishes. Wear rate is plotted as a function of maximum transfer film thickness in Figure 3-3. Despite varying particle phase size and surface finish, wear rate is approximately proportional to the maximum thickness of the transfer film cubed. Not only do thicker films imply larger debris, but it is suggested that thick transfer films are more easily removed by the passing pin and as a consequence need more rapid replenishment.

It is well known that under certain low speed sliding conditions, PTFE deposits very thin and oriented transfer films [36, 37, 62-65]. The orientation produces a model sliding condition where chain entanglement is minimized and pure axial sliding of PTFE chains past one another results in the very low friction coefficients observed under these conditions ($\mu = 0.03$-0.07). It is hypothesized that the role of the filler is to reduce gross damage to PTFE which promotes the formation of thin, aligned PTFE films under severe sliding conditions and enables low wear of the nanocomposite.
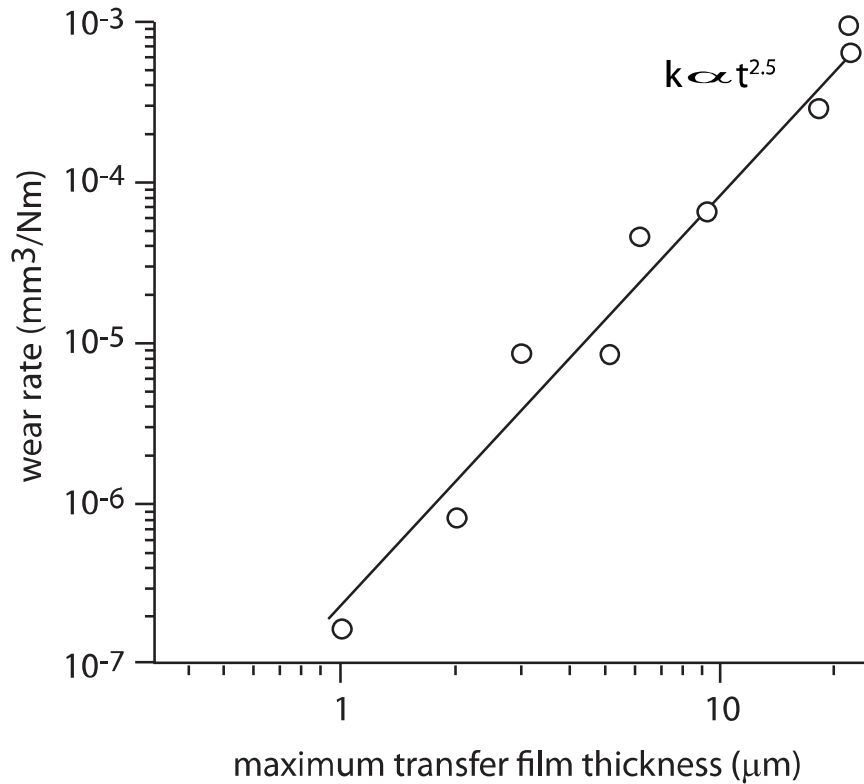
Figure 3-3. Wear rate plotted versus the maximum transfer film thickness as measured with optical interferometry. This data includes results of 5 wt% 44 nm Δ:Γ, 80 nm α and 0.5 μm α composites against the best and worst performing counterfaces, and 5 wt% 80 nm and 0.5 μm composites and unfilled PTFE against polished surfaces. Wear rate is proportional to the maximum transfer film thickness cubed.

The friction and wear properties of the films themselves were measured using microtribometry to test the hypothesis that thin, aligned films of unfilled PTFE are wear resistant. Model films of neat PTFE were deposited onto a thin steel foil with a sliding velocity of 254 μm/s for 1000 reciprocation cycles at 25°C under 6.3 MPa of normal pressure. Atomic force microscopy was used to estimate an average film thickness of 50 nm; an AFM image of a PTFE transfer film formed during low speed, unidirectional sliding on bare polished silicon is shown in Figure 3-4. It is evident that such films are highly aligned in the sliding direction and on the nanometer size scale.
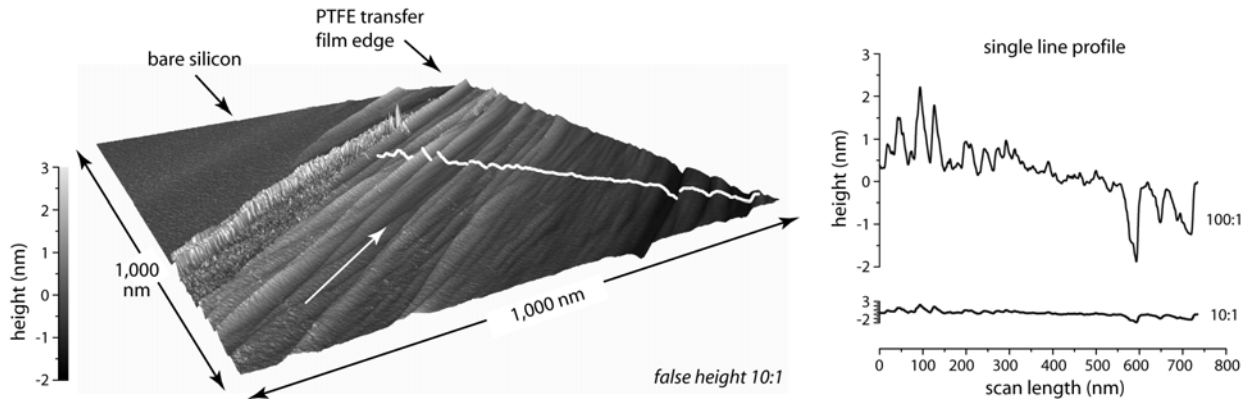
Figure 3-4. An AFM image of the transfer film produced through unidirectional sliding of PTFE on a polished silicon wafer. The white arrow inside the PTFE transfer film indicates the sliding direction. The single line profile (shown in white on the trimetric view) portrays a relatively smooth film; features within the image clearly document the fibrillated and oriented nature of the transfer film. Topographic data measured across the film edge indicate a transfer film thickness at this location of substantially less than 10 nm. AFM studies were conducted by Professor Scott Perry's group at the University of Florida.

After creation, the film covered foils were cut into rectangular samples for testing. Custom designed sample mounts fixed opposing foils into a crossed-cylinder geometry. This geometry reduces misalignment sensitivity, minimizes edge effects and helps reduce pressures to values more typical of those found in macro-scale testing. Parallel (chains oriented in the direction of sliding) and perpendicular (chains oriented against the direction of sliding) aligned films were tested to study the hypothesized tribological anisotropy of aligned PTFE films. Normal and friction forces were continuously measured at the stationary pin, while a 600μm reciprocation displacement was imposed on the counterface. Tests with an average sliding speed of 100 μm/s and a normal load of 500 mN were conducted over 250 sliding cycles. The contact patch was estimated with *ex-situ* optical observation to be 200 μm in diameter; this translates into an average pressure of 15 MPa. The results of the microtribometry experiments are shown in Figure 3-5.
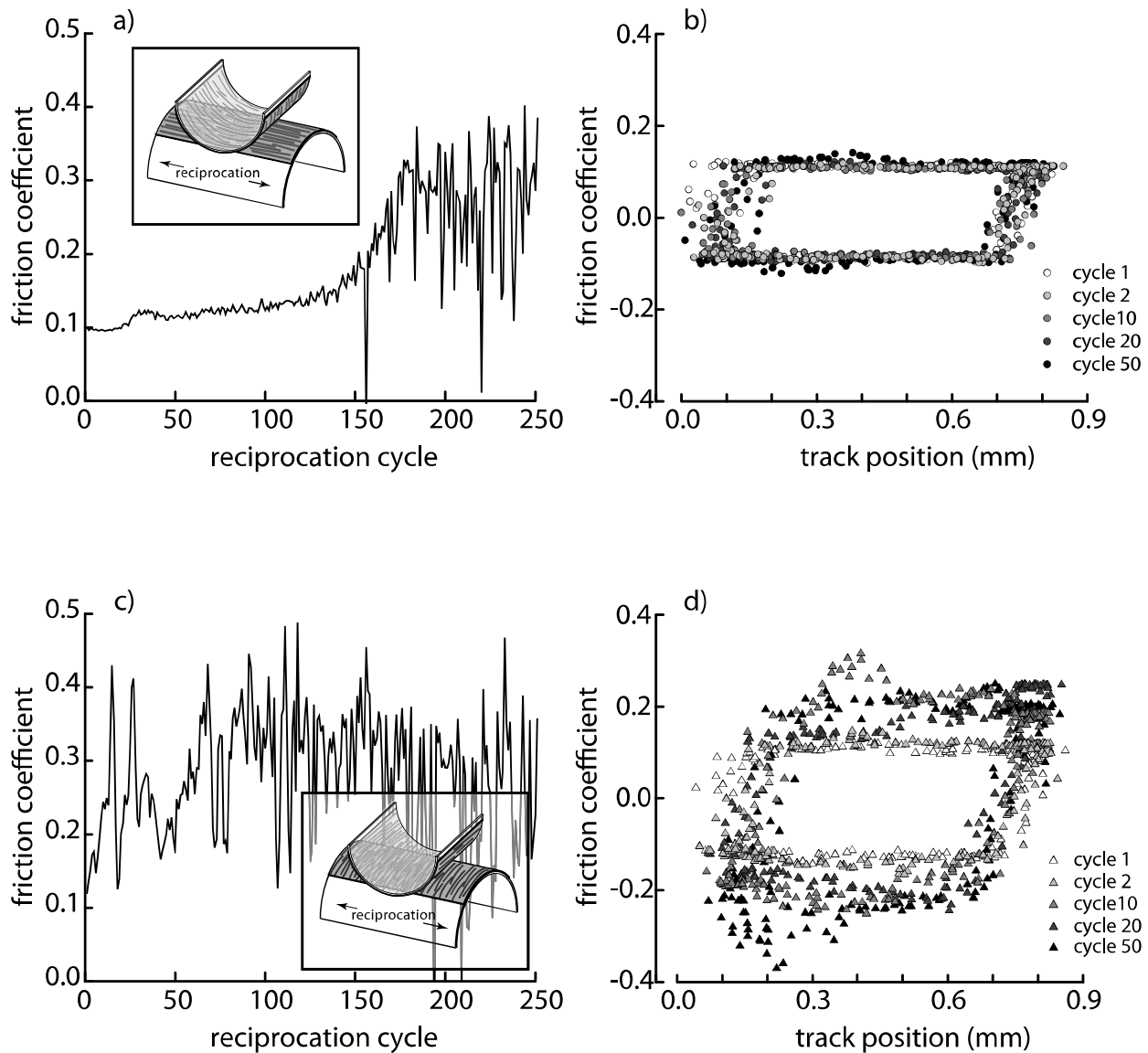
Figure 3-5. Microtribometry friction results for the crossed cylinder oriented PTFE transfer film tests. Friction coefficient is examined versus reciprocation cycle for a) parallel and c) perpendicular configuration. The evolution of friction coefficient along the reciprocation track is also plotted for both the b) parallel and d) perpendicular configurations. The perpendicular alignment of the films leads to rapid failure of the films.

In line with the hypothesis that orientation in the sliding direction facilitates low friction and wear, perpendicular alignment of the films led to complete failure of the film (denoted by $\mu > 0.2$) in about 10 cycles, while parallel aligned films were at least 10X more wear resistant.

Despite having similar average values of friction coefficient for the first few passes, differences can be seen in the positionally resolved friction data on the right of Figure 3-5. Examining the first pass, the parallel sample has a steady friction loop, while the perpendicular friction loop has significant scatter. The mechanism of motion accommodation appears more damaging in the case of the perpendicularly aligned films, and the tendency of these films to reorient into the direction of sliding is likely responsible for the erratic friction and wear behavior. The parallel aligned films have much lower wear presumably as a result of the stable orientation. A hybrid configuration, which consisted of a perpendicular top film and a parallel bottom film, was created to test the hypothesis that sliding preferentially occurs at parallel interfaces in samples with different possible sliding orientations. The frictional behavior was nearly identical to that of the parallel configuration which suggests that the parallel interface is the preferred interface for sliding.

Since protective transfer films are necessary to reduce wear of these nanocomposites against counterface asperities, the wear rate of the transfer film places a lower limit on the wear rate of the composite. An estimate of wear rate for the parallel aligned films was calculated to determine whether model films of unfilled PTFE could possibly support low wear sliding. The contact area on the top foil (pin) and bottom foil (counterface) are 0.033 and 0.12 mm^2, respectively, so failure of the top film should occur first, followed by direct asperity contact and rapid deterioration of the bottom film. Failure of the top film in parallel alignment occurred after approximately 150 cycles. The wear rate in this case is calculated as,

$$k = \frac{50x10^{-6}\,mm}{15N/mm^2 \cdot 150cycles \cdot 1.2x10^{-3}\,m/cycle} = 2x10^{-5}\frac{mm^3}{Nm} \qquad \text{Eq. 3-1}$$

Despite the superiority of the parallel aligned transfer film, estimation of the wear rate reveals that rates are still orders of magnitude higher than those found for many low wear PTFE

nanocomposites (~10^{-5} versus 10^{-7} mm^3/Nm). It can be concluded that even model thin and aligned transfer films of PTFE are incapable of supporting low wear sliding. The films formed by sliding of a low wear nanocomposite must therefore be comprised of composite material or some more wear resistant variant of PTFE.

Similar experiments were conducted for transfer films of a low wear 10 wt% PEEK filled PTFE composite. In each configuration, the composite film had lower and more stable friction coefficients for the duration of 1000 cycle tests with no obvious signs of wear in post test analysis. Clearly, the compositions and chemistries of these films are additional factors that require quantification for a more complete understanding of these nanocomposite systems.

Transfer Film Composition

Though X-Ray photoelectron spectroscopic (XPS) chemical and compositional analyses of unfilled polymer and micro-composite transfer films have been conducted by several investigators [48, 49, 66], it is unclear how composition and chemistry evolve in the transfer films of PTFE nanocomposites or how this evolution influences tribological phenomena observed during testing. XPS was used to test the hypothesis that transfer films consist of composite material. PTFE nanocomposites were created with $^1/_8$%, $^1/_2$% and 1% (by volume) loadings of 40 nm α alumina nanoparticles. In a control set, the particles were untreated and in a second set of samples, the nanoparticles were treated with a fluorinated silane. The treatment was hypothesized to improve dispersibility and compatibility with the matrix. Treated (fluorinated) and untreated samples were compression molded, machined and tested. The tribological experiments were conducted on a linear reciprocating tribometer. Photoelectron spectra of the C, O, F, Al and Si regions were collected using a PHI 5700 Xray Photoelectron spectrometer equipped with a monochromatic Al Kα X-ray source (hv=1486.7 eV) incident at

90° relative to the axis of a hemispherical analyzer. The spectrometer was operated at high resolution with a pass energy of 23.5eV, a photoelectron take off angle of 45° from the surface normal and an analyzer spot diameter of 1.1mm. All spectra were collected at room temperature with a base pressure of 1×10^{-9} torr. Electron binding energies were calibrated with respect to the C1s line at 291.6eV (C-F).

Even at very low loadings, alumina was found to transfer to the counterface with the PTFE (trace amounts of Si were also found in fluorinated samples). The atomic fraction of aluminum in the transfer films is plotted versus the aluminum content in the bulk in Figure 3-6. Aluminum in the transfer films of fluorinated samples (filled circles) was found in direct proportion to the loading in the bulk sample. The untreated $\frac{1}{8}$% sample had an unexpectedly high amount of aluminum in the film, possibly due to poor dispersion or agglomeration during processing. Alternatively, aluminum could have accumulated in the transfer film with wear of the sample -- this sample had 50X higher wear than any of the other samples -- Blanchet and Han [67, 68] have previously described this mechanism as one of preferential removal of PTFE from the system which leaves the interface rich with filler.

$k\sim10^{-5}$ mm^3/Nm

$k\sim10^{-7}$ mm^3/Nm

Al in transfer film (atomic%)

Al in bulk (atomic %)

○ untreated
● treated
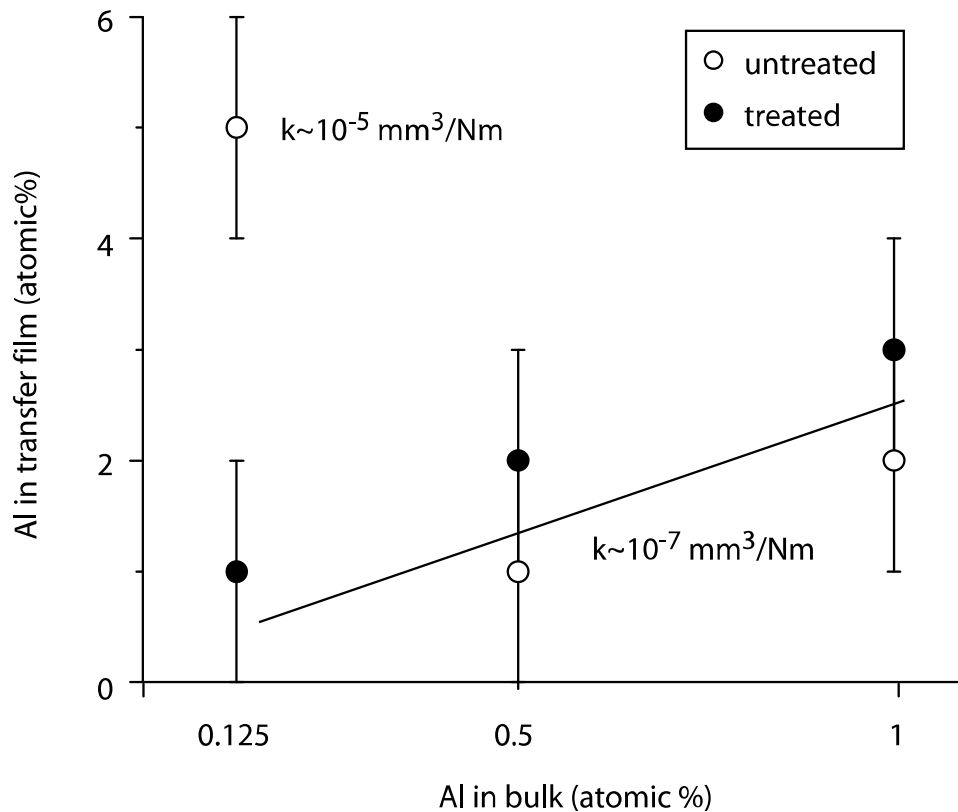
Figure 3-6. Aluminum atomic content (%) in the transfer films of virgin and fluorinated nanocomposites plotted versus the atomic content as prepared in the bulk. Measurements were made in the center of each wear track. In low wear samples the aluminum content in the transfer film is linearly proportional to the aluminum content in the bulk sample. Evidence of filler accumulation was observed for the less wear resistant sample. XPS studies were led by Professor Scott Perry's group at the University of Florida.

Similar XPS analyses of transfer films formed from both types of alumina particles revealed a higher proportion of oxygen than would otherwise be predicted based on the aluminum present, suggesting tribo-chemical oxidation of the PTFE during extended sliding. Furthermore, these measurements demonstrate a correlation between friction coefficient and the oxygen content of the transfer film (Figure 3-7). It is unclear whether an increase in friction of the fully formed transfer film drives the oxidation or if oxidation itself, occurring in the creation of the transfer films, leads to the higher friction coefficients.
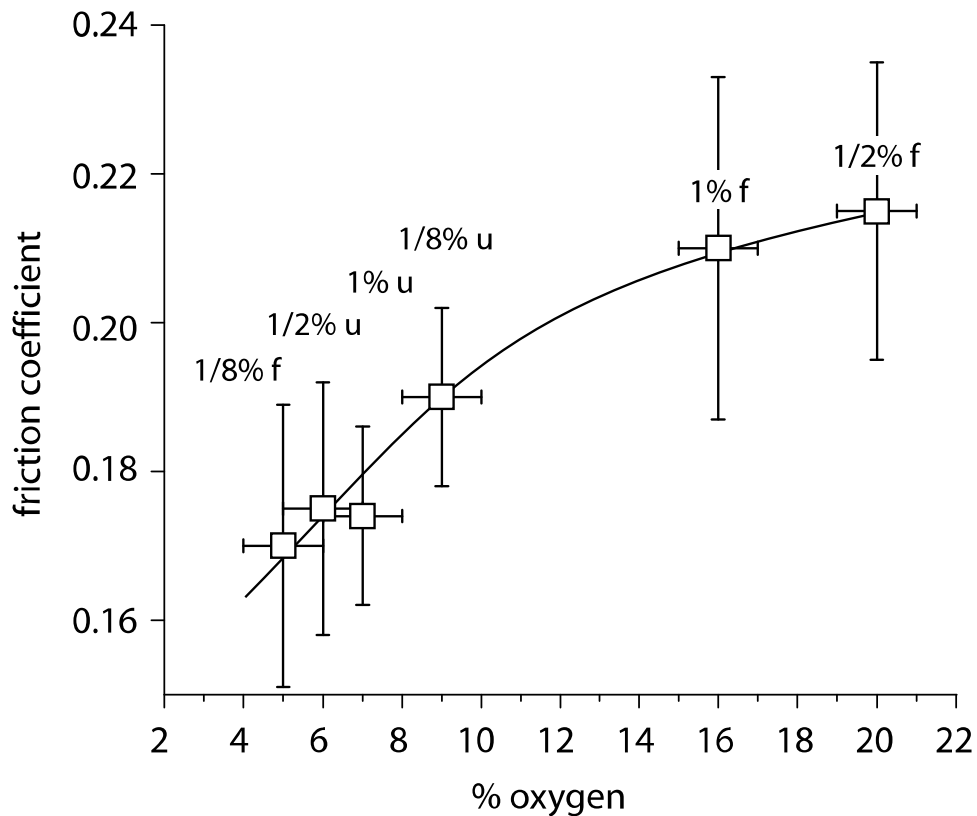
Figure 3-7. Friction coefficient plotted versus oxygen content as measured using X-Ray photoelectron spectroscopy. The symbol 'u' denotes untreated alumina and 'f' denoted fluorinated alumina. XPS studies were led by Professor Scott Perry's group at the University of Florida.

The transfer films formed from PTFE nanocomposites containing fluorinated alumina exhibited frictional behavior uncharacteristic of PTFE; friction coefficients were lowest at the reversals (ends of the wear track) and highest in the center. Based on this behavior and the oxygen-friction coefficient correlation presented above, it was predicted that oxygen content decreases toward the ends of the wear track where friction was found to be lowest. Figure 3-8 shows friction coefficient, transfer film thickness and oxygen content as functions of the pin center track position over half of the track for a 2 wt% fluorinated 40 nm α phase alumina-PTFE nanocomposite. XPS was used to determine oxygen content in the films and three dimensional mapping stylus profilometry was used to map film thickness; the thickness envelope shown in Figure 3-8 reflects averaged results of mapping stylus profilometric measurements of the transfer

film plus and minus one standard deviation. Both oxygen content and thickness correlate well

with the friction coefficient along the wear track for the final cycle of sliding.
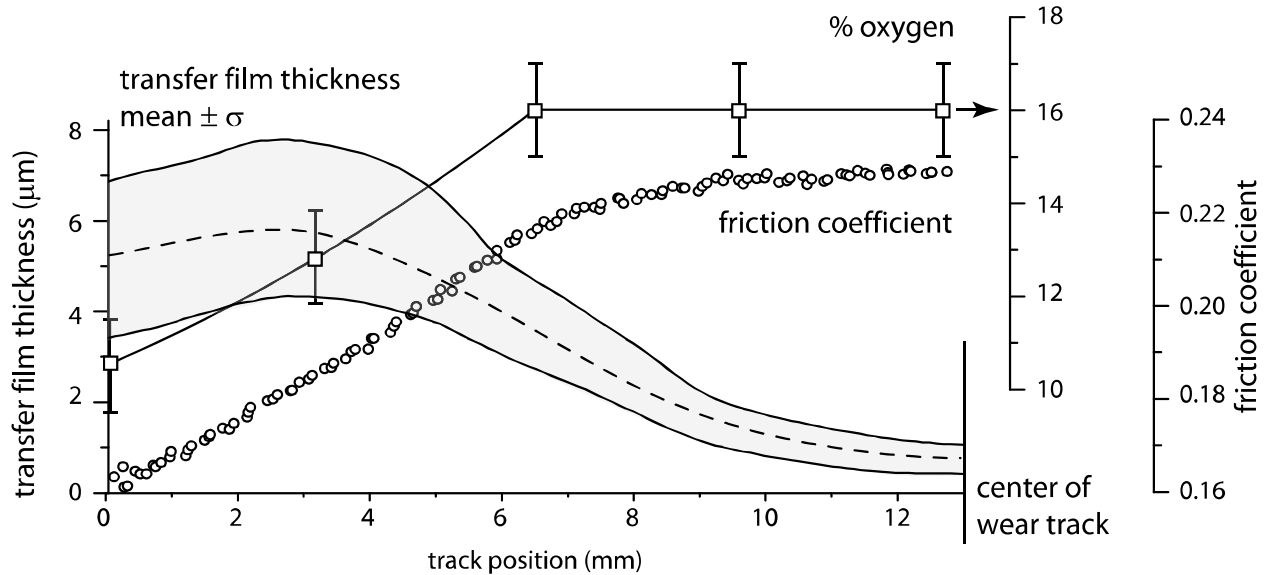
Figure 3-8. Transfer film thickness, oxygen content and friction coefficient plotted versus track
position over half of the wear track for a 1% fluorinated sample. The transfer film
thickness envelope represents the mean plus and minus one standard deviation. The
position dependent friction coefficient correlates well with both oxygen content and
thickness.

Transfer Film Chemistry

The oxidation of PTFE is initially surprising given its known chemical inertness.

However, very wear resistant materials produce very thin transfer films that are exposed to

prolonged frictional energy dissipation at the interface. Over extended sliding distances,

sufficient energy can be absorbed by these thin layers to initiate even low probability chemical

events. XPS analysis of a 5 wt% 80 nm α alumina transfer film after sliding with a wear rate of

10^{-7} mm^3/Nm further probed the tribo-chemical degradation of low wear PTFE. The comparison

of the core level C 1s spectra of unfilled PTFE to that of the nanocomposite transfer film shown

in Figure 3-9 demonstrates clear evidence of a chemical transformation of PTFE in the process

of transfer film deposition and wear.
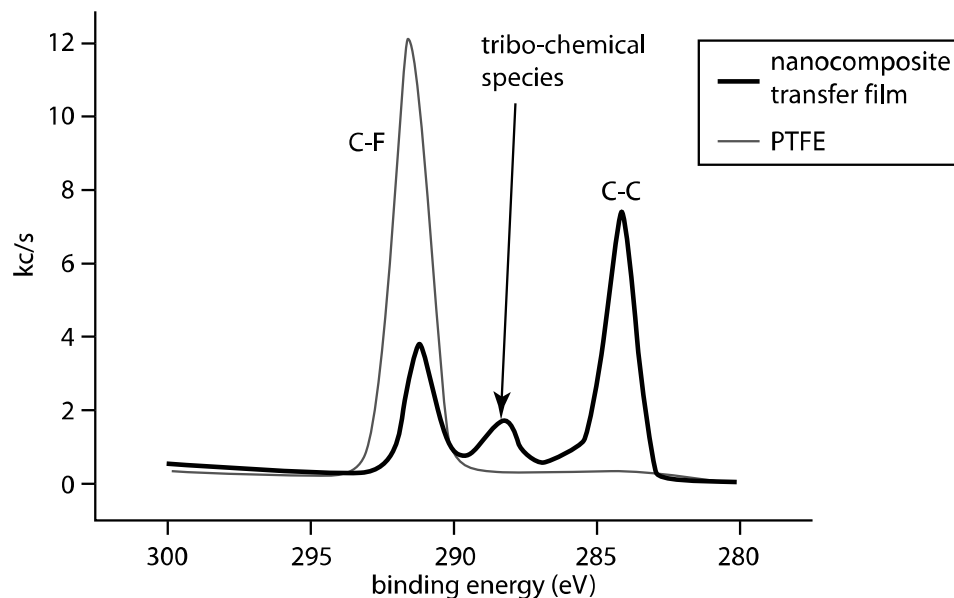
Figure 3-9. Comparison of the core level C 1s spectra of unfilled PTFE to that of the nanocomposite transfer film. The appearance of a new peak at 288 eV provides evidence of a chemical transformation in the PTFE that occurs during wear. XPS studies were led by Professor Scott Perry's group at the University of Florida.

The data confirm a reduction in C-F intensity at 292 eV, consistent with de-fluorination of the transfer film and the measured reduction in the F 1s integrated intensity (data not shown). This change is accompanied by the appearance of new C species giving rise to intensity at 288 eV and 284 eV. While the relative changes in the 292 eV and 284 eV regions could be rationalized through the adsorption/deposition of adventitious carbon during sliding or sample preparation, the 288 eV feature can be correlated with the relative wear resistance of filled PTFE transfer films.

Several investigators have intentionally degraded PTFE using various techniques including gamma ray, electron beam, and ultraviolet irradiation and have correlated chemical degradation with changes in mechanical properties [69-72]. For example, Zhao *et al.*[73] noted a rapid fluorine loss on the surface of PTFE when exposed to vacuum ultraviolet radiation as well as increased optical absorbance due to carbon exposure which resulted in a brownish appearance of the sample. Similar brown discolorations are often found in low wear transfer films. Lappan *et*

al.[74, 75] and Oshima *et al.*[76] used infrared spectroscopy to identify various reaction products from the degradation, noting processes involving defluorination and chain scission which produce terminal and branched CF_3 groups, carbon-carbon double bonds and branched (cross-linked) carbon structures. COF and COOH have also been observed. High speed magic angle spinning nuclear magnetic resonance (HS MAS NMR) spectroscopy measurements of degraded PTFE by Katoh *et al.*[77] and Fuchs *et al.*[78] provided evidence of cross-linking in degraded PTFE. Oshima *et al.*[76] used the HS MAS NMR data to identify chemical structures of CF_2, -CF (cross-linked) and =CF (double bonded carbon) in XPS spectra. These degraded PTFE structures showed very similar spectroscopic signatures to the 288 eV peak found in wear resistant transfer films.

Blanchet *et al.*[14, 79, 80] previously conducted tribology experiments on irradiated PTFE and FEP composites and demonstrated that the wear resistance of each was improved by several orders-of-magnitude with 30 Mrad doses of electron irradiation. More recently, an analogous study was conducted to further explore the influence of degradation on the tribological properties of PTFE. A commercial chemical etch was used to emulate tribo-chemical degradation by stripping fluorine from the surface of an unfilled PTFE wear sample. Intensity at 288 eV was verified in the XPS spectrum of the etched surface. The tribological properties of the degraded PTFE surface coating were measured for linear reciprocating sliding at 6.3 MPa and 50 mm/s. The degraded PTFE was found to be 100X more wear resistant than unfilled PTFE, verifying that conjugated PTFE offers the possibility of increased wear resistance. This period of wear resistance was followed by a sharp increase in wear and a 10% reduction in friction coefficient as the more wear resistant degraded surface wore through to the virgin PTFE beneath. The rate of material consumption due to wear here was greater than the rate of tribo-chemical degradation,

and it is likely that in these nanocomposite systems, the degradation mechanism supplements the other more dominant mechanisms that enable degradation to occur.

Role of Transfer Films

It has been shown that transfer film morphology, composition and chemistry all play important roles in determining the wear rate of the films and thus the tribo-system. It has also been shown that certain surface characteristics can destabilize the transfer film which disables low wear sliding. It is clear that the presence of a high quality transfer film is a necessary condition for low wear sliding of PTFE nanocomposites; it is unclear whether it is a sufficient condition for low wear. To test this hypothesis, an alumina-PTFE nanocomposite known to ordinarily produce poor quality transfer films (5wt% 44 nm Δ:Γ alumina) was tested upon a pre-deposited transfer film formed under ultra-low wear sliding conditions ($k<10^{-8}$ mm^3/Nm [9]). It was found that the composite had the same wear rate (7×10^{-5} mm^3/Nm) whether it was tested against a wear resistant transfer film or a fresh counterface. Despite the presence of an ultra-low wear transfer film, thick platelets indicative of delamination wear were deposited on top of the pre-existing transfer film. The abrasive wear that is reduced by the transfer film appears to have a negligible influence on the wear rate of this nanocomposite due to the severity of its delamination wear. *In-situ* optical microscopy of the wear track revealed that the transferred material is very unstable, moving appreciably after each cycle. Clearly the mechanics of the nanocomposite itself dominate the properties of this system and govern the development of the transfer film. These results suggest that while thin transfer films are required for low wear, they are more likely a consequence of the low wear debris morphology than the source of wear resistance.

Investigations of Internal Interfaces

The critical role of transfer films in enabling low wear of PTFE nanocomposites has been demonstrated, but bulk properties of the composite seem to dictate the initiation and development of the films as well as the ability of the composite to achieve low wear against high quality transfer films. Bahadur and Tabor [50] and Blanchet and Kennedy [39] noted a trend of decreased wear debris size with decreased wear rate and suggested that the primary role of the filler was to reduce the size of the wear debris. Because the wear rate is proportional to volume, which is proportional to the cube of a characteristic diameter of the debris, reducing debris size inherently reduces the wear rate, promotes engagement of debris with the surface and improves transfer film stability. Burris and Sawyer [8] hypothesized that the size and shape of the debris during run-in were critical in the development of these transfer films, and that the film morphology observed during low wear was a consequence of low wear rather than the cause. They envisioned a wear model proposed by Blanchet and Kennedy [39], where the cracks that lead to the destructive delamination in PTFE were effectively arrested by the filler, resulting in reduced debris size and stable transfer film formation. The strength of the interface would have a critical influence on such a system.

Often, nanoparticles and polymer matrices are inert by design to limit environmental sensitivity of the tribological response. This inertness limits chemical interaction at the filler/matrix interface and can lead to inherent weakness. Wagner and Vaia [55] articulated the importance of the bonding at the interface for a nanotube reinforced polymer. They calculated interfacial shear strength to be 3 MPa with only van der Waals interactions present, and in excess of 100 MPa with only 1% covalent bonding of the carbon atoms. Many investigators have successfully improved interfacial bonding in composites with surface coatings that compatibilize the filler with the matrix. He *et al.*[57] found improved mechanical properties and dispersion

when the nanoparticles were plasma-modified, and Eitan *et al.*[25] found improved load transfer via strain dependent Raman spectroscopy and improved bulk mechanical properties of a treated MWCNT filled polycarbonate over the nanocomposite with untreated nanotubes. While the studies of Burris and Sawyer [8] showed a strong dependence of wear rate on alumina phase suggesting the potential importance of these internal interfaces in tribology, it was unclear whether observed differences were due to particle phase or size since both phase and size varied in the experiments. Recently, a series of experiments were conducted on PTFE nanocomposites with smaller α phase alumina to evaluate the potential size effect. Figure 3-10 shows TEM images of the 44 nm Δ:Γ, 40 nm α and 80 nm α phase nanoparticles. The α phase particles have an irregular plate-like morphology while the Δ:Γ particles are spherical.
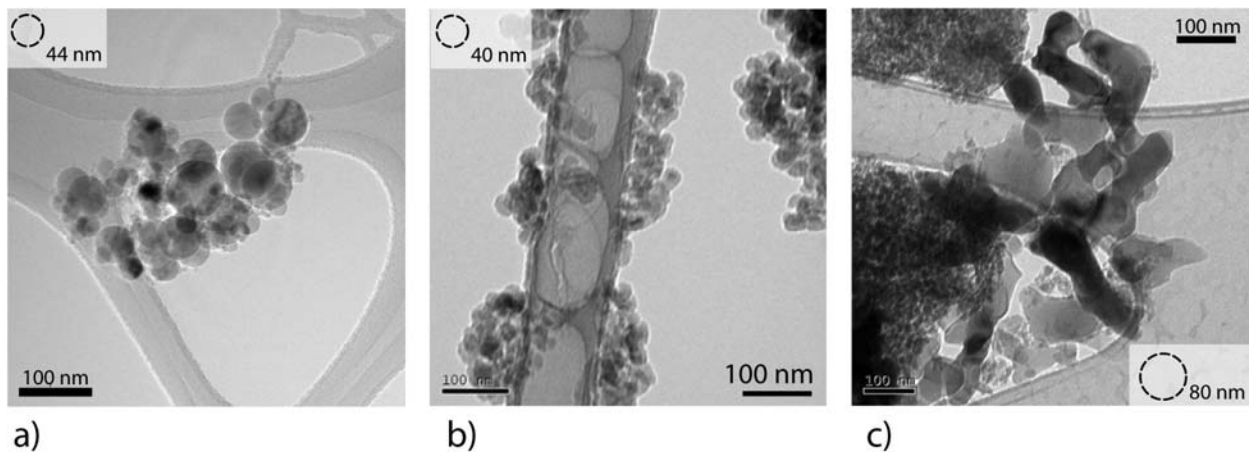
Figure 3-10. Transmission electron images of a) 44 nm Δ:Γ, b) 40 nm α and c) 80 nm α particles.
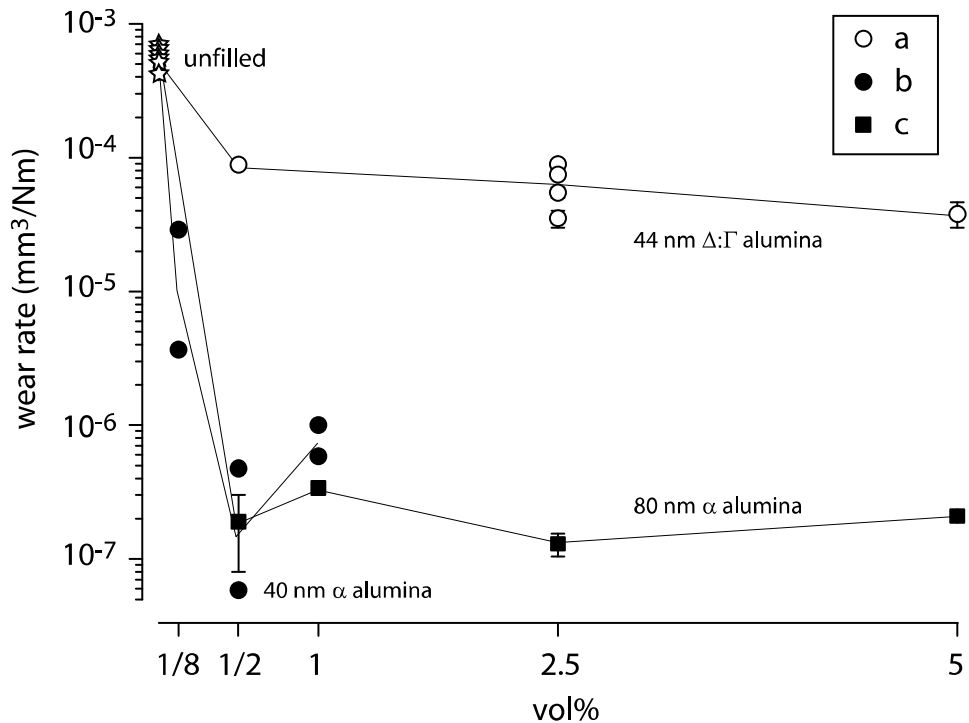
Figure 3-11. Wear rate plotted versus alumina loading for alumina-PTFE nanocomposites with varying nanoparticles against a lapped counterface: a) 44 nm Δ:Γ phase alumina, b) 40 nm α phase alumina, c) 80 nm α phase alumina. Error bars represent the combined standard uncertainty in the wear rate.

Tribological experiments were conducted on nanocomposites of these particles at various loadings against lapped 304 stainless steel counterfaces in standard laboratory conditions at 50 mm/s and 6.3 MPa of normal pressure. Wear rate is plotted versus alumina loading in Figure 3-11. The wear rates of the 40 and 80 nm α alumina-PTFE nanocomposites are insensitive to size and loading in the range from ½ -5% filler and these particles provide additional 100-10,00X improvements in wear resistance over comparably loaded Δ:Γ phase alumina-PTFE nanocomposites. It can be concluded that the differences in wear rates are not attributable to particle size, and although these dispersions have not yet been characterized, the difference is thought not to be due to dispersibility since the 40 nm α phase particles have higher specific surface area and were observed to agglomerate substantially more than the other particles during

nanoparticle imaging. Though the wear reduction mechanism of the α phase particles remains

unclear, it appears to be related to the nature of the interface.

It was hypothesized that additional gains in tribological performance could be achieved by

compatibilizing the nanoparticles with the matrix. A nanoparticle surface fluorination was

thought to not only provide compatibility with the matrix, but the decrease in nanoparticle

surface energy due to the fluorination was thought to aid dispersion; poor dispersibility was

suspected as the source of the unusual scatter in the 40 nm α nanocomposites.   The 40 nm α

phase particles were chemically treated with 3,3,3 Trifluoropropyl Trimethyoxysilane. Infrared

absorption spectroscopy confirmed the presence of the fluorinated groups and thermal

gravimetric analysis was used to estimate the mass fraction at 3%. Nanocomposites with filler

loadings of $^1/_8$, $^1/_2$ and 1 % untreated and fluorinated nanoparticles were tested to investigate the

effects of the interface treatment on the tribological properties of the nanocomposite. Wear

volume is plotted versus the sliding distance in Figure 3-12a.
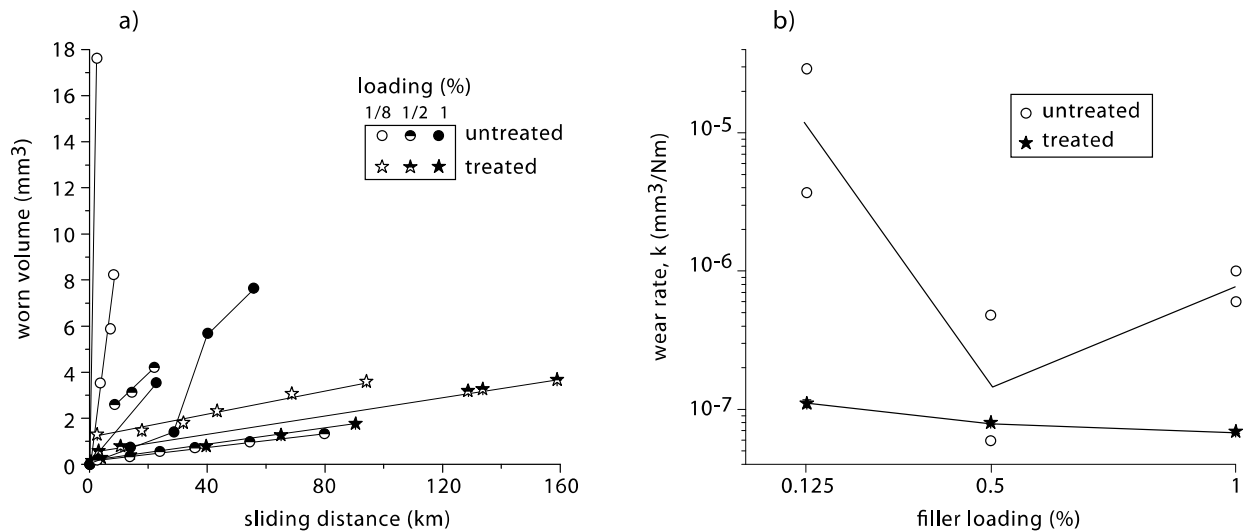
Figure 3-12. Tribological results of test with untreated and fluorinated silane treated 40 nm α
        phase alumina-PTFE nanocomposites: a) worn volume plotted versus sliding distance
        b) wear rate plotted versus filler loading Linear reciprocation experiments were
        conducted against lapped 304 stainless steel counterfaces under standard laboratory
        conditions with a normal load of 250 N.

57

In general, the fluorinated samples were very well behaved in comparison to the untreated samples. Transients are steeper and longer lasting with more material removed for less filled samples. The untreated alumina nanocomposites behaved erratically by comparison. Steady state wear rates are plotted versus filler loading in Figure 3-12b. The large sample to sample variation of the untreated nanocomposites is clear with the low wt% samples having nearly an order-of-magnitude difference in wear rates of identically prepared samples. The wear rates of the functional nanocomposites differ by less than 2X from $^1/_8$% to 1% and decreases linearly with increasing filler loading; variations in wear rates of 2X or less for PTFE nanocomposites are rare even for sample to sample variations. With the addition of $^1/_8$% functional nanoparticles, the wear resistance of PTFE was improved by over 5,000X. It is unclear whether the variations in wear rates were dominated by dispersion, interface strength or both.

Investigations of PTFE Phase and Morphology

Previous studies have shown that subtle changes such as nanoparticle shape or phase can have dramatic effects on the wear rate of the PTFE nanocomposite. A previous hypothesis was that these factors increased the particle/matrix interface strength, but, filler particle surfaces can also affect the local phase, morphology and mobility of the polymer chains at the interface. This layer of affected polymer in the vicinity of the particle is known as the interfacial region, interaction zone and interphase. It will be referred to here as an interfacial region. Due to its characteristic nanometer size scale, it is often appropriately neglected in microcomposites. However, the interfacial region can often be comparable in thickness to nanoparticle fillers and can therefore dominate the properties of a nanocomposite. In amorphous polymers, the primary impact is on the chain morphology and mobility. Sternstein *et al.*[59, 60] did a systematic study of the particle/matrix interface strength effects on the rheology of nanocomposites and proposed a theory for reinforcement and nonlinear viscoelasticity of polymer nanocomposites that is based

on the trapped entanglements of chains near the polymer/matrix interface and the consequent far-field effects on other polymer chains. Maiti and Bhowmick [58] used atomic force microscopy (AFM) to measure interfacial thickness, and found thickness of the region to increase with increased filler/matrix compatibility. Eitan *et al.*[25] observed a similar relationship for treated and untreated nanotubes in a polycarbonate matrix. Additionally, it was found that fracture occurred preferentially within the matrix itself rather than at the filler/matrix interface, suggesting that the interface and interfacial region can both be stronger than the unfilled polymer. The manifestations of interface effects in amorphous polymers have been observed by numerous researchers and include changes in glass transition temperature, modulus, toughness and rheology [25, 27-29, 56, 59, 60, 81]. In semi-crystalline polymers, nanoparticles can alter the crystalline phase [82], morphology [83, 84] and the degree of crystallinity [85, 86] which can extend the influence of the nanoparticles. Such changes in crystalline morphology can have significant influences on mechanical behavior, but it is unclear whether such effects are present in PTFE nanocomposites or to what extent tribological properties are altered due to these effects. The role of crystallinity and crystal phase is explored in the following paragraphs.

PTFE is a semi-crystalline polymer known to have a complex molecular organization with three phases existing near room temperature at ambient pressure. Phase II [87-92] is typically stable below 19°C, and is characterized by a triclinic unit cell with a=b=0.559 nm and γ=119.3°. The molecular conformation is described by Clark [88] as a non-commensurable 13/6 helix. As the temperature increases above 19°C, phase IV becomes stable, the molecules untwist to a possibly commensurable 15/7 helix and the unit cell becomes hexagonal with a 1% increase in the lattice parameter (a=b=0.566 nm) [88]; macroscopically, this results in an increase in volume [90]. Additionally, Kimmig *et al.*[93] noted a rapid increase in the density of coherent helical

reversal defects possibly associated with the onset of helix commensurability. As the

temperature increases above 30°C, the hexagonal unit cell becomes distorted [94], the Bragg

reflection at $2\theta = 42°$ broadens [95] and molecular disorder increases [85, 93, 96] as

intramolecular forces begin to dominate intermolecular forces [93]. It has been suggested that

the observed disorder is due to axial and rotational oscillations of molecules becoming more

pronounced while helical reversal defects increase in length and become incoherent.

While it has been shown that the degree of crystallinity has a minimal role on the wear rate

of PTFE [97], phase and temperature have both been found to have dramatic influences on the

mechanical and tribological properties of PTFE. Flom and Porile noted a dramatic effect of the

phase of PTFE on its tribological properties [98]. They performed sliding experiments with self-

mated PTFE at speeds of 11 and 1890 mm/s and found an abrupt and reversible increase in the

friction coefficient as the background temperature increased above a threshold value near room

temperature in both cases. They hypothesized that the increase was associated with the phase

transition from II to IV at 19°C. Steijn [99] also found increased friction coefficients as the

temperature increased from 19 to 30°C despite the more global trend of reduced friction

coefficient with increased temperature. Makinson and Tabor [36] found evidence of strong

adhesion to the counterface and proposed a lamellar effect of intercrystalline shear governed by

van der Waals interactions between polymer chains. Studies by Steijn [99], Tanaka *et al.*[38],

Blanchet and Kennedy [39], McCook *et al.*[100] and Burris *et al.*[101] supported this hypothesis

finding frictional responses of PTFE to be thermally activated and consistent with van der Waals

interactions. More generally, Joyce *et al.*[102], Brown *et al.*[103-106] found similar

dependencies of various mechanical properties to temperature in the range from 200-400K. The

measured property in each of these studies has been normalized by the room temperature

measurement and is plotted versus temperature in Figure 3-13.
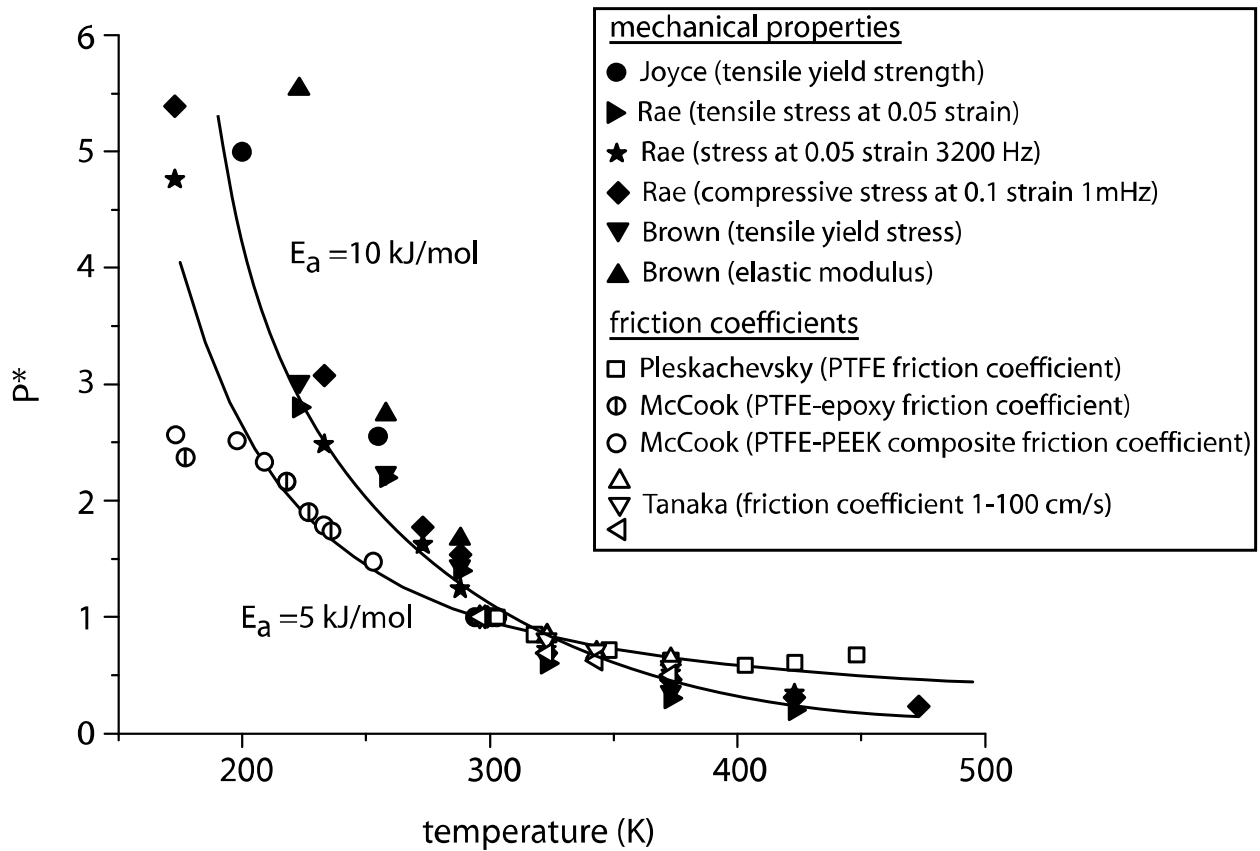
Figure 3-13. Normalized properties plotted versus temperature for variable temperature studies available in the literature. The normalized property is defined as the ratio of the value at temperature to the room temperature value. Various tribological and mechanical experiments suggest that deformation of PTFE is a thermally activated process.

Tanaka *et al.*[38, 46] focused on the characteristic bands of PTFE that contain both

crystalline and amorphous material. In a study investigating the wear mechanisms of PTFE, they

found insensitivity of wear rate to crystallinity, but found that with certain processing conditions,

the characteristic size of the banded structure could be reduced with a subsequent reduction in

the wear rate. In varying the background temperature and sliding speed of PTFE during testing,

a transition to low wear rate was found to occur as temperature increased past a critical

temperature. At the 50 mm/s sliding speed used here, the data from Tanaka *et al.*[38] indicates a

transition temperature near the IV to I phase transition of PTFE (30°C). A recent study of the effects of PTFE phase on toughness by Brown and Dattelbaum [103] helps explain this result. Increased fracture toughness was found for phase I (T>30°C) over phases II (T<19°C) and IV (19°C<T<30°), especially at high strain rates. Phase II was characterized by brittle fracture, while ductility and fibrillation were observed in the high toughness phase I. The fibrils were thought to bridge cracks and reduce the stress concentrations at crack tips. These results have important implications to tribology because both fracture and wear require energy to create new surfaces. These results also suggested superiority of phase I over phases II and IV in wear applications, since the events that occur in tribological contacts typically occur with high strain rates.

One constant observation in low and ultra-low wear PTFE based composites is of fibrillation under stress at room temperature [9]. SEM imaging was used to study the wear surface of a 5% 80 nm α phase alumina-PTFE nanocomposite with a wear rate of k~10^{-7} mm^3/Nm. Figure 3-14 shows the results of these observations at two magnifications. In the low magnification image, 'mudflat' cracking is observed on the wear surface. The mudflats are on the order of 10 μm in diameter and while they appear to be poorly connected to the bulk, vacancies from debris liberation are not observed. Higher magnification imaging reveals fibrils spanning the cracks and appearing to prevent the liberation of the cracked material as debris. The same alumina-PTFE nanocomposite was fractured in bending at 25°C and the resulting crack imaged. This crack is shown in Figure 3-15. Fibrils are observed to span the entire length of the 150 μm crack. This degree of fibrillation is extraordinary for PTFE under these conditions and suggests that the nanoparticles influence the crystalline morphology of the PTFE, and possibly stabilize the tougher phase I.
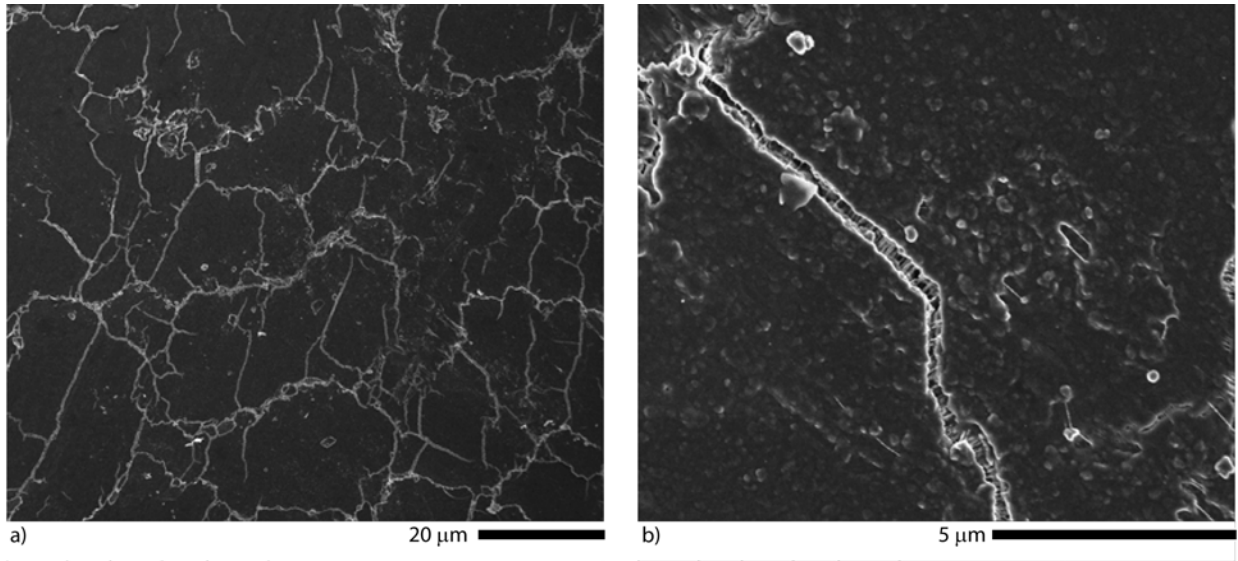
Figure 3-14. SEM images of the worn surface of a 5% 80nm α phase alumina-PTFE nanocomposite: a) low magnification, b) high magnification. The 'mudflat' cracking is a characteristic that is repeatedly observed for these wear resistant PTFE nanocomposites. Wear debris appears to be on the order of 1 µm, while the cracking patterns encompass 10's of micrometers of material. The liberation of large wear debris appears to be inhibited by fibrils spanning the cracks.
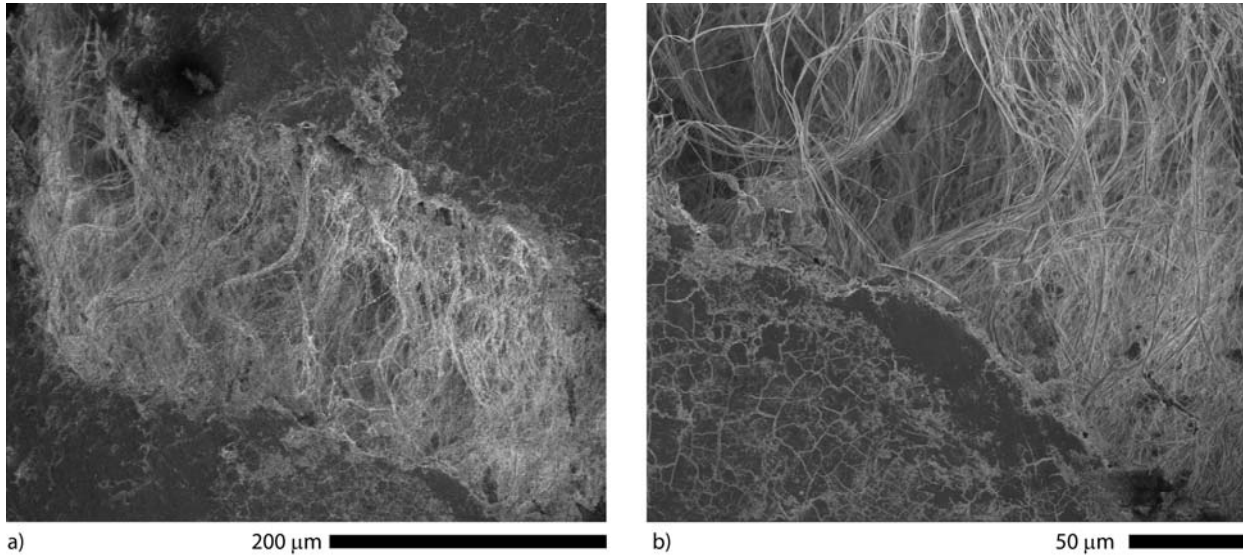
Figure 3-15. SEM images of the worn surface of a 5% 80nm α phase alumina-PTFE nanocomposite after being fractured at room temperature: a) low magnification, b) high magnification. Fibrils completely span a 150 µm crack.

63

It is clear from the literature that the phase and morphology of PTFE are important in determining toughness and ease of fibrillation [103, 104]. It is also well known that nanoparticles can stabilize metastable crystalline phases in polymers and change the crystalline morphology [83]. Therefore, one of the mechanisms that could explain the dramatic changes in wear rate at such small particle loadings is an effect of particle loading on the polymer phase and morphology. The following studies were conducted on a wear resistant 1 wt% 40 nm a phase alumina-PTFE nanocomposite to explore the effects of crystalline structure, morphology and phase on the tribology of PTFE.

In order to determine the role of morphology in the nanofilled PTFE, the melting behavior was monitored using differential scanning calorimetry (DSC) and the structure examined using X-Ray diffraction (XRD). Figure 3-16 shows the XRD results of PTFE and a PTFE nanocomposite. The nanocomposite has a full width half maximum (FWHM) at the main diffraction peak (18 degrees) that is twice that of the unfilled PTFE with a larger amorphous background. This implies that the nanoparticles have interrupted the lamellar crystalline structure. There is also a slight shift in the peak value suggesting an interruption of the unit cell. The high temperature DSC results, shown in Figure 3-17, support this result. The neat polymer and the untreated nanocomposite have the traditional 327°C melt temperature of melt-processed PTFE. However, the nanocomposite has a much larger melt peak at a higher temperature of about 345°C; this temperature is consistent with the melt temperature of virgin PTFE before melt processing. The higher melt temperature is often attributed to the larger, more perfect crystals of the virgin resin [95, 107, 108]. Despite being processed under identical conditions (360°C, 4 MPa), the unfilled PTFE has melt characteristics indicative of melt processed PTFE, while the nanocomposite retains the melt characteristics of virgin resin. The nanoparticles may impede the

mobility of PTFE molecules, requiring greater amounts of thermal energy before reorganization

of the PTFE to the lower order 'gel' state can occur.
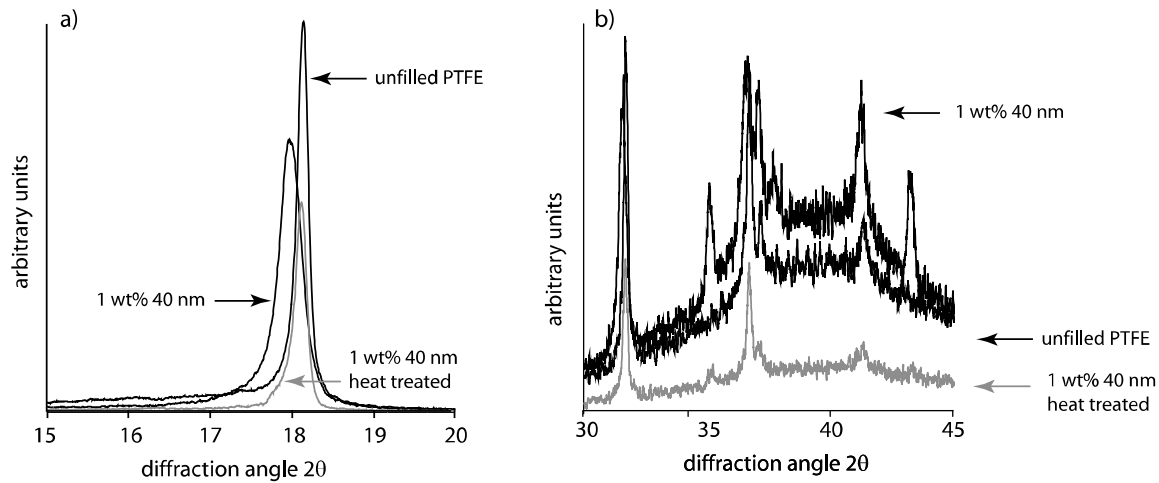
Figure 3-16.   X-Ray diffraction for neat PTFE, a low wear nanocomposite and the same
nanocomposite after a 400°C heat treatment: a) the main reflections at 2θ=18° and b)
the phase sensitive region from 30° < 2θ < 45°. XRD studies were led by Professor
Linda Schadler's group at Rensselaer Polytechnic Institute.
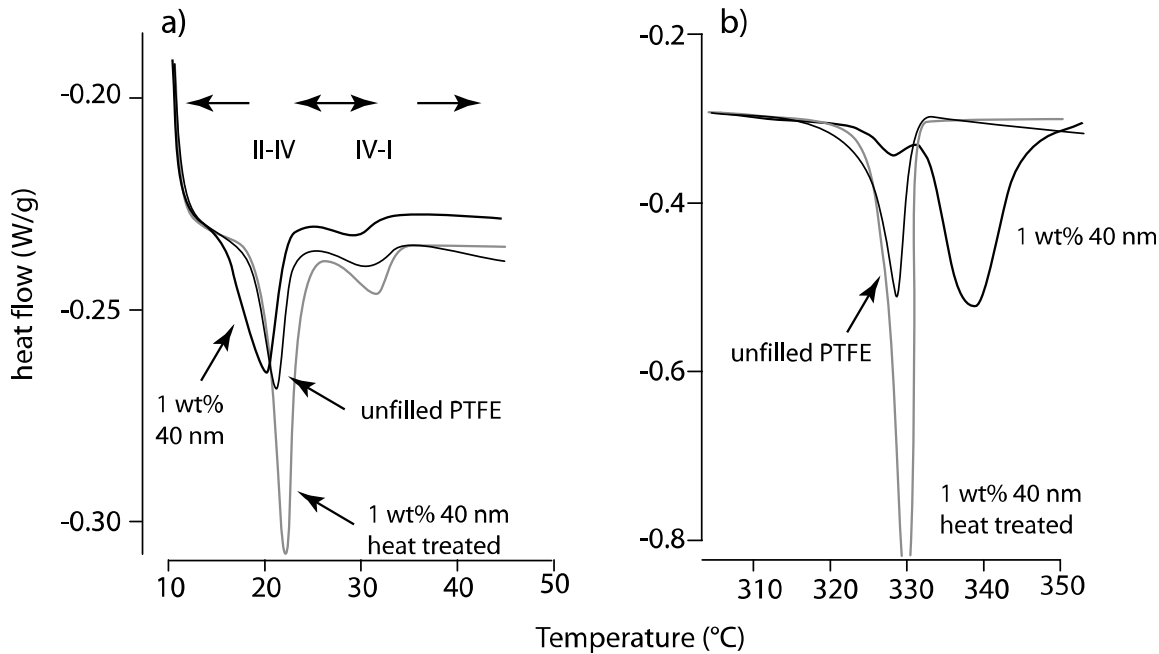
Figure 3-17.   Differential scanning calorimetry (DSC) of neat PTFE, a low wear nanocomposite
and the same nanocomposite after a 400°C heat treatment: a) in the phase sensitive,
low temperature region and b) in the high temperature region during PTFE melting.
Phase II typically exists at temperatures below 20°C, IV between 20°C and 30°C, and
I above 30°C. DCS studies were led by Professor Linda Schadler's group at
Rensselaer Polytechnic Institute.

One hypothesis for wear resistance of these systems is that the virgin structure facilitates fibrillation of the nanocomposites during wear. Another is that the mechanical destruction that occurs during jet-mill processing results in a fibrillated structure that is stabilized by the nanoparticles to temperatures above the process temperature. In either case, it is hypothesized that the nanoparticles stabilize otherwise unstable structures to elevated temperatures. To test this hypothesis, the sample was characterized following a 400°C heat treatment designed to anneal the crystalline structure induced during the original processing. After the heat treatment, the XRD peak at 18 degrees has sharpened and returned to the same position as the unfilled PTFE (Figure 3-16). In the region most sensitive to the phases present, the 1 wt% nanofilled resin has the lowest peak height to amorphous background ratio (1.5 to 1) compared to the neat resin (3 to 1) and the heat treated 1 wt% nanofilled resin (about 2 to 1). As the proportion of phase I increases, the peaks (especially the peak at 42 degrees) decrease in intensity compared to the background. Because these samples are a mixture of at least 2 phases, it is difficult to ascertain exactly what structure is present. These results, however, imply that the 1 wt% nanofilled resin has the most phase I and the least phase IV of the materials shown and that the heat treatment to 400°C leads to the most phase IV. This is also supported by the DSC data at low temperature shown in Figure 3-17. The data show that the 1 wt% nanofilled sample has much less of a phase I to IV transition than the unfilled PTFE, while the heat treated composite shows a significant I-IV transition. Therefore, one would expect more phase I in the 1 wt% nanofilled composite and the least in the heat treated 1 wt% nanofilled composite. In addition, the transformation temperature from I-IV is lower for the 1 wt% nanofilled sample further supporting the argument that it has the most phase I present. Finally, at room temperature the IV-II transition has begun in the heat treated sample; Brown and Dattelbaum found that phase II

had the lowest toughness [103]. This would also explain the significantly higher ordering in this sample seen during XRD measurement. Both XRD and DSC provide evidence that more of the tough phase I is present in the untreated nanocomposite than either the heat treated nanocomposite or the unfilled PTFE at room temperature.

Atomic force microscopy was used to probe the PTFE morphologies in the nanocomposite before and after heat treatment. The AFM measurements shown in Figure 3-18 support the features observed in XRD and DSC. Clear differences can be seen before and after heat treatment with the nanocomposite before heat treatment having much thinner and more organized lamellae than it had after heat treatment. Before heat treatment, the lamellae are well aligned and appear to have the folded-ribbon morphology that is often cited for virgin PTFE [95, 107, 108], while after heat treatment, lamellae are thick, tangled and packed into substantially larger characteristic regions. Marega *et al.*[95] suggest that the reduction in the IV-I transition peak and the shifts in the phase transition temperature to lower temperatures (DSC) are indicative of increased molecular disorder and thinned lamellae. XRD and AFM measurements of the control nanocomposite show evidence of increased molecular disorder, and thinned lamellae, respectively. These characteristics may explain the stability of phase I for this sample at lower temperatures, and the high degree of lamellar alignment over the field of view supports the hypothesis that the nanoparticles stabilized the virgin morphology during processing.
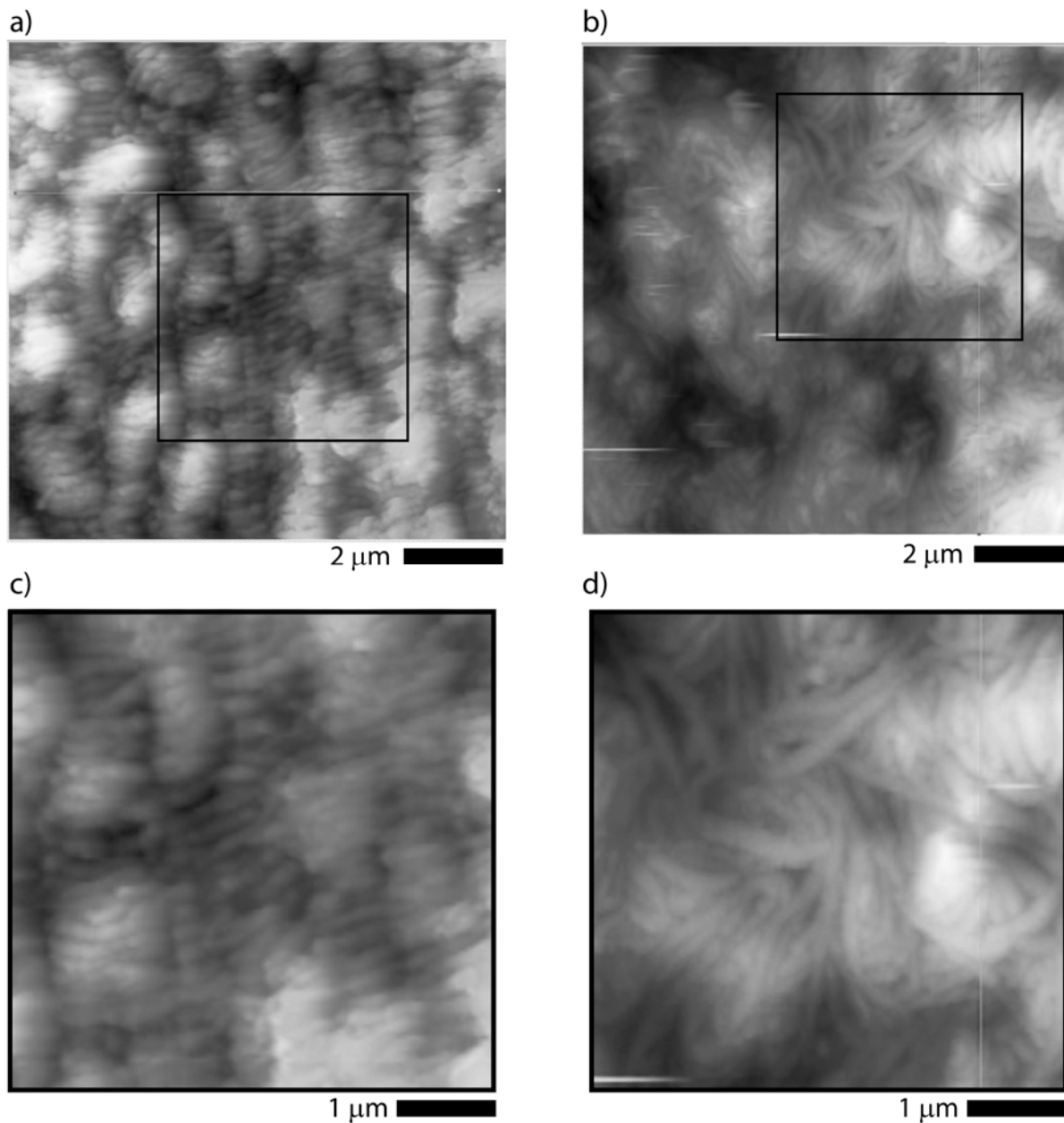
Figure 3-18. Atomic force microscopy of the crystalline morphology of a 1 wt% 40 nm alumina-PTFE nanocomposite a) before heat treatment, b) after heat treatment, c) before heat treatment higher magnification and d) after heat treatment higher magnification. As-prepared, the nanocomposite has very small lamellae with finer-scale, more ordered packing than after heat treatment. Regions c) and d) are outlined in a) and b), respectively. AFM studies were led by Professor Scott Perry's group at the University of Florida.

To test the hypothesis that the effects of the nanoparticles on the morphology of PTFE reduce wear, tribological experiments were conducted on the same nanocomposite before and after heat treatment. The control experiment was conducted on the 1 wt% 40 nm α alumina filled PTFE sample in linear reciprocation with 50% relative humidity at a temperature of 25°C. The sliding speed and normal pressure were 50.8 mm/s and 6.3 MPa, respectively. After standard processing, the nanocomposite was tested for approximately 80 km. The sample was then removed and heat treated. A new counterface was used, the sample was faced, removing only the material necessary to make it flat, and the experiment was continued. After the heat treatment, the friction coefficient was reduced by about 10%, wear rate increased by 100X and transfer film thickness and discontinuity increased. The tribological results are shown in Figure 3-19. The tribological benefits of the crystalline effects of the nanoparticles on the PTFE are vast. The nanoparticle phase, chemistry, size, loading and dispersion are nominally identical before and after the heat treatment, so the increase in wear rate is attributed only to these effects on the crystalline structure of the PTFE.
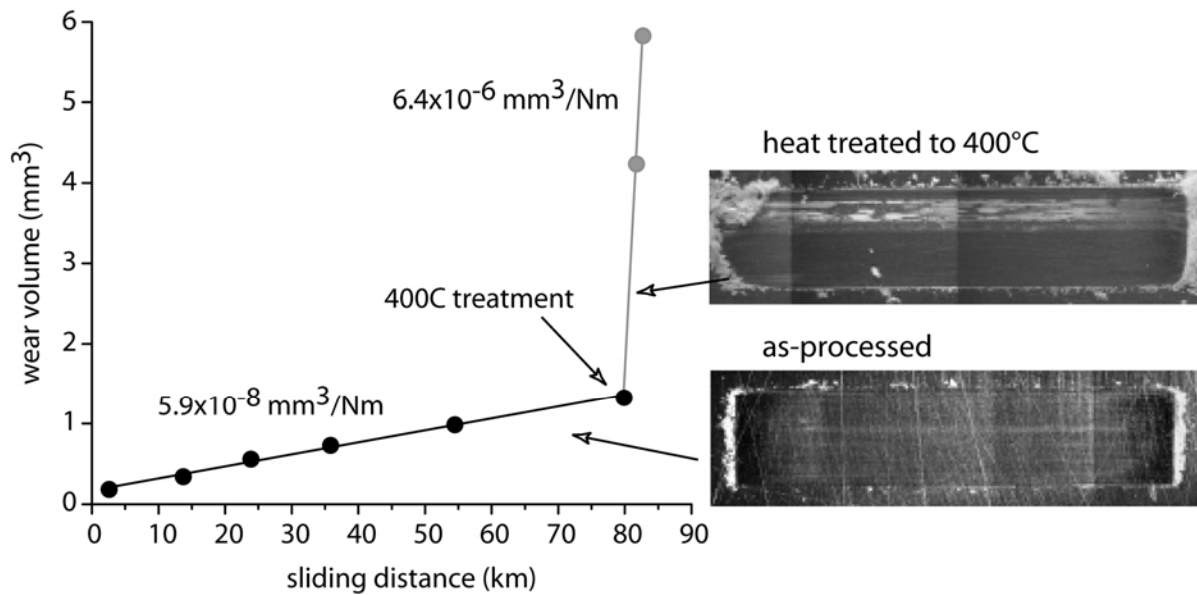
Figure 3-19. Wear volume plotted versus sliding distance for a 1 wt% 40 nm alumina-PTFE nanocomposite before and after a heat treatment to 400°C. The microstructural benefits of the nanoparticles are lost after heat treatment and the wear rate increases by 100X. Optical images of the transfer film before and after heat treatment are shown on the right.

A variable temperature tribological experiment was conducted to test the hypothesis that a transition to phase II results in reduced toughness and increased wear. An additional nanocomposite test specimen was cut from the original low wear 1 wt% 40 nm α phase alumina-PTFE puck described earlier. The sample was run-in on a fresh counterface for 2500 m of sliding with 6.3 MPa of pressure at 40°C. The wear rate during run-in was 6×10^{-7} mm^3/Nm; this is consistent with the run-in observed in the original experiment. Forecasting from the original experiment, the wear rate after a 2500m run-in is near steady state and on the order of $k \sim 10^{-7}$ mm^3/Nm. After an additional 25 m of sliding, the temperature was continuously decreased over the next 30 m to a target of 10°C; the dew point temperature was 8°C. Because thermal expansions during the test dominate volumetric measurements, in situ displacement measurement techniques could not be used. In order to capture the transition from low to high wear, a videoscope was used to track debris generation at the reversal of each cycle.

The results of the varied temperature experiment are shown in Figure 3-20 with wear rate

and counterface temperature plotted as functions of sliding distance. The wear rate curve was

estimated from mass loss measurements and *in-situ* observation of the transition. The data

shown here was recorded after the initial run-in period. For the first 47 m of sliding, no

observable debris was liberated from the contact indicating retention of the low wear state. At

47 m, the temperature was 14°C and the first wear fragment appeared. This was followed by

rapid deterioration of performance until a steady state wear rate of k ~ $5x10^{-4}$ mm^3/Nm was

reached at 52m and about 12°C.
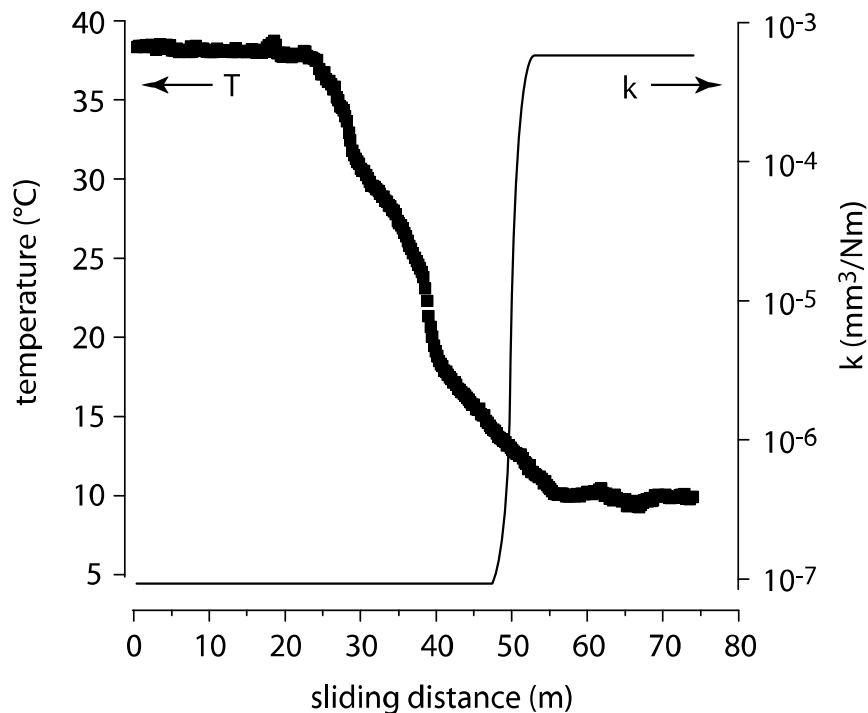
Figure 3-20. Wear rate and counterface temperature versus sliding distance for variable
temperature tribology testing of a wear resistant PTFE nanocomposite. Wear rate is
an estimate based on mass measurements and in-situ observation of the transition.
Normal pressure and sliding speed were 6.3 MPa and 50 mm/s, respectively. An
abrupt and drastic change in the wear mechanism occurs as the temperature is
reduced below about 14°C.

It was hypothesized that the wear resistance of the nanocomposite was due to a disruption

of the crystalline structure by the nanoparticles that resulted in increased disorder, stabilization of

the higher toughness phase to lower temperatures and fibrillation under stress. The results from

DSC of this sample are plotted versus temperature in Figure 3-21. The transition to high wear

occurs when most of the sample has transitioned to the low toughness phase II. In addition to

being more brittle, Brown *et al.*[103] found phase II to be stronger and stiffer than phases I and

IV. It is possible that as temperature is dropped and the material begins to transition to phase II,

deformation preferentially occurs in the remaining phase IV material. At a critical point, enough

of the material has been converted such that phase II must contribute to motion accommodation.

Eventually, crack initiation, propagation and gross failure occur. The fact that unfilled PTFE

does not exhibit high wear resistance at comparable locations on the phase diagram suggests that

facilitation of fibrillation is one of the critical wear resistance mechanisms in PTFE

nanocomposites. The breakdown of wear performance coinciding with transition to phase II

suggests that the beneficial fibril related toughening mechanism that results from the

nanoparticle filler, is disabled in phase II.
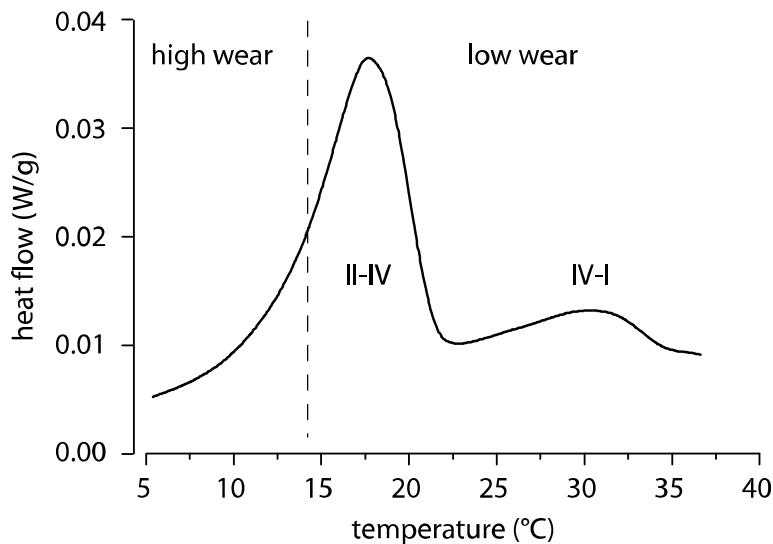
Figure 3-21. Normalized DSC power plotted versus temperature. The transition to high wear
occurs at a critical point after the low toughness phase II transition temperature.

Summary

The contributions of nanoparticles span well beyond the traditional rules of mixtures models that adequately describe many of the commercial PTFE microcomposites, with nanoparticle dispersion, surface morphology and chemistry likely driving the fundamental wear resistance mechanisms that synergistically couple to produce low wear. Recent experiments indicate that tenacious, high quality transfer films are necessary but not sufficient for wear resistance, and likely result from a pre-existing condition of wear resistance. In addition, mechanical effects such as crack pinning and deflection are unlikely sources of the substantial improvements in wear resistance observed at low nanoparticle loadings. The filler/matrix interface appears to have a dramatic impact on the mobility of the polymer, and the resulting effects on polymer morphology and phase likely drive the tribological properties. In one experiment, an annealing heat treatment erased many of the morphological signatures of the low wear PTFE nanocomposite and increased wear by 100X despite the fact that critical parameters such as nanoparticle loading, dispersion, size, shape and phase remained nominally unchanged. These findings strongly suggest that the nanoparticle effects on the matrix phase and morphology dominate other wear resistance mechanisms in PTFE, but many unanswered questions remain regarding the exact nature of this particular wear resistance mechanism. The goal of the present study is to answer some of these basic remaining questions. Thermal, mechanical and tribological properties of neat PTFE are characterized as functions of mechanical and thermal history to eliminate the effects of the nanoparticles. Nanoparticle dispersion, thermal, mechanical and tribological characterization of PTFE nanocomposites follow. Mechanical and thermal histories are removed as variables to study the direct effects of the dispersion technique, nanoparticle loading, dispersion and phase.

CHAPTER 4
EXPERIMENTAL METHODS

Materials

DuPont 7C PTFE is used as the matrix material in these studies; it is a virgin, compression moldable PTFE resin. It has a molecular weight that ranges from approximately 10^6-10^7 Da and an average manufacturers claimed particle size of 35 μm. As received, the particles are agglomerated into aggregates on the 100 μm – 10 mm size-scale. Scanning electron images of a representative agglomeration are shown in Figure 4-1.
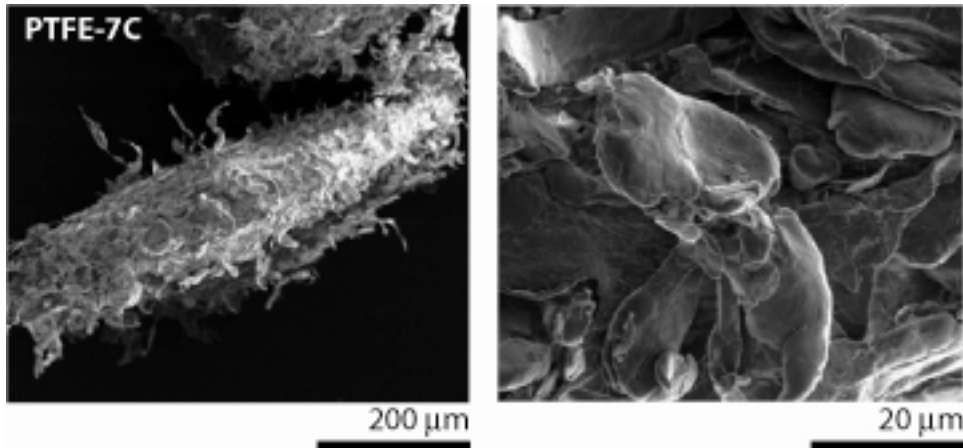
Figure 4-1. Secondary electron images of Teflon 7C as received from DuPont. Agglomerations range from 100 μm – 10 mm. The average individual particles size is reported to be 35 μm. This value is consistent with measurements made using scanning electron microscopy (SEM).

The primary filler selected for use in this study is Al_2O_3, or alumina. Alumina is very hard, wear resistant, chemically stable, and widely available as laboratory and commercial grade materials with particle diameters ranging from tens of nanometers to millimeters. Variables related to the alumina in this study are filler loading (volume %), average particle size (APS) and crystalline phase. The crystalline phases used in this study are 70% Δ: 30% Γ (referred to as Δ:Γ) and 99% alpha (referred to as α), and have spherical and irregular particle shapes, respectively.

Powder Blending

The same unique properties that make PTFE an attractive solid lubricant also make PTFE nanocomposites inherently difficult to process. The most effective dispersion techniques, namely liquid dispersion/*in-situ* polymerization and high shear rate melt mixing are precluded for PTFE. As a result, various reputably inefficient dry powder blending techniques are commonly used; the most typical techniques are examined here.

One method used here is absent from the literature and will be referred to as a shear sieve (a common powder sugar sifter). This technique is studied here because it is low energy and nondestructive, but has the potential to fibrillate PTFE. The shear sieve consists of a hemispherically shaped 20 mesh sieve through which the powers are classified. A rotating rod interferes with and stretches the sieve; the powders separating the two elements are compressed and sheared as the bar scrapes across the sieve. Agglomerates are broken and powders are sheared into a collection bin. This process is repeated until all of the powder has been classified.

The second blending method studied here is referred to as a rotary shear mixer; this apparatus was described previously by McElwain [52]. Briefly, a mixing arm is rotated in one direction. At the end of the arm is the mixing cup which is mounted at an angle that is about 30° off axis from the arm. This cup is rotated in the opposite direction about its own axis of revolution. This motion path creates high acceleration gradients and rapid mixing. Powders in this study are mixed at an arm speed of 1500 RPM for 30 seconds.

The third method under study is ultrasonication [10, 11, 17, 18, 32, 33]. Powders are placed in an ultrasonic ethanol bath for 30 minutes. The forth technique under investigation is blade mixing [31]; the blade mixer used here is essentially a high speed, high power blender. Powders were placed in the blade mixer and a blade speed of 30,000 RPM was maintained for 40 seconds.

The fifth blending method is jet-milling; this technique has been described in detail previously by Sawyer *et al.*[8, 16, 19]. Briefly, the powders are fed into an alumina lined grinding chamber with a high speed circumferential flow of dry air. Upon entry into the chamber, powders are impacted at high speed, agglomerates are broken, and hard nanoparticles are imbedded into softer matrix particles. Centrifugal forces drive the heaviest particles to the periphery for further grinding while small particles are preferentially forced into the collection chamber in the center.

Sample Preparation

After blending, powders are sintered using compression molding. The powder ensemble is placed in a mold and inserted into a compression molding station. Two PID controlled heating platens are mounted to the pressure platens of a hydraulic laboratory press. The 7C PTFE used in these studies has a reported maximum initial melt temperature of 352˚C, and enters a viscous 'gel' state rather than a liquid state. As the temperature is increased, the viscosity decreases until degradation begins at a temperature above ~425˚C. Following cooling and recrystallization, subsequent melting occurs at 327˚C. Since the material is under pressure in the mold during processing, the actual temperature required for melting is likely a bit higher. The samples in this study are first cold pressed at 60 MPa for 15 minutes to evacuate the air from the powder. After cold pressing, the pressure is reduced to 4 MPa where it remains for the duration of the schedule; this hold pressure evacuates potential volatiles from the powder ensemble. Next, the temperature is increased to 380˚C at a rate of 2˚C/min. Upon reaching 380˚C, the temperature drops to 362˚C where it is held for 3 hours. The temperature spike to 380˚C occurs due to the tuning of the PID controller (overshoot), and ensures initial melt is reached by the entire part. Once the hold

schedule is complete, the mold is cooled at 2˚C/min. The compression molded puck is machined

to final sample dimensions using computer numerical control.

Dimensional measurements are made with a digital micrometer. This measurement has a

reported repeatability of 1 μm resulting in a Type B uncertainty of 5 μm (5X the reported

repeatability). Sample mass is measured on a precision analytical balance having a Type B

uncertainty of 50 μg. The density of the sample is calculated following dimensional and mass

measurements using the following formula.

$$\rho = \frac{m}{l \cdot h \cdot w}$$
<div style="text-align:right">Eq. 4-1</div>

where m is the mass, l is the length, h is the height and w is the width. According to the *law of*

propagation of uncertainty, the square of the uncertainty of the measurand (density in this case)

is equal to the sum of the sensitivities of each measurement. The sensitivity of a measurement is

defined as the square of the product of partial derivative of the measurand with respect to the

measurement and the uncertainty of the measurement. The square of the uncertainty in the

density is calculated as follows,

$$U_c^2(\rho) = \left(\frac{1}{l \cdot w \cdot h}\right)^2 \cdot u_c^2(m) + \left(\frac{-m}{l^2 \cdot w \cdot h}\right)^2 \cdot u_c^2(l) + \left(\frac{-m}{l \cdot w^2 \cdot h}\right)^2 \cdot u_c^2(w) + \left(\frac{-m}{l \cdot w \cdot h^2}\right)^2 \cdot u_c^2(h) \quad \text{Eq. 4-2}$$

Characterization

Morphology and Dispersion

A Tescan Vega XMU variable pressure scanning electron microscope (SEM) was used to

characterize PTFE morphology and nanoparticle dispersion in this study. This microscope has a

differentially pumped column that enables backscattered and secondary electron imaging at

pressures ranging from 10^{-2} to 10^3 Pa. This high pressure capability is essential for the

characterization of the nonconducting polymeric tribology samples used in this study. At low

<div style="text-align:center">77</div>

pressures or high vacuum, the nonconductive nature of these samples results in a high

concentration of charge and heat near the probe during electron impingement. Thin conductive

coatings are typically applied to the surface to combat the issues of heating and charging, but

such coatings are invasive and destructive, potentially introducing misleading artifacts and

rendering the tribological sample useless following observation.

Thermal Properties

Thermal characterization was conducted using a TA instruments Q20 differential scanning

calorimeter (DSC). A schematic representation of this system is shown in Figure 4-2. The

sample bases are heated and the temperature difference between the sample and the reference

sample is measured. The heat flux is obtained using the following formula,

$$q = \frac{\Delta T}{R}$$

Eq. 4-3

where q is the power conducted between the two samples, ΔT is the temperature difference and R

is the thermal resistance between the samples. The reference pan is empty and the sample pan

contains the polymeric sample. Because the sample pan has a higher thermal capacity (due to

the additional mass and thermal capacity of the sample), the reference pan temperature increases

more rapidly causing a temperature difference during heating and resulting in conductive heat

flow to the sample pan. This power or temperature difference is approximately constant due to

constant differences in heat capacity until glass, phase or state transitions occur. A glass

transition results in a change in heat capacity which is detected as a change in the 'baseline'

power or the temperature difference between the samples during heating or cooling. Phase and

state transitions require heat to rearrange the material into the more thermodynamically stable

configuration before temperature can increase. These transitions are detected as peaks or wells

in the thermogram.
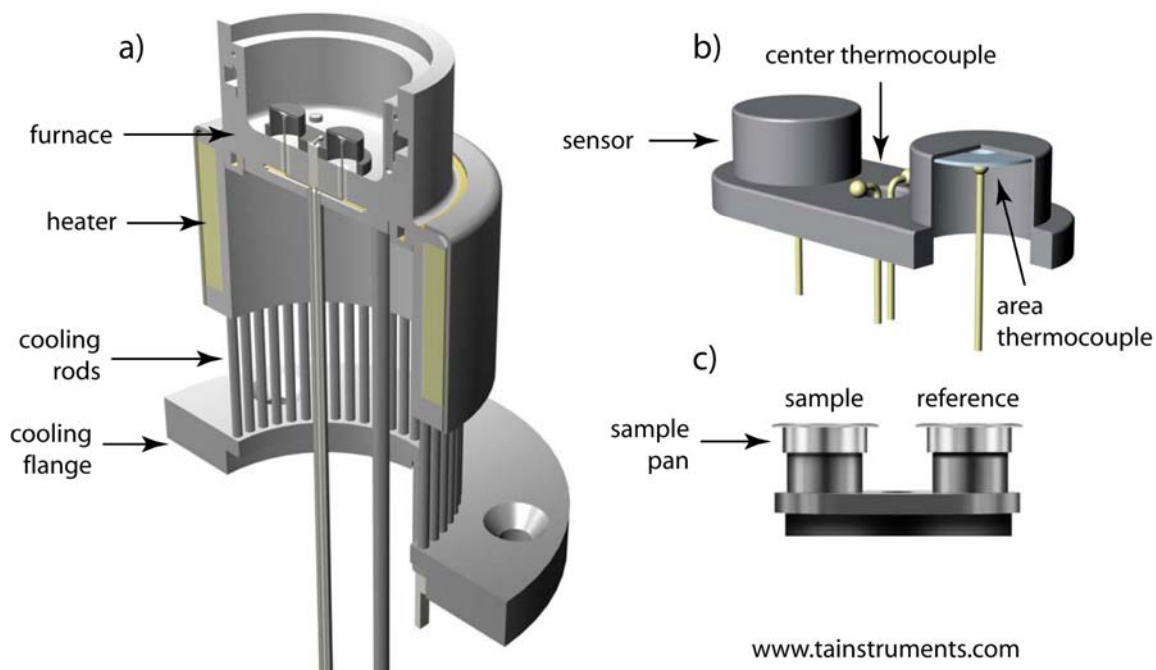
Figure 4-2. Schematic representations of the components comprising the TA instruments Q20 differential scanning calorimeter (DSC); a) the components responsible for heating and cooling the sample, b) the sensor and c) the sensor with the sample and reference sitting on the respective sample platforms. Schematics from www.tainstruments.com.

The heart of the design is the thermal cell which contains the samples. The two sample pans are designed with thicker and significantly flatter bases than those of traditional DSC pans to reduce thermal contact resistance. In addition to the structural improvements of the pans, repeatability is improved with a self-locking pan crimping press that ensures pans are crimped with consistent force. These crimped pans rest on polar ends of the monolithic constantan sample holder. Directly beneath each of the two sample mounts are area thermocouples. These area thermocouples are more accurate than traditional point thermocouples. An additional thermocouple is located near the center of the conducting material between the samples for a more accurate measurement of the transition temperatures over the more typically reported furnace temperature. Mounted below the sample holder is a silver base which conducts heat from the furnace below to the samples. The furnace is mounted above a cooling flange via

nickel rods that conduct heat away form the furnace. The axial design greatly reduces temperature gradients in the thermal cell.

This DSC has a manufacturer reported absolute uncertainty in the measurement of temperature of 0.1ºC. The uncertainty in the measurement of energy is reported to be 1% relative to the measured value. The instrument is calibrated using a standard indium sample and heats of fusion are reported as the Joules of energy of a given transition per gram of the sample (J/g). The uncertainty in the measurement of heat of fusion is therefore dependent upon the uncertainty in the mass measurement. In this case, the mass measurement uncertainty is 50μg. According to the *law of propagation of uncertainty*, the square of the uncertainty in the measurement of heats of fusion is calculated as,

$$U_c^2\left(\Delta H\right) = \left(\frac{1}{m}\right)^2 \left(0.01 \cdot \Delta E\right)^2 + \left(\frac{-\Delta E}{m^2}\right)^2 \left(0.00005\right)^2 \qquad \text{Eq. 4-4}$$

where *ΔH* is the heat of fusion, *m* is the mass in grams and *ΔE* is the heat of the transition in Joules. Considering a typical heat of fusion for PTFE of 50 J/g and a sample mass of 0.005 g, the mass and energy measurements contribute equally to provide an uncertainty of 0.7 J/g.

Mechanical Properties

Mechanical characterization was conducted using the MTS 858 Mini Bionix II load frame shown schematically in Figure 4-3a. The design is symmetric with a 1,000 lb load cell located at the bottom of the load frame and a steel hydraulically controlled ram located in the center of a height adjustable cross-beam provides the deformation displacements and loads. A Linear Variable Differential Transformer (LVDT) provides closed-loop feedback for the hydraulic ram and displacement data for strain measurements.
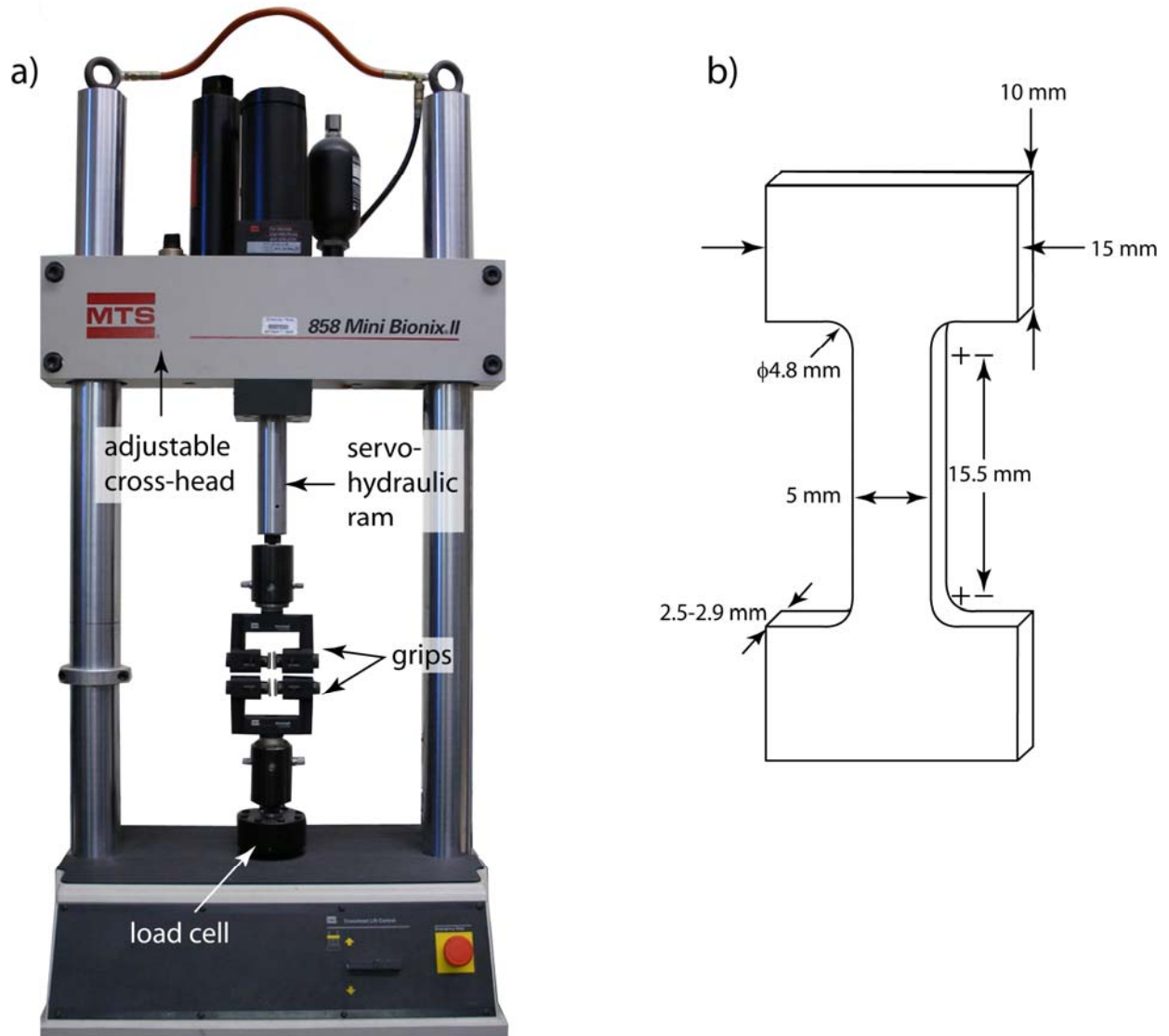
Figure 4-3. A) MTS 858 Mini Bionix II load from used for characterizing mechanical
properties. A uniaxial load cell measures tensile force on the sample and has an
approximate Type B measurement uncertainty of 1N. A Linear Variable Differential
Transformer is mounted coaxially with the servo-hydraulic ram for displacement
measurement. The approximate Type B uncertainty in displacement is 0.02 mm. B)
Sample and sample dimensions.

Samples for mechanical testing are created using the standard processing procedures

outlined in the sample preparation section above. Following compression molding, the

polymeric samples are machined to the shape shown in Figure 4-3b using computer numeric

control (CNC) for consistent sample dimensions. The sample is gripped and the pulling force

can only be achieved through friction at the clamp interface. Assuming a friction coefficient of

0.1 and a maximum clamp stress equal to the yield stress, a free-body diagram reveals that the

clamp face area must be five times the tensile cross-section. Thus a 'dogbone' shape is required

to prevent slip. The final dimensions provide a factor of safety of two to ensure that the clamp

does not slip during the test.   The corners of the dogbone are eased such that the shape provides

a well-defined tensile section in the center of the sample where strain can occur without

significant stress concentration.

The quantities of interest during mechanical testing are stresses and strains in the tensile

section. The calculations of these quantities are as follows,

$$\sigma = \frac{F}{h \cdot w}$$ Eq. 4-5

$$\varepsilon = \frac{l - l_0}{l_0} = \frac{\Delta l}{l_0}$$ Eq. 4-6

where σ is the stress, F is the axial force, h is the sample height, w is the sample width, ε is the

engineering strain, l is the length during loading and l_0 is the original sample length.   The

uncertainties in the measurements of σ and ε depend on the uncertainties in the measurements of

F, h, w, Δl and l_0 through the *law of propagation of uncertainty*. The quantities h and w are

measured using a digital micrometer with a resolution of 1µm. Thus, the Type B uncertainty in

the measurement is 5 µm. However, the geometric irregularities in the samples were found to be

on the order of 10 µm. The uncertainties in these measurements are therefore conservatively

taken as 20µm. The uncertainty in the force measurement is calculated by comparing the force

measurements of various standard masses against those from scales with known uncertainties.

The uncertainty is conservatively estimated to be ~1 N. The displacement (Δl) uncertainty was

calculated using the same method of comparison with measurements of known uncertainty. This value is estimated to be approximately 20μm. The length l_0 was prescribed by the machining g-code but was difficult to measure accurately due to the radius at the corner. The accuracy with which the CNC milling machine can hold a dimension over this length has been found to be approximately 40 μm. Therefore, the uncertainty conservatively ascribed to this dimension is 200μm. Using the law of propagation of uncertainty, the squares of the uncertainties in stresses and strains are,

$$U_c^2(\sigma) = \left(\frac{1}{h \cdot w}\right)^2 u(F)^2 + \left(\frac{-F}{h^2 \cdot w}\right)^2 u(h)^2 + \left(\frac{-F}{h \cdot w^2}\right)^2 u(w)^2 \qquad \text{Eq. 4-7}$$

$$U_c^2(\varepsilon) = \left(\frac{1}{l_0}\right)^2 u(\Delta l)^2 + \left(\frac{-\Delta l}{l_0^2}\right)^2 u(l_0)^2 \qquad \text{Eq. 4-8}$$

Each term on the right of these equations can be divided by the combined standard uncertainty squared to give the sensitivity of the measurand uncertainty to the measurement uncertainty in question. For example, the second term on the right of Eq. 4-8 divided by the left hand side of Eq. 4-8 is the sensitivity of strain to the uncertainty in l_0. Despite the relatively large uncertainty in the value of l_0 over Δl, it accounts for less than 20% of the uncertainty in strain calculations.

Tribological Properties

A laboratory designed linear reciprocating pin-on-flat tribometer, shown schematically in Figure 4-4, is used to test the wear and friction of the samples. This testing apparatus and the uncertainties associated with the experimental measurements are described in detail in Schmitz *et al.*[3, 4]. Although open to the air, the entire apparatus is located inside a class 10,000 soft-walled cleanroom (for reduced particulate abrasion) with conditioned laboratory air at 25°C and from 25-50% relative humidity. In all cases, the normal load is $F_n = 250$ N, reciprocation length

is S = 25.4 mm (50.8 mm/cycle), sliding speed is V = 50.8 mm/s, apparent contact area is A = 40

mm^2 and the nominal contact pressure is P_0 = 6.3 MPa. In general, the length of the test depends

on the wear resistance of the material.
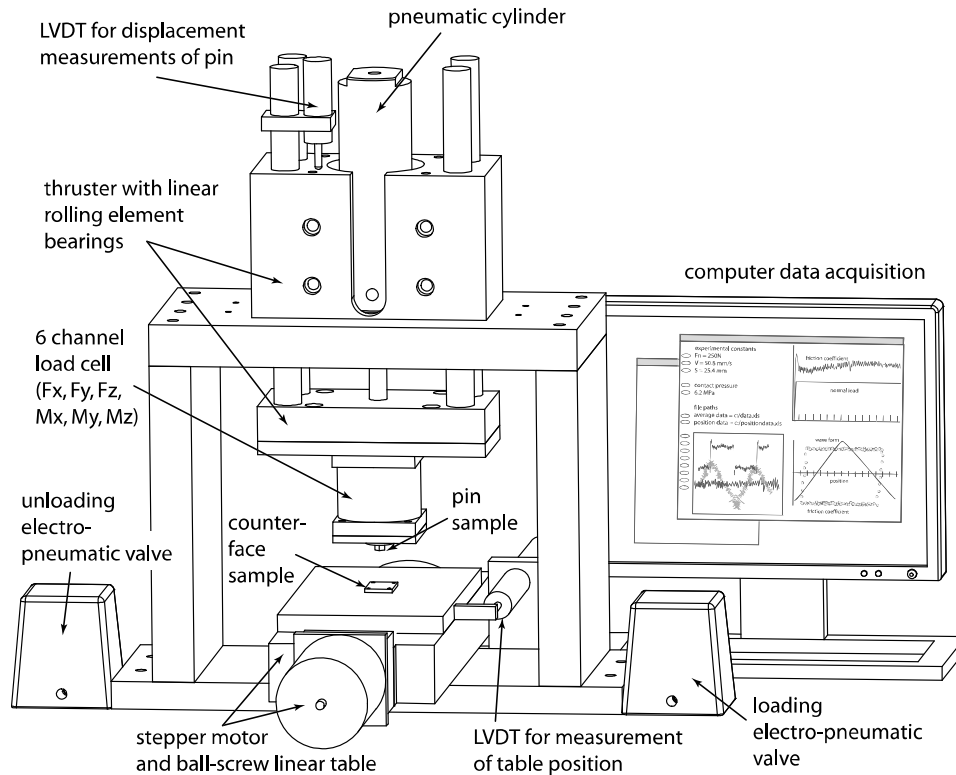
Figure 4-4. Tribometer used for friction and wear testing. A pin of the bulk test material is pressed flat against a linearly reciprocating counterface. A 6-channel load cell reacts all of the loads incurred by the sample. The conditions are constant throughout the test i.e. as wear occurs.

Tribological systems depend strongly on a number of factors. One very important factor in

the study of soft solid lubricants is the tribological counter-surface or counterface; surface

metrology is a scientific field that focuses on the accurate measurement, characterization and

tribological exploration of such surfaces. A wide variety of statistical parameters are used to

describe these surfaces. A common feature to most tribological counterfaces is a negative skew.

Negative skew is a statistical term used to describe distributions with long tails on the negative

side of the mean line. Negatively skewed surfaces are those that have valleys that are deeper

than the heights of the surface protuberances, or asperities. This is important in tribology

because the high asperities abrade the solid lubricant while the deep valleys have little effect

aside from potentially providing lubricant reservoirs and anchoring beneficial transfer films.
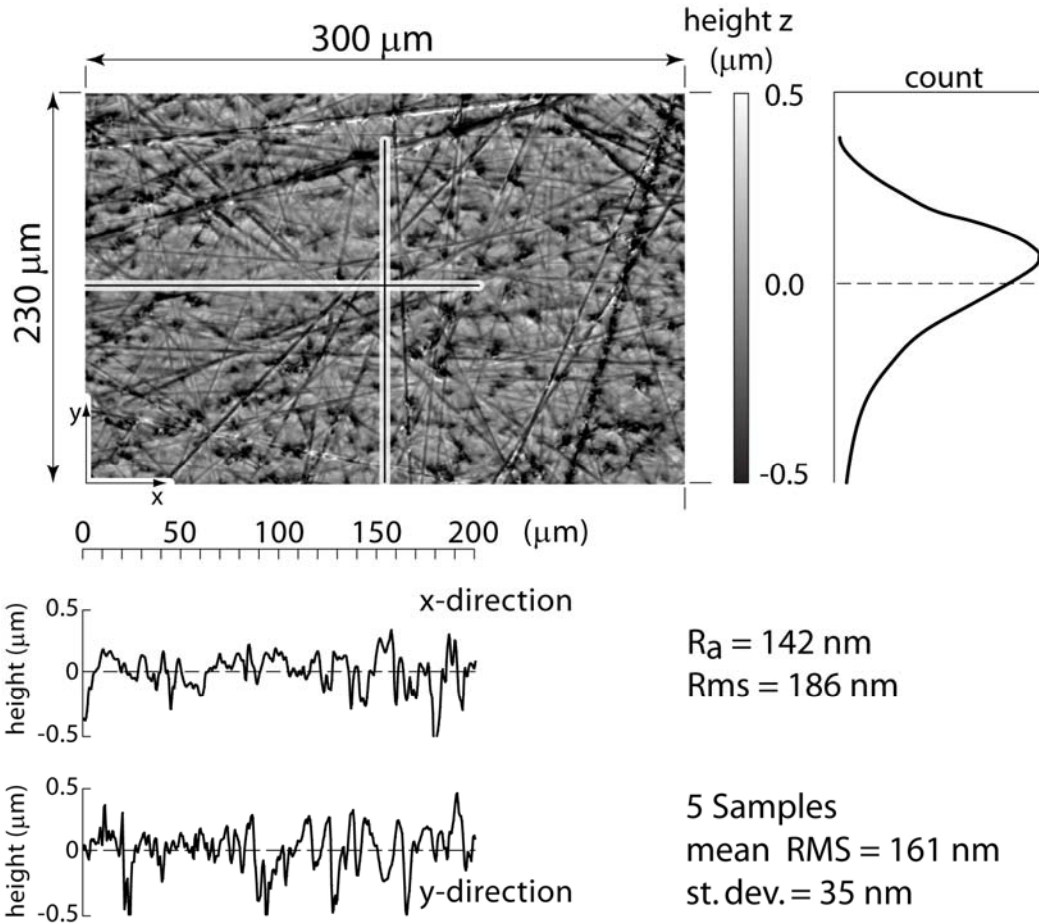
Figure 4-5. Scanning white light interferometry measurement of a representative lapped
stainless steel (304) counterface. The surface has a negative skew and the average
and standard deviation of root mean squared roughness (Rq) were found to be 161 nm
and 35 nm, respectively.

AISI 304 stainless steel is used as the counterface material; it is corrosion resistant and

relatively soft (measured hardness of 87 kg/mm^2 Rockwell B) which allows for easy detection of

abrasion from the filler. New counterfaces are used for each experiment, so efforts were made to

ensure that each nominally identical counterface sample was created under the same conditions.

Five random samples were measured over a 230 x 300 μm area using a scanning white light

interferometer. A representative measurement is shown in Figure 4-5. The surface map reveals a relatively flat surface cut by a number of deep scratches. The negative skewness is evident from the height histogram next to the map. Surface profiles are also shown in the x and y directions with the vertical axes magnified 65X. From the five random measurements, the average and standard deviation of the root mean squared roughness (R_q) were found to be 161 nm and 35 nm, respectively.

Prior to testing, the counterface and composite pin are cleaned with methanol, and dried with a laboratory wipe. The composite samples are mounted directly to a 6-channel load cell which reacts all of the forces and moments on the pin sample. The counterface is mounted to a linear reciprocating stage beneath the pin sample. A pneumatic cylinder is used to apply a normal force, which is continuously reacted and measured by the load cell, and computer controlled using an electro-pneumatic valve. A linear thruster isolates the pneumatic cylinder from frictional loads. Four 1 inch diameter rods located within an aluminum housing are guided by linear bearings and provide high stiffness in the transverse direction. An LVDT mounted to the thruster monitors pin displacement. A stepper motor is controlled within custom data acquisition software. The stepper motor rotates the ball screw that drives the linear table. Another LVDT continuously measures the table position.

Instantaneous data is collected for normal load, friction force, table position and pin position at 1000 Hz over 1 cycle at specified intervals. Data for one cycle is extracted using the positional LVDT. The instantaneous data are also averaged over two cycles and saved at a specified interval that depends on the length of the test.

Experimental Uncertainty for Friction Coefficients

The primary function of this tribometer is to obtain values of friction coefficients and wear rates for different tribological systems of interest. Neither friction coefficient nor wear rate can be directly measured, so they must be calculated based on other measurable quantities. The uncertainties associated with the calculation of friction coefficient and wear rate based on this tribometer were analyzed by Schmitz *et al.*[3]. The friction coefficient is defined as,

$$\mu = \frac{F_f}{F_n} \qquad\qquad\qquad \text{Eq. 4-9}$$

where F_f and F_n are the friction and normal forces, respectively. Often, the measurement axes, X and Y, are used to calculate an approximate friction coefficient,

$$\mu' = \frac{F_X}{F_Y} \qquad\qquad\qquad \text{Eq. 4-10}$$

where the measurement axes are not necessarily aligned with the normal and frictional axes. These misalignments inevitably arise from kinematic chains of imperfect machining, assembly and compliance. These misalignments can cause substantial errors in the calculation of friction coefficient if unaddressed. Figure 4-6 illustrates these effects. The measurement axes, X and Y are assumed to be orthogonal and biased from the normal (N) and frictional (F) axes by an angle, α.
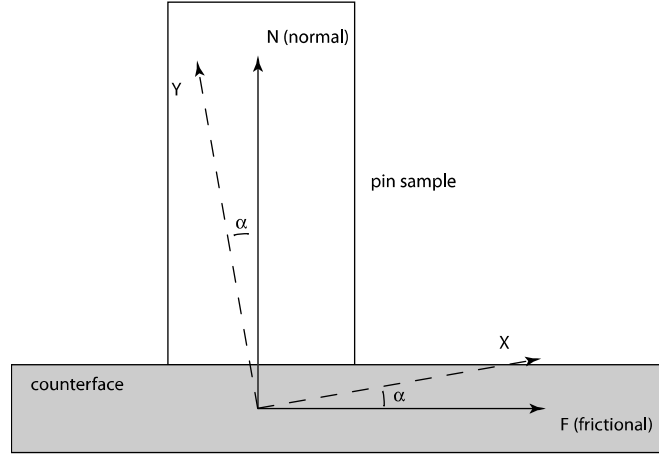
Figure 4-6. Model representation of misaligned measurement axes. The measurement axes are assumed orthogonal and are rotated about the normal and frictional axes by an angle, α.

The measured force responses to the tribological interactions are,

$$F_x = f_f \cos(\alpha) + f_n \sin(\alpha) = \mu f_n \cos(\alpha) + f_n \sin(\alpha) = f_n \left(\mu \cos(\alpha) + \sin(\alpha) \right)$$

Eq. 4-11

$$F_Y = f_n \cos(\alpha) - f_f \sin(\alpha) = f_n \cos(\alpha) - \mu f_n \sin(\alpha) = f_n \left(\cos(\alpha) - \mu \sin(\alpha) \right)$$

Eq. 4-12

resulting in,

$$\mu' = \frac{F_X}{F_Y} = \frac{f_n \left(\mu \cos(\alpha) + \sin(\alpha) \right)}{f_n \left(\cos(\alpha) - \mu \sin(\alpha) \right)} = \frac{\left(\mu \cos(\alpha) + \sin(\alpha) \right)}{\left(\cos(\alpha) - \mu \sin(\alpha) \right)}$$

Eq. 4-13

Defining an error fraction E as,

$$E = \frac{\mu' - \mu}{\mu} = \frac{\mu \cos(\alpha) + \sin(\alpha)}{\mu \left(\cos(\alpha) - \mu \sin(\alpha) \right)} - 1 = \frac{\sin(\alpha)(1 + \mu^2)}{\mu(\cos(\alpha) - \mu \sin(\alpha))} \approx \frac{\alpha(1 + \mu^2)}{\mu - \mu^2 \alpha}$$

Eq. 4-14

The misalignment angle, α, can be found by monitoring the force response to a stationary loaded pin sample. Schmitz *et al.*[3] finds α to be approximately 2° using this method on the tribometer used in this study. For a friction coefficient of $\mu = 0.1$, the corresponding measurement error is 35%. Thus, the measured friction coefficient is extremely sensitive to these misalignments. One could conceivably apply a coordinate transformation to force data with the measured value of α

to calculate the true value of μ, but the angular measurement would still vary slightly from test to test, making this type of analysis very cumbersome. Instead, if a reversal technique is used, the error in the approximate friction coefficient calculations is largely eliminated. The aforementioned analysis will apply to the forward direction, so,

$$\mu_f' = \frac{(\mu\cos(\alpha)+\sin(\alpha))}{(\cos(\alpha)-\mu\sin(\alpha))} \qquad\qquad \text{Eq. 4-15}$$

Upon reversal, $F_{xr}=-\mu f_n \cos(\alpha)+f_n \sin(\alpha))$ and $F_{yr}=f_n\cos(\alpha)+\mu\sin(\alpha)$, and

$$\mu_r' = \frac{(-\mu\cos(\alpha)+\sin(\alpha))}{(\cos(\alpha)+\mu\sin(\alpha))} \qquad\qquad \text{Eq. 4-16}$$

By subtracting μ'_r from μ'_f and dividing by two (average of absolute values), we obtain a new value of the approximate friction coefficient μ',

$$\mu' = \frac{\dfrac{(\mu\cos(\alpha)+\sin(\alpha))}{(\cos(\alpha)-\mu\sin(\alpha))} + \dfrac{(\mu\cos(\alpha)-\sin(\alpha))}{(\cos(\alpha)+\mu\sin(\alpha))}}{2} = \frac{\mu}{\mu^2\cos(\alpha)^2-\mu^2+\cos(\alpha)^2} \approx \mu \qquad \text{Eq. 4-16}$$

With a friction coefficient of 0.1 and a maximum angular misalignment of 4º, this reversal technique introduces a bias in the friction coefficient of 0.0005; i.e. the measured friction coefficient is 0.0005 greater than the true friction coefficient. Without reversals, the bias would be 0.0711, or about 350X the bias with reversals. The angular misalignments are not measured for each experiment and the bias' in friction coefficient measurements are therefore treated as single ended uncertainties which are added to the experimental uncertainty in the measured friction coefficient μ'

The measured friction coefficient μ' has uncertainties associated with the measurements of the forces F_x and F_y. The squared combined standard uncertainty in the measured friction coefficient is calculated using Eq. 4-17.

$$U_c^2(\mu') = \left(\frac{1}{F_y}\right)^2 u_c^2(F_x) + \left(\frac{-F_x}{F_y^2}\right)^2 u_c^2(F_y)$$
<div align="right">Eq. 4-17</div>

The uncertainties in the normal force and friction force directions are approximately 2N and 1N, respectively, and are dominated by time dependent thermal drift. With a normal load of 250N, the uncertainty in the measured friction coefficient is not particularly sensitive to friction coefficient, and ranges from 0.0040 to 0.0044 with values of measured friction coefficient ranging from $\mu = 0.05$ to $\mu = 0.25$. The uncertainty in the force dominates the angular uncertainty and it is thus appropriate and conservative to prescribe error bars with a magnitude of 0.005 to friction coefficient data.

Experimental Uncertainty of Wear Rate

The volume of material lost during the wear process is generally proportional to the normal load and the sliding distance by a wear rate, k. The wear rate of a material can be used to determine component life and is defined as,

$$k = \frac{V}{F_n D}$$
<div align="right">Eq. 4-18</div>

Where V is the volume lost, F_n is the normal load and D is the sliding distance. Often, wear volume is calculated by making displacement measurements of a given cross section or by measuring the mass before and after a test. In many polymer systems, specifically, for wear resistant polymers, creep and thermal expansion can become significant portions of the total volume calculation. Mass loss measurements become difficult in situations where environmental uptake is expected. Since PTFE is known to have a high creep rate and coefficient of thermal expansion, as well as low water uptake and outgassing, mass measurements are used to quantify wear in these studies. The volume lost is then, $V = \frac{\Delta m}{\rho}$, where $\rho = \frac{m_i}{L_1 L_2 L_3}$. The change in

<div align="center">90</div>

mass is Δm, ρ is the density, m_i is the initial mass, and L_1, L_2 and L_3 are the lengths of the rectangular solid sample. The sliding distance is $D = 2SN$, where S is the reciprocation length (for $^1/_2$ cycle) and N is the number of reciprocation cycles. The wear rate can be expressed in terms of the measured quantities as,

$$k = \frac{\Delta m L_1 L_2 L_3}{2 m_i \bar{\bar{F}}_n SN}$$

Eq. 4-19

The *law of propagation of uncertainty* can be applied to Eq. 3-11 to find the combined standard uncertainty or the expected dispersion of values obtained for the wear rate. The sensitivity of each measurement is calculated by taking the partial derivative of the measurand, k, with respect to the measurement. Each sensitivity term is then squared and multiplied by the square of the uncertainty in that measurement. These contributions are added to find the square of the combined standard uncertainty of the wear rate, as

$$u_c^{\,2}(K) = \left(\frac{\partial K}{\partial \Delta m}\right)^2 u^2(\Delta m) + \left(\frac{\partial K}{\partial L_1}\right)^2 u^2(L_1) + \left(\frac{\partial K}{\partial L_2}\right)^2 u^2(L_2) + \left(\frac{\partial K}{\partial L_3}\right)^2 u^2(L_3) +$$

$$\left(\frac{\partial K}{\partial \bar{\bar{F}}_N}\right)^2 u^2(\bar{F}_n) + \left(\frac{\partial K}{\partial m_i}\right)^2 u^2(m_i) + \left(\frac{\partial K}{\partial S}\right)^2 u^2(S)$$

Eq. 4-20

Evaluating the partial derivatives gives,

$$u_c^{\,2}(K) = \left(\frac{L_1 L_2 L_3}{2\bar{F}_n m_i SN}\right)^2 u^2(\Delta m) + \left(\frac{\Delta m L_2 L_3}{2\bar{F}_n m_i SN}\right)^2 u^2(L_1) + \left(\frac{\Delta m L_1 L_3}{2\bar{F}_n m_i SN}\right)^2 u^2(L_2) +$$

$$\left(\frac{\Delta m L_1 L_2}{2\bar{F}_n m_i SN}\right)^2 u^2(L_3) + \left(\frac{-\Delta m L_1 L_2 L_3}{2\bar{F}_n^{\,2} m_i SN}\right)^2 u^2(\bar{F}_n) + \left(\frac{-\Delta m L_1 L_2 L_3}{2\bar{F}_n m_i^{\,2} SN}\right)^2 u^2(m_i) + \left(\frac{-\Delta m L_1 L_2 L_3}{2\bar{F}_n m_i S^2 N}\right)^2 u^2(S)\text{Eq. 4-21}$$

where nominal values of the measurements are used in numerical calculation. Determining the uncertainty of each measurement requires Type A or Type B evaluation consisting of either statistical methods or engineering judgment, respectively. A detailed analysis can be found in

Schmitz *et al.*[4]. Briefly, the uncertainties of the sample length and mass measurements are taken conservatively as five times the manufacturers' specified repeatability; 0.005 mm and 0.05 mg respectively. The uncertainty *u(Δm)* is calculated using the *law of propagation of uncertainty*.

$$\Delta m = m_i - m_f \qquad\qquad \text{Eq. 4-22}$$

Taking the partial derivative of this function with respect to the measurements, m_i and m_f gives,

$$u^2\left(\Delta m\right) = \left(\frac{\partial \Delta m}{\partial m_i}\right)^2 u^2\left(m_i\right) + \left(\frac{\partial \Delta m}{\partial m_f}\right)^2 u^2\left(m_f\right) = \left(1\right)^2 u^2\left(m_i\right) + \left(-1\right)^2 u^2\left(m_f\right) \qquad \text{Eq. 4-23}$$

Since the initial and final masses are approximately the same, it is reasonable to assume that the uncertainties in these measurements are equal, and Eq. 3-15 becomes,

$$u^2\left(\Delta m\right) = 2u^2\left(m_i\right) \qquad\qquad \text{Eq. 4-24}$$

and,

$$u\left(\Delta m\right) = \sqrt{2}\cdot u\left(m_i\right) \qquad\qquad \text{Eq. 4-25}$$

The uncertainty in the normal load due to time dependent fluctuations was found to overwhelm angular misalignment errors and short term scatter, and the uncertainty is taken conservatively as *u(Fn)*=2N, twice the observed thermal drift of the load cell and electronics. The uncertainty in the number of cycles is zero and the uncertainty in the reciprocation length is *u(S)*= 0.2mm which results from a combination of an assumed angular misalignment of 2°, and one standard deviation of measurements for commanded motions.

Many materials exhibit initial wear transients, which preclude the use of single point mass measurements. Often, a least squares regression of the steady data is used to obtain a more representative value for the wear rate of a material. A modified numerical approach to the above uncertainty analysis is required for such regressions [4]. Interrupted measurements are made

periodically during each test and are used to distinguish the steady region of wear from the

transient region. A Monte Carlo simulation uses the uncertainties ($U_c(\Delta V)$ and $U_c(Fn*D)$) and

nominal values of measurement to calculate the average regression slope and standard deviation

of the slopes from 1,000 simulated data sets. The regression represents the wear rate and the

standard deviation of the slope represents the uncertainty in wear rate. The uncertainty intervals

on wear rate data represent the experimental uncertainty in the measurement.

CHAPTER 5
DESIGN OF EXPERIMENTS

Effects of Mechanical Blending

Various techniques, including centrifugal mixing, ultrasonication, blade mixing and jet-milling, have been used throughout the nanocomposite literature to disperse nanoparticles. Jet-milling has proven to be a particularly successful technique, especially at low loadings, but it is unclear if this success is a product of mechanically induced morphological changes or simply the result of improved dispersion. One hypothesis is that the high energy of the jet-milling technique results in a fibrillated structure that promotes wear resistance when stabilized by nanoparticles during sintering. Fibrils of PTFE are oriented and extremely strong compared to the bulk material and are often the source of improved strength, stiffness, toughness and creep resistance [13, 103, 105, 109, 110]. In this experiment, the morphological and structural changes induced by the mechanical history of the sample are studied to test the hypothesis that the success of the jet-mill is due to fibrillation induced during processing.

Neat PTFE particles are treated with one of five mechanical blending techniques, which include, elastic sieve classification, centrifugal mixing, ultrasonication, blade mixing and jet-milling. The experimental treatment and the treatment operating conditions are shown in Table 5-1. The first goal of this study is to characterize the thermal characteristics of the virgin powder. The second goal is to establish the effects of mechanical mixing on the structure and morphology of the PTFE. This study is critical in determining whether the fibrils observed for wear resistant materials are formed during mechanical processing or wear events. Scanning electron microscopy (SEM) is used to evaluate the topographical structural effects of the mechanical treatments. Particle reduction, deformation and fibrillation are of interest. The melt behavior of PTFE is very sensitive to the nature of the crystalline structure and morphology, and

as a result, it is also reputably sensitive to mechanical history. Differential Scanning Calorimetry (DSC) is used to study the thermal response of the powders here to provide insight into the resulting crystalline structure after each processing technique. Melt peaks, crystallinity and matrix mobility are of interest. These complimentary techniques can provide structural information from the nanoscale to the micro-scale, and provide a much more complete understanding of the effects of these dispersion techniques on the matrix itself than is currently available.

Table 5-1. Blending treatments of neat PTFE to simulate the effects of nanoparticle dispersion on the polymer. The morphological and thermal characteristics of the powders are studied following treatment.

Sample	Powder treatment	Conditions
1	None	Control; virgin as-received powder
2	None	Control; virgin as-received powder
3	None	Control; virgin as-received powder
4	None	Control; virgin as-received powder
5	None	Control; virgin as-received powder
6	Shear sieve	1 pass through 10 mesh sieve
7	Ultrasonication	Ultrasonic agitation; 30 minutes
8	Hauschild rotary mixer	1500 RPM for 30 seconds
9	Blade mixer	30,000 RPM for 40 seconds
10	Jet-mill	150 psi; 3 passes; ~5g/min

Processing Temperature and Crystalline Morphology

The melt behavior of PTFE is very unique, and the characteristics of its thermal behavior are widely known to depend strongly on the thermal and mechanical history of the sample [94, 95, 111, 112]. This is due to the strong sensitivity of its crystalline structure to both, and the strong relationship between crystalline structure and thermal response. In general, the more ordered the crystalline structure, the higher the melt temperature [95, 107, 108]. Virgin PTFE from the reactor has large regions of high order, and has a reported melt temperature of 353°C. Following melting and recrystallization, PTFE is relatively disordered and has the more

95

commonly cited melt temperature of 327°C. Figure 5-1 shows differential scanning calorimetry

(DSC) thermograms for virgin PTFE powder. During the first heat, the melt temperature of the

powder is 343°C with a large melt peak indicative of high crystallinity (~75% using a heat of

fusion of 82 J/g for perfectly crystalline PTFE [113]). Following melt, the sample was cooled

and the material crystallized. During the second heat, melting occurs at a temperature of 327°C

with less consumed energy indicating lower crystallinity (~25%). In a preliminary thermal

characterization study of a 1 wt% PTFE nanocomposite, a large melt peak of 340°C was

observed even though the sample was processed using standard processing with a spike to 380°C

and a hold at 362°C. This result suggested that the nanoparticles may inhibit PTFE mobility at

these temperatures, and thus stabilize the ordered virgin morphology of the PTFE.
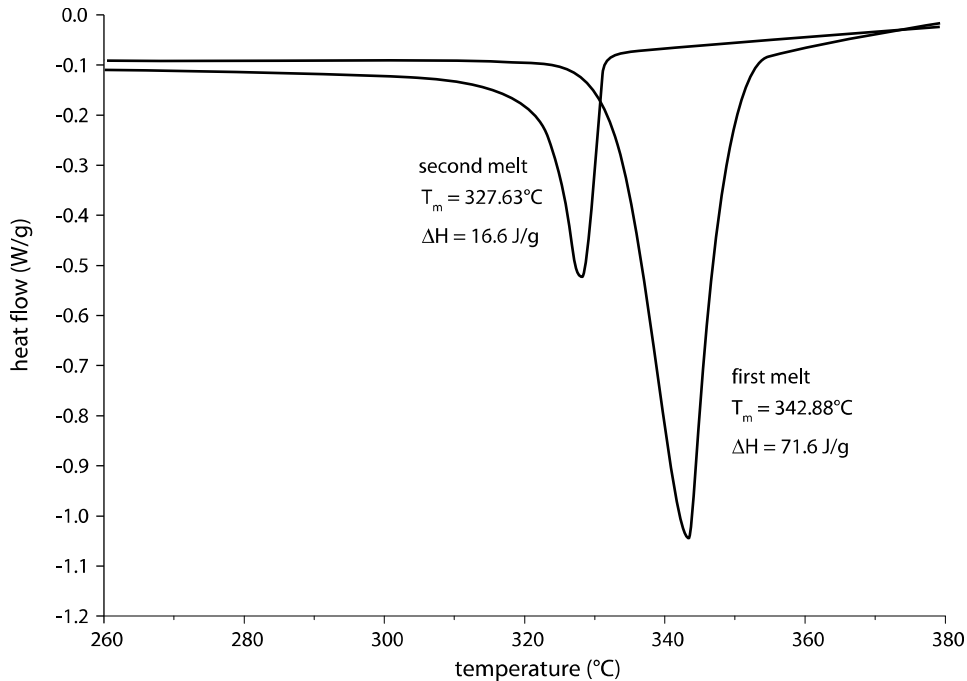
Figure 5-1. Differential Scanning calorimetry thermogram of as-received virgin PTFE during a heat/cool/heat cycle. The first melt is indicative of virgin PTFE, while the second melt occurs after the first melt and recrystallization. Following melt and recrystallization, both the melt temperature and crystallinity are lower.

96

A working hypothesis for wear resistance in PTFE nanocomposites is that the nanoparticles stabilize the virgin 'folded ribbon' morphology of the PTFE. This structure may facilitate fibrillation during deformation which provides an efficient deformation mechanism and a strengthened running surface in the sliding direction [103-105, 114-117]. Based on this wear reduction mechanism, virgin PTFE is hypothesized to have improved wear resistance over melt processed PTFE. This study investigates the thermal, tribological and mechanical characteristics of PTFE as a function of processing temperature to test the hypothesis that the virgin morphology facilitates fibrillation and promotes wear resistance in the absence of nanoparticles. Because the PTFE particles in the sample require melting for effective sintering and mechanical integrity, the morphology of the PTFE cannot be separated from the cohesion and strength of the sample. Various temperatures in the vicinity of the melt temperature were employed in order to achieve the best possible balance of inter-particle cohesion and virgin morphology. At intermediate temperatures, low melt structures may melt to form cohesive particle boundaries while high temperature structures remain un-melted to promote fibrillation during wear.

Virgin PTFE was compression molded at five experimental temperatures. The control temperature is 362°C; at this test condition, the sample should fully melt and recrystallize into a more disordered, less crystalline structure with a melt peak near 327°C. This fully sintered PTFE is known to have a high wear rate on the order of $k=10^{-3}$ mm^3/Nm under typical conditions [8, 9]. Additional temperatures of 300°C, 327°C, 345°C and 353°C were used to study the thermal, tribological and mechanical characteristics of virgin PTFE as a function of the sintering temperature. Virgin powders were used to fill a mold and the sample was compacted at 80 MPa for 15 minutes. A temperature ramp of 2°C/minute was used to heat the sample at a light hold

pressure of 4 MPa. The sample is held at the process temperature for 3 hours and is then cooled

at the same rate.

The experimental matrix for this study is shown in Table 5-2. Tribological experiments

were conducted on a linear reciprocating tribometer at 50.8 mm/s and 6.3 MPa of pressure.

Mechanical tensile tests were conducted with a strain ramp of 1%/minute, and thermal

measurements were carried out using differential scanning calorimetry and a ramp rate of

10°C/minute.

Table 5-2. Experimental matrix investigating the effects of sinter temperature on the
tribological, thermal and mechanical properties of unfilled virgin PTFE.

Sample	Sintering temperature (°C)	Experiments
11	300	Thermal and tribological
12	327	Thermal and tribological
13	345	Thermal and tribological
14	353	Thermal and tribological
15	362	Thermal and tribological
16	300	Thermal and mechanical
17	327	Thermal and mechanical
18	345	Thermal and mechanical
19	353	Thermal and mechanical
20	362	Thermal and mechanical

Mechanical Processing on Nanoparticle Dispersion

The processing of PTFE and PTFE composites is inherently difficult. The same unique

thermal and chemical properties that make PTFE an attractive extreme environment solid

lubricant also make PTFE nanocomposites inherently difficult to process. The most effective

polymer matrix dispersion techniques, namely liquid dispersion/*in-situ* polymerization and high

shear-rate melt-mixing [118-120], are precluded for PTFE. As a result, filler materials must be

dispersed into dry PTFE powders with any of a number of dry powder blending techniques. This

method cannot create a 'uniform' dispersion. In a best case scenario, fillers and matrix particle

agglomerations are disbanded, perfectly dispersed and equally distributed to decorate each PTFE

particle. The limit of uniformity, in this case, is the largest particle being dispersed. This is important in nanocomposite synthesis since the size-scale of the characteristic repeating unit in the dispersion is orders of magnitude larger than the filler particle.

In addition to these inherent dispersion and processing limitations of PTFE, nanoparticles are notoriously difficult to disperse with dry powder blending techniques. The potential benefits of the nanoparticle fillers result from large interfacial areas and number densities for a given volume of material. This also makes the surface forces large compared to the body forces which results in agglomeration. Dry powder blending techniques are not particularly effective in disbanding nanoparticle agglomerates because they primarily rely on accelerations and inertias for particle dispersion. In a worst case scenario, agglomerations are not disbanded, and the composite mimics the dispersion characteristics of a microcomposite.

As a result of the processing difficulties of PTFE nanocomposites, dispersion and the role of dispersion on the tribological properties of the nanocomposite are among the largest of uncertainties in PTFE nanocomposites tribology. The polymer nanocomposites tribology literature is full of examples where poor performance is likely the result of poor dispersion, but due to the paucity of dispersion characterization, this relationship has not yet been established [8, 10, 11, 16, 17, 19, 31-34, 46, 121]. In parallel studies by Burris *et al.*[19] and McElwain [52] similar performance was obtained at 5 wt% loading of 80 nm α phase alumina mixed using a jet-mill and a hauschild mixer, respectively. However, while Burris *et al.*retained high wear resistance at 1 wt% loading, McElwain found a 0.8wt% nanocomposites to be 5,000X less wear resistant. The hauschild mixer is suspected to have poor dispersion ability at low loadings. Dispersion is also the factor which contributes most to the difficulty in interpreting the state of the field. This is mostly due to a lack of dispersion characterization and a lack of standard

processing techniques. In addition, important factors such as blade speed and time of dispersion are seldom mentioned.

In this study, nanoparticle dispersions are examined. The experimental matrix is shown in Table 5-3 and includes three nanoparticle loading conditions (1, 2 and 5 wt%) and two nanoparticle dispersion techniques (none and jet-milling). In each case the neat PTFE powders are jet-milled prior to nanoparticle inclusion to separate dispersion effects from blending effects. Following jet-milling, the appropriate weights of the constituents are combined and mixed for 1 minute by hand to obtain gross homogeneity. The control sample is untreated and the test samples are further dispersed using a jet-mill. Following blending, the samples are studied using scanning electron microscopy to interrogate the effects of the dispersion treatments on the nanoparticle dispersions.

Table 5-3. Experimental matrix examining the effect of loading and dispersion technique on the powder dispersion of nanoparticles and PTFE. Nanoparticles are 80 nm alpha phase alumina.

sample	wt%	Dispersion treatment	test
21	1	Hand-mixed	Dispersion characterization
22	1	Jet-milled	Dispersion characterization
23	2	Hand-mixed	Dispersion characterization
24	2	Jet-milled	Dispersion characterization
25	5	Hand-mixed	Dispersion characterization
26	5	Jet-milled	Dispersion characterization

Nanoparticles on the Melt Behavior of PTFE

A standing hypothesis for the wear resistance in PTFE nanocomposites is that the nanoparticles stabilize the virgin PTFE structure to temperatures that would otherwise destroy this structure. This structure is thought to promote wear resistance by facilitating an energy-absorbing fibril-forming deformation-mechanism during sliding. This hypothesis is largely based on a thermal and tribological study of one 1 wt% wear resistant alumina-PTFE

nanocomposite. In this study, a very wear resistant nanocomposite had a DSC thermogram with

a large high temperature melt peak indicative of the virgin PTFE structure. It was hypothesized

that the nanoparticle inclusion resulted in retention of the virgin structure which promoted

fibrillation and wear resistance. To test this hypothesis, the nanocomposite was heat treated to

400ºC to destroy the virgin structure.   Following heat treatment, the thermogram reflected

melted and recrystallized PTFE and wear resistance was lost.

Table 5-4. Experimental matrix for experiments studying the influence of nanoparticles on the thermal response of the PTFE powder. All samples are jet-milled identically.

sample	wt%	Dispersion treatment	test
21	1	Hand-mixed	Thermal analysis
22	1	Jet-milled	Thermal analysis
23	2	Hand-mixed	Thermal analysis
24	2	Jet-milled	Thermal analysis
25	5	Hand-mixed	Thermal analysis
26	5	Jet-milled	Thermal analysis

It is clear that the morphological characteristics of the PTFE itself has a significant impact

on the tribological properties of the material since nanoparticle material, size, shape, loading and

dispersion were nominally constant before and after heat treatment. It is unclear what role the

nanoparticles play in the stabilization of the virgin morphology. It is possible that the

nanoparticles retard melting to higher temperature, in which case the polymer would not have

melted during compression molding. This is unlikely since the melt temperature of the

nanocomposite sample was found to be no higher than that of virgin PTFE using differential

scanning calorimetry. Another possibility is that the polymer melts during processing, but the

high nanoparticle density and surface area limit polymer mobility during melt and nucleate

recrystallization upon cooling. In this study, differential scanning calorimetry is used to study

the thermal behaviors of PTFE and PTFE nanocomposite powder ensembles. The experimental

matrix for this test schedule is shown in Table 5-4.

Filler Dispersion on Nanocomposite Properties

An essential part of understanding the tribological and deformation mechanisms of a

material is a thorough understanding of the material under investigation, but this combination of

material science and tribology is almost completely absent from the literature [121]. In this

study, the thermal, tribological and mechanical properties of compression molded samples are

investigated. The powder ensembles are compression molded into test pucks using the standard

compression molding procedure outlined in the sample preparation section. The experimental

matrix describing this study on compression molded nanocomposites is shown in Table 5-5.

Table 5-5. Experimental matrix investigating the effects of nanoparticle loading on the thermal,
tribological and mechanical properties of the compression molded nanocomposite.
Nanoparticles are 80 nm alpha phase alumina. PTFE powders are jet-milled prior to
nanoparticle inclusion to eliminate PTFE agglomeration and size as variables.

sample	wt%	Dispersion treatment	Test
27	1	Hand-mixed	Thermal, tribological
28	1	Jet-milling	Thermal, tribological
29	2	Hand-mixed	Thermal, tribological
30	2	Jet-milling	Thermal, tribological
31	5	Hand-mixed	Thermal, tribological
32	5	Jet-milling	Thermal, tribological
33	1	Hand-mixed	Thermal, mechanical
34	1	Jet-milling	Thermal, mechanical
35	2	Hand-mixed	Thermal, mechanical
36	2	Jet-milling	Thermal, mechanical
37	5	Hand-mixed	Thermal, mechanical
38	5	Jet-milling	Thermal, mechanical

Tribological properties are characterized using the linear reciprocating tribometer

discussed in Chapter 4 using a sliding speed of 50 mm/s, a normal pressure of 6.3 MPa and a

track length of 25 mm. The length of the test will be a function of the wear resistance of the

sample and will persist until the sample loses ~50 mm^3 of material or accumulates ~750,000

sliding cycles. An additional compression molded puck is processed for mechanical

characterization. Tensile tests are conducted on each sample at 1%/min until the sample can no

longer support load. Thermal samples are extracted from each compression molded puck prior

to machining.

Filler Material on Nanocomposite Properties

A study by Burris and Sawyer found that the α phase of the alumina nanoparticles was

much more effective than the $\Delta{:}\Gamma$ phase [8]. A more recent study has shown that this is also true

when filler particle size is held constant. These results are unusual and suggest that the shape or

chemistry dominate the dispersion or the effects of the particles on polymer structure, mobility,

nucleation or recrystallization, and as a consequence, dominates the tribological properties of the

composite. In this study, the influences of particle phase are investigated in terms of dispersion,

thermal effects on the matrix, tribological properties and mechanical properties.

Following dispersion and thermal studies of the powders, the ensembles are compression

molded for thermal, tribological and mechanical characterization of the processed

nanocomposites. Thermal studies on compression molded samples utilize a heat-cool-heat from

-10-400°C to study the phase transitions, glass transition and melt behavior of the pressure-

sintered and free-sintered material. The experimental matrix is shown in Table 5-6. Tribological

and mechanical characterizations are conducted as described in Chapter 4.

Table 5-6. Experimental matrix for experiments studying the influence of nanoparticles on the
thermal, mechanical and tribological response of the PTFE nanocomposites. All
samples are jet-milled and compression molded according to the procedures outlined
in Chapter 4.

Sample	Loading (wt%)	APS (nm)	Phase
15	0	N/A	N/A
39	12.5	80	α
40	12.5	44	$\Delta{:}\Gamma$

CHAPTER 6
RESULTS

Mechanical Blending

Characterization of Particle Morphology

Representative images from SEM analysis of the PTFE particles following varying

mechanical blending treatments are shown in Figure 6-1. Box plots for the estimated mean

particle sizes, standard deviations and upper and lower quartiles are shown in Figure 6-2.

Pseudo-quantitative estimates of the particle sizes from these studies are listed in Table 6-1. The

manufacturer reported average particle size (APS) of the Teflon ™ 7C compression molding

resin is 35 µm, but SEM analysis of the as-received powders (Figure 6-1a) suggests an average

particle size of approximately 20 µm. The vast majority of the particles are round with a

characteristic size near 20 µm, but there are also particles that are highly elongated with the long

dimension being on the 50-100 µm size scale and the short dimension being on the 1-5 µm size

scale. The distribution is positively skewed and contains only a small fraction of particles with a

characteristic dimension less than ~15 µm.

Similar analyses of the sieved, ultrasonicated, rotary mixed and blade mixed powders in

Figure 6-1(b-e) reveal particle distributions and morphologies that are nominally identical to the

virgin powders to within the detection limits of the SEM surveying method employed. Each

powder predominantly contains round 20 µm particles intermixed with smaller round particles

and larger elongated particles. PTFE Teflon™ 7C is reputably difficult to grind due to the small

size and high toughness of the resin; this is evidenced by the lack of influence the various

blending techniques had on particle size and morphology. The blender in particular was

expected to effect both given the severity of the operation with steel grinding blades rotating

through the powders at 30,000 RPM, but even this technique had a negligible effect.
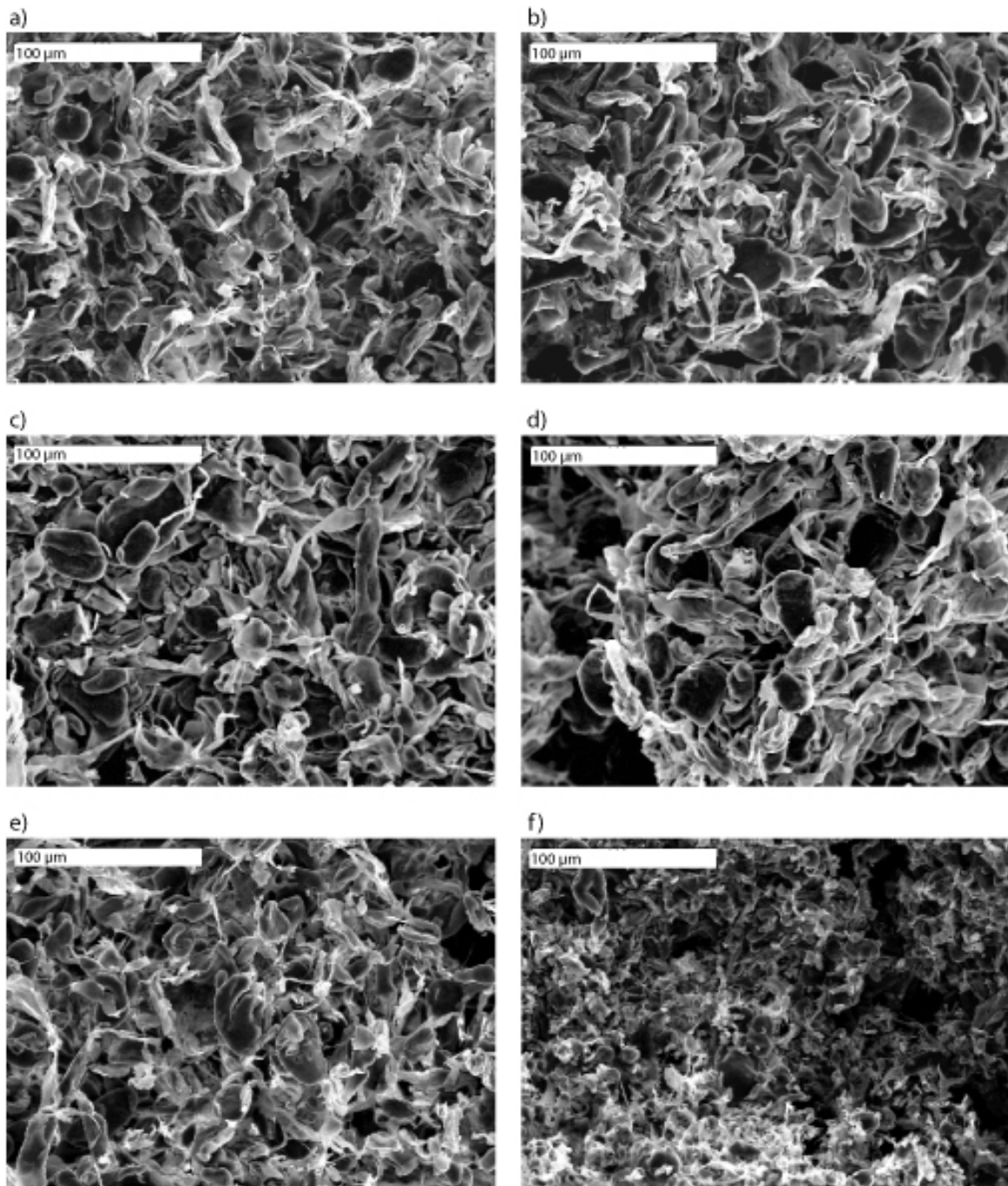
Figure 6-1. SEM images of virgin PTFE following varying mechanical treatments typically used in particle dispersion: a) untreated, b) sieved, c) ultrasonicated, d) rotary mixed, e) blade mixed and f) jet-milled.

This lack of influence is contrasted by gross effects of the jet-milling operation to both the particle size distribution and the particle morphology. Jet-milled powders have a substantially smaller mean near 5µm and do not contain any of the highly elongated structures possessed by the other powders. Despite resisting any size reductions from the other grinding operations in the study, nearly all of the PTFE particles in the as-received powders were ground to ¼ the original diameter on average. This equates to a 4X increase in particle surface area and a 64X increase in the number of particles, both of which may have an impact on the melt and crystallization characteristics of the resin as well as any compartmentalization effects in a tribological nanocomposite [8, 16, 51]. One of the most important features of the jet-milled powders, however, is the complete lack of a fibrillated morphology. It can be concluded that the PTFE fibrils observed in the running surfaces of very wear resistant PTFE nanocomposites are products of deformation processes during sliding and are not created during powder blending.
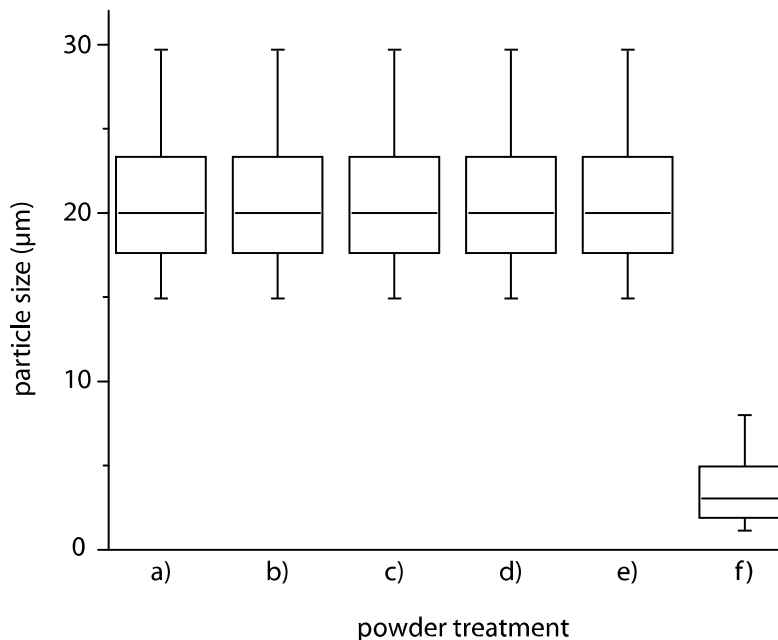
Figure 6-2. Estimated particle size results of virgin PTFE following varying mechanical treatments: a) untreated, b) sieved, c) ultrasonicated, d) rotary mixed, e) blade mixed and f) jet-milled. Averages, standard deviations and quartiles are estimated from SEM surveying.

Thermal Characterization

Measurements of the thermal characteristics of the powders were made to interrogate the thermal implications of the mechanical processing and the resulting PTFE morphologies. The resulting thermograms from DSC measurement of PTFE powders following the mechanical treatments under investigation are shown in Figure 6-3. Five independent control samples with no mechanical treatment were created and tested to evaluate material variability, sample preparation variability and measurement variability. These five independent experiments are shown in blue in Figure 6-3. The measurements fall very close to one another and indicate excellent repeatability in the material, sample preparation and thermal measurement. Measurements of melt temperatures and enthalpies from these thermograms are tabulated in Table 6-1 and the results are shown graphically in Figure 6-4.

A mean first melt peak for untreated, as-received PTFE powders of 342.76°C was calculated. The standard deviation in the measurements was 0.08°C. Using the t statistic (because of the small sample size) with 4 degrees of freedom, the limits of the true population mean can be calculated for a desired confidence percentage. For 99% confidence in this case, the t statistic is 3.747. From the central limit theorem, the standard deviation for the distribution of mean values from random sampling can be calculated as

$$\sigma_{\bar{y}} = \frac{s}{\sqrt{n}} = \frac{0.08}{\sqrt{5}} = 0.036 \, ^\circ\text{C} \qquad\qquad \text{Eq. 6-1}$$

The lower limit on the true mean for 99% confidence is,

$$\mu > \bar{y} - \frac{ts}{\sqrt{n}} = 342.76 - \frac{3.747 \times 0.08}{\sqrt{5}} = 342.63 \, ^\circ\text{C} \qquad\qquad \text{Eq. 6-2}$$

i.e. there is less than 1% probability that the 5 random samples used in these experiments came from a population with a mean of 342.63°C or less.
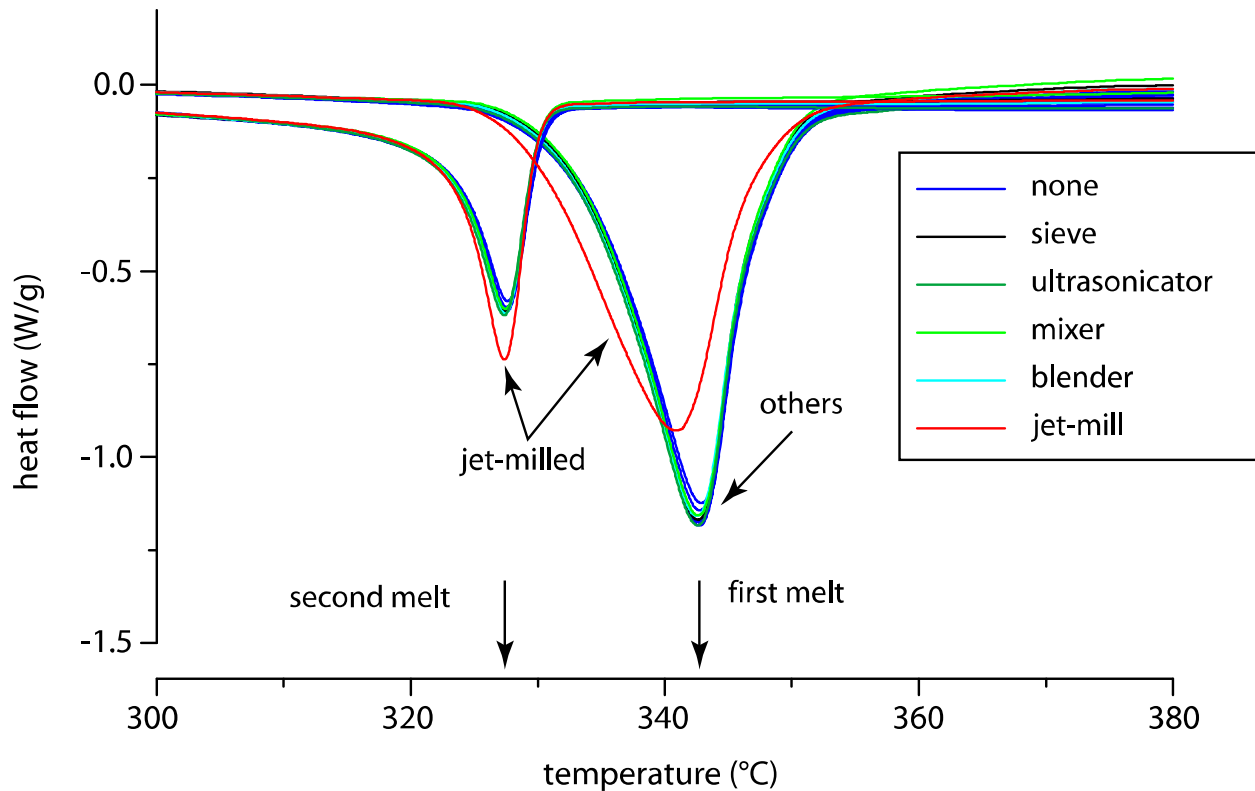
Figure 6-3. Differential scanning calorimetry of PTFE powders with varying mechanical history. Jet-milling provided the only significant deviation from the thermal behavior of virgin PTFE.

Once the lower limit for the true untreated population mean has been quantified, the probability that the other samples did or did not belong to the same population can be computed. The values of first melt for the sieved and rotary mixed samples lie in between the upper and lower limits for the true population mean for virgin powders, and it cannot be concluded that these powders have different first melts. The sonicated and blade mixed samples were 0.13σ and 1σ below the lower limit for the mean. Since ~16% of the data lies greater than 1σ below the mean, it cannot be concluded that either of these powders have a different first melt temperature than the untreated powder. The first melt temperature of the jet-milled powder however, is 22σ below the lower limit for the mean first melt temperature of virgin PTFE. Less than 3×10^{-5} % of the data lies above 5σ, so there is essentially zero probability that the jet-milled PTFE

108

sample came from the untreated distribution and it can be concluded that its first melt temperature of the PTFE has been reduced due to jet-milling with nearly 100% confidence.

From the data collected, none of the other operations had an effect on size or ordering of the polymer, but the lower melt temperature of the jet-milled sample suggests that the crystals have been reduced in size and/or reduced to a less ordered morphology. This implication is consistent with SEM observation of the powders which shows significant reductions in the sizes of nominally single crystal particles in the resin. The lowering of the melt temperature following jet-milling suggests that the crystals have become smaller and less ordered.

The same analysis can be conducted for the first and second enthalpies of formation and the second melt. For the first heat of formation, there is significantly more scatter for nominally identical samples than there was for the first melt temperature. This is partially attributable to the 1% uncertainty in energy and the uncertainty of mass measurements, but it also likely reflects a true variation in crystallinity within the powder. The lower limit for the mean first enthalpy of formation of the untreated resin is 70.4 J/g with a standard deviation of 1.2 J/g. Each of the treated, non-jet-milled samples lie within the limits of the true population mean for untreated powders. The jet-milled powder had a heat of formation that was 1σ below this lower limit, but with only 84% confidence, there is insufficient evidence to conclude that the two samples have different population means. A lack of change in the heat of formation is not completely surprising; the particle bulk does not appear to be appreciably deformed with the vast majority of the mechanical destruction occurring on and near the particles surfaces which constitute only a very small fraction of the total mass contributing to the signal.
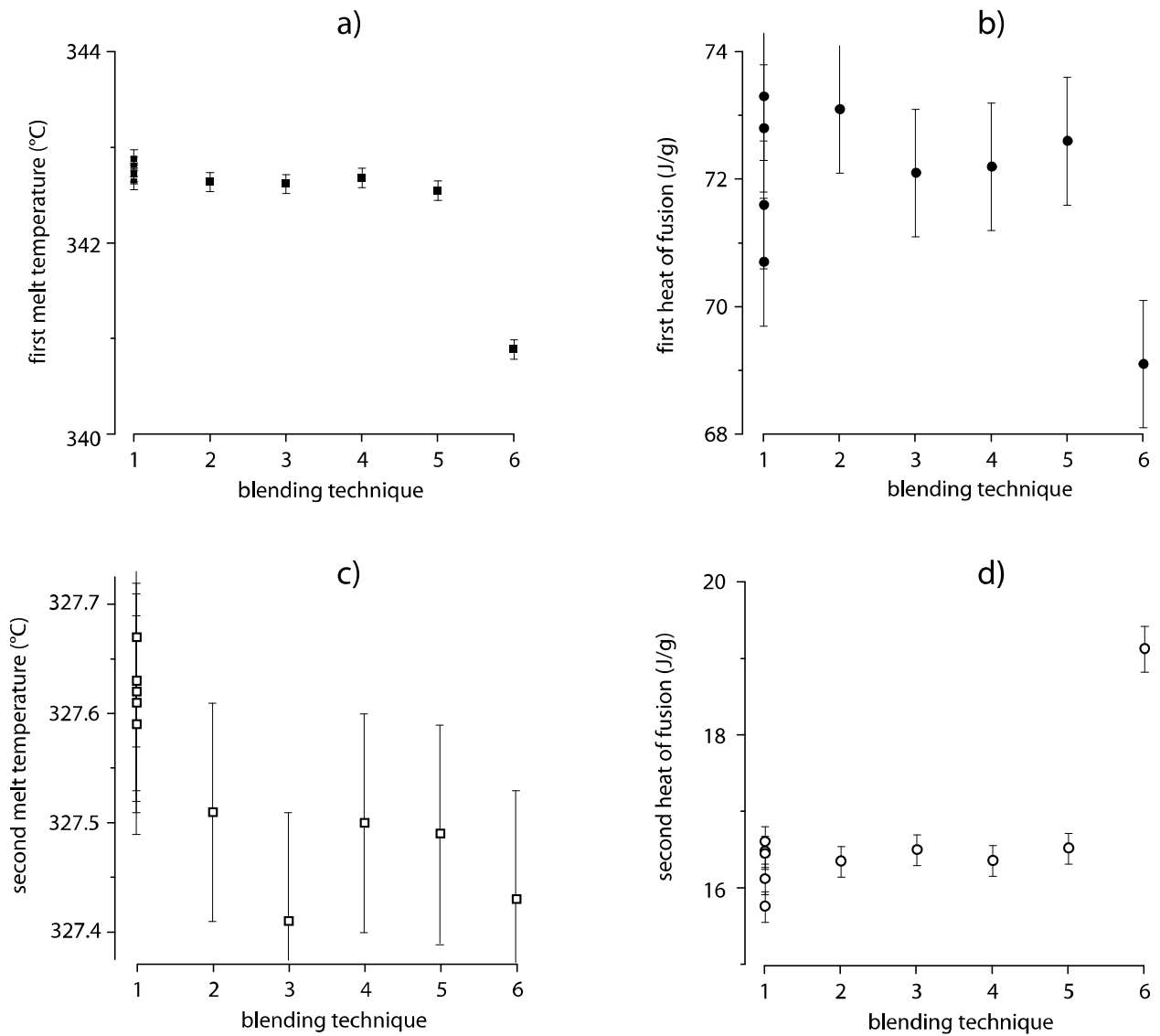
Figure 6-4. Quantified results of differential scanning calorimetry of PTFE powders with
varying mechanical history: a) first melt peak temperature, b) first heat of fusion, c)
second melt peak temperature and d) second heat of fusion. Treatments are labeled as
follows: 1) untreated, 2) sieved, 3) ultrasonicated, 4) rotary mixed, 5) blade mixed
and 6) jet-milled.

For the second melt, a lower limit of 327.57°C for the virgin population mean is

calculated. In this case all of the samples have melt temperatures far enough below the lower

mean limit to conclude with better than 97% confidence that melt temperatures are below that of

the untreated control sample. Sieved, rotary blended and blade mixed samples are ~2σ below the

untreated lower limit, while sonicated and jet-milled samples are ~5σ below. Despite having

statistically different second melt temperatures than the untreated samples, these samples had, at

most, a 0.2°C melt temperature difference as opposed to the 2°C difference for the jet-milled

sample on first melt. It is unclear what, if any implications this slight temperature difference has,

especially when considering the 0.1°C uncertainty in the measurement.

Table 6-1. Blending treatments of neat PTFE to simulate the effects of nanoparticle dispersion
on the polymer. Sizes are reported using lower quartile, mean and upper quartile,
respectively. Five independent samples of the unprocessed PTFE were tested for
control statistics on thermal behavior. Uncertainty on temperature data is 0.1°C.

	Morphology	Thermal properties					
	Size (µm)	T_{m1}(°C)	ΔH_{m1}(J/g)	$U(\Delta H_{m1})$	T_{m2}(°C)	ΔH_{m2}(J/g)	$U(\Delta H_{m2})$
1 untreated	15,20,30	342.88	71.6	1.0	327.63	16.6	0.2
2 untreated	15,20,30	342.80	70.7	1.0	327.67	15.8	0.2
3 untreated	15,20,30	342.74	72.8	1.0	327.62	16.1	0.2
4 untreated	15,20,30	342.66	73.3	1.0	327.61	16.5	0.2
5 untreated	15,20,30	342.72	73.3	1.0	327.59	16.5	0.2
1-5 mean	20	342.76	72.4	1.0	327.62	16.3	0.2
1-5 σ	3	0.08	1.2		0.03	0.3	
6 sieved	15,20,30	342.64	73.1	1.0	327.51	16.4	0.2
7 sonicated	15,20,30	342.62	72.1	1.0	327.41	16.5	0.2
8 rotary	15,20,30	342.68	72.2	1.0	327.50	16.4	0.2
9 blade	15,20,30	342.55	72.6	1.0	327.49	16.5	0.2
10 jet-mill	1,3,7	340.89	69.1	1.0	327.43	19.1	0.3

An upper limit of 16.8 J/g is computed for the true population mean of the second heat of

fusion of untreated virgin PTFE resin. The scatter in this data is significantly smaller than it was

for the first heat of fusion. This is likely due to the carefully controlled cooling rate following

melt and it's regulating effect on the crystallinity of the samples. Each of the non-jet-mill treated

samples had heats of fusion that are between the population mean limits for 99% confidence.

The jet-milled sample has a heat of fusion that is nearly 8σ above the upper limit of the untreated

PTFE for 99% confidence. It can be concluded with essentially 100% confidence that the melt recrystallized jet-milled sample has a greater crystallinity than the untreated resin. The jet-milled powder had approximately 50 times the number of particles for a given mass. This may have increased the number of nucleation sites to promote increased crystallinity.

Processing Temperature and Crystalline Morphology

Thermal Characterization

Previous studies have shown that successful melt-processed PTFE nanocomposites shared the thermal and X-Ray diffraction characteristics of virgin PTFE prior to melting. Naturally this observation led to a hypothesis that the role of the nanoparticles was to stabilize the virgin morphology of PTFE during melt processing. It remains unclear if this morphological signature alone accounts for the wear resistance of the low wt% nanocomposites, or if the nanoparticles lead to wear resistance through other mechanisms. Here, PTFE test specimens were prepared at varying hold temperature to investigate the role of PTFE morphology in the absence of the nanoparticles.

Following compression molding, the tribological samples were machined from the compression molded puck, with the wear surface being located at the axial center of the cylinder. DSC samples were taken from a location of the puck that is within 2 mm of the wear surface. The resulting DSC thermograms are shown for each of the five samples in Figure 6-5. The evolution of the thermal behavior is clearly seen in Figure 6-5a. The 300°C, 327°C and 345°C samples exhibit similar melt behavior to the virgin powder; thus, very little if any of the sample ever 'melted' during compression molding. At higher temperatures, only the low ordered crystals in the lower temperature regime of the melt curve enter the 'gel' or 'melt' state during processing. These melted regions recrystallize and exhibit the lower melt temperature of the lower ordered recrystallized PTFE. The effects of this partial melting are clearly visible for the

112

345°C, 353°C and 362°C samples with the amount of 'recrystallized' material at the ~327°C

melt temperature increasing with increased hold temperature. It is interesting to note that the

samples with hold temperatures that are significantly higher than the 'melt' temperature of the

material do not fully melt. This is clearly the case at the 362°C hold temperature. The

thermocouple measured temperature at a location very near the test area and despite being heated

20°C-30°C over the melt peak, a small fraction of the material did not melt. During compression

molding, the sample is under pressure. This pressure likely inhibits mobility of the polymer, and

additional thermal energy is necessary to induce melting.
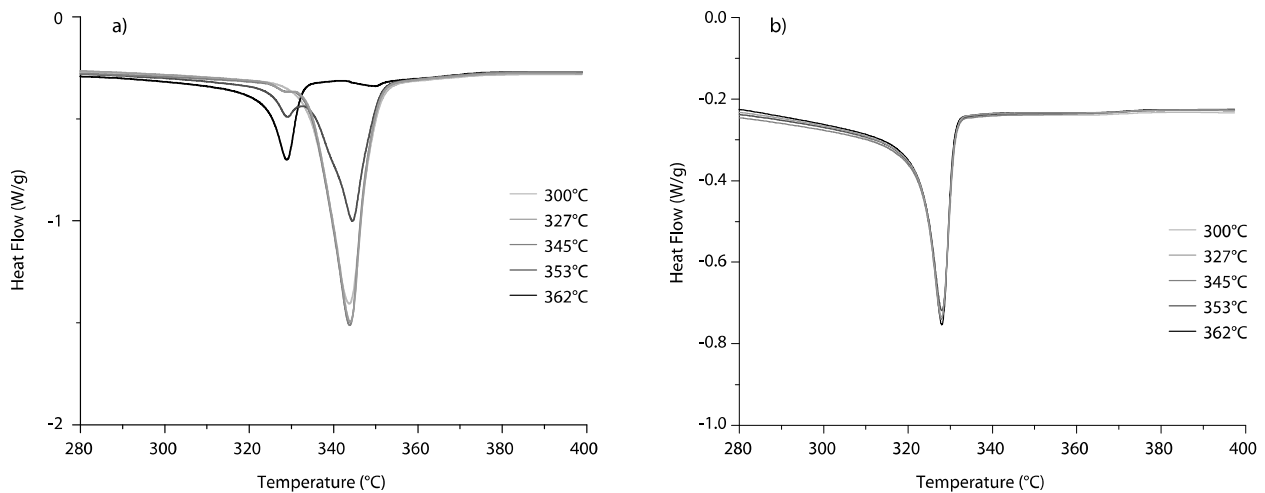
Figure 6-5. Differential scanning calorimetry of PTFE samples compression molded with
varying sintering hold temperatures; a) first melt following compression molding, b)
second melt following recrystallization at a cooling rate of 10°C/min. The first melt
curves show a gradual transition from the virgin morphology having a melt peak of
~343°C and the melt crystallized morphology having a melt peak of ~327°C.
Following recrystallization from 400°C at 10°C/min, the thermal characteristics are
nearly identical.

Melt peaks and enthalpies are plotted versus hold temperature in Figure 6-6. These results

are tabulated in Table 6-2. The melt peak remains nominally unchanged as more and more

melting occurs until the magnitude of the 327°C melt peak height exceeds that at 344°C. The

362°C sample was the only sample where the low temperature peak height exceeds the high

temperature peak height. Once melting begins, there appears to be an approximately linear

decrease in crystallinity (enthalpy) with increased peak temperature.
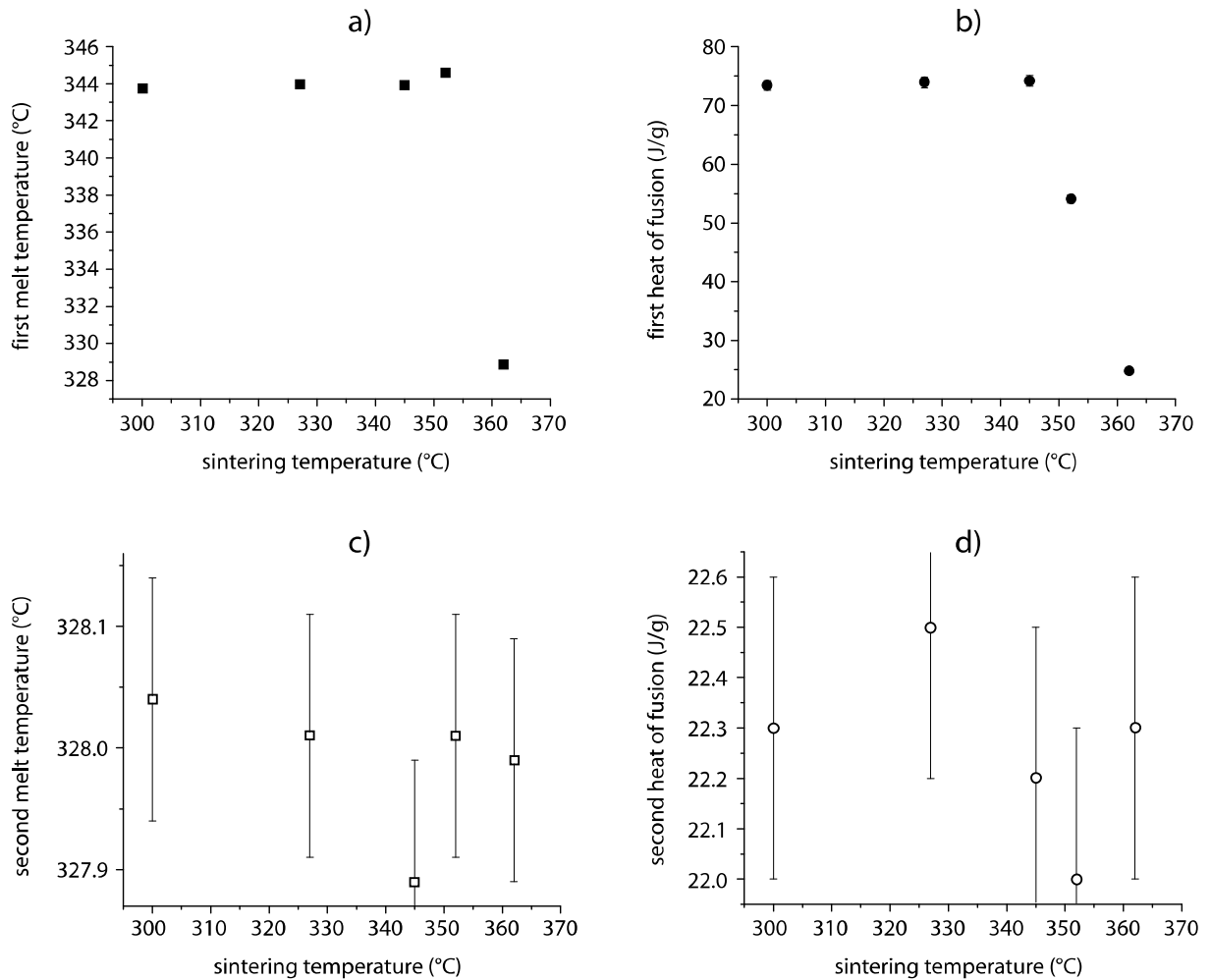
Figure 6-6. Results of differential scanning calorimetry of PTFE samples compression molded
with varying sintering hold temperatures; a) first peak melt temperature, b) first heat
of fusion, c) second peak melt temperature following recrystallization at a cooling
rate of 10°C/min, d) second heat of fusion following recrystallization at a cooling rate
of 10°C/min. There is a gradual transition from the virgin morphology to the
recrystallized morphology as more melting occurs.

These DSC results show that the morphology of the PTFE can be controlled using hold

temperature variations in the absence of nanoparticles. This study is not entirely fair since the

nanocomposites are heated and held at 362°C. The consequence of the low hold temperature is

the potential for improper sintering and reduced continuity between the particles. However, the

surfaces of the particles have lower ordering than the internal bulk and are therefore thought to melt preferentially. Thus, the 345°C and 353°C samples should offer a strong opportunity to study samples with virgin bulk morphology and strong interparticle connectivity.

Mechanical Properties Characterization

The virgin morphology is thought to promote wear resistance by facilitating fibrillation during deformation and therefore increasing the energy required to remove material during sliding. The mechanical properties of these samples were studied to investigate the role of fibrillation and toughness on the wear properties of the sample. Stress is plotted versus engineering strain in Figure 6-7 for the hold temperatures of 327°C, 345°C, 353°C and 362°C. The sample held at 300°C was not resilient enough to endure machining and broke during fixturing. The 345°C, 353°C and 362°C samples had similar moduli on the order of 300 MPa, with the 362°C sample being slightly less stiff. This may be due to the lower crystallinity of the 362°C sample. While the 362°C and 353°C samples followed a continuous trend until exceeding the ultimate stress, the 345°C sample appears to have experienced several local rupture events before failing and slowly losing load carrying capacity from 2.5-5% strain. The 327°C sample had a much lower initial elastic modulus and stiffened slightly with strain before failing at 1.2% strain.   The early failure and low stiffness is likely related to a lack of coherence from improper sintering and easy crack propagation. It is interesting that the lower hold temperature samples had slower stress decay after 'failure'. This could be an indication of low stress fibrillation events occurring to a greater extent for materials with the virgin morphology. Ultimate stress and engineering strain are plotted versus hold temperature in Figures 6-8a and 6-8b, respectively. There is a clear trend of increased ultimate stress, strain and toughness with increased hold temperature.
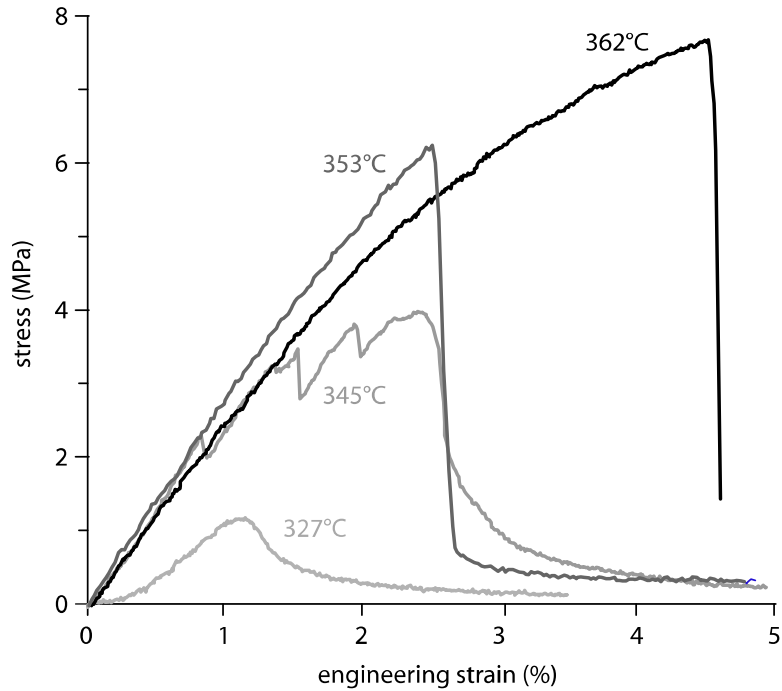
Figure 6-7. Results of mechanical testing of PTFE samples compression molded with varying sintering hold temperatures. The extension rate was 1mm/min which corresponds to a strain rate of approximately 7%/min. There is a significant increase in ultimate strength, strain and toughness as the sintering temperature increases. The 300ºC sample broke during machining and could not be tested.
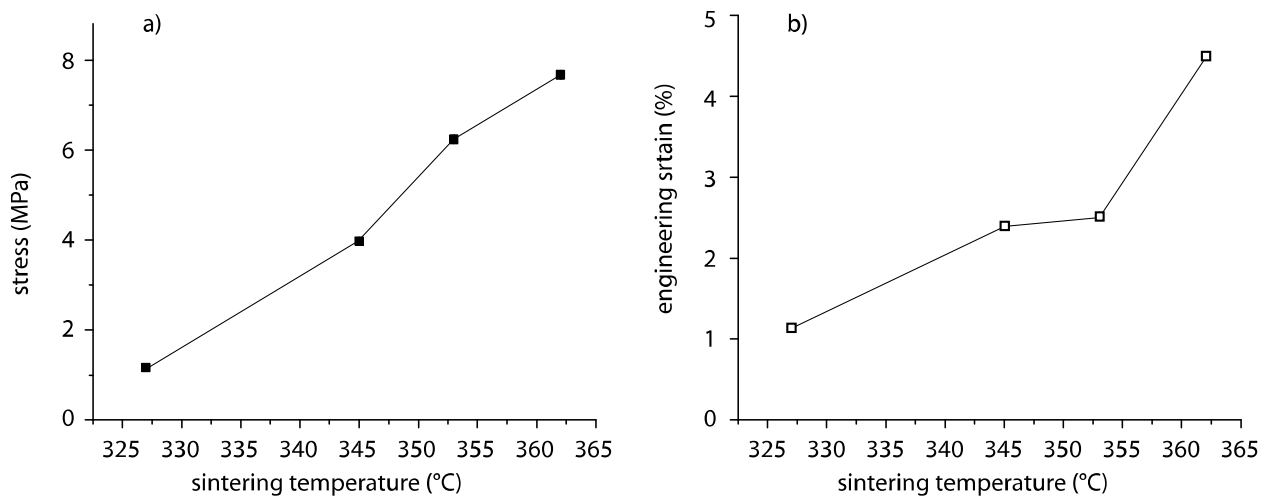
Figure 6-8. Quantified results of mechanical testing of PTFE samples compression molded with varying sintering hold temperatures; a) ultimate stress plotted versus sintering temperature, and b) ultimate strain versus sintering temperature. There is a significant increase in ultimate strength, strain and toughness as the sintering temperature increases.

These fracture surfaces were studied using SEM to gain insight into the mechanical properties observed during testing. Figure 6-9 shows backscattered electron images of the fractured surfaces at 300X. The 372°C surface is very smooth in comparison to the other surfaces. The protrusions from the other surfaces represent areas of concentrated strain at the cusp of failure. Brown and Dattelbaum illustrated three basic modes of failure for PTFE: 1) brittle fracture, 2) microvoid coalescence and 3) fibril formation, alignment and extension [103]. The smooth surface of the 327°C sample suggests a brittle fracture mode, but the stress-strain behavior resembled ductile behavior with a slow transition from maximum load carrying capacity to no load carrying capacity. There are a number of protrusions scattered sparsely across the surface of this sample. This sample likely experienced brittle fracture at 1.2% elongation across the majority of the surface leaving a low area fraction of PTFE in tact for fibrillation and load transfer during the remainder of the test. The higher temperature samples failed via microvoid nucleation and coalescence; the protruding material reflects the material on the periphery of the microvoids. The surface topography of the 345°C sample had a higher number of protrusions standing proud from the surface, but a number of cracks and step elevation changes (one shown) were observed. Brittle fractures over poorly sintered sections likely account for the step decreases in load. The 353°C and 362°C samples appear similar but close inspection reveals a higher content of smooth areas and less prominent protrusions on the surface of the 352°C sample. A larger concentration of weak areas resulted in a larger number of nucleated microvoids and a smaller area in between for load support and deformation. This resulted in lower ultimate stress and strain.

Secondary electron images of these surfaces, shown in Figure 6-10, were taken at 600X to highlight the fibrils and other more detailed aspects of each surface. In accordance with the

117

hypothesis that the virgin morphology facilitates fibrillation, the lower temperature samples were observed to have more and finer fibrils pulled from the surface during fracture than higher temperature samples. Very fine fibrils were pulled from the surface of the 327°C sample, though these features are difficult to resolve in the image. Bundles of fibrils are observed to have been drawn in large numbers from the surface of the 345°C sample. Far fewer but oriented fibril bundles are observed on the surface of the 353°C sample, and even fewer are observed on the surface of the 362°C sample. The SEM observation suggests that finer and less frequent the characteristic deformation structure on the surface, the more concentrated the load, the more localized the stress and the lower the load carrying capacity of the sample. The virgin morphology was hypothesized to facilitate fibrillation and improve tribological properties through damage compartmentalization and improved toughness. While the low sintering temperatures were shown to facilitate fine-scale fibrillation, they also lead to lower area fractions for fibrillation, a general lack of coherence in the sample and diminished mechanical properties including toughness. The lack of coherence may contribute to low wear however by compartmentalizing damage within smaller volumes of material and therefore limiting rates of wear and promoting transfer film initiation and growth.
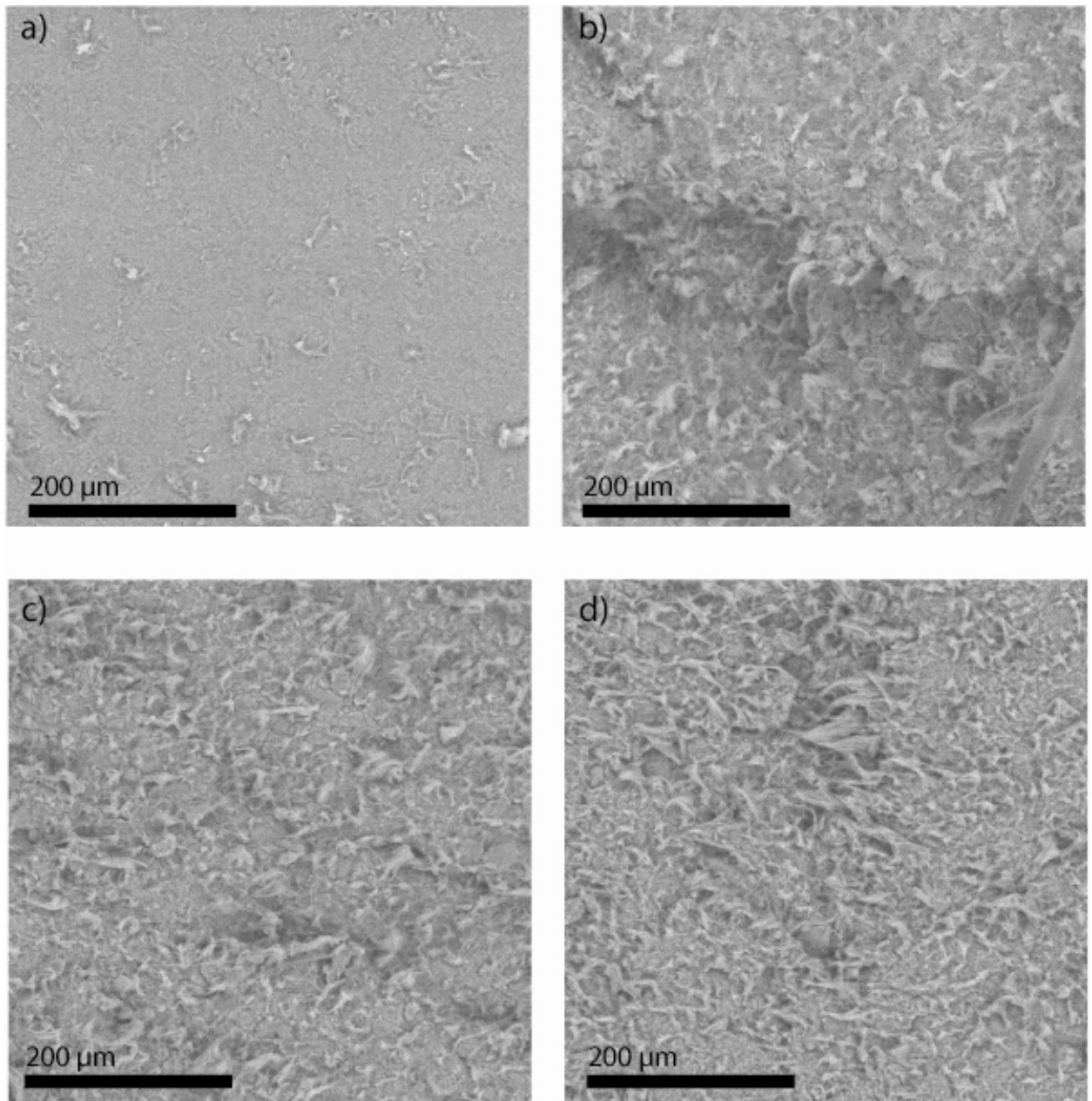
Figure 6-9. Backscattered electron images of the fracture surfaces of PTFE with varying sintering temperatures; a) 327ºC, b) 345ºC, c) 353ºC and d) 362ºC. With increasing sintering temperature, stress and strain to failure, there is an increased area fraction of elongated material protruding from the surface. This elongated material is thought to dominate the ductile mode of failure (microvoid coalescence), while the area not covered by elongated protrusions likely experienced brittle fracture from poor interparticle cohesion.
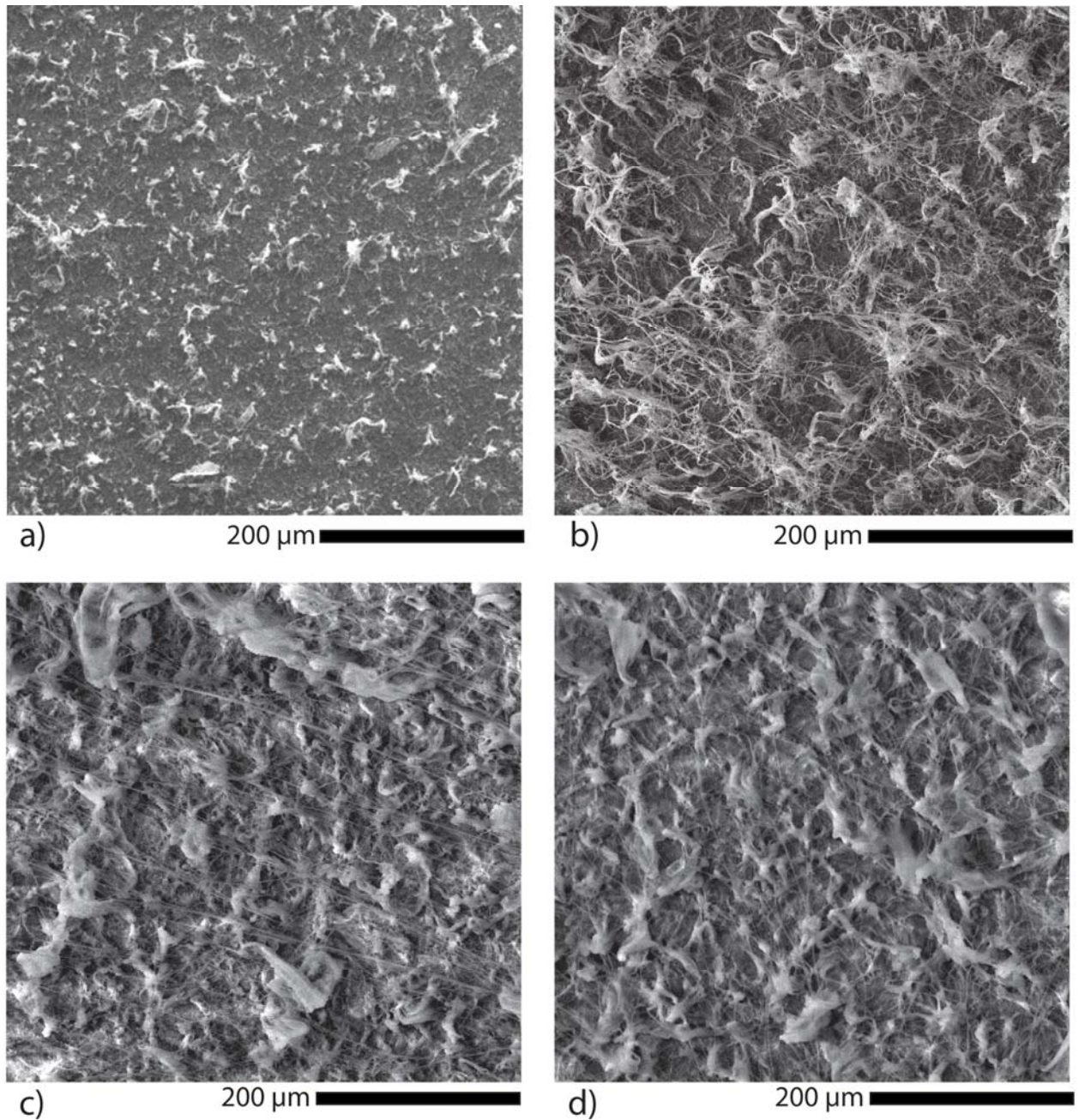
Figure 6-10. Secondary electron images of the fracture surfaces of PTFE with varying sintering temperatures; a) 327ºC, b) 345ºC, c) 353ºC and d) 362ºC. Fibrils were drawn from each of the surfaces during fracture. With increasing sintering temperature, stress and strain to failure, the fibril bundles tend to be thicker and denser, suggesting that a much larger fraction of the material was involved in the support of the load.

Tribological Characterization

Average friction coefficients and wear rates for samples created with varying hold temperatures are listed in Table 6-2. Friction coefficient and volume loss are plotted versus sliding distance in Figures 6-11a and 6-11b, respectively. In each case the friction coefficient decreased with increased sliding distance. This is typical of PTFE; as it runs in, transfer films are formed on the counterface and the near surface region of the polymer becomes more oriented. Optical images of the transfer films throughout testing are shown in Figure 6-12. The first frictional data point was taken largely out of the influence of transfer films. The initial friction coefficient varied from $\mu = 0.135$ to $\mu = 0.155$. Interestingly, this initial friction coefficient was lowest for the fully sintered 362°C sample, but there was no trend with temperature as the 353°C sample had the highest initial friction coefficient. Statistically, these differences are significant, but they are likely driven by the unknown deterministic influences of the chemical and topological natures of the counterface and pin rather than the bulk pin morphology.

In general, the friction coefficient decreased with increased sliding distance in a manner consistent with transfer film formation and surface orientation. Slight deviation from this trend was observed for the 345°C sample. The friction coefficient increases sharply following a gradual decrease near 50m of sliding. A dramatic decrease follows with an abrupt increase occurring just before the third test interruption at 1600m of sliding. Upon restarting the test, the friction coefficient again decreased, reaching near steady-state at a friction coefficient of about $\mu = 0.105$ before the forth test interruption at 2600m. Qualitatively, the transfer film morphology of the 345°C sample after 2600 m of sliding is striated in the sliding direction with a banded structure having a characteristic length of about 100 µm, while many of the other images capture the more typical plate-like transfer morphology. The surface topographies were also

quantitatively studied using a stylus profilometer. Surface measurements across the transfer film

of each sample are shown for 2600 m of sliding in Figure 6-13. Both the 327ºC and the 345ºC

transfer films cover a significantly high fraction of the counterface and both are thick (~30-40

µm) compared to the 353ºC and 362ºC samples (5-15µm). The 327ºC sample also had striations

in the sliding direction that are on the order of 10 µm high, while the low friction 345 ºC transfer

film was striated with a height of 30 µm . Both striated transfer films appeared to have formed

on top of pre-deposited plate-like transfer with a characteristic height of ~20 µm. During the

period of striated transfer and low friction for the 345ºC sample, a transition to low wear also

occurred (Figure 6-11b). Despite the fact that the 345 ºC was able to form a striated transfer film

which led to low friction and wear, the underlying transfer was unstable and the sample was

unable to retain low friction and wear for a significant proportion of the total sliding distance.
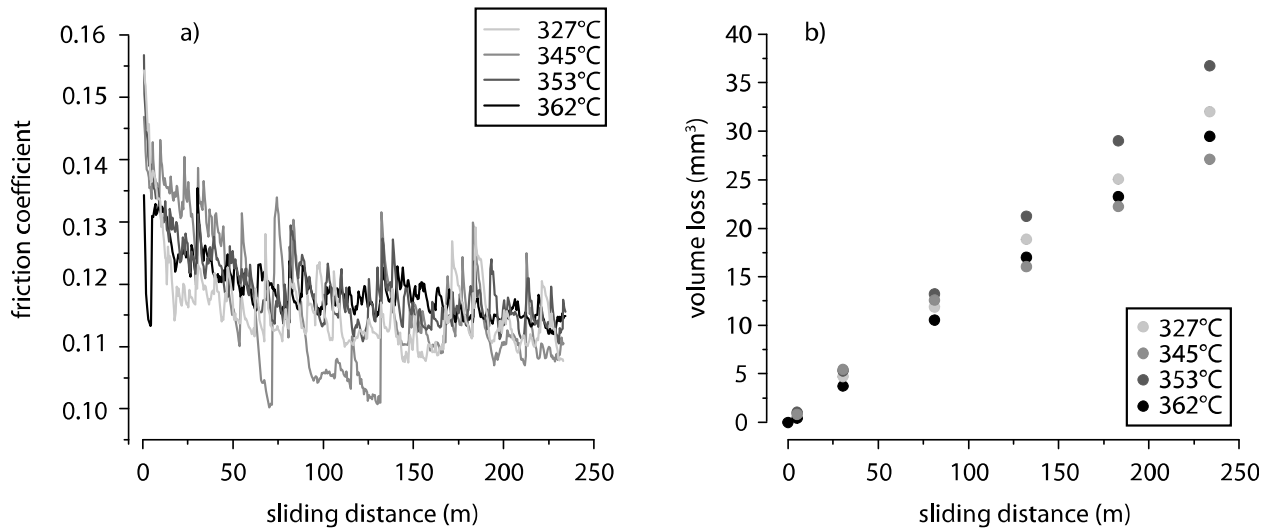
Figure 6-11. Tribological results of wear testing PTFE samples with varying sintering
temperature; a) friction coefficient plotted versus sliding distance and b) wear volume
loss plotted versus sliding distance. The normal load was 250 N and the normal
pressure was 6.3 MPa. The sliding speed was 50 mm/s and the reciprocation length
was 25.4 mm. The tribological properties are largely independent of the sintering
temperature, crystalline morphology, strength and toughness.
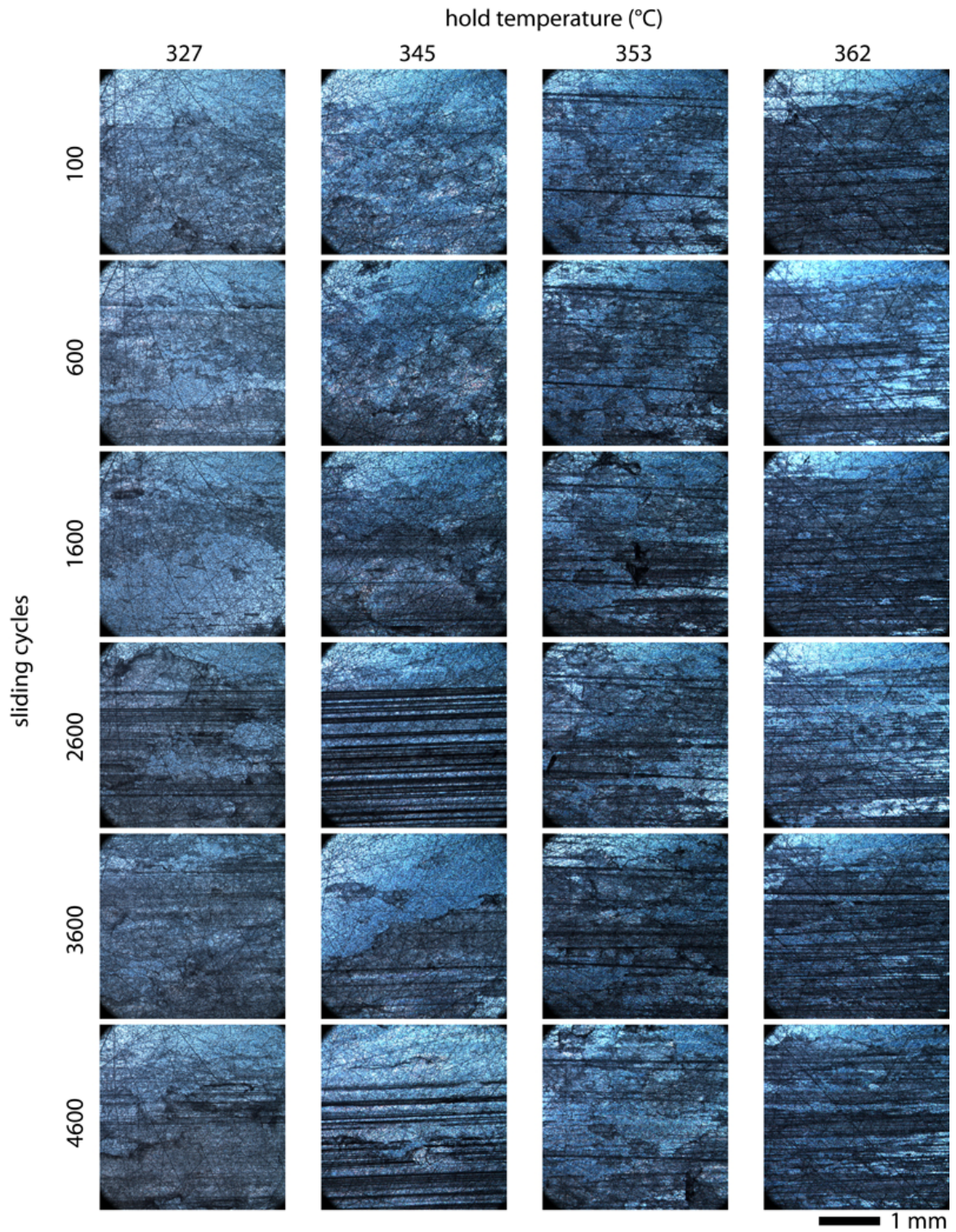
Figure 6-12. Optical images of the transfer films of PTFE samples with varying sintering temperatures following test interruptions at various sliding distances. The transfer morphologies range from a striated transfer morphology aligned into the sliding direction to the thick plate-like transfer typically cited for PTFE.
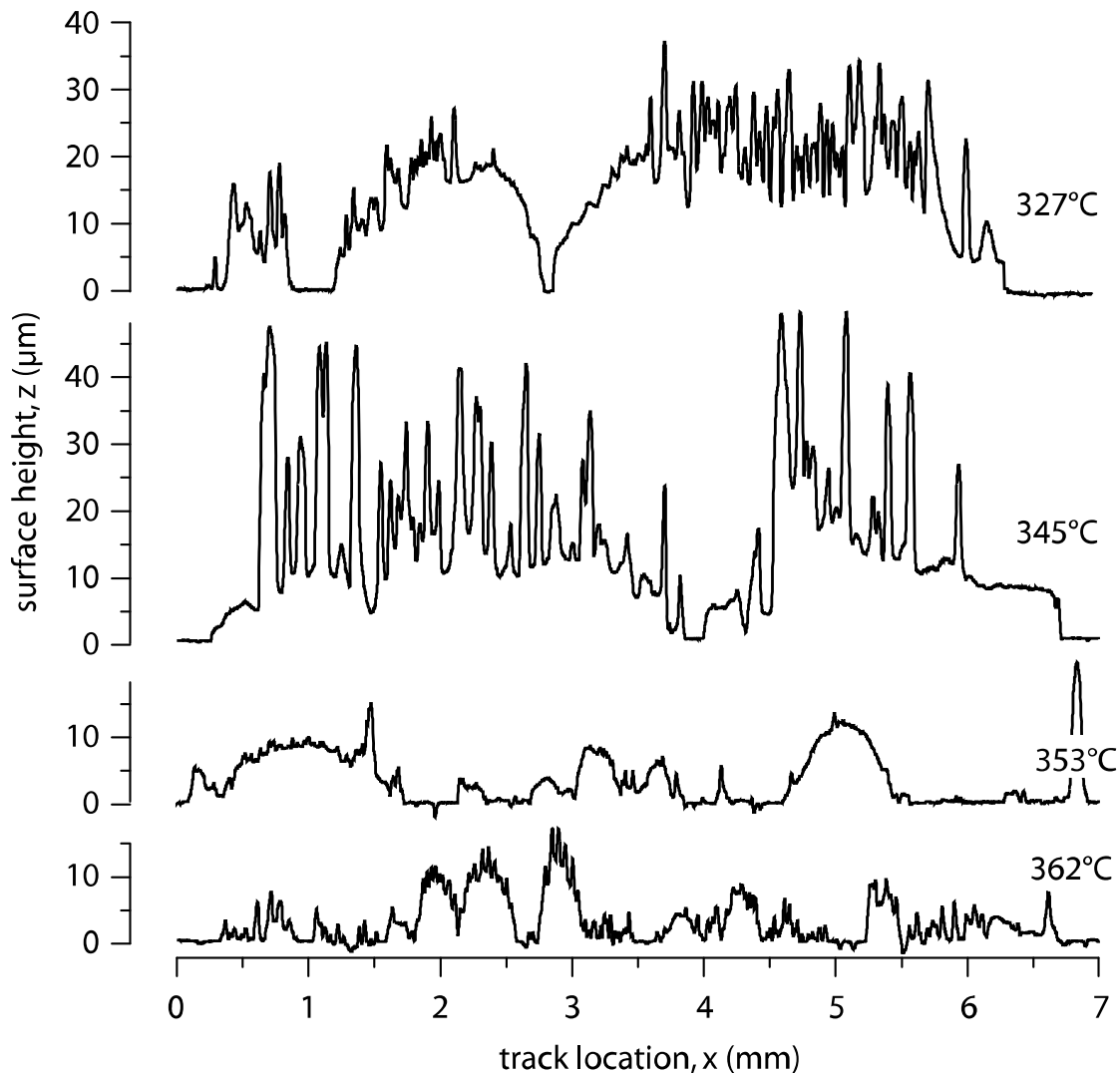
Figure 6-13. Stylus profile measurements across the transfer films of PTFE samples of varying sintering temperature following 2600 m of sliding at 6.3 MPa. The transfer films of the 327°C and 345°C samples were significantly thicker than those of the 352°C and 362°C samples. The large striations (~100µm wide by ~20 µm tall) of the 345 °C sample coincided with a period of low friction and low wear sliding. The uncertainty in the measurement is on the order of 10nm in the vertical direction and 1 µm in the horizontal.

The average friction coefficients and steady wear rates are plotted versus sintering temperature in Figure 6-14. There is a 40% difference in wear rate from 345°C to 353 °C. Though significantly larger than the uncertainty and a seemingly substantial difference, such differences are found with nominally identical samples of unfilled PTFE. The variation in

friction coefficient is also small compared to variations that are typically found. Therefore the tribological differences observed here are insignificant despite the extreme differences in the crystalline morphology and in the mechanical strength and elongation to failure. While the 345ºC sample morphology did promote a striated transfer morphology and significantly lower friction and wear for short durations, even these differences were negligible when compared to samples with trace (<1%) loadings of certain nanofillers in prior studies. The effects of the nanoparticles likely extend beyond mechanical load support and stabilization of the virgin morphology.
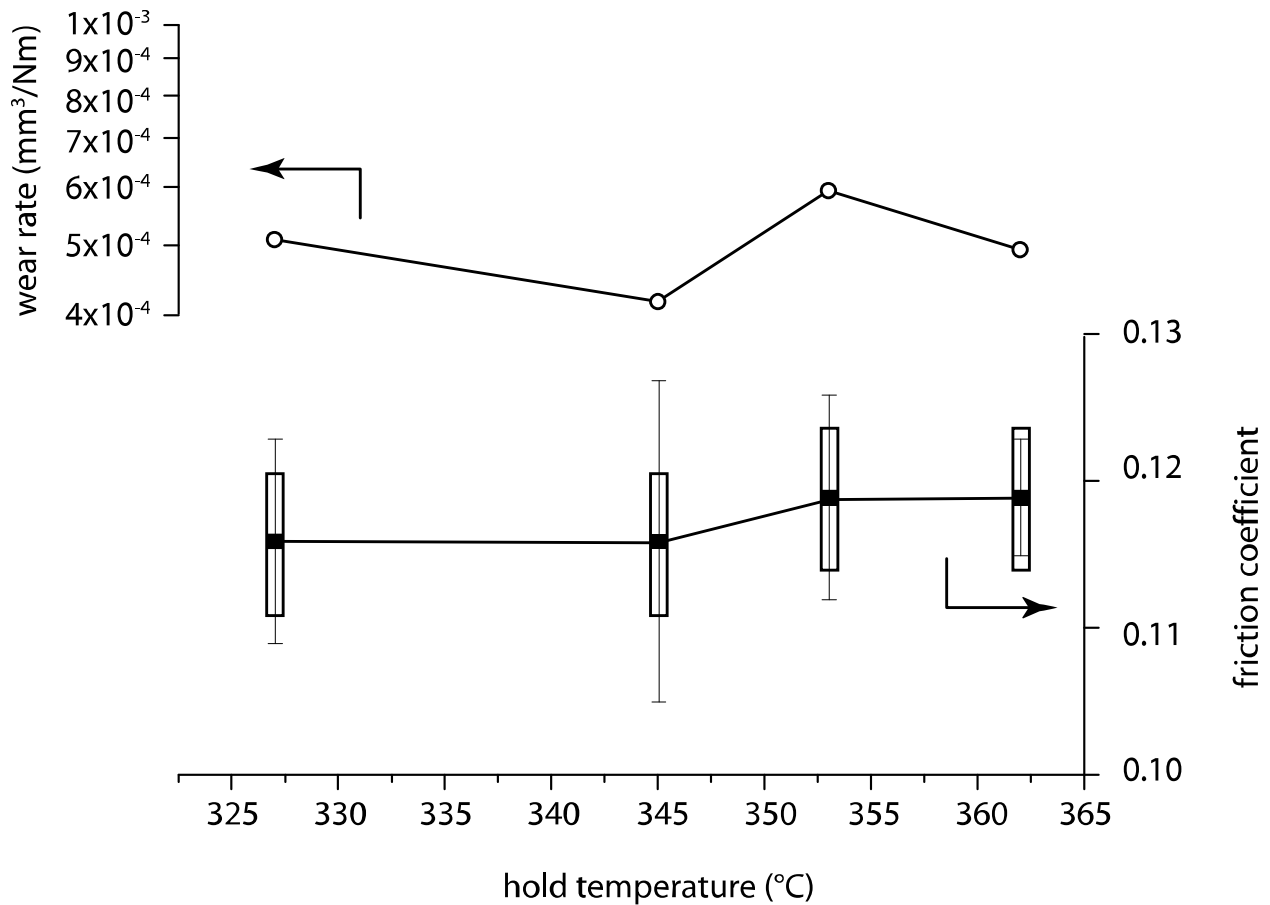
Figure 6-14. Wear rate and friction coefficient plotted versus sintering temperature. Uncertainty confidence intervals on wear rate data are much smaller than the data points. The boxes on friction coefficient data represent the experimental uncertainty while the error bars represent the standard deviation throughout the test.

Table 6-2. Experimental matrix investigating the effects of sinter temperature on the tribological, thermal and mechanical properties of unfilled virgin PTFE. The uncertainty on melt temperature measurements is 0.1°C.

Temperature (°C)	300	327	345	353	362
T_{m1} (°C)	343.75	343.97	343.89	344.60	328.90
ΔH_{m1} (J/g)	73.4	73.9	74.2	54.1	24.8
$U_c(\Delta H_{m1})$	0.8	0.9	0.9	0.7	0.3
T_{m2} (°C)	328.04	328.01	327.89	328.01	327.99
ΔH_{m2} (J/g)	22.3	22.5	22.2	22.0	22.3
$U_c(\Delta H_{m2})$	0.3	0.3	0.3	0.3	0.3
ρ (mg/mm^3)	2.230	2.210	2.221	2.150	2.107
$U_c(\rho)$ (mg/mm^3)	0.012	0.011	0.011	0.010	0.010
σ_u (MPa)	N/A	1.17	3.98	6.24	7.67
$U_c(\sigma_u)$	N/A	0.08	0.07	0.10	0.10
ε_u (%)	N/A	1.14	2.40	2.51	4.49
$U_c(\varepsilon_u)$	N/A	0.01	0.01	0.01	0.01
μ	N/A	0.116	0.116	0.119	0.119
$\sigma(\mu)$	N/A	0.007	0.011	0.007	0.004
$U_c(\mu)$	N/A	0.005	0.005	0.005	0.005
$k \times 10^6$ (mm^3/Nm)	N/A	508	418	593	493
$U(k \times 10^6)$	N/A	3	2	3	2

Mechanical Processing on Nanoparticle Dispersion

The beneficial thermal and chemical properties that make PTFE an attractive extreme environment solid lubricant also make it a particularly difficult matrix to work. The available techniques consist of dry powder blending and powder ultrasonication in an aqueous bath. Neither of these techniques is used for most other polymeric nanocomposites as *in-situ* polymerization and melt mixing have proven to be far superior nanoparticle dispersion techniques. One hypothesis for the success of prior nanocomposites alumina-PTFE nanocomposites processed using a jet-mill powder blending technique is that the high amount of mechanical energy used in this process results in superior disbanding of the nanoparticle agglomerates which leads to improved nanoparticle dispersion. It is thought that the benefits of polymeric nanocomposite can only be realized once the nanoparticles have been effectively dispersed.

In this study, the effects of nanoparticle agglomerate disbanding and dispersion are under investigation. Three alumina nanoparticle loadings, namely, 1wt%, 2wt% and 5wt%, were mixed by hand. Half of each batch was then blended using the jet-mill. It should be recalled that the jet-mill was the only technique energetic enough to alter the thermal behavior, size and shape of the virgin powder. All of the PTFE in the study was jet-milled prior to nanoparticle inclusion to remove jet-milling effects as variables. The hand-mixing technique was used as a very low energy, worst-case extreme to counter the high energy jet-milling technique. Following powder blending, the powders were observed using high vacuum secondary electron microscopy. Ten random samples of each powder condition were observed, and the numbers of alumina particles visible on the much larger PTFE particles were noted.
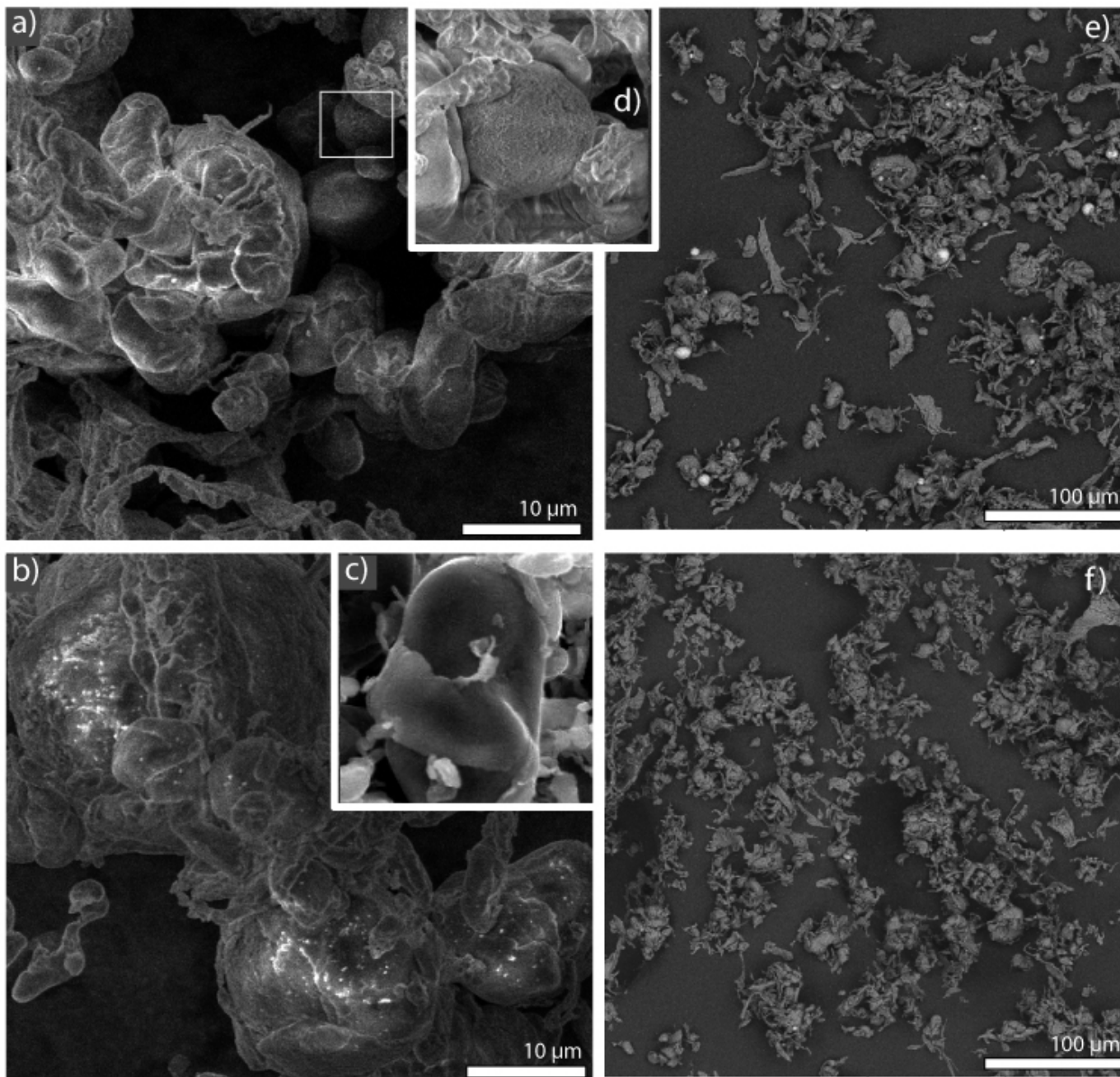
Figure 6-15. Representative SEM images of a) 5 wt% 80 nm α phase alumina hand-mixed with PTFE (secondary electrons), b) 5 wt% 80 nm α phase alumina jet-milled with PTFE (secondary electrons), c) neat jet-milled PTFE (secondary electrons), d) hypothesized nanoparticle agglomerate (secondary electrons), e) 5 wt% 80 nm α phase alumina hand-mixed with PTFE (backscattered electrons), f) 5 wt% 80 nm α phase alumina jet-milled with PTFE (backscattered electrons) .

Representative images of the hand-mixed and jet-milled powder dispersions at 5wt% loading are shown in Figure 6-15a-b. These images can be contrasted to the inset image of neat PTFE shown in 6-15c. In the images of the nanoparticle-PTFE powder ensembles (Figures 6-15a and 6-15b), submicron domains with high brightness were easily observed with a 50 µm field of view. Spectroscopy was not conducted to determine the composition of these domains, however, comparable regions were never observed on neat PTFE powders and the densities increased with increased nanoparticle loading for a given blending condition. These facts suggest that these bright submicron regions are alumina nanoparticles. Under this assumption, these images suggest a large discrepancy in the number of particles decorating the PTFE after hand-mixing and jet-milling. In the case of the hand-mixed samples, 2-15 µm particles with nodular surfaces were observed with the density increasing with increased nanoparticle loading. The appearance of these particles is consistent with secondary electron images of the agglomerations in the as-received 40 nm α phase alumina powder of McElwain [52]. Backscattered electron imaging of these powders show bright contrast for these regions. Given the higher atomic weight of Al and large interaction volume (~1µm) for backscattered electrons, these results suggest that the nodular regions are nanoparticle agglomerates. Lower magnification backscattered electron imaging of the powders, illustrated by representative images in Figures 6-15e-f, revealed the presence of larger and more spatially frequent agglomerates in the hand-mixed powders. Observations of dispersions of individual nanoparticles (using secondary electron imaging) and nanoparticle agglomerates (using backscattered electron imaging) qualitatively suggest that jet-milling effectively disbanded agglomerates and dispersed nanoparticles while hand-mixing did not.
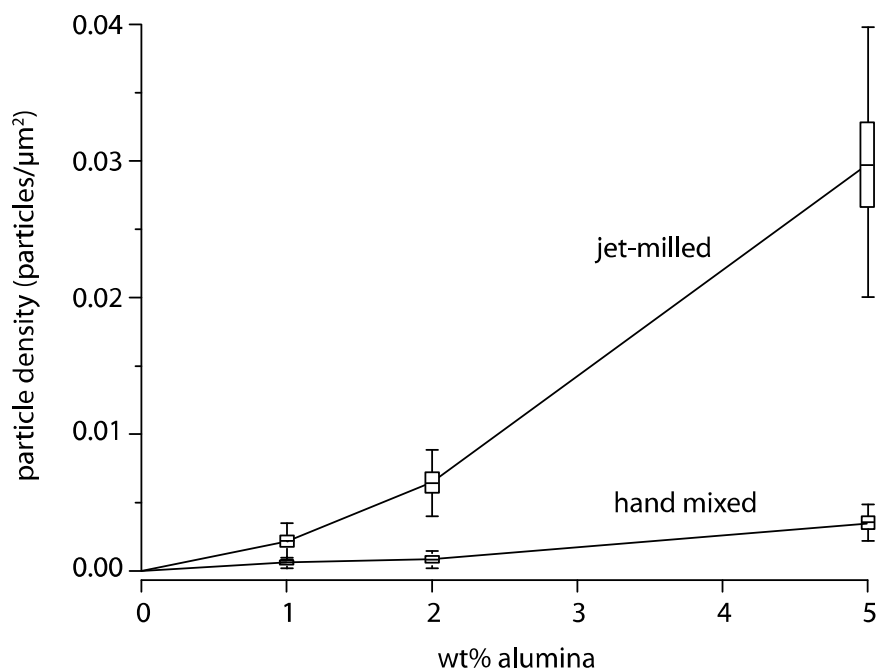
Figure 6-16. Estimated nanoparticle density plotted versus alumina loading for hand-mixed and jet-milled powder samples. The error bars represent the standard deviation in the ten random measurements. The center line is the calculated average and the box represents plus and minus one standard deviation of the distribution of averages calculated from 10 random samples from the population (*i.e.* the average of the population lies within the box with 68% confidence).

Table 6-3. Estimated nanoparticle density results of SEM observation of nanoparticle decorated PTFE powder following mixing via hand-mixing and jet-milling for 1wt%, 2wt% and 5 wt% 80 nm α alumina in PTFE. Ten random samples were taken from each condition. The mean and standard deviation of the ten measurements are tabulated.

Sample	Mixing technique	Alumina wt%	particle density μ (particles/μm^2)	particle density σ (particles/μm^2)
1	Hand-mixed	1	5.85×10^{-4}	3.91×10^{-4}
2	Hand-mixed	2	8.18×10^{-4}	6.41×10^{-4}
3	Hand-mixed	5	35.3×10^{-4}	13.4×10^{-4}
4	Jet-milled	1	21.5×10^{-4}	13.3×10^{-4}
5	Jet-milled	2	64.2×10^{-4}	24.3×10^{-4}
6	Jet-milled	5	299×10^{-4}	98.8×10^{-4}

The estimated nanoparticle densities from SEM observations of the powders are tabulated in Table 6-3. A comparator plot of the estimated nanoparticle density (number of particles divided by the area of coverage) versus alumina wt% is shown in Figure 6-16; nodular particles

or nanoparticle 'agglomerates' are only counted once. While there are clearly substantial errors associated with the calculation of number density with this technique, relative comparisons are thought to be fair.

The error bars represent the standard deviation of the measurement and the box represents the standard deviation of the calculated mean. The error bars are therefore about three standard deviations out, and the population mean lies within those error bars with 99.7% confidence. It can therefore be concluded that there are substantially more nanoparticles (approaching an order of magnitude) decorating the surfaces of PTFE powders following jet-milling than following hand-mixing. Based on the number of hypothesized agglomerations observed during surveying of the hand-mixed powders, the difference is attributable to the relatively poor disbanding of nanoparticle agglomerates in the case of the hand-mixed powders. In addition, the jet-mill is an open system and it is thought that many of the fine nanoparticles may be lost during the jet-milling procedure, while the closed-system in the hand-mixing procedure ensures an average loading of 5 wt%. Sawyer *et al*. [16] used thermal gravimetric analysis to estimate the loss of 60% of the nanoparticles during jet-milling. It is clear from this study that the high energy of the jet-mill helps break-up notoriously 'sticky' nanoparticle agglomerations and leads to a much higher density of nanoparticle coverage despite potentially having a lower alumina weight fraction.

Nanoparticles on the Melt Behavior of PTFE

In the previous study it was shown that the number density of jet-milled powders is significantly higher than that of hand-mixed powders for a given nanoparticle loading. One of the potential wear resistance mechanisms is the alteration of the crystalline structure and morphology of the PTFE by the nanoparticle inclusions. It is hypothesized that, because the nanoparticles are of the same-size scale as the polymer lamellae, they may nucleate

crystallization and promote a finer crystalline structure than is otherwise possible. The size

reduction of the characteristic 'banded structure' of PTFE was previously cited by Tanaka as a

wear resistance mechanism. In Tanaka's experiments, the cooling rate following sintering was

used to alter the size of the banded structure, not nanoparticles.

Figure 6-17. Thermograms from differential scanning calorimetry of alumina-PTFE powder
ensembles blended by hand and by jet-milling. These curves are compared to jet-
milled unfilled PTFE powders. All of the PTFE powders in this study were et-milled
prior to nanoparticle inclusion.

In this study, the thermal characteristics of the alumina-PTFE powder ensembles are

studied using differential scanning calorimetry at a heating and cooling rate of 10ºC/minute.

Each powder was heated to 400ºC, equilibrated, cooled to 250ºC, equilibrated and reheated to

400ºC. With this experiment, the first melt, crystallization and second melt of the powders are

studied in the absence of other thermal or mechanical histories. The thermograms from these

measurements are shown in Figure 6-17. The quantified results from these measurements are tabulated in Table 6-4 and are plotted versus filler wt% in Figure 6-18.

First consider Figure 6-18a, where the first peak melt temperature is plotted versus the filler wt%. The jet-milled powder ensembles behaved in a manner similar to the jet-milled PTFE, although with a slightly higher melt temperature after nanoparticle inclusion. The hand-mixed powder ensembles had a significantly higher first melt temperature regardless of the loading. In fact, these powders had a first melt temperature similar to the values found for virgin, sieved, ultrasonicated, rotary mixed and blade mixed PTFE at around 342.5ºC. It is possible that the large nanoparticle agglomerations tend to increase the melt temperature to a greater extent than the smaller singular nanoparticles in the jet-milled powder ensemble, but one would expect temperature to increase with alumina content. Given that the melt temperature was reduced slightly with increased loading, a more probable cause for this is the hand mixing action and the lack of nanoparticle coverage. The hand mixing may have led to agglomeration of the relatively 'sticky' PTFE. Because the nanoparticles did not effectively decorate the PTFE surfaces, the particles may tend to stick during mixing. This would also lead to a reduced melt temperature with increased alumina content since the higher particle density would deter agglomeration of the polymer. The increase in the first melt of the jet-milled powders does appear to be statistically significant. This phenomenon may be related to the original hypothesis that the nanoparticles stabilize the PTFE to slightly higher temperatures by immobilizing the contacting lamellae. However, the difference is much less than 1°C and is insignificant in the context of the polymer processing.

The heat of fusion of the first melt is shown in Figure 6-18b. There is a clear trend of decreased heat of fusion with increased loading. However, the mass of the sample included the

mass of the alumina which does not contribute to the power signal. If the 'as-prepared' alumina loading is considered, an iso-crystalline line can be constructed. This line represents the behavior of the nanocomposite if it contained the as-prepared mass of alumina and had the same polymer crystallinity as the unfilled polymer. Thus, we can use the iso-crystalline line to compare the crystallinity of the nanocomposite to that of the neat polymer. After considering the iso-crystalline line, it is clear that the crystallinities of the nanocomposites are comparable to those of the unfilled polymer. The 5wt% samples may have had slightly lower heats of fusion and thus crystallinity, but the difference is not substantial enough to draw any conclusions.

The recrystallization behavior is shown in Figures 6-18c and 6-18d. The recrystallization temperatures (6-18c) of the nanocomposites fluctuate about the value obtained for unfilled jet-milled PTFE in a non-systematic manner with magnitudes that are greater than the uncertainty in temperature. This scatter is insignificant. The uncertainty in power is rather large (~1%) and the recrystallization peak is broad. The peak temperature is determined as the location where peak power is measured. As a result, even though the measurement of temperature is much more accurate than the fluctuation, the fluctuation of power on the broad curve tends to make determination of the peak temperature difficult and increases the uncertainty of peak temperature in this case.   Hence, despite the hypothesis that the nanoparticles may nucleate crystallization and promote a finer scale crystalline structure, evidence of this was not observed in the crystallization behavior of the nanocomposites.

In the heat of recrystallization curves in Figure 6-18d, differences between the jet-milled and hand-mixed powders are found; the low wt% jet-milled powders behaved like the unfilled powder, while the hand-mixed powders had a lower heat of fusion. Once again, this difference is comparable to that found between the treated and untreated powders in the earlier thermal studies

of neat PTFE at about 2 J/g. This further supports the hypothesis that the hand mixing action

may tend to agglomerate the PTFE leading to virgin-like characteristics. Both sets of powders

showed a slight tendency to increase crystallinity with increased loading; the hand-mixed

powders showed a greater tendency than the jet-milled powders. This may be a result of the

higher nanoparticle density decreasing the agglomeration tendency.

The results from the second melt are shown in Figures 6-18e and 6-18f. The differences in

the peak melt temperatures shown in Figure 6-18e are statistically insignificant. This supports

the hypothesis that the differences in the crystallization temperatures are insignificant and are

simply the result of the uncertainty in power measurements and the inherently low sensitivity due

to the broadness of the crystallization peak. As expected, the heats of fusion in Figure 6-18f
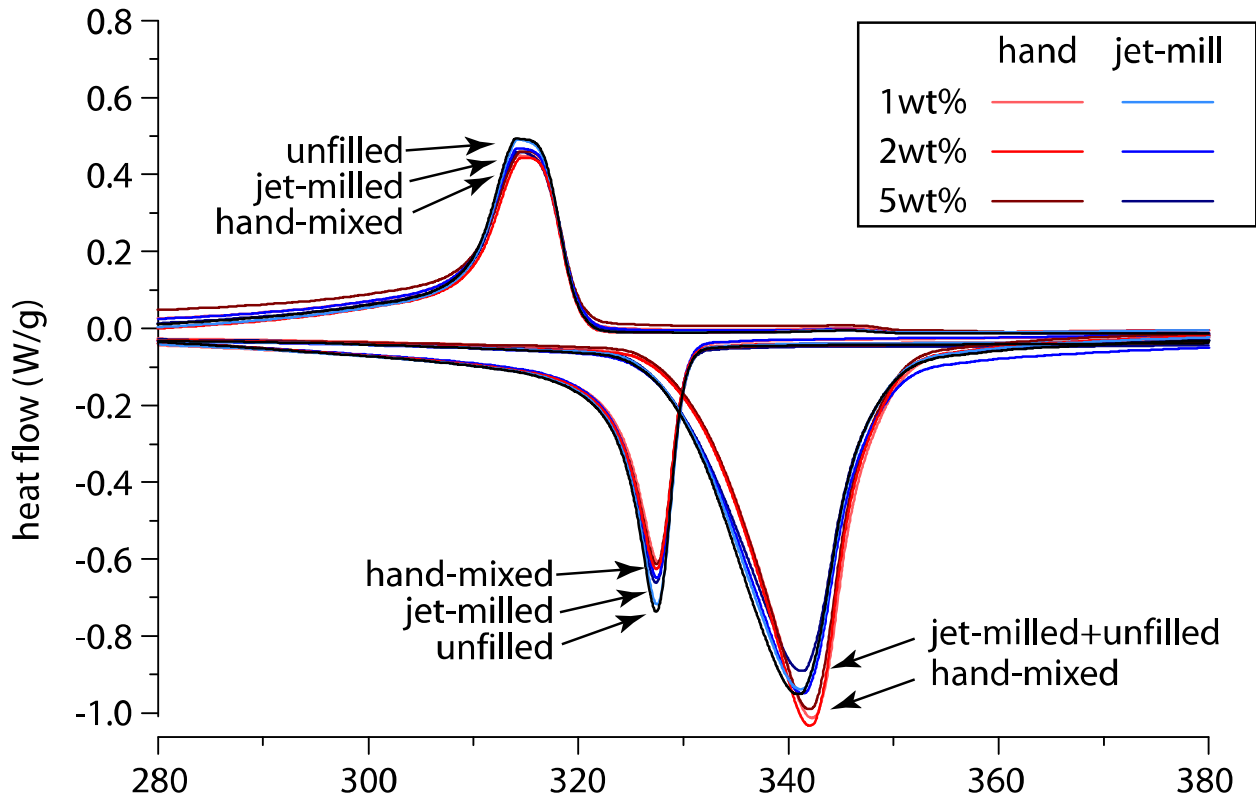
almost replicate the heat of crystallization data in 6-18d.
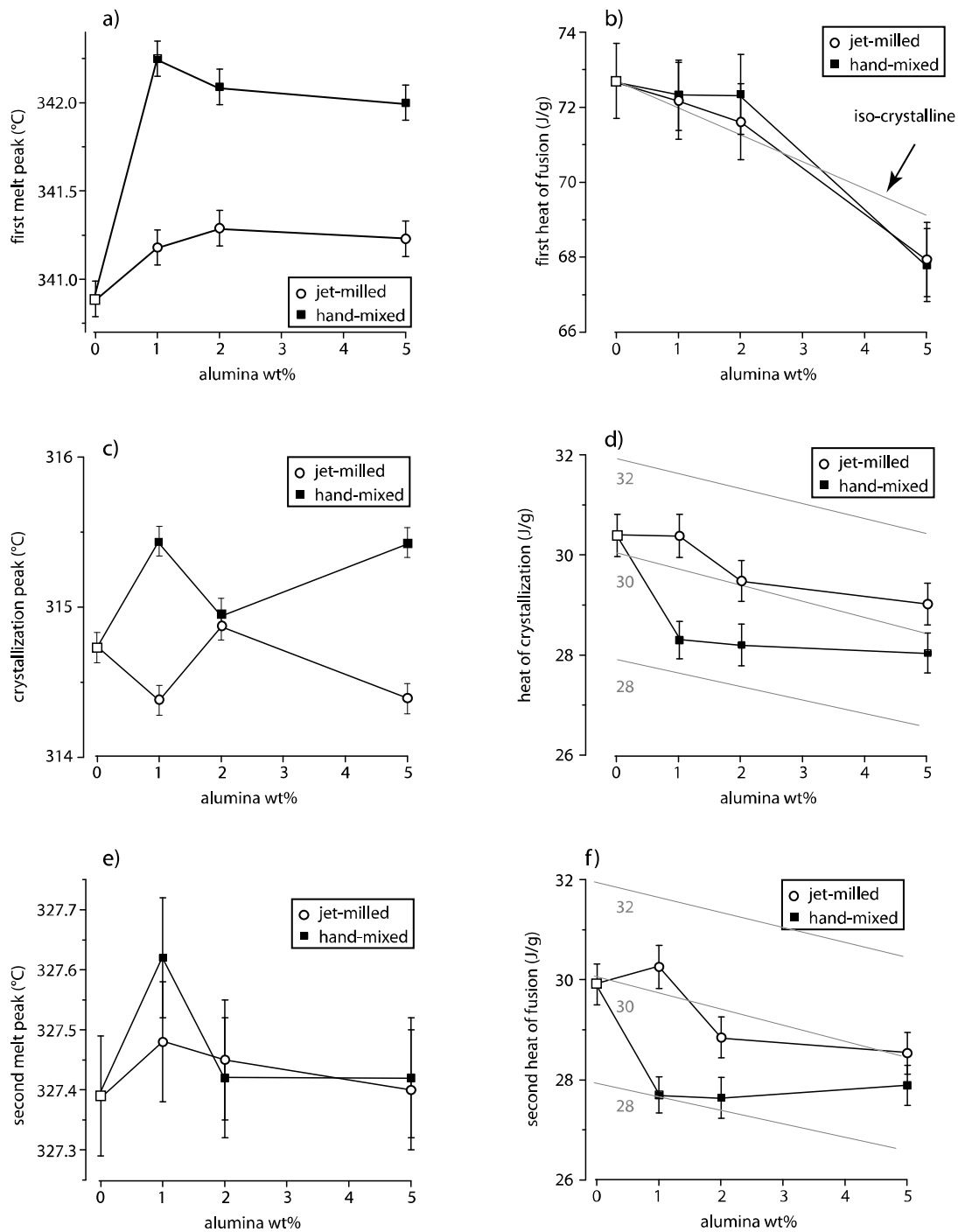
Figure 6-18. Quantified results from differential scanning calorimetry of alumina-PTFE powder ensembles blended by hand and by jet-milling; a) first peak melt temperature plotted versus alumina wt%, b) first heat of fusion plotted versus alumina wt%, c) peak crystallization temperature plotted versus alumina wt%, d) heat of fusion during crystallization plotted versus alumina wt%, e) second peak melt temperature plotted versus alumina wt% and f) second (melting) heat of fusion plotted versus alumina wt%. Error bars represent the experimental uncertainty in each case.

Table 6-4. Results of DSC of powder ensembles following mixing via hand-mixing and jet-milling for 1wt%, 2wt% and 5 wt% 80 nm α alumina in PTFE. The uncertainty of temperature measurements is 0.1°C

	Jet-milled	Hand-mixed			Jet-milled		
	Unfilled	1 wt%	2 wt%	5 wt%	1 wt%	2 wt%	5 wt%
T_{m1} (°C)	340.9	342.3	342.1	342.0	341.2	341.3	341.2
ΔH_{m1} (J/g)	72.7	72.3	72.3	67.8	72.2	71.6	67.9
$U_c(\Delta H_{m1})$	1.0	0.9	1.1	1.0	1.0	1.0	1.0
T_{c1} (°C)	314.7	315.4	315.0	315.4	314.4	314.9	314.4
ΔH_{c1} (J/g)	30.3	28.2	28.1	28.0	30.3	29.4	29.0
$U_c(\Delta H_{c1})$	0.4	0.4	0.4	0.4	0.4	0.4	0.4
T_{m2} (°C)	327.4	327.6	327.4	327.4	327.5	327.5	327.4
ΔH_{m2} (J/g)	29.9	27.7	27.6	27.9	30.3	28.9	28.5
$U_c(\Delta H_{m2})$	0.4	0.4	0.4	0.4	0.4	0.4	0.4

Filler Dispersion on Nanocomposite Properties

Thermal Characterization

In the prior investigation of the influences of nanoparticles on the melt and recrystallization behavior of PTFE, the nanoparticles were found to have little effect. Deviations were found between the two dispersion techniques, namely, jet-milling and hand mixing, and were attributed to a tendency of the PTFE particles to re-agglomerate during hand mixing due to the poor nanoparticle decoration observed in the previous dispersion study. However, very different phase and melt characteristics were found previously for effective nanocomposites and unfilled PTFE, so the thermal characteristics of the processed nanocomposites were studied here to include the thermal and pressure history of the compression molding process.

The differential scanning calorimetry thermograms for 1, 2 and 5 wt%, hand-mixed and jet-milled alumina-PTFE nanocomposites are shown from 280°C to 380°C in Figure 6-19. One repeat of each sample was conducted. Unfilled PTFE is also shown as the control sample. The unfilled PTFE processed at 362°C has the traditional low temperature melt peak at about 327°C, but it also has a subtle melt peak at the high temperature melt of about 350°C. The 2 wt%

137

samples had a prominent high temperature melt peak, while the 1 and 5 wt% samples only showed the low temperature melt peak. The repeat tests verify that the unusual discontinuity in behavior at 2 wt% is repeatable with repeated sampling of the same compression molded specimen. In order to test whether this is truly a function of the loading or a coincidence of varying processing conditions, a repeat specimen was compression molded under nominally identical conditions. The DSC results for the first melt of the repeat specimens are shown in Figure 6-20. These results show only the low temperature melt peak for the 2 wt% jet-milled sample and suggest inconsistency in the processing either due to dispersion or the compression molding process.

Such stark behavioral differences were not observed during the well controlled cooling and heating conditions of the recrystallization and second melt in the DSC which further suggests that the behavioral differences observed in the first melt were due to unknown deterministic variations from compression molding rather than differences in dispersions. The samples with the high melt peak likely had higher pressures during processing which increased the melt temperature. Even during well-controlled crystallization conditions in the DSC, the nanocomposites had a tendency to have higher crystallinities than the unfilled PTFE.

Figure 6-19. Heat flow plotted versus temperature from differential scanning calorimetry of hand-mixed and jet-milled 0, 1, 2 and 5 wt% alumina-PTFE nanocomposites compression molded at 362°C: a) first melt, b) crystallization and second melt.
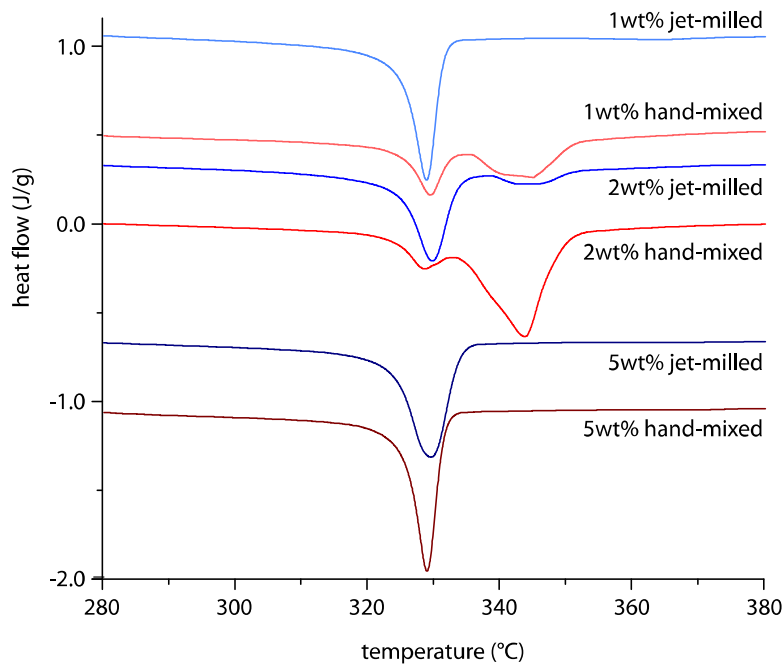
Figure 6-20. Heat flow plotted versus temperature from differential scanning calorimetry of repeat specimens of hand-mixed and jet-milled 0, 1, 2 and 5 wt% alumina-PTFE nanocomposites compression molded at 362°C. Samples with nominally identical composition, dispersion and processing were found to have significant thermal behavioral differences in some cases.

The quantified results with experimental uncertainties for these studies are found in Table 6-5 and peak temperatures and heats of fusion are plotted versus filler wt% in Figure 6-21. Consider 6-21a in which the first melt peak temperature is plotted versus filler wt%. The peak melt temperature remains nominally unchanged for all of the samples except for the 2 wt% nanocomposites; these first melt peak differences are likely due to inconsistencies in the processing. The heat of fusion is plotted versus filler wt% in figure 6-21b; lines of constant heat of fusion have also been plotted. Overall, there is a strong trend of increased heat of fusion, and therefore, crystallinity as the filler loading increases. The lack of a high temperature melt peak for any of the 5 wt% samples suggests that the sample were fully sintered and the 30% increase in crystallinity of these samples suggests that the nanoparticles may have facilitated crystallization. The very high crystallinity of the 2 wt% samples is attributable mostly to incomplete sintering (indicated by the high melt peak temperatures). One jet-milled 2 wt% sample was fully sintered (low first melt temperature) and had increased crystallinity consistent with the trend from the 5 wt% samples.

The recrystallization behavior is shown in Figures 6-21c and 6-21d. The effects of pressure and thermal history are attenuated after the first heat, so the recrystallization behavior mostly reflects the nanoparticle effects on recrystallization of the polymer. It should be noted that the effects are not totally erased since most of the incompletely sintered samples are entering first melt while others enter the second melt. There is essentially no difference between the recrystallization temperatures. The heats of fusion for recrystallization in Figure 6-21d again support a trend of increasing crystallinity with increasing filler content, but there is now lower crystallinity of the 2 wt% samples than for the other nanocomposites. This is attributed to the differing processing histories prior to the first melt of DSC. The second melt behaviors shown in

140

Figures 6-21e and 6-21f are expectedly quite similar to the recrystallization behaviors in Figures

6-21c and 6-21d.

Table 6-5. Results of DSC of hand-mixed and jet-milled 1wt%, 2wt% and 5 wt% 80 nm α alumina-PTFE compression molded nanocomposites. The first two samples originate from the same compression molded sample used for tribological testing while the third sample (first melt only) originated from another compression molded sample used for mechanical testing. The uncertainty of temperature measurements is 0.1°C. The uncertainty of enthalpy calculations is 0.4 J/g unless specified otherwise.

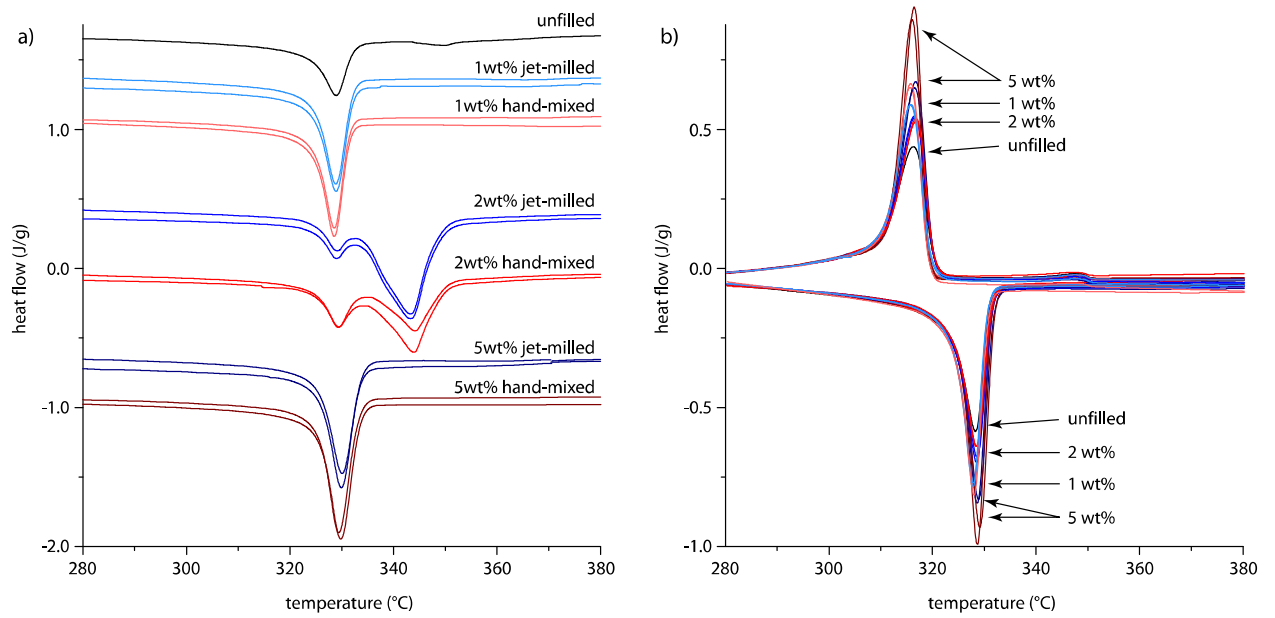|	Jet-milled	Hand-mixed			Jet-milled		
	Unfilled	1 wt%	2 wt%	5 wt%	1 wt%	2 wt%	5 wt%
T_{m1} (°C)		328.5	344.0	329.4	328.9	343.3	329.9
	328.9	328.6	344.2	329.8	329.0	343.3	330.0
		329.4	344.2	328.9	329.7	329.7	329.5
ΔH_{m1} (J/g)		33.4	53.5	41.8	35.7	63.0	43.0
	32.5	30.8	49.1	42.3	38.2	62.7	40.2
		40.5	49.2	33.8	34.4	38.9	35.6
$U_c(\Delta H_{m1})$		0.4	0.7	0.6	0.5	0.8	0.6
	0.4	0.4	0.7	0.6	0.5	0.8	0.6
		0.6	0.7	0.4	0.4	0.5	0.5
T_{c1} (°C)		315.5	316.5	316.2	315.7	316.3	316.6
	316.1	315.6	316.6	315.8	315.5	316.4	316.3
ΔH_{c1} (J/g)		31.4	28.9	35.2	32.4	31.9	35.33
	29.3	34.6	30.2	35.7	33.4	30.9	33.9
T_{m2} (°C)	328.0	327.7	328.2	328.5	327.6	328.2	328.4
		327.7	328.2	328.9	327.6	328.3	328.6
ΔH_{m2} (J/g)	28.6	31.0	29.4	36.2	31.1	30.9	34.0
		31.9	29.9	36.3	31.4	30.8	34.0
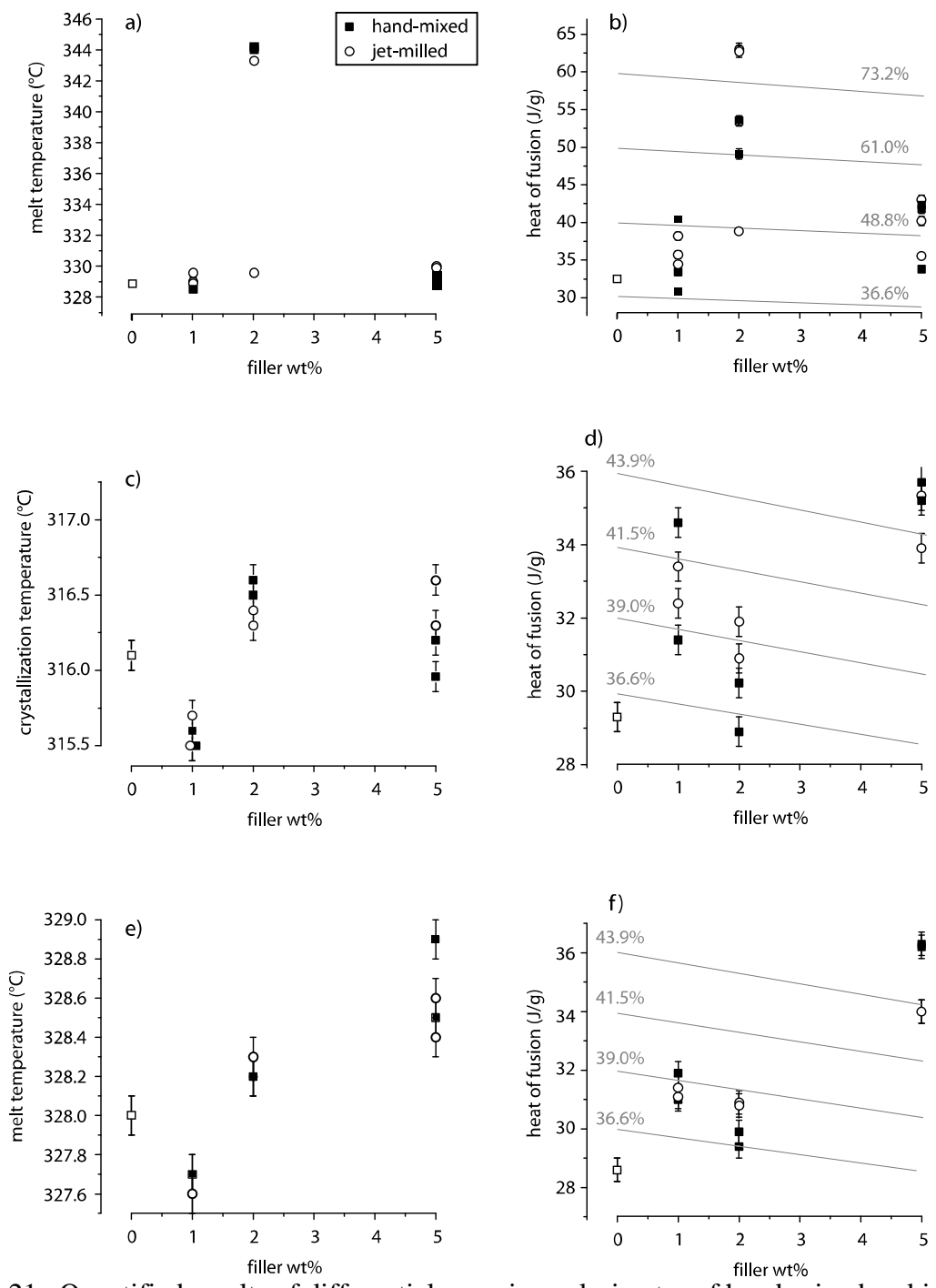
Figure 6-21. Quantified results of differential scanning calorimetry of hand-mixed and jet-milled 0, 1, 2 and 5 wt% alumina-PTFE nanocomposites compression molded at 362°C: a) first peak melt temperature plotted versus filler wt%, b) first heat of fusion plotted versus filler wt%, c) peak crystallization temperature plotted versus filler wt%, d) heat of fusion for crystallization plotted versus filler wt%, e) second peak melt temperature plotted versus filler wt%, f) second heat of fusion plotted versus filler wt%. Error bars represent the experimental uncertainty in each case.

142

Mechanical Characterization

Wear rates and friction coefficients are often strongly correlated to various mechanical properties of the materials involved [122]. Since wear is a process of material removal, resilience and toughness often have the best correlation with low wear. In past studies, extraordinarily low wear rates of these nanocomposite materials were found to accompany extensive fibrillation of the PTFE under concentrated loadings [9]. In this study, the mechanical properties of these nanocomposite materials are quantified using a calibrated load frame to study the effects of the nanoparticles on load support, elongation to failure and toughness of the polymer.

Sections of the compression molded specimens were removed and polished prior to mechanical testing. These samples were studied under an optical microscope at 20X magnification. Figure 22 shows the results of optical microscopy. Despite the vast differences observed in the dispersions of the jet-milled and hand-mixed powders, the compression molded samples show the same unique microstructure which has what appears to be ~10 μm diameter inclusions that increase in proportion to the loading. Studying just these images, one might presume that the inclusions are simply alumina agglomerations, but such a model is difficult to rationalize given the previous SEM observations of the powder ensembles, which showed that the hand-mixed samples contained alumina agglomerations on the ~2-15 μm size scale with sparsely distributed singular nanoparticles, while jet-milled powders had less frequent and smaller alumina agglomerations (1-5μm) with an order of magnitude higher density of singular nanoparticles decorating the PTFE powder surfaces. It is possible, but unlikely, that the alumina sought itself and diffused through the melt resulting in substantially different dispersions before and after melting has occurred. Another possibility is that the domains appear opaque due to an alteration of the crystalline structure of the PTFE. This could occur as a result of a high

143

nanoparticle concentration in the vicinity of the PTFE particle. Such an explanation would be

consistent with several observations: 1) the nanoparticles were found in high concentration only

on the large round PTFE particles, 2) the crystallinity of the PTFE tended to increase with

nanoparticle loading, 3) The average domain size corresponds much more closely to the larger

round PTFE particles than to the alumina agglomerations observed in electron microscopy of the

powders. Mapping Raman spectroscopy was used to determine if alumina was more or less

prevalent within these regions. The mapping region was divided into 100 pixels, and 20 spectra

were taken at each pixel. Standard samples of PTFE and alumina were examined and the peaks

of each sample were established. The 20 spectra taken at each pixel were averaged, and the

alumina peak was normalized to the defining PTFE peak. A contour plot of the relative alumina

intensity is plotted for the area in the accompanying optical micrograph in Figure 6-23(a-b). The

results of Raman spectroscopy indicate that the opaque domains are alumina rich. In a parallel

study, one of these domains was plucked from the matrix, smashed between two glass

microscope slides and observed using SEM (Figures 6-23(c-f)). The bulk within the domain

does contain individual nanoparticles but appears to be primarily comprised of the polymeric

matrix. The cause and structure of these domains remain unclear, but preliminary results are

consistent with the hypothesis that they are nanoparticle rich regions of PTFE with altered

crystalline structure.
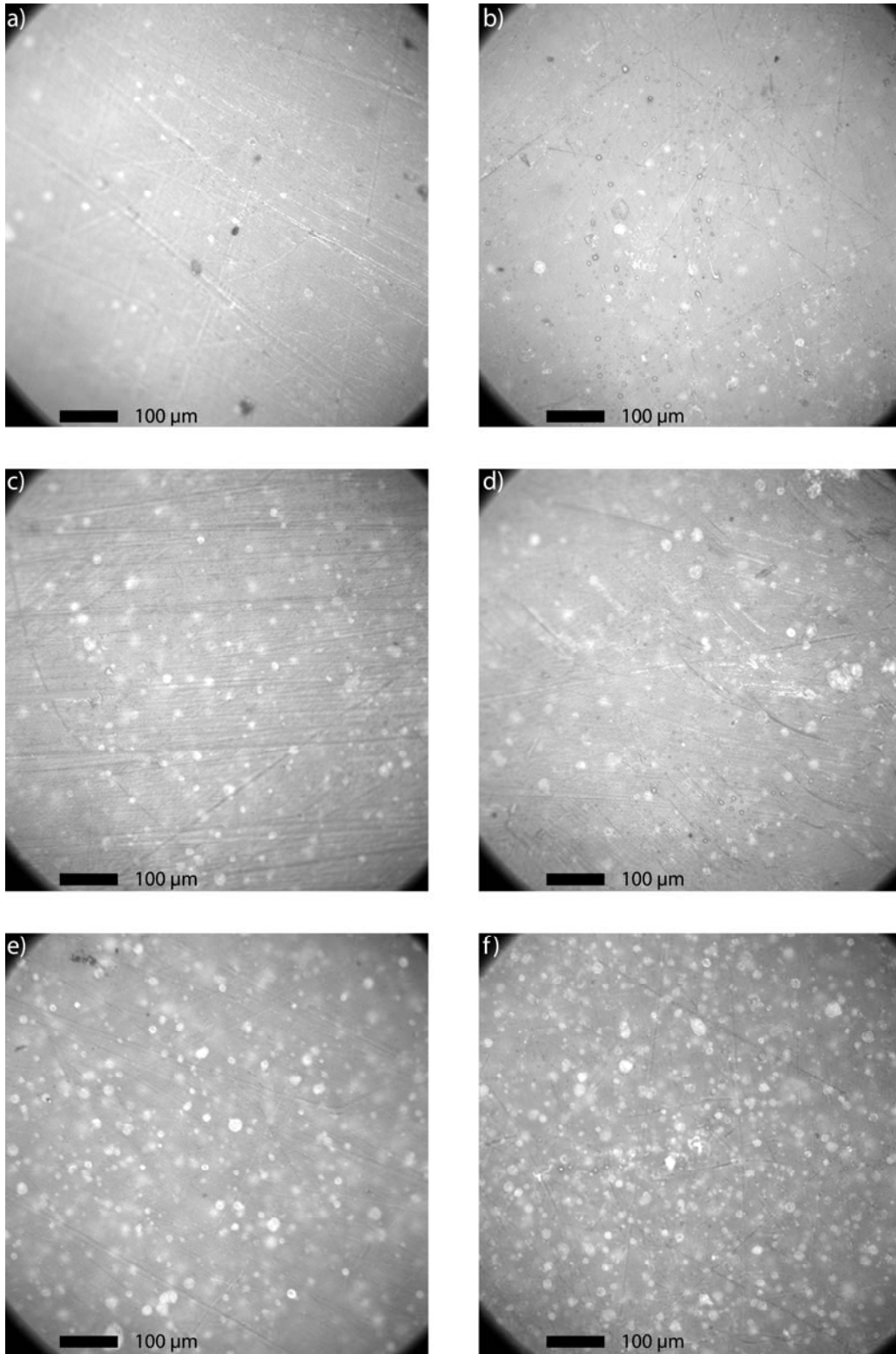
Figure 6-22. Optical micrographs of the micrstructure of the nanocomposites at 20X magnification: a) 1 wt% jet-milled, b) 1 wt% hand-mixed, c) 2 wt% jet-milled, d) 2 wt% hand-mixed, e) 5 wt% jet-milled, f) 5 wt% hand-mixed.
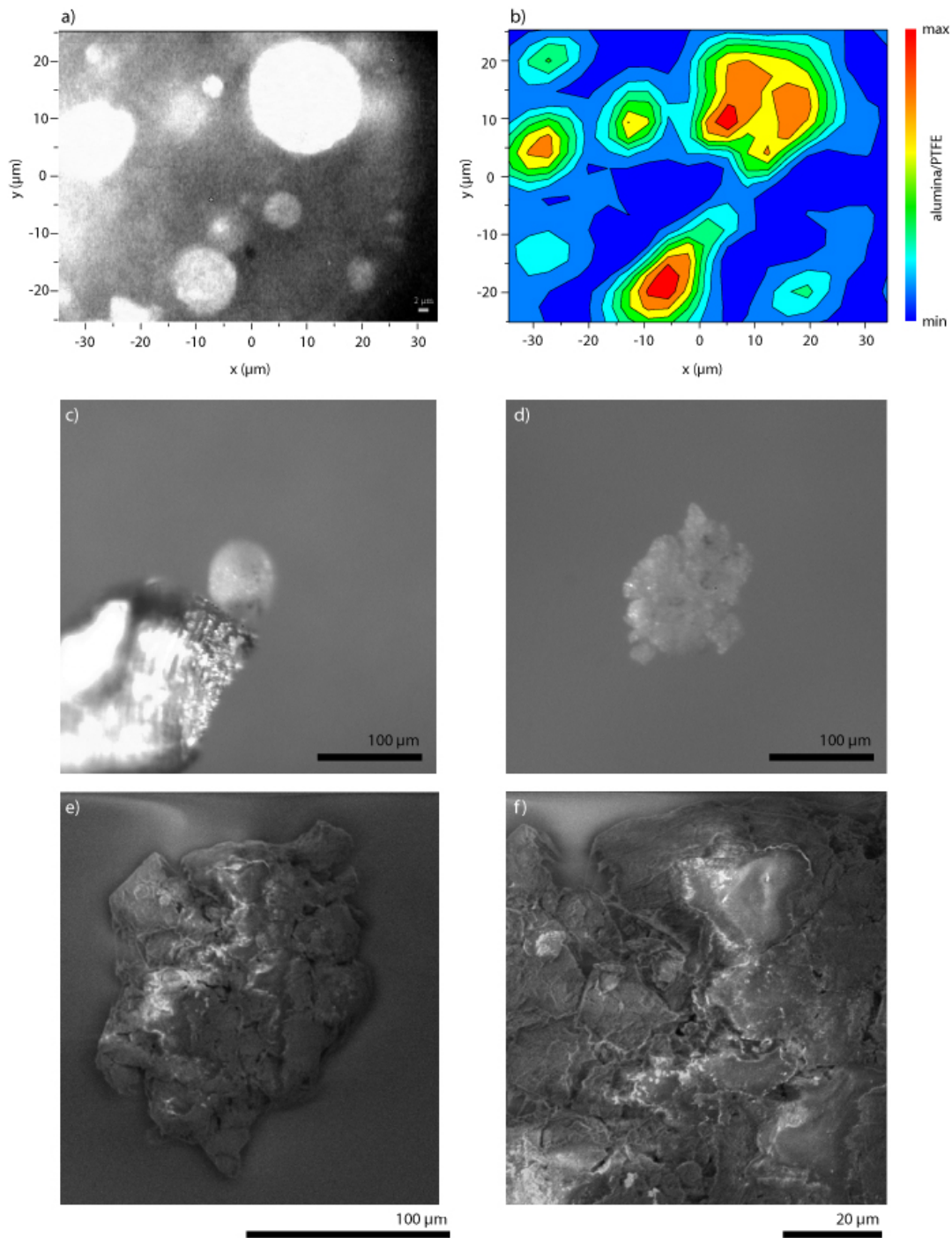
Figure 6-23. Results from analysis of opaque microstructural domains within the nanocomposites: a) optical image of the area of Raman spectroscopic analysis, b) contour maps of the alumina peak normalized to the PTFE peak following Raman spectroscopic mapping, c) a single domain plucked from the nanocomposite, d) the domain smashed between glass microscope slides, e) 50/50 overlay of a secondary electron image and a backscattered electron image of the smashed domain and f) 50/50 SE/BSE image of a region of the smashed domain at higher magnification.

The results of mechanical testing of the nanocomposites are shown in Figure 6-24. Stress is plotted versus engineering strain for jet-milled and hand-mixed nanocomposites in Figures 6-24a and 6-24b, respectively. Ultimate stress and strain are plotted versus filler wt% in Figures 6-24c and 6-24d, respectively. Similar ranges of ultimate stresses and strains, namely, 8-16 Mpa and 250-600%, respectively, were obtained for both jet-milled and hand-mixed dispersion treatments. This result was unexpected given the original hypothesis that the dispersions drive the nanocomposite properties and that the hand-mixed dispersion represents a worst-case scenario while the jet-milling technique was thought superior to other more traditional techniques. Even more unexpected was the fact that the hand-mixed samples actually outperformed the jet-milled samples in terms of consistency in a qualitative sense. The poorest performing hand-mixed sample was the 2 wt% sample. The bottom half of this sample yielded after about 20% strain and was unable to support enough tensile load to yield the rest of the sample. The cause of this selective failure is unclear but a thermal and/or pressure gradient is suspected to have cause incomplete sintering of only part of the sample. The DSC scan in Figure 6-20 from a section near the center of this sample supports the hypothesis showing that only partial sintering occurred. Despite the weakness in this part of the sample, the total strain was nearly 300%, and the length corrected ~600% strain to failure is consistent with the rest of the hand-mixed field. The jet-milled samples were less consistent, showing no trend with loading or with the thermal behaviors shown in Figure 6-20.

Despite these nanocomposites having a degree of inconsistency in their mechanical behaviors, all of the samples were strengthened and toughened significantly due to the nanoparticles with the least tough nanocomposite being over 100X tougher than unfilled PTFE sample processed at the same conditions. In addition to the impressive gains in ultimate strain,

147

the stresses shown here reflect the nominal pre-strained cross-sectional areas of the samples and not the true area. Therefore, given the amount of strain in the cross-section, the true stresses at failure were substantially higher. For example, the 2 wt% jet-milled sample had a final unstressed cross-sectional area of about 5 mm^2 and the true stress carried by the sample at failure was approximately 40MPa. These stress and strain differences over neat PTFE are impressive considering the low loading of the nanoparticles and suggest that the improvements arise from a unique crystalline structure that results from the nanoparticle influence rather than a direct load carrying effect of the nanoparticles.
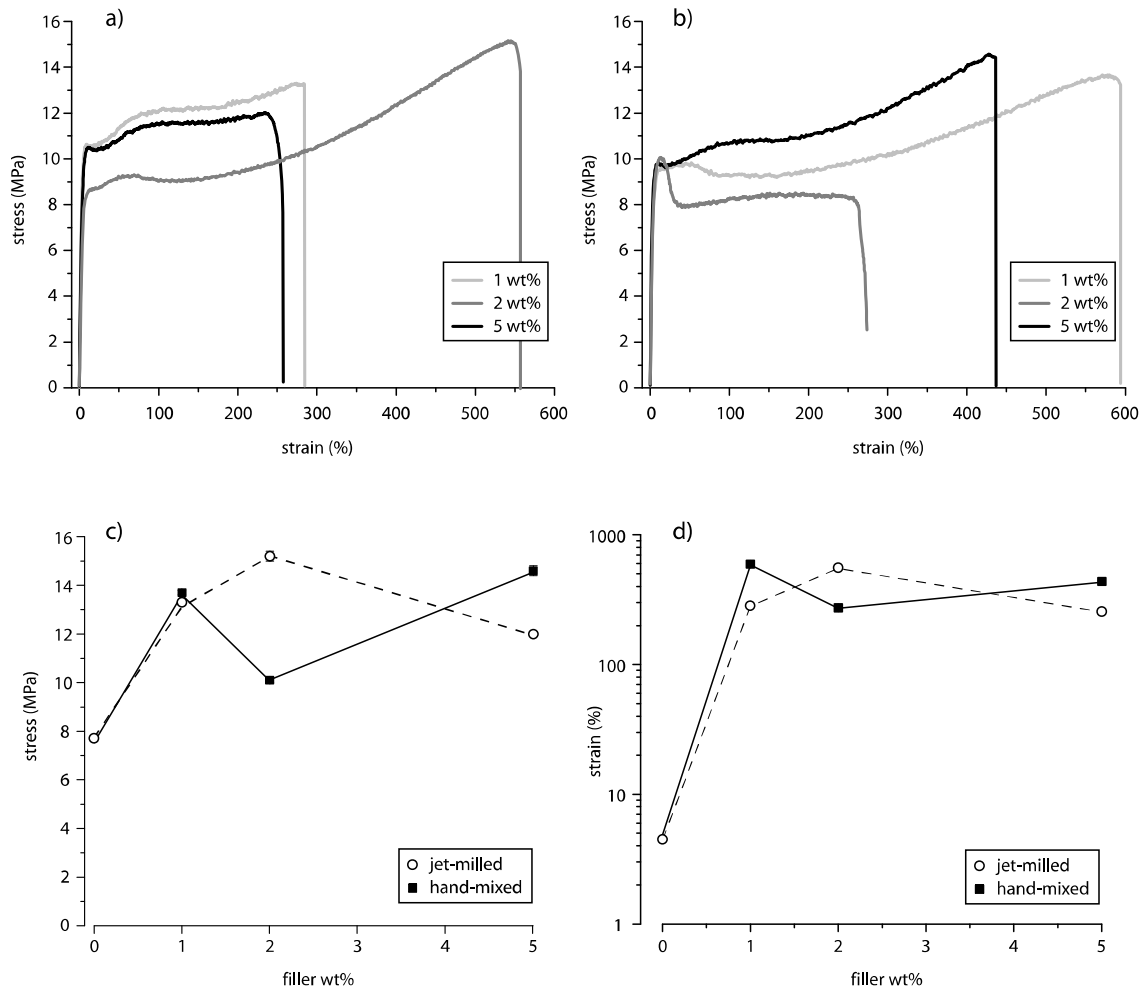
Figure 6-24. Results from mechanical characterization of 80 nm alpha phase alumina-PTFE nanocomposites, a) stress versus strain for jet-milled nanocomposites, b) stress versus strain for hand-mixed nanocomposites, c) ultimate stress versus filler wt%, d) ultimate strain versus filler wt%.

Scanning electron microscopy images of the fracture surfaces are shown in Figure 6-25. The alumina rich domains that appear in optical microscopy also appear bright in backscattered electron imaging. The domains have not been strained appreciably (or at all) during mechanical testing and do not appear to directly contribute to the load carrying capacity of the composite. Various voids can be found where domains have been plucked out during fracture. Evidently, there is poor cohesion between the domains and the matrix as removal of the domains results in imperceptible damage to the surrounding matrix.

Varying matrix fracture morphologies accompany the variations in mechanical behaviors. In all cases, the failure mechanism is characterized by extensive fibrillation. The deformation behavior of the matrix is drastically different from that of the unfilled polymer, which suggests that nanoparticles inhabit and alter the matrix in between the alumina rich domains. The surfaces of the 1 wt% jet-milled and 5 wt% hand-mixed nanocomposites are smooth and suggest the least local fibril extension and rapid break at failure. It should be noted that the bright, smooth regions on the 1 wt% jet-milled sample represent locations where the fibrils were smashed flat from contact with the sample holder. The 2 wt% jet-milled and 1 wt% hand-mixed samples had the best combination of stress and strain at failure and demonstrate uniformly and substantially strained and elongated material at the surfaces. The 2 wt% hand-mixed sample shows extensive small-scale fibrillation at the fracture surface which reflects ductile failure of highly strained material. Recall that the true strain of this sample was closer to 600% rather than the reported 270% due to yielding and straining of only about half of the sample. The 5 wt% jet-milled sample also demonstrated small-scale fibrillation. Portions of this surface appear very smooth indicating brittle failure. Following failure of this portion of the surface, only very small areas remained for load support resulting in gross fibrillation and gradual loss of load carrying

capacity. Fibrils are very strong and can endure massive elongations before failure. As a result, both samples showing small-scale fibrillation (2wt% hand-mixed and 5 wt% jet-milled) required 10-15% strain to completely lose load carrying capacity after 'failure' while the other samples required less than 0.1%.

Interestingly, Michler [117] suggests that particle inclusions (*e.g.* alumina rich domains in this case), with weak interfacial strength with the matrix, provide a toughness mechanism in polymers by creating a stress concentration that results in local yielding and fibrillation (crazing). Higher magnification imaging of this weak interface did confirm such local fibrillation, but this mechanism was surely swamped by the effects of the nanoparticles on the remaining fibrillated matrix. The same mechanism may have been activated by the nanoparticles in the regions in between the domains. Michler also notes a thin-layer yielding mechanism where very small lamellae exhibit large-scale deformation which manifests itself into >100X increases in toughness and elongation. This is opposed to the smaller toughness increases found for the crazing mechanism that typically occurs at the particle interface. It is thought that the nanoparticles may reduce the PTFE lamellae size to that which facilitates the thin-layer yielding deformation mechanism. Evidence for such a mechanism is provided by the AFM imaging shown in Figure 3-18.

Table 6-6. Results of mechanical testing of hand-mixed and jet-milled 1wt%, 2wt% and 5 wt% 80 nm α alumina-PTFE compression molded nanocomposites.

	Jet-milled	Hand-mixed			Jet-milled		
	Unfilled	1 wt%	2 wt%	5 wt%	1 wt%	2 wt%	5 wt%
σ (MPa)	7.7	13.7	10.1	14.6	13.3	15.2	12.0
$U_c(\sigma)$	0.1	0.1	0.1	0.2	0.1	0.2	0.1
ε (%)	4.49	594	271	437	285	557	257
$U_c(\varepsilon)$	0.01	8	5	6	4	7	3
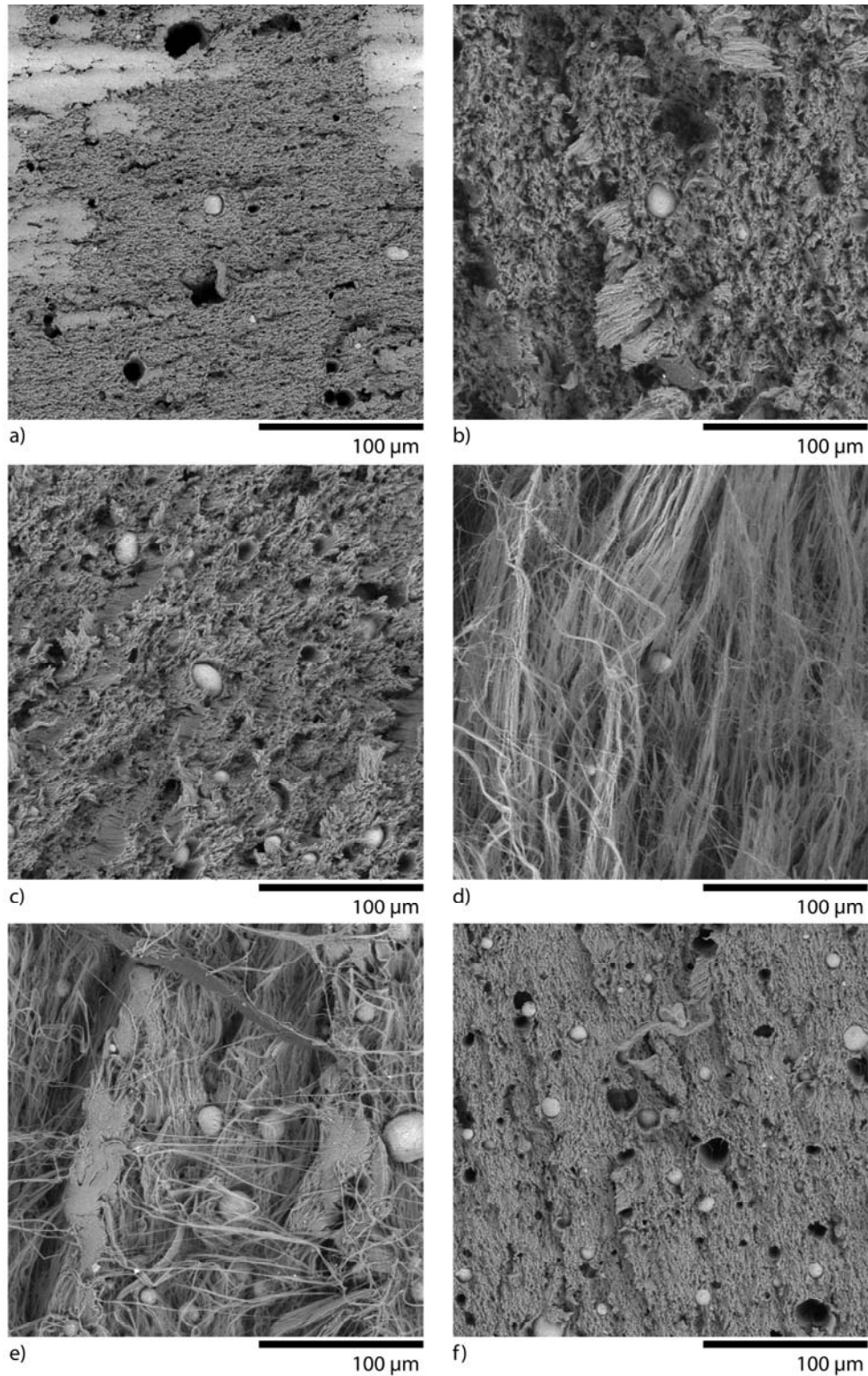
Figure 6-25. Scanning electron microscopy of the fracture surfaces of a) 1 wt% jet-milled alumina-PTFE, b) 1 wt% hand-mixed alumina-PTFE, c) 2 wt% jet-milled alumina-PTFE, d) 2 wt% hand-mixed alumina-PTFE, e) 5 wt% jet-milled alumina-PTFE, f) 5 wt% hand-mixed alumina-PTFE.

Tribological Characterization

　　The tribological properties of the 1, 2 and 5 wt% jet-milled and hand-mixed

nanocomposites were tested using a reciprocating tribometer with a normal pressure of 6.3 MPa,

a sliding speed of 50 mm/s and 50 mm of travel per cycle of sliding. The results of tribological

testing are shown in Figure 6-26.   First consider the friction coefficients plotted versus sliding

distance for the jet-milled nanocomposites in Figure 6-26a. The 1 wt% sample ran for 5 km

before reaching the maximum allowable volume loss of 50 mm^3; this is about an order of

magnitude more sliding than could be endured by unfilled PTFE. The friction coefficient of this

sample was fairly steady for the 5 km duration of the test at $\mu = 0.17$. The 2 wt% sample had

significantly more variation in the friction coefficient than did the 1 wt% sample. For the first 5

km, the friction coefficient was actually lower for the 2 wt% sample than for the 1 wt% sample

despite having a higher concentration of the hard alumina filler. However, after 10 km of

sliding, the friction coefficient began to increase until reaching a steady state value of $\mu = 0.22$.

Throughout the test, the friction coefficient is observed to decrease and then increase abruptly.

These abrupt changes are due to the test interruptions for the mass loss measurements. The

decrease in friction coefficient is likely due to a combination of contaminant adsorption after

separation of the contact, and reduced contact area from the pin and counterface running surfaces

being re-assembled out of registry. At 5 wt%, the initial friction coefficient during run-in was

again lower than for both the 1 and 2 wt% samples, but quickly transitioned to a higher steady

state value of $\mu = 0.27$.   The friction coefficients of the hand-mixed samples are plotted versus

sliding distance in Figure 6-26b. The 1 wt% sample had a friction coefficient behavior very

similar to that of the jet-milled 1 wt% sample; this sample ran nearly twice the sliding distance of

the jet-milled sample and showed a decrease in friction coefficient to $\mu = 0.15$ toward the end of

the test. The 2 wt% sample had the highest average friction coefficient among hand-mixed

samples and both the 2 and 5 wt% samples had significantly shorter transient periods of low

friction than the jet-milled samples. In almost every case, the friction coefficient varied

dramatically with sliding distance. This is unlike the behavior observed for unfilled PTFE;

unfilled PTFE had a transient friction coefficient that started at approximately $\mu = 0.15$ and

decayed to around $\mu = 0.12$ as sliding continued with short-range variations of about 0.01.
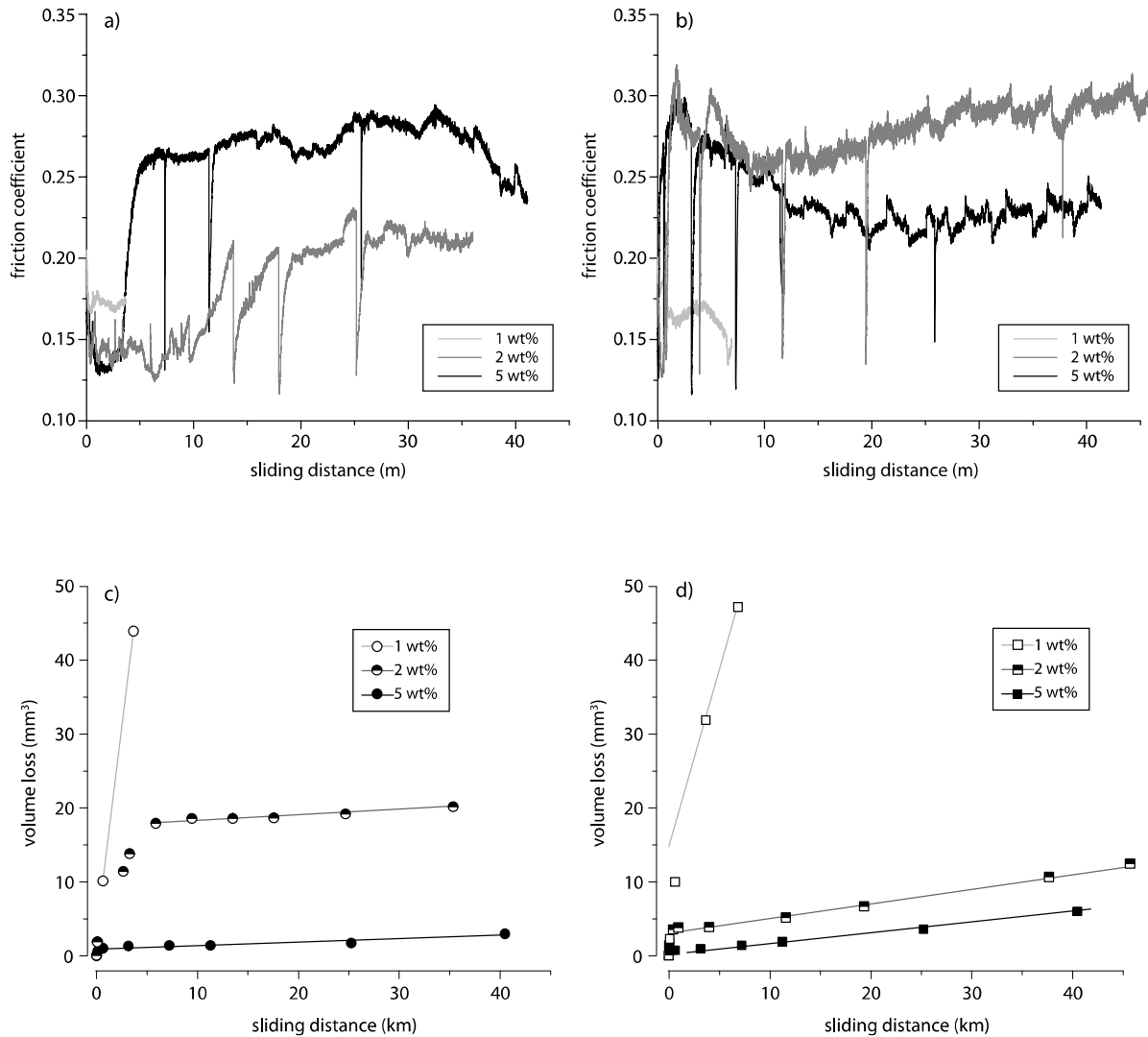
Figure 6-26. Results of tribology experiments of hand-mixed and jet-milled 0, 1, 2 and 5 wt%
alumina-PTFE nanocomposites compression molded at 362°C: a) friction coefficient
versus sliding distance for jet-milled nanocomposites, b) friction coefficient versus
sliding distance for hand-mixed nanocomposites, c) volume loss versus sliding
distance for jet-milled nanocomposites, d) volume loss versus sliding distance for
hand-mixed nanocomposites.

The results of wear volume measurements are plotted in Figure 6-26c and 6-26d for jet-milled and hand-mixed samples, respectively. In both cases, enormous changes in the friction and wear behavior occurred with increased filler loading. The largest range of behaviors occurred in the jet-milled samples; the 1 wt% sample wore 45 mm^3 of material in 4 km of sliding, while the 5 wt% sample wore less than 5 mm^3 in 40 km of sliding. The rate of wear of the 1 wt% samples continuously decreased as sliding distance increased, suggesting that the entire test occurred under effectively transient sliding conditions. The 2 wt% jet-milled sample also had a substantial transient period of sliding where the wear rate continuously decreased with increased sliding distance until a steady state was reached at 5 km of sliding. The 5 wt% jet-milled sample had little to no transient sliding before reaching steady conditions for the remainder of the test. In every case, the hand-mixed samples showed shorter and less severe transient periods of wear. Despite having significant agglomeration and relatively poor nanoparticle dispersion, the 2 and 5 wt% hand-mixed samples quickly reached low steady state wear rates comparable to those found for jet-milled samples. Following a brief period of low wear sliding, however, a change in the tribo-system caused an increase in the wear rate of about 2-4X. Wear rate is plotted versus filler wt% in Figures 6-27. The wear rates of hand-mixed and jet-milled samples behaved similarly as a function of filler wt%. Wear rate appears to correlate with the alumina loading and density of the opaque, alumina rich domains in the material rather than the degree of nanoparticle agglomeration and dispersion.
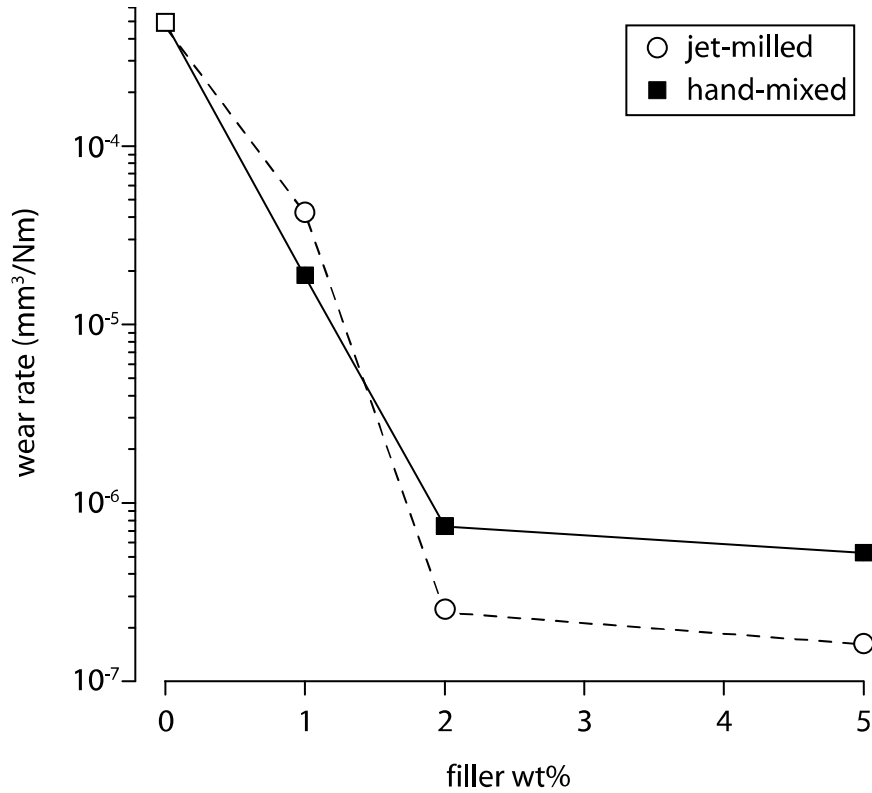
Figure 6-27. Wear rate versus alumina nanoparticle wt% for hand-mixed and jet-milled 0, 1, 2 and 5 wt% alumina-PTFE nanocomposites compression molded at 362°C.

Table 6-7. Results of tribological testing of hand-mixed and jet-milled 1wt%, 2wt% and 5 wt% 80 nm α alumina-PTFE compression molded nanocomposites. The uncertainty in the friction coefficient measurements is less than $U_c(\mu)$=0.005.

	Jet-milled	Hand-mixed			Jet-milled		
	Unfilled	1 wt%	2 wt%	5 wt%	1 wt%	2 wt%	5 wt%
μ	0.119	0.165	0.276	0.243	0.173	0.169	0.239
$\sigma(\mu)$	0.004	0.010	0.027	0.029	0.005	0.029	0.053
k (x 10^{-7} mm^3/Nm)	4930	189	7.43	5.27	423	2.54	1.64
U_c(k (x 10^{-7} mm^3/Nm))	20	4	0.05	0.03	3	0.1	0.02

Each transfer film was measured using 3D stylus profilometric mapping. The area measured by profilometry was examined using SEM; backscattered electron images are shown below the accompanying topography maps in Figures 6-28 and 6-29. It is clear from the profilometry that the nanocomposites were abrasive to the counterfaces. It is also clear that the

155

hand-mixed samples were significantly more abrasive to the counterfaces than were the jet-milled samples. This is likely the cause of the 2-4X higher steady state wear rates of the hand-mixed samples. The portions of the surfaces covered by transfer films appear are represented by the dark regions of the surface in the backscattered images.
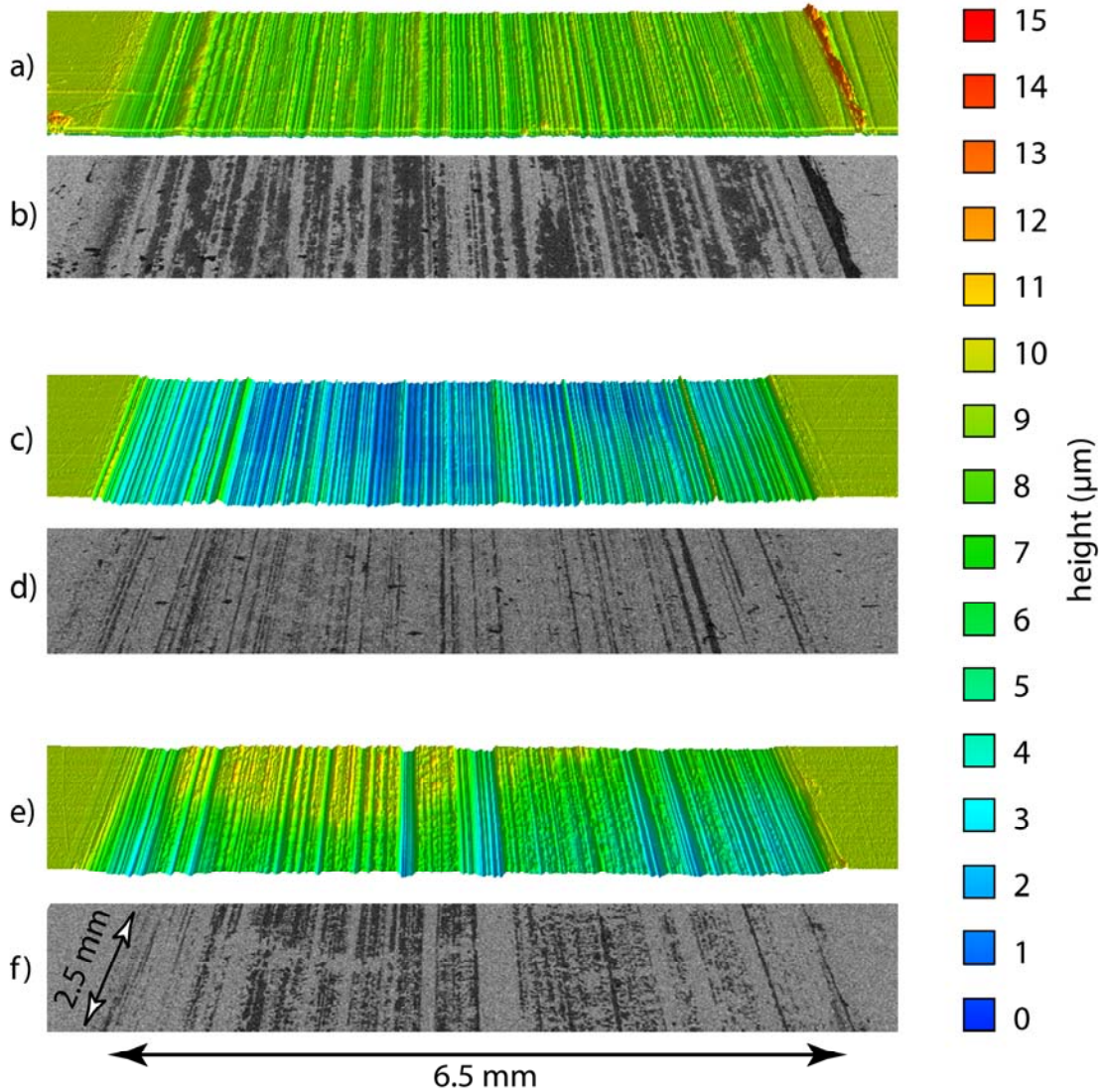
Figure 6-28. Analyses of wear tracks following the tribological experiments with hand-mixed nanocomposites: a) stylus profilometric map of the wear track for the 1wt% composite, b) backscattered electron image of the area from profilometry for the 1wt% composite, c) stylus profilometric map of the wear track for the 2wt% composite, d) backscattered electron image of the area from profilometry for the 2wt% composite, e) stylus profilometric map of the wear track for the 5wt% composite, f) backscattered electron image of the area from profilometry for the 5wt% composite
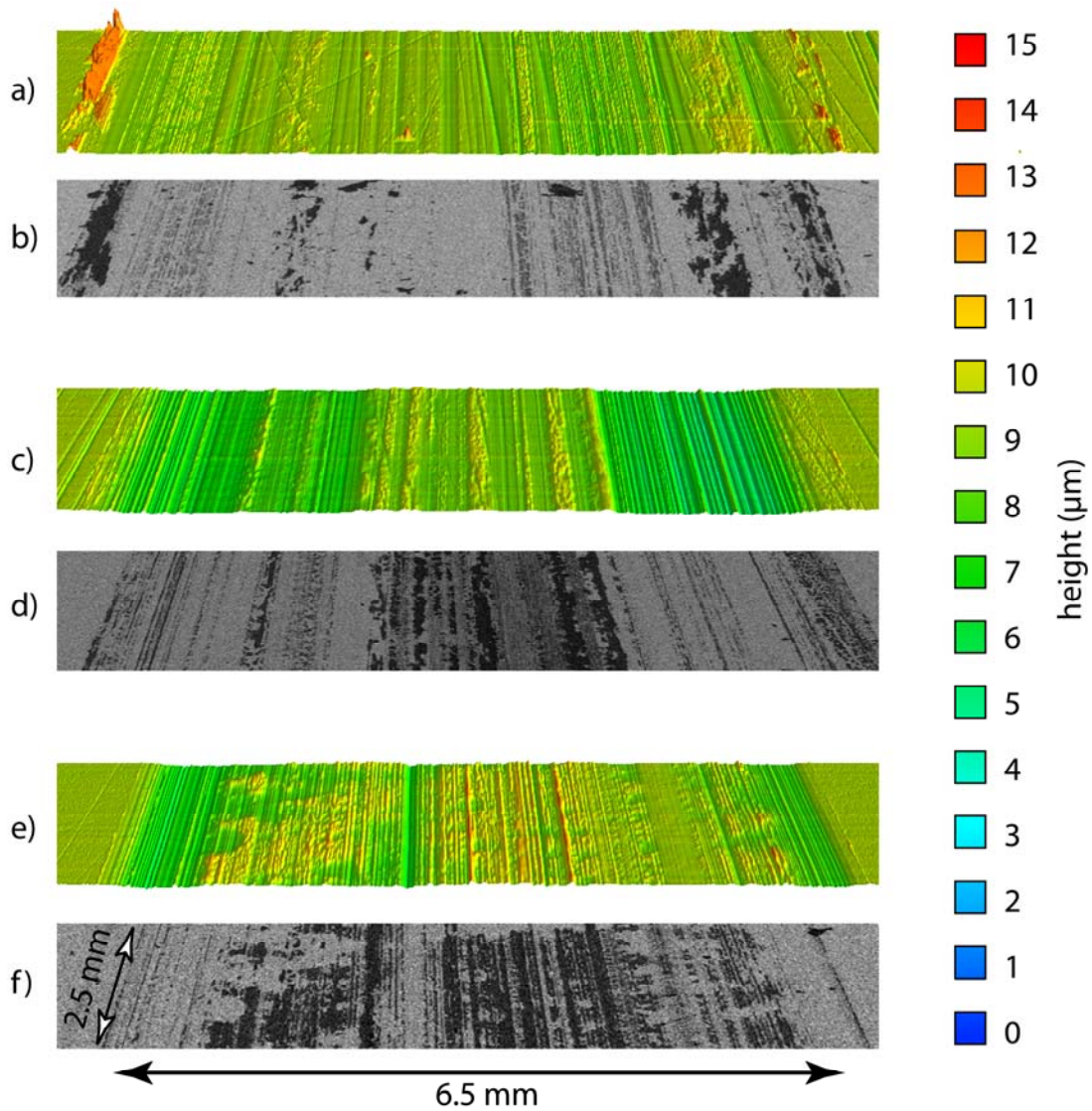
Figure 6-29. Analyses of wear tracks following the tribological experiments with jet-milled nanocomposites: a) stylus profilometric map of the wear track for the 1wt% composite, b) backscattered electron image of the area from profilometry for the 1wt% composite, c) stylus profilometric map of the wear track for the 2wt% composite, d) backscattered electron image of the area from profilometry for the 2wt% composite, e) stylus profilometric map of the wear track for the 5wt% composite, f) backscattered electron image of the area from profilometry for the 5wt% composite.

Filler Material on Nanocomposite Properties

Nanoparticle Dispersion

It was hypothesized previously that the dominant factor in the tribological success or failure of a PTFE nanocomposite is the nanoparticle dispersion. Nanoparticles are inherently difficult to disperse due to the large ratio of the surface forces to the inertial forces, and PTFE is a difficult matrix to disperse nanoparticles within due to its high melt viscosity, difficult polymerization and 'sticky' nature. Hand-mixed and jet-milled nanocomposites were created and tested with the intention that the hand-mixed dispersions would be as poor as one would expect in practice, while the jet-milled samples were thought to have a very good dispersion. SEM observations of the powders confirmed that the hand-mixed powders primarily consisted of agglomerated filler (with agglomerates being of the 2-15 µm size scale), while jet-mill samples had few small agglomerations and an order of magnitude more individual nanoparticles decorating the PTFE surfaces. Unexpectedly, the hand-mixed samples performed comparably to jet-milled samples in mechanical testing and tribological testing being orders of magnitude tougher and more wear resistant than unfilled PTFE. These results suggest that perhaps the shape or chemistry of the nanoparticles dominate the behavior of the nanocomposites rather than dispersion. In a previous study, it was found that if the α phase alumina nanoparticles of the current investigation were treated with a fluorinated silane coupling agent, the tribological properties of the nanocomposites improved. It was thought that a reduction in surface energy contributed to improved dispersion which resulted in improved properties at lower loadings, but the latest results suggest that the differences may be due to some beneficial property of the treated surfaces. Previous studies also found that $\Delta:\Gamma$ phase alumina nanoparticles result in poorer tribological performance when compared to the α phase alumina particles. It is

hypothesized that the wear resistance mechanism of the nanoparticles is to alter the crystalline structure of the polymer. These changes affect the mechanical properties, which determine the size, morphology and number density of debris particles generated. The debris particles affect the formation and stability of the transfer film and the transfer film determines the tribological properties of the system. This investigation studies the thermal, mechanical and tribological properties of 12.5 wt% jet-milled α phase and Δ:Γ phase alumina-PTFE nanocomposites to further explore this hypothesis.

Figure 6-30 shows SEM images of the 12.5 wt% jet-milled alumina-PTFE powder ensembles. The Δ:Γ phase particles used in this study (44 nm reported average particle size) are clearly smaller than the alpha phase alumina particles (80 nm reported average particle size), but the effects of particle size have previously been found to be small. Few small agglomerations were found in these powders and both dispersions are characterized by a large number of nanoparticles decorating the surfaces of the PTFE particles. The same dispersion characteristics were observed for the jet-milled samples of the previous study which varied greatly from the agglomerated nature of the hand-mixed dispersion.
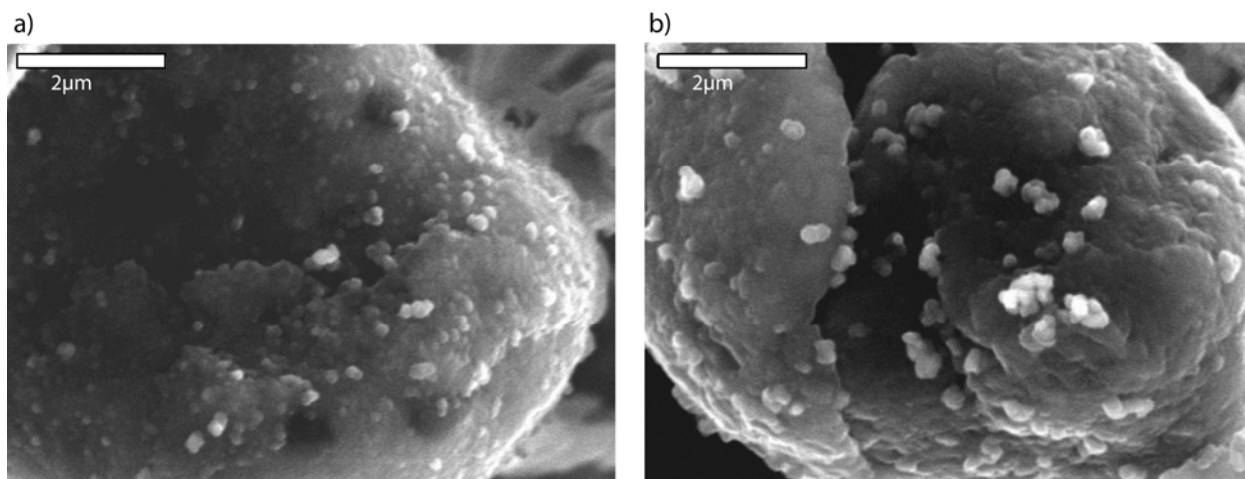
Figure 6-30. Powder dispersions for 12.5 wt% alumina nanoparticles in PTFE: a) 40 nm Δ:Γ phase alumina, b) 80 nm α phase alumina.

Thermal Characterization of Powder Ensembles

Thermal characterizations using DSC were conducted to explore the potential effects of the

nanoparticles on the mobility, melt, crystal nucleation and lamellae of PTFE. The results of

these characterizations are shown in Figure 6-31. The neat PTFE began melting first, the α

phase alumina filled PTFE melted second and the $\Delta{:}\Gamma$ phase alumina filled PTFE melted third.

In general, the melt distributions of the filled samples were narrower. This may be an indication

that as low order structures melt at low temperatures, the nanoparticles act to nucleate and

recrystallize higher ordered structures synchronously. The recrystallization curve reflects the

steeper melt curve, and the nanocomposite powders show lower crystallinity which likely

reflects the lack of contribution of the 12.5 wt% of alumina filler.
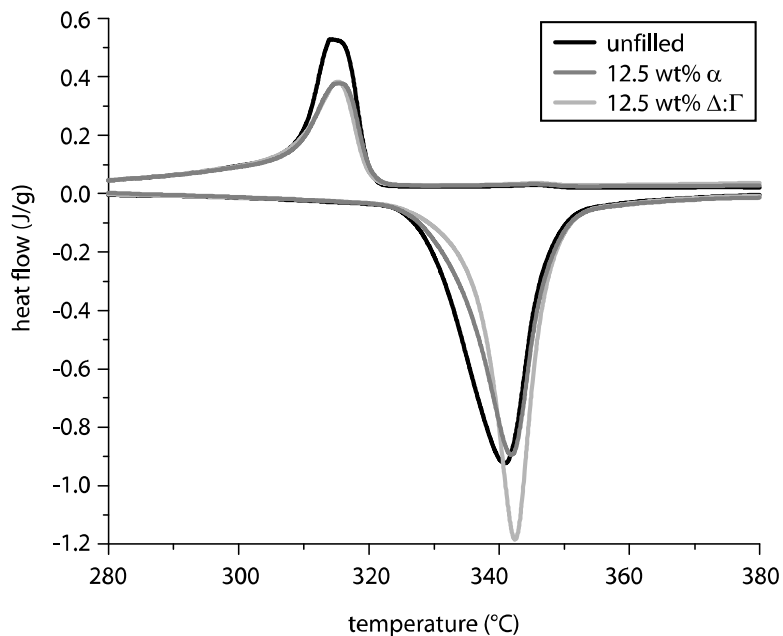
Figure 6-31. DSC heat flow plotted versus temperature for heating and cooling of powder
ensembles of unfilled PTFE, 12.5 wt% α phase alumina nanoparticle in PTFE
and12.5 wt% $\Delta{:}\Gamma$ phase alumina in PTFE.

The results of these thermal characterization experiments have been quantified and are

plotted versus filler wt% in Figure 6-32 and are tabulated in Table 6-8. The first peak melt

160

temperature is plotted versus filler wt% in Figure 6-32a. The previous results for jet-milled

powders are also included for the interpretation of trends. There is a clear trend of increasing

melt temperature with increasing filler wt%. This is not due to a shift in the curve, but rather to a

reduction in the low temperature portion of the signal of neat PTFE. This may have to due with

nucleation and recrystallization of the PTFE into higher order structures because of the

nanofiller; determination of this effect will require modulated DSC. The effect occurs with both

α and Δ:Γ phase nanofillers, but to a greater extent with the smaller Δ:Γ phase alumina.

The enthalpy of fusion for the first melt is plotted versus filler wt% in Figure 6-32b. There

is a clear trend of decreased crystallinity with increased filler. This decrease is consistent with

the prepared loading of the inactive nanoparticles that are included in the initial mass

measurement. The global crystallinity of the jet-milled PTFE is not expected to vary as a result

of the nanoparticle inclusion. The jet-mill is an open system and based on previous thermal

gravimetric analysis, it has long been thought that as many as 60% of the nanoparticle fines are

preferentially lost during powder blending. These results suggest that the loadings of the

nanocomposites are equal to the loadings as prepared.

The peak recrystallization temperature is plotted versus filler wt% in Figure 6-32c. As

with the first melt temperature, this is due to narrowing of the curve. It is unclear why the curve

has become narrower, but it is possible that the nanoparticles promote an increase in the ordering

of initially low order crystals. The enthalpy of recrystallization is plotted versus filler wt% in

Figure 6-32d.   Lower wt% nanocomposites show no change in crystallinity, but both 12.5 wt%

samples showed a reduction in crystallinity of nearly 5%. Repeat samples of the virgin material

were tested to determine variability and the results showed a standard deviation of 0.3 J/g. The

12.5 wt% nanoparticle-PTFE powder ensembles had 4 J/g lower heats of fusion than the control

sample after recrystallization.   These results suggest that the PTFE powders recrystallize with

lower crystallinity in the presence of the nanoparticles and in the absence of pressure.
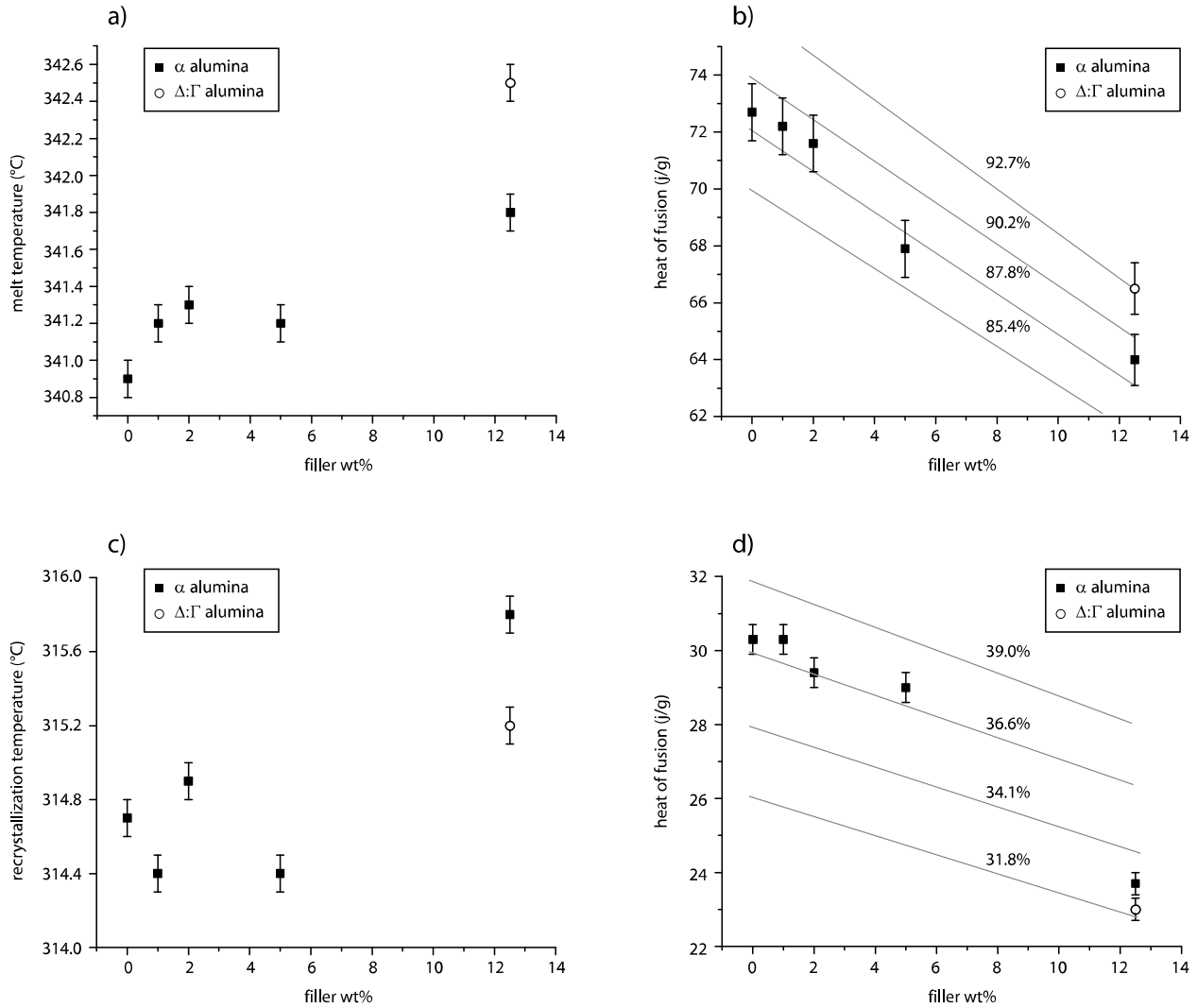
Figure 6-32. Quantified results of differential scanning calorimetry of a and Δ:Γ phase alumina nanoparticles dispersed in PTFE plotted versus filler wt%: a) first peak melt temperature plotted versus filler wt%, b) first heat of fusion plotted versus filler wt%, c) peak crystallization temperature plotted versus filler wt%, d) heat of fusion for crystallization plotted versus filler wt%. Error bars represent the experimental uncertainty in each case.

Table 6-8. Results of DSC of jet-milled 12.5 wt% 80 nm α phase and 44 nm Δ:Γ phase alumina-PTFE powder ensembles..

Alumina phase	α					Δ:Γ
loading	0 wt%	1 wt%	2 wt%	5 wt%	12.5 wt%	12.5 wt%
T_{m1} (°C)	340.9	341.2	341.3	341.2	341.8	342.5
ΔH_{m1} (J/g)	72.7	72.2	71.6	67.9	64.0	66.5
$U(\Delta H_{m1})$	1.0	1.0	1.0	1.0	0.9	0.9
T_{m1} (°C)	316.1	314.4	314.9	314.4	315.8	315.2
ΔH_{m1} (J/g)	26.6	30.3	29.4	29.0	23.7	23.0

Thermal Characterization of Nanocomposites

The thermal characteristics of the compression molded nanocomposites were studied to determine the role of the nanoparticles under relevant compression molding conditions. The results from DSC measurements of neat PTFE, 12.5 wt% 80 nm α phase alumina-PTFE and 12.5 wt% 44 nm Δ:Γ phase alumina-PTFE nanocomposite are shown in Figure 6-33; the much larger melt peaks of the nanocomposite samples were unexpected considering the opposite trend found from thermal characterization of the powders. A repeat sample of the neat PTFE was included in these measurements and showed nearly identical behavior to the first sample.

Both unfilled samples had a small high temperature melt peak near 350°C suggesting that a small fraction of the material did not melt during processing. The lack of any comparable high temperature melt peak for the nanocomposites indicates that these samples were fully sintered. This is somewhat counterintuitive given the powder DSC results which showed an increase in first melt temperature with nanoparticle loading. The heats of fusion were also significantly higher for the nanocomposites than for the neat samples contrary to the powder results which showed a small tendency to reduce crystallinity with nanoparticle loading.   Following melting, the samples showed a comparable heat of fusion during recrystallization despite the relatively high loading of inactive filler.
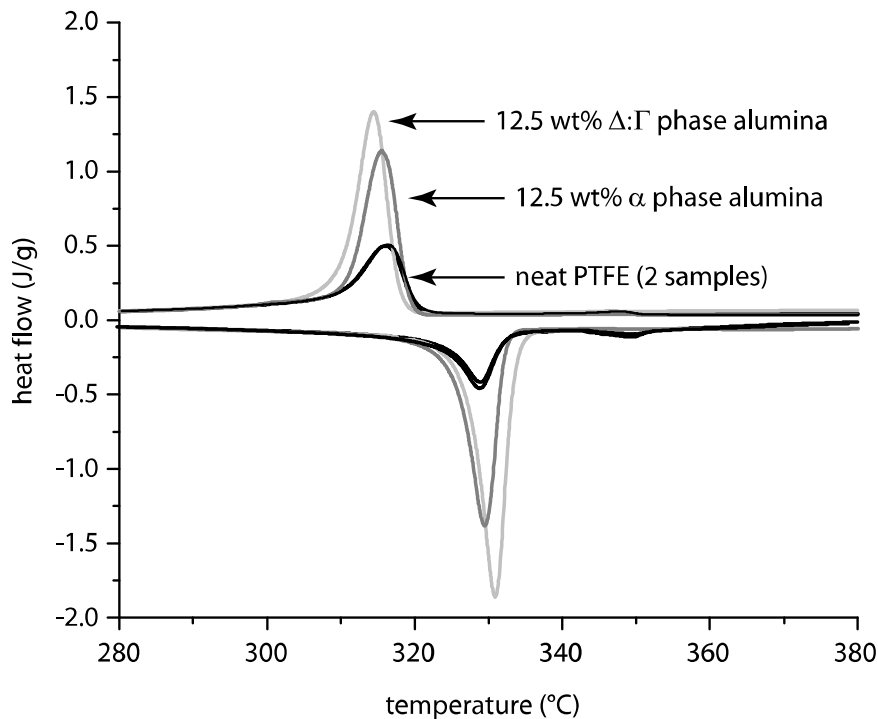
Figure 6-33. DSC heat flow plotted versus temperature for heating and cooling of compression molded samples of unfilled PTFE (x2) and nanocomposites of 12.5 wt% α and Δ:Γ phase alumina-PTFE.

The quantified results from DSC studies of the α and Δ:Γ phase alumina-PTFE nanocomposites are shown in Figure 6-34 and tabulated in Table 6-9. The first melt temperature is shown plotted versus filler wt% in Figure 6-34a. The outlying data points at 2 wt% were due to incomplete sintering of the samples. The other samples all show a slight tendency of increased melt temperature with increased loading. The 12.5 wt% Δ:Γ sample had the most dramatic increase in melt temperature due to a shift of the melt curve; it is unclear whether the increased temperatures for α phase samples are significant.   The heat of fusion for the first melt is plotted versus filler wt% in Figure 6-34b. The unusually high crystallinity of the 2wt% samples is due to incomplete sintering and therefore can not be correlated with the rest of the data. For fully sintered samples, there is a clear trend of increased heat of fusion and crystallinity with filler loading. The Δ:Γ phase alumina filled sample showed a greater increase

in crystallinity than did the α phase alumina filled sample. This is consistent with the hypothesis

that the nanoparticles act as nucleation sites for crystallization. The Δ:Γ phase particles are

smaller and therefore have a greater number of nucleation sites for a given loading.

The recrystallization temperature is plotted versus filler wt% in Figure 6-34c. The α phase

nanocomposites did not show a dependence of recrystallization temperature on filler loading.

The Δ:Γ particles appear to have reduced the recrystallization temperature by approximately 2°C.

Examination of 6-33 reveals that these particles caused a shift in the recrystallization behavior to

lower temperatures. The heat of fusion for recrystallization is plotted versus filler wt% in Figure

6-34d. Even after well controlled cooling conditions, the trend of increased crystallinity with

increased nanoparticle loading; the crystallinity of the PTFE increased by 50% and 66% with

12.5 wt% α and Δ:Γ phase alumina, respectively.

Table 6-9. Quantitative results of DSC for jet-milled 12.5 wt% 80 nm α phase and 44 nm Δ:Γ
        phase alumina-PTFE compression molded nanocomposites.

Alumina phase	α					Δ:Γ
loading	0 wt%	1 wt%	2 wt%	5 wt%	12.5 wt%	12.5 wt%
T_{m1} (°C)	328.9	328.9	343.3	329.9	329.5	330.9
	328.9	329.0	343.3	330.0		
		329.7	329.7	329.5		
ΔH_{m1} (J/g)	32.5	35.7	63.0	43.0	46.8	58.6
	32.5	38.2	62.7	40.2		
		34.4	38.9	35.6		
$U(\Delta H_{m1})$	0.4	0.5	0.9	0.6	0.6	0.8
	0.4	0.5	0.9	0.6		
		0.5	0.5	0.5		
T_{c1} (°C)	316.1	315.7	316.3	316.6	315.6	314.4
	316.1	315.5	316.4	316.3		
ΔH_{c1} (J/g)	29.3	32.4	31.9	35.3	43.7	48.3
	26.6	33.4	30.9	33.9		
$U(\Delta H_{c1})$	0.4	0.4	0.4	0.5	0.6	0.7
	0.4	0.4	0.4	0.4		
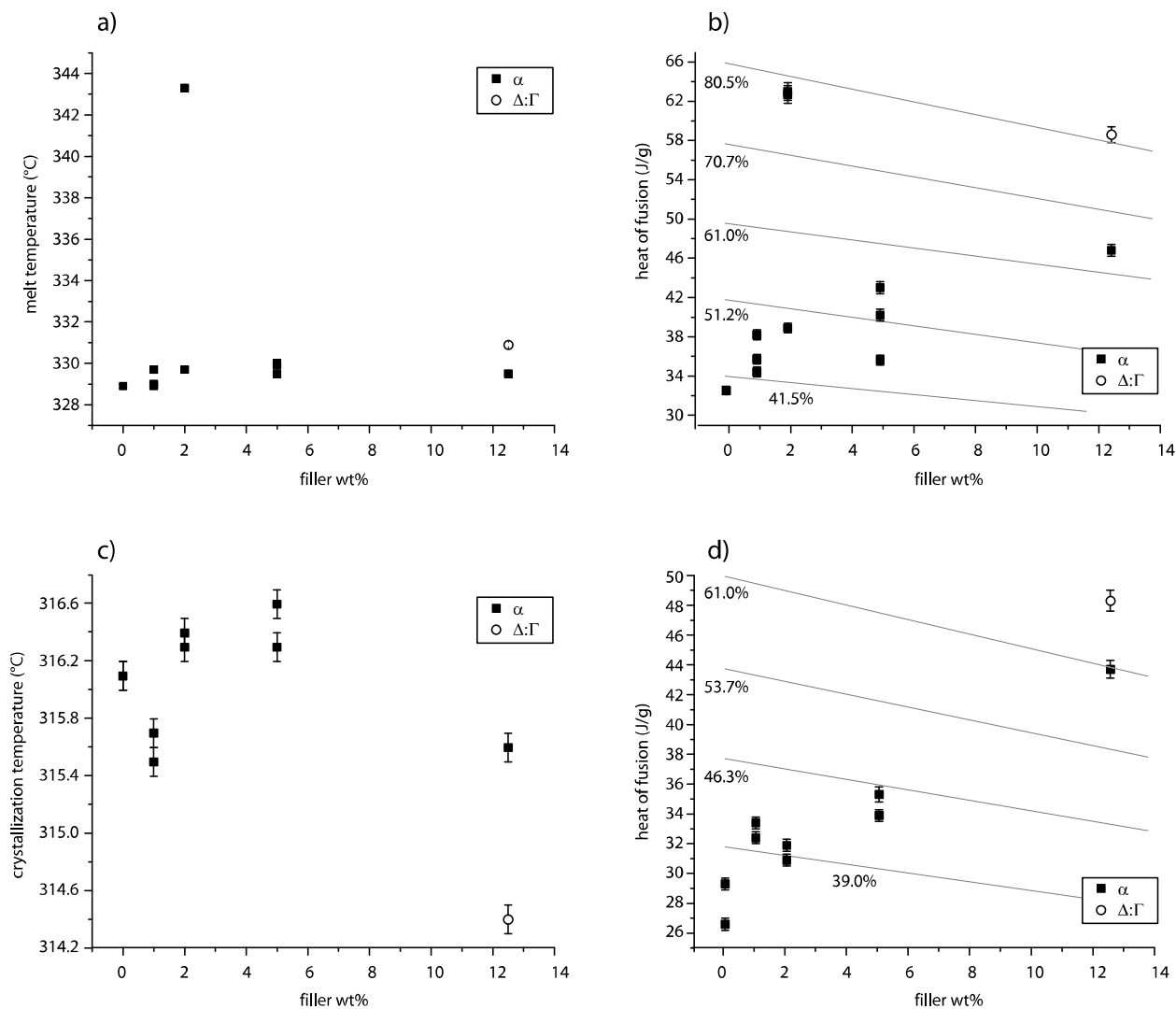
Figure 6-34. Quantified DSC results plotted versus filler wt% from unfilled PTFE and nanocomposites of 12.5 wt% α and Δ:Γ phase alumina-PTFE: a) first peak melt temperature plotted versus filler wt%, b) first heat of fusion plotted versus filler wt%, c) peak crystallization temperature plotted versus filler wt%, d) heat of fusion for crystallization plotted versus filler wt%.

Mechanical Characterization of Nanocomposites

Mechanical testing of the 12.5 wt% α and Δ:Γ phase alumina-PTFE nanocomposites was carried out to investigate the potential roles of nanoparticle surface characteristics on strength, strain, toughness and fracture mechanisms of the polymer. Stress is plotted versus strain for these samples in Figure 6-35. The stress of the α phase alumina filled sample increased with

strain consistent with an elastic modulus of ~330 MPa until failure occurred at a stress of 5 MPa.

The Δ:Γ phase alumina filled sample had a modulus of ~140 MPa and an ultimate stress of

approximately 1.4 MPa. Failure occurred at a strain of only 1.5% for both samples. In both

cases, failure was followed by a slight increase in stress and a slow loss of load carrying capacity

until the samples became completely severed.
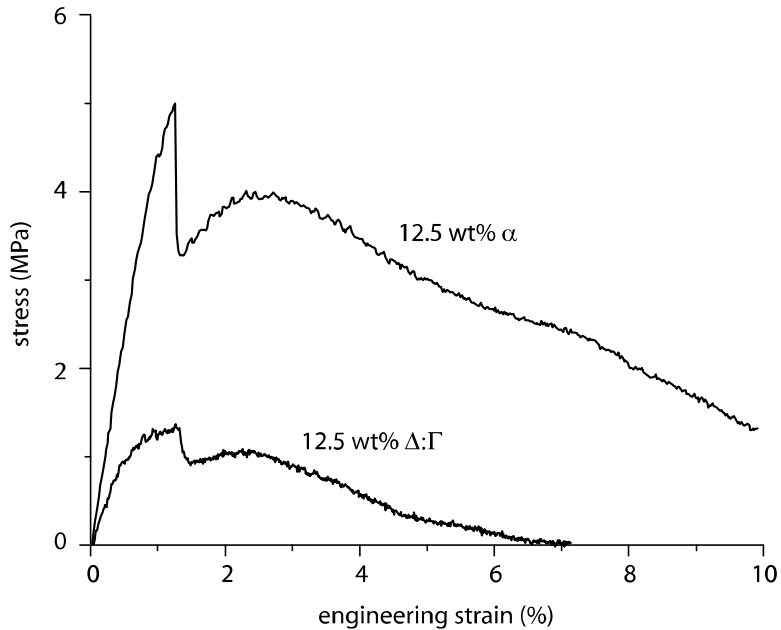
Figure 6-35. Stress plotted versus engineering strain for 12.5 wt% α and Δ:Γ phase alumina-
      PTFE nanocomposites.

Failure stress is plotted versus filler wt% in Figure 6-36a and failure strain is plotted versus

filler wt% in Figure 6-36b. The nanocomposites show an optimum in strength, strain and

therefore, toughness at a nanoparticle loading of 2 wt% α phase 80 nm alumina. Coincidentally,

this corresponds to a tendency for incomplete sintering of the 2 wt% samples during compression

molding. Previous modeling by Burris [51] suggested that the volume fraction for complete

monolayer coverage by the filler can be approximated as,

$$\upsilon_f = \frac{4D^*}{4D^*+1}$$ Eq. 6-3

where D* is D_{filler}/D_{matrix}. At monolayer coverage, the matrix particles have very limited connectivity which likely limits mechanical performance. Given 80nm filler and 3µm matrix particles, monolayer coverage occurs at 10% by volume, or 20 wt%. Optimum mechanical properties occur here for ~10% monolayer coverage.

a)

b)
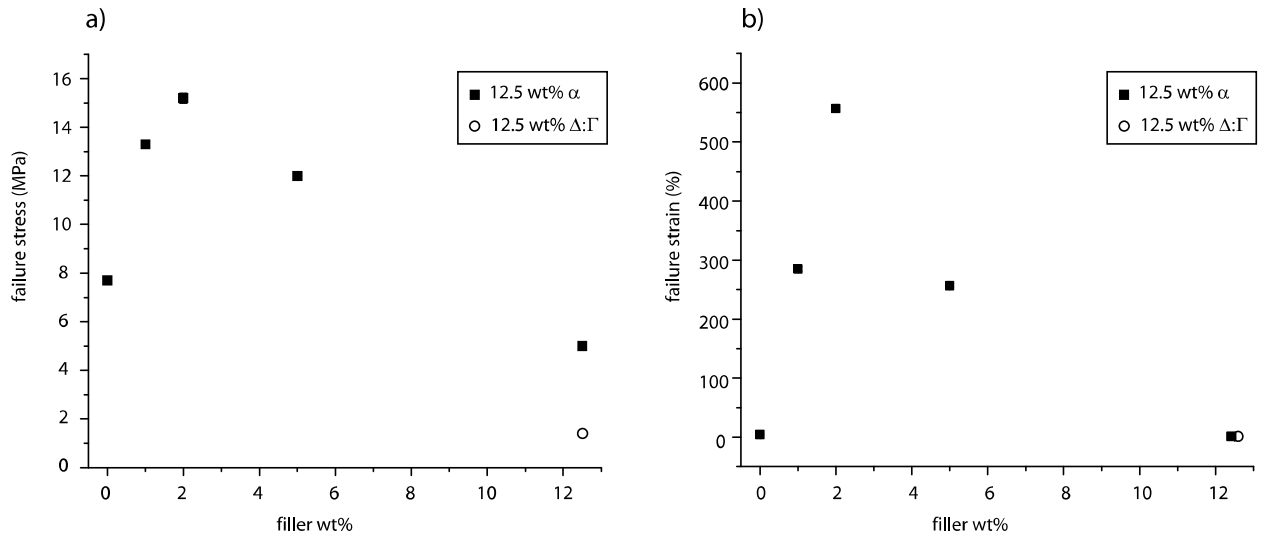
Figure 6-36. Quantified results from mechanical tests of 12.5 wt% α and Δ:Γ phase alumina-PTFE nanocomposites: a) failure stress versus filler wt%, b) Failure strain versus filler wt%.

Electron images of the fracture surfaces of 0, 1, 2, 5 and 12.5 wt% α phase and 12.5 wt% Δ:Γ phase alumina-PTFE nanocomposites are shown in Figure 6-37. The unfilled PTFE shows a corrugated surface structure. The majority of the load support and strain accommodation likely occurred via the protruding material on the surface following microvoid nucleation and coalescence. The 1 wt% α phase alumina filled sample has a relatively smooth and fibrillated surface profile. Domains of alumina rich material are identifiable as either bright inclusions or as dark regions where the inclusions have been removed. These domains are not affected by the applied stress and persist as whole entities within one of the halves of the fractured part. This sample was significantly stronger and more elastic than the neat control sample and the entire cross section appears to have been uniformly stressed, strained and failed. The 2wt% α phase

sample is far less smooth with cords of strained PTFE being evident and oriented across the

surface.   The alumina rich domains are clearly present. At 5 wt%, the surface morphology is

clearly different with smaller, more distinct ropes of PTFE clearly decorating the fracture surface

intermixed with loose fibrillated material and very smooth domains where brittle fracture likely

occurred. The topography of the 12.5 wt% sample is very tortuous with comparatively large

changes in elevation occurring across the surface. The bulk of the surface now appears to have a

brittle fracture morphology with many thin fibrils protruding from the surface as a result of the

highly localized stresses following failure of the bulk of the surface. The domains are more

difficult to distinguish due to the greater extent of the topographical contrast.   The 12.5 wt%

Δ:Γ phase alumina-PTFE sample has a very different fracture morphology than the 12.5 wt% α

phase alumina-PTFE sample despite their comparably poor mechanical properties. The entire

surface of this sample has a brittle fracture morphology.   Few very fine fibrils are also present

on the surface, but they are too fine to distinguish at the scale shown.   Various other large-scale

cracks on and within the fracture surface are clearly visible. The morphology of this sample

apparently gives little resistance to crack initiation and propagation.

Table 6-10. Results of mechanical testing of jet-milled 12.5 wt% 80 nm α phase and 44 nm Δ:Γ
         phase alumina-PTFE compression molded nanocomposites.

Alumina phase	α					Δ:Γ
loading	0 wt%	1 wt%	2 wt%	5 wt%	12.5 wt%	12.5 wt%
σ (MPa)	7.7	13.3	15.2	12.0	5.0	1.4
$U_c(\sigma)$	0.1	0.1	0.2	0.1	0.1	0.1
ε (%)	4.49	285	557	257	1.3	1.3
$U_c(\varepsilon)$	0.01	4	7	3	0.1	0.1
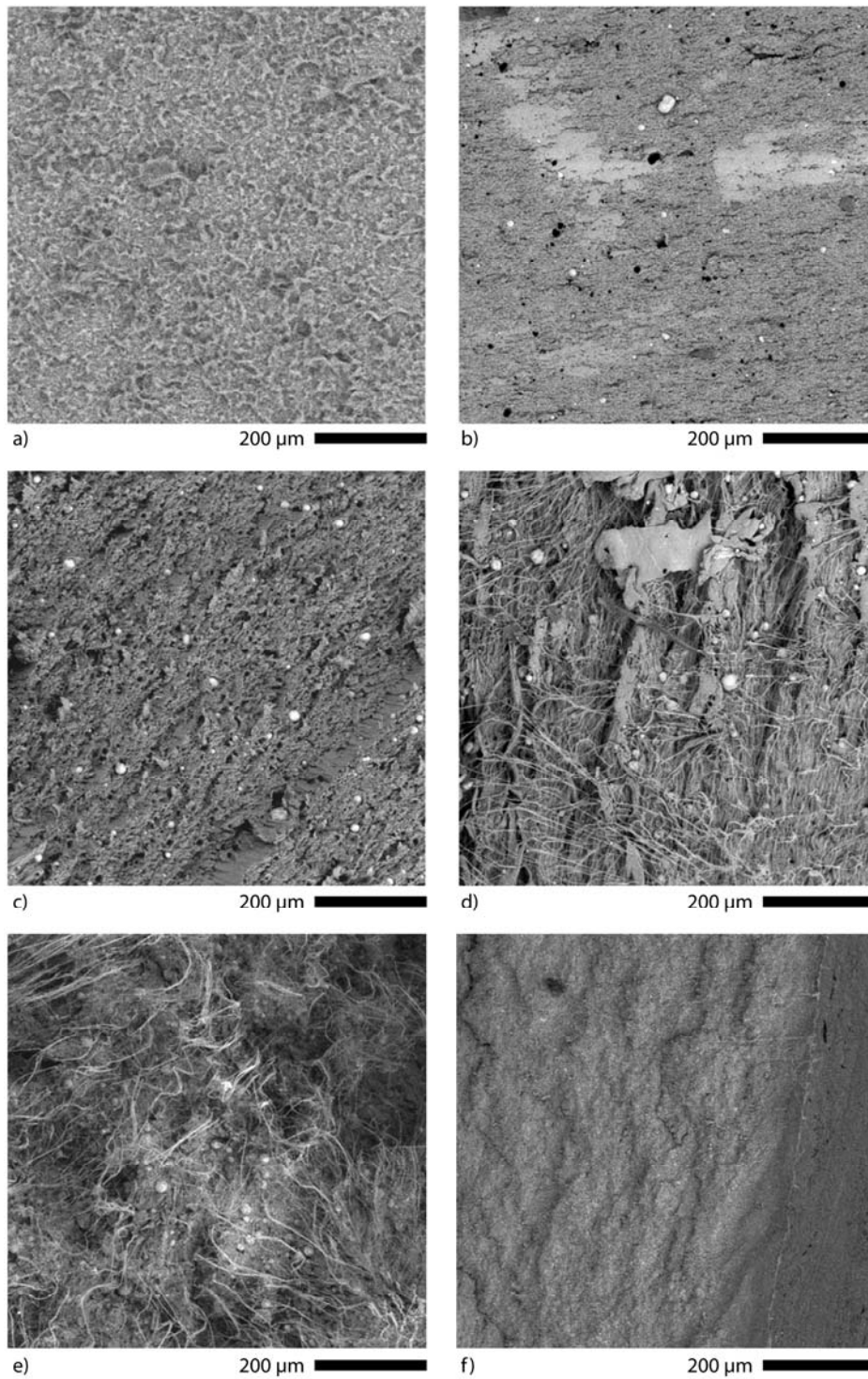
Figure 6-37. SEM images of the fracture surfaces of alumina-PTFE nanocomposites: a) 0 wt% α phase alumina-PTFE, b) 1 wt% α phase alumina-PTFE, 2 wt% α phase alumina-PTFE, 5 wt% α phase alumina-PTFE, 12.5 wt% α phase alumina-PTFE, 12.5 wt% Δ:Γ phase alumina-PTFE.

Tribological Characterization of Nanocomposites

Friction coefficient and wear volume loss are plotted versus sliding distance in Figures 6-38a and 6-38b for α and Δ:Γ phases of alumina, respectively. Quantitative results are given in Table 6-11. Stylus profilometry measurements of the transfer films after varying numbers of cycles are shown in Figure 6-39. Though SEM showed material transfer into surface scratches, the stylus profilometer could not distinguish transfer films from the counterfaces for cycles 1 and 11. In a manner consistent with the lower wt% jet-milled samples of the previous study, the friction coefficient of the α phase alumina filled sample was minimized during the transient period of sliding at $\mu = 0.13$ after 20 m of sliding. At steady state, the friction coefficient fluctuated between $\mu = 0.25$ and $\mu = 0.30$. The cause of the friction minimum and the relatively abrupt jump to a rather high friction coefficient are unclear. Surface profilometry of transfer film during steady state sliding shows very thin transfer morphology with evidence of mild abrasion to the counterface after 1,111,111 sliding cycles. The extent of the abrasion is less at 12.5 wt% than it was at 1,2 or 5 wt% loading. This is counterintuitive based on a model including alumina as the only abrasive element. The lower abrasion at the higher loading must be due to the development of a more tenacious and protective transfer film.
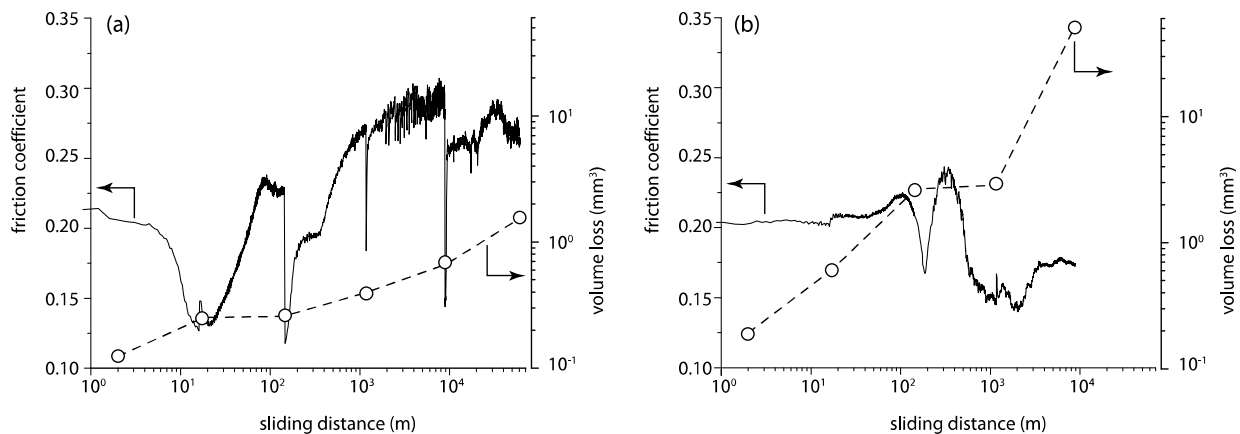
Figure 6-38. Friction coefficient and wear rate plotted versus sliding distance for a) jet-milled 12.5 wt% α phase alumina-PTFE nanocomposites, b) jet-milled 12.5 wt% Δ:Γ phase alumina-PTFE nanocomposites.
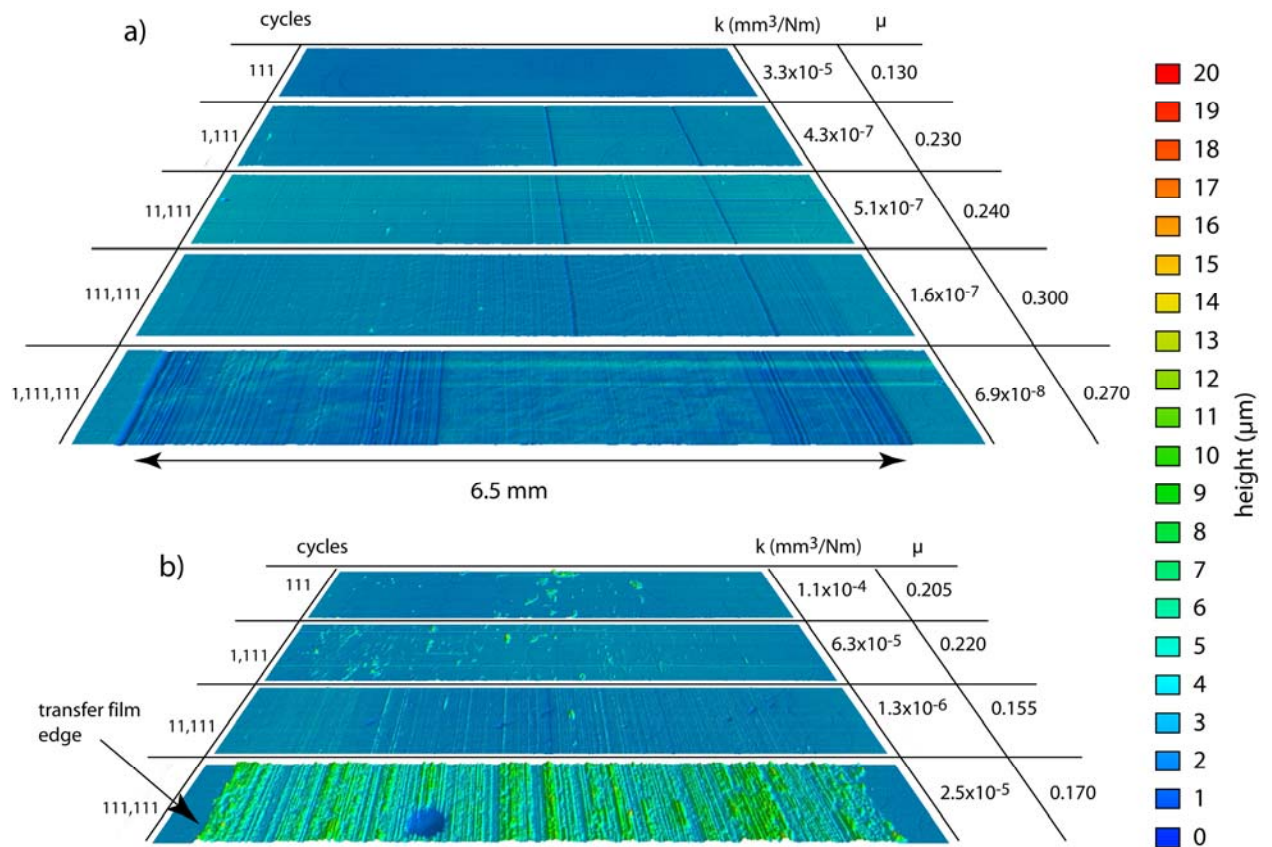
Figure 6-39. Stylus profilometric measurements of the surfaces of transfer films. Transfer film morphologies are plotted versus sliding cycle for alumina-PTFE nanocomposites with a) α phase alumina filler, b) Δ:Γ phase alumina filler.

Burris and Sawyer [8] previously found a power law relationship between transfer film thickness and wear rate. The wear rate is plotted versus average transfer film thickness for these tests in Figure 6-41. This data reinforces the hypothesis that the wear rate is a strong function of the transfer film thickness, and therefore the debris size and shape, and cohesion of the nanocomposite since these factors determine the film thickness.
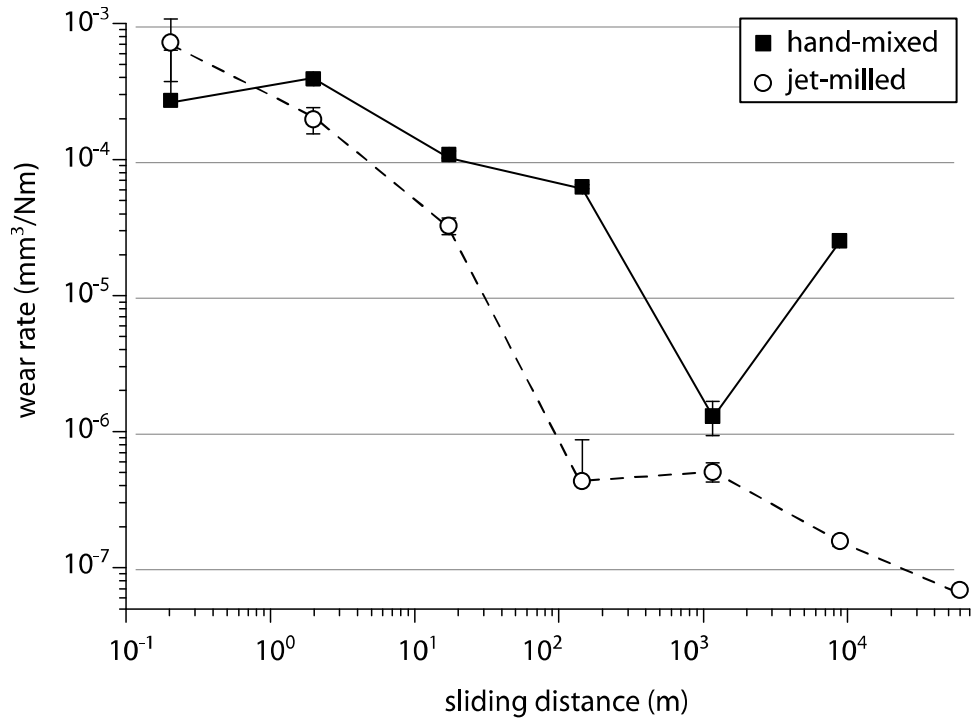
Figure 6-40. Wear rate plotted versus sliding distance for jet-milled 12.5 wt% α and Δ:Γ phase alumina-PTFE nanocomposites.
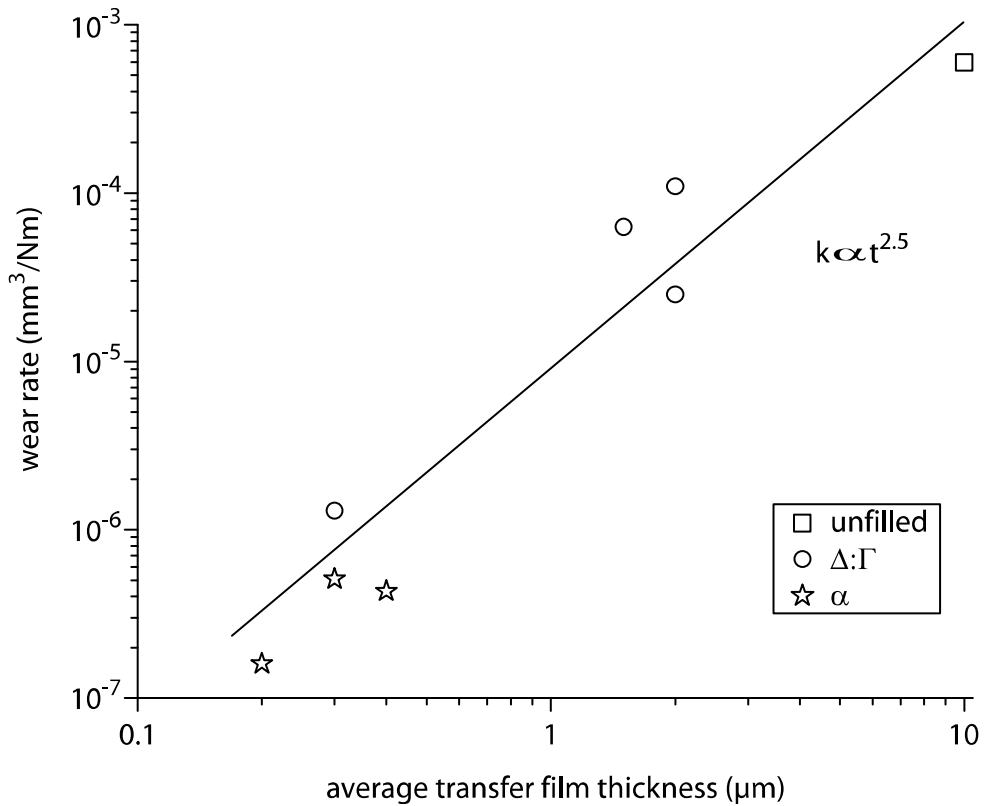
Figure 6-41. Wear rate plotted versus maximum transfer film thickness for alumina-PTFE nanocomposites of various particle phase, size shape and loading.

Table 6-11. Results of tribological testing of hand-mixed and jet-milled 1wt%, 2wt% and 5 wt% 80 nm α alumina-PTFE compression molded nanocomposites. The uncertainty in the friction coefficient measurements is less than $U_c(\mu)=0.005$.

Cycles	12.5 wt% α phase alumina				12.5 wt% Δ:Γ phase alumina			
	K	U(k)	μ	σ(μ)	K	U(k)	μ	σ(μ)
1	7.2×10^{-4}	4×10^{-4}	N/A	N/A	2.7×10^{-4}	4×10^{-4}	N/A	N/A
11	2.0×10^{-4}	4×10^{-5}	0.212	0.003	3.9×10^{-4}	4×10^{-5}	0.202	0.002
111	3.3×10^{-5}	5×10^{-6}	0.170	0.030	1.1×10^{-4}	6×10^{-6}	0.204	0.001
1,111	4.3×10^{-7}	4×10^{-7}	0.205	0.033	6.3×10^{-5}	2×10^{-6}	0.215	0.006
11,111	5.1×10^{-7}	8×10^{-8}	0.236	0.034	1.3×10^{-6}	4×10^{-7}	0.179	0.032
111,111	1.6×10^{-7}	1×10^{-8}	0.287	0.010	2.5×10^{-5}	7×10^{-7}	0.169	0.010
1,111,111	6.9×10^{-8}	4×10^{-9}	0.270	0.013	N/A	N/A	N/A	N/A

CHAPTER 7
DISCUSSION

Polymer nanocomposite tribology is an exceedingly difficult area in which to conduct

fundamental research. Tribo-systems contain chemical, mechanical and topographical

interactions over a wide range of length and times scales, making tribology an inherently

multidisciplinary area. The tribological interface is buried, inaccessible and dynamically

evolving throughout the wear process. As a result, tribologists must often resort to forensic

science to make inferences about the evolution of the system during sliding.   In addition,

polymer nanocomposite materials contain many complex materials science challenges.   The

study of the molecular, lamellar and crystalline structures and organizations of neat PTFE is

arduous and the additional complexities introduced into this system with the inclusion of

nanoparticles are vast. Myriad hypotheses for wear resistance mechanisms of such systems have

been proposed. The results from these studies help clarify the state of our understanding of the

wear resistance mechanisms of PTFE nanocomposites by refuting some hypotheses and

reinforcing others.

Fibrillation

The first studies in this work confirmed the hypothesis that the jet-mill dispersion

technique is more energetic and destructive to the PTFE than other common blending techniques

by a statistically significant margin.   Jet-milling not only disbands the agglomerations of PTFE,

but it damages individual particles, reducing average size by about 75%. Contrary to a

hypothesis that the jet-mill fibrillated the PTFE and led to stabilization of a fibrillated structure

via the nanoparticles during compression molding, none of the techniques were found to result in

fibrillation of the PTFE. Rather, the PTFE appeared to have been damaged in a brittle fracture

mode and did not contain any more fibrillated material than the virgin material did. It is now

clear that nanoparticle stabilization of fibrils produced during jet-milling is not a wear resistance mechanism.

Crystalline Morphology and Crystallinity

Preliminary investigations of the heat-treating effects on the tribology of an originally wear resistant PTFE nanocomposite had a significant impact on the way we think about these nanocomposite systems. These studies showed that wear resistance could vary by orders of magnitude simply due to the crystalline structure of the PTFE for nominally constant particle material, shape, size, loading, and dispersion. Before the heat treatment, the wear resistant nanocomposite showed thermal characteristics of the virgin PTFE morphology while the thermal characteristics of the high-wear heat-treated sample reflected melt processed PTFE. Based on these results, it was hypothesized that the role of the nanoparticles is to stabilize the virgin morphology during processing. Virgin crystals are highly ordered and were thought to promote fibrillation under stress. It was therefore conjectured that unfilled PTFE with the virgin morphology should be wear resistant. Samples were sintered at temperatures that should melt and sinter the lower order particle boundaries without affecting the highly ordered particle bulks. DSC showed that the processing led to a dual PTFE morphology, the degree of which varied with hold temperature, but none of the samples had unique wear resistance. Thus, the nanoparticles do provide benefits aside from the simple stabilization of the virgin PTFE morphology.

Several nanocomposite samples in this study did have the thermal signature of the virgin morphology, but this feature did not correlate with wear resistance. Rather, wear resistance correlated strongly with both alumina loading and phase. The crystallinity of the nanocomposite samples increased dramatically with increased nanoparticle loading suggesting that the

176

nanoparticles do in fact nucleate and promote crystallization. However, while both $\Delta:\Gamma$ phase alumina and α phase alumina filler led to a similar increase in crystallinity, the samples had very different wear performance. Thus, the *crystallinity* did not universally correlate with wear resistance. There are many factors related to crystalline structure and morphology that cannot be deciphered from these DSC measurements, including lamellar size, thickness, organization and homogeneity. Such factors may play dominant roles in the microstructure, deformation mechanisms and wear behavior of the PTFE. The AFM images shown in Figure 3-18 provide possible evidence of such a mechanism but clarification of these factors will likely require further studies using lamellae-scale probing techniques.

Mechanical Properties

It has been long hypothesized that the most effective nanoparticles are those that promote toughness and high strains to failure. While the low wt% nanocomposites were found to have higher strength, two orders of magnitude higher elongation to failure, and three orders of magnitude higher wear resistance than neat PTFE, the very wear resistant 12.5 wt% α phase alumina filled sample had diminished strength and elongation to failure compared to the neat PTFE. In addition, while the mechanical properties of the 12.5 wt% $\Delta:\Gamma$ and α phase alumina nanocomposites were comparably poor, their wear resistances differed by orders of magnitude. The differing microstructural effects of the α and $\Delta:\Gamma$ phase nanoparticles were clearly illustrated by their fracture surfaces. The $\Delta:\Gamma$ phase alumina produced a relatively smooth brittle fracture surface, while the α phase nanoparticles led to a very fibrillated and tortuous fracture surface.

Dispersion

Nanoparticle dispersion is one of the most discussed but least characterized factors in nanocomposite research. This is largely due to the difficulty in achieving good dispersion, the

difficulty in observing nanoparticles and characterizing dispersion, and the idealization of dispersion as uniform in most mental models. In this study, the extremes of dispersion were studied in an attempt to more clearly define the role of dispersion in these unusual PTFE-based systems. SEM observation of hand-mixed powders showed that the nanoparticles were poorly dispersed and mostly resided within agglomerates; very few agglomerations were found within the jet-milled powders. Tribological testing of both sets of samples showed that hand mixed samples had comparable low wear rates to jet-milled samples. In addition, jet-milled $\Delta:\Gamma$ phase alumina and α phase alumina filled samples had very similar powder dispersions but very different tribological characteristics. These results also suggest a secondary role of dispersion to the more primary effects of the filler.
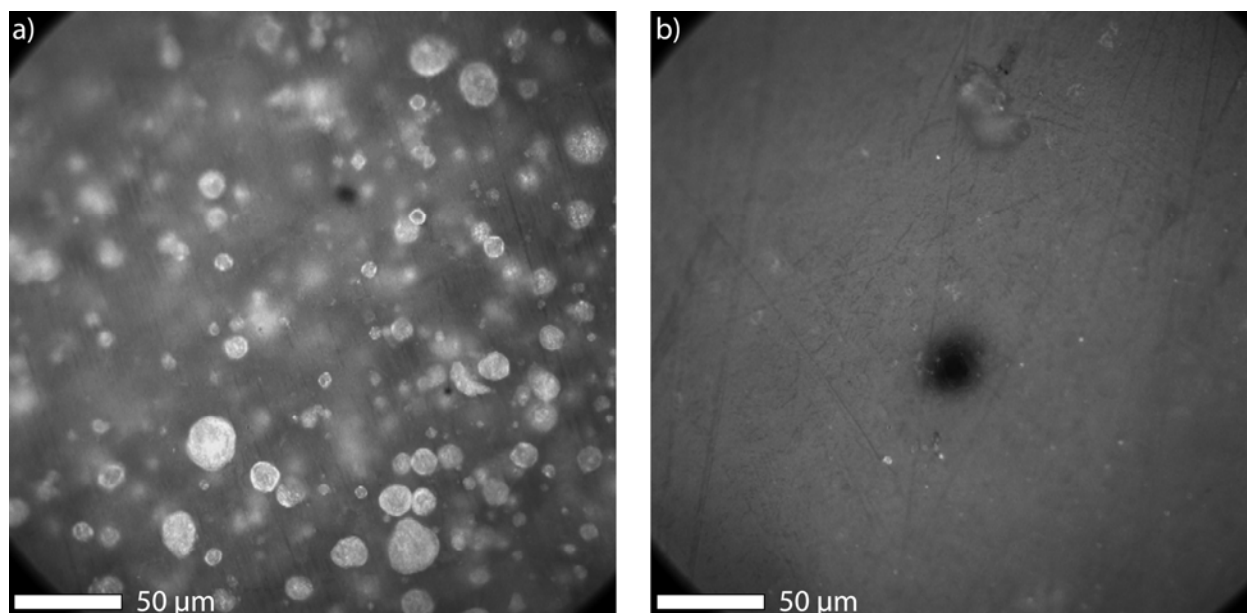
Figure 7-1. Optical images of polished sections of 12.5 wt% a) α and b) $\Delta:\Gamma$ phase alumina-PTFE nanocomposites.

One constant between the effective α phase alumina filled samples was the presence of ~5-20 μm domains; these domains were not observed in the high wear $\Delta:\Gamma$ phase alumina filled samples. Optical images of polished sections of these samples are shown in Figure 7-1. Raman

spectroscopy revealed that these regions were alumina rich. Fracture and SEM observations of individual domains suggest that these domains are nanoparticle rich PTFE rather than nanoparticle agglomerates. It remains unclear what these domains are, why they appear within α phase alumina filled systems and not within the Δ:Γ phase alumina-PTFE nanocomposites. It is hypothesized that the surface properties of the α phase alumina promotes changes in the crystalline structure that do not occur with the Δ:Γ phase alumina. The opacity of these regions is hypothesized to be the result of these crystalline changes to the PTFE.

Crack Arrestment, Debris Generation and Transfer

In 1984, Bahadur and Tabor hypothesized that the role of the fillers in PTFE, in general, is to regulate the size and shape of the debris [50]. After numerous studies and hypotheses regarding the wear resistance mechanisms of fillers in PTFE, the observation that small wear debris accompany wear resistance of PTFE-based materials is universally noted, making it one of, if not the only unrefuted hypothesized wear resistance mechanism in these materials. In 2005, following observations of unprecedented wear resistance, optimum surface texture, and strong correlation between transfer film thickness and wear rate, Burris and Sawyer extended this hypothesis [8]. It was suggested that the reduction of debris size by successful fillers not only reduces wear directly by reducing the volume of each particle, but it also facilitates engagement of the small debris into the counterface thereby enabling the development of tenacious and protective transfer films. These well-adhered, wear resistant, and protective films have been found to be a necessary condition for low wear ($<10^{-6}$ mm^3/Nm) sliding. The results collected in these studies reaffirm this hypothesis.

Blanchet and Han [67, 68] showed that effective wear-resistant micron-scale fillers tend to accumulate at the surface resulting in a continuously decreasing wear rate that is followed by low

wear at steady state. In a manner consistent with the filler accumulation of microcomposites, wear rate was found to decrease with increased sliding distance for the effective (α phase alumina) nanocomposite systems in this study. Wear rate is plotted versus sliding distance for the 12.5 wt% a phase alumina-PTFE nanocomposite in Figure 7-2. Backscattered electron images of wear surfaces of various α phase alumina-PTFE nanocomposites are shown connected to their corresponding wear rates for illustration of the evolution of the wear surface. The alumina rich domains were never observed on unworn, machined surfaces. Initial wear rates are similar to those found for unfilled PTFE at these test conditions and are likely driven by asperity plowing of the nanocomposite. As sliding continues, domains begin to populate the wear surface and wear rates decrease. The domains reside within or on top of material that appears to be equivalent to the bulk. Optical microscopy of b) revealed that many domains were deposited over previously worn grooves on the surface suggesting that they were first removed as debris and then back-transferred to the pin. After sufficient sliding distance, low wear rates ($<10^{-6}$ mm^3/Nm) accompany the presence of a coherent coating that populates the remaining regions. Optically, this coating has a brown tint and the material has been identified as de-fluorinated and possibly conjugated PTFE [61]
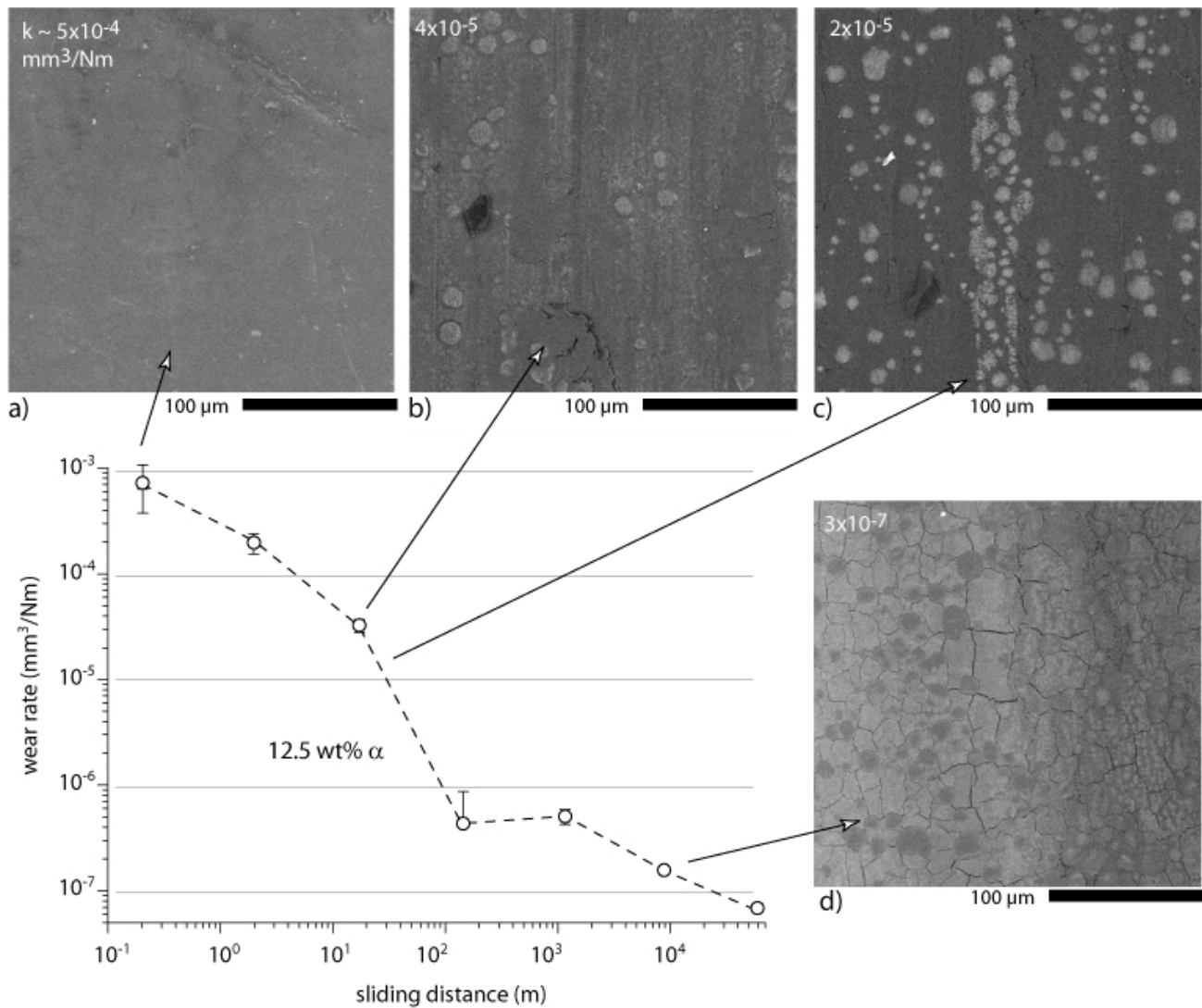
Figure 7-2. Wear rate versus sliding distance for jet-milled a phase alumina-PTFE nanocomposites with backscattered electron images of wear surfaces at corresponding wear rates: a) 2 wt% jet-milled (unworn), b) 1 wt% jet-milled (worn), c) 1 wt% hand-mixed (worn) and d) 2 wt% jet-milled (worn).

This coating is referred to as a running film and is thought to provide a protective barrier against wear. The achievement of low wear steady state conditions likely coincides with the initiation of this film.   These running films are cracked with the orientation of the cracks running parallel and perpendicular to the sliding direction. The appearance of the cracking is consistent with the notion that the films are harder and more brittle than the bulk, and the cracks likely formed during local asperity contacts. It is unclear if the brittle properties are due to degradation

from frictional energy, or if brittle sections within the bulk are preferentially fractured and transferred. Interestingly, many of the cracks begin and end at the film/domain interface but never penetrate the domains; it is unclear if the domains serve to arrest the cracks or if they initiate the cracks due to a weak interface.

The worn 2 wt% jet-milled sample was retested against a fresh counterface to determine if the transfer film itself was wear resistant. The results of the original and follow-up tests are shown in Figure 7-3. Originally, the 2 wt% jet-milled sample lost nearly 20 mm^3 of volume and required more than 5 km of sliding distance before achieving low-wear, steady-state sliding. The 5 wt% sample had a much shorter transient period. Despite having the same bulk properties, the presence of the running film immediately made the 2 wt% resistant to wear against an unprotected counterface.
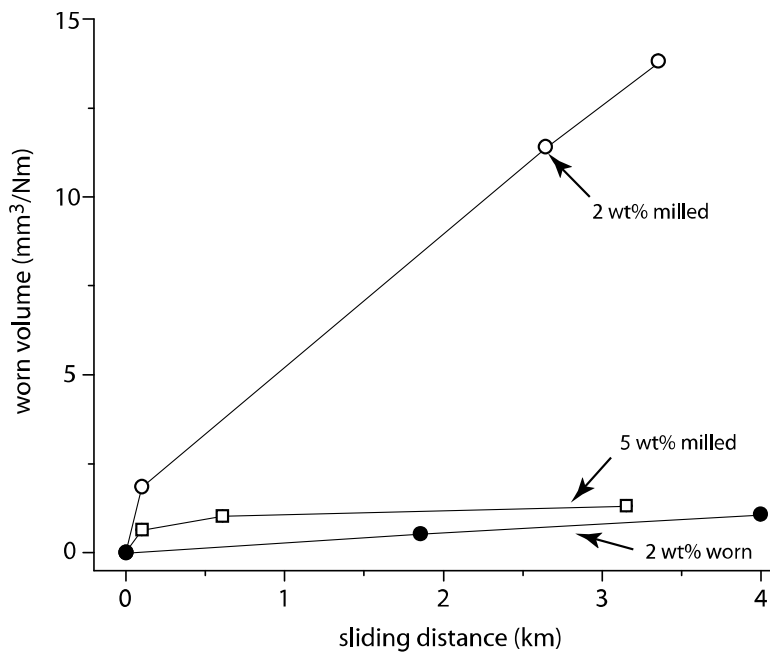
Figure 7-3. Worn volume versus sliding distance for the 2 and 5 wt% α phase alumina nanocomposites. The 2 wt% nanocomposite was tested against a fresh counterface to test the hypothesis that the running films provide increased wear resistance in the absence of pre-existing transfer films.

Wear rate is Figure 7-4 plotted versus sliding distance for jet-milled α phase alumina-

PTFE nanocomposites. In each case, the wear rate decreased with increased sliding distance

consistent with accumulation of a wear resistant phase at the surface. In addition, the rate of

decrease, increased with increasing alumina wt%, *i.e.* shorter sliding distance were required for

higher wt% samples to achieve low wear sliding (defined as a wear rate less than 10^{-6} mm^3/Nm).

The optical images of polished samples of 1, 2 and 5 wt% alumina (Figure 6-22) show that the

number density of the bright domains correlates well with the nanoparticle loading. The strong

decrease in the transient period of sliding with increased filler wt% and domain density suggests

that the domain concentration in the bulk dictates the initial condition for the debris regulation

process, the rate of accumulation and the initiation of the coherent running film which drives

wear resistance.
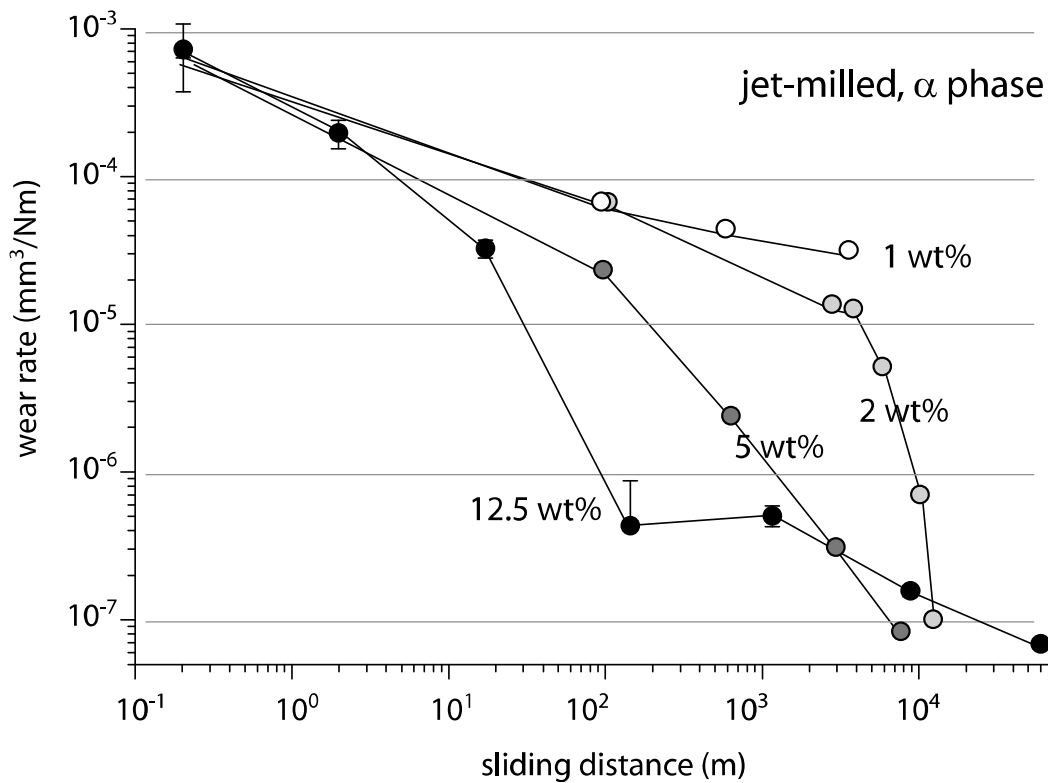
Figure 7-4. Wear rate versus sliding distance for jet-milled a phase alumina-PTFE
        nanocomposites.

Despite hypotheses that PTFE nanocomposites would be nonabrasive, the SEM and stylus images in Figures 6-28 and 6-29 show clear signs of counterface abrasion to relatively soft 304 stainless steel counterfaces. The counterface abrasion depth was measured using stylus profilometry and the abrasion rates are plotted versus filler wt% in Figure 7-5. There is a counterintuitive trend of decreased counterface abrasion with increased filler loading for jet-milled samples. This is most likely related to the number of passes by the abrasive pin before the protective surface films were formed. The 12.5 wt% filled system evolved quickly due to a large initial concentration of the crack arresting domains producing reduced particle size. The hand mixed samples were significantly more abrasive than the jet-milled samples despite evolving more quickly in general. This is further evidence that the nanoparticles were highly agglomerated in these samples. These large abrasive aggregates likely tear easily through sections of the transfer film and counterface leaving fresh metal surfaces to further damage the pin. As a result, steady state wear rates of hand-mixed samples were 2-3 times higher than those of the jet-milled samples.
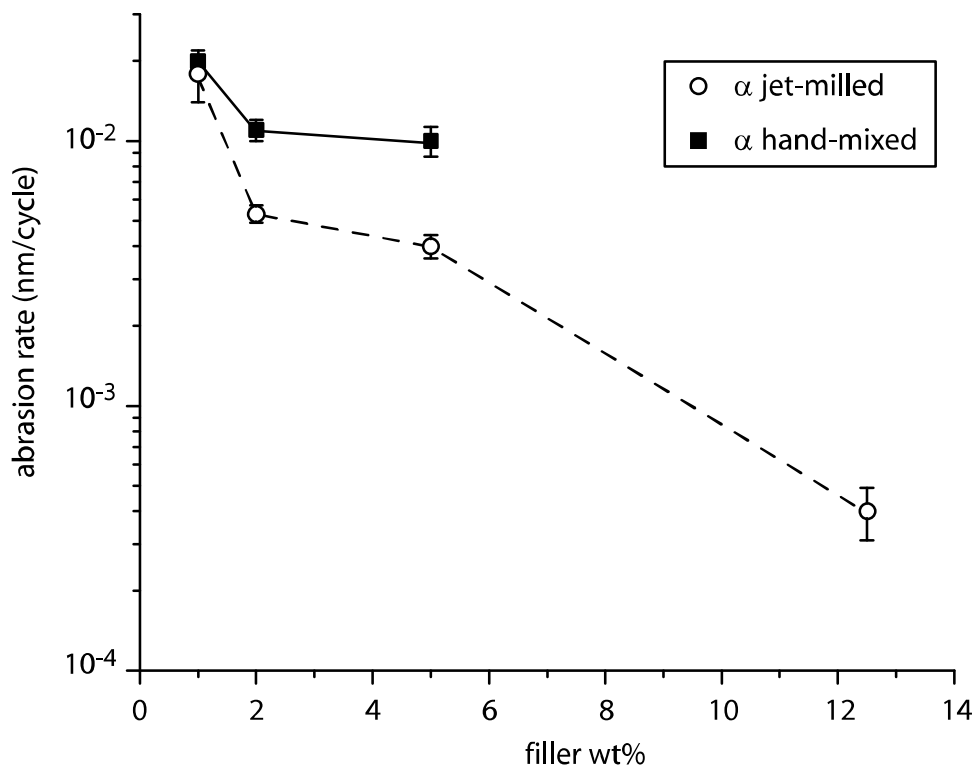
Figure 7-5. Abrasion rate to the counterface plotted versus filler wt%. Rates are calculated as an average value using post-test stylus profilometry measurements.

The results and observations collected in theses studies suggest the hypothesized wear resistance model illustrated schematically in Figure 7-6. It has been well documented that PTFE transfers immediately after contacting foreign surfaces. At first contact of these tribo-systems, the asperity level interactions lead to instant transfer of molecular-scale PTFE transfer films and potentially, to local cracking of the material. The exact cause of damage localization in these systems remains unclear, but nanoparticle alteration of the lamellar structure of the PTFE may contribute by enabling extensive fibrillation around the crack. The alumina rich domains may also localize damage by interfering with crack propagation. The compartmentalization of damage results in reduced debris size, engagement of debris into the counterface roughness and onto the worn pin surface. Because the domains are responsible for crack arrestment, the extent of the damage during the transient period decreases as the density of the alumina rich domains

185

near the surface increases. These domains also appear to transfer first, acting to initiate the transfer and running films. As material is continuously worn, more of the domains are liberated. For a given amount of wear, the probability of liberating a domain for transfer and film initiation increases as filler wt% increases. Thus, the volume of wear needed to initiate the films decreases with increased filler wt%. As the wear surface becomes rich in the domains, the composite wear debris, which likely consists of a nanoparticle altered, highly fibrillated and tough form of PTFE, populates the space in between the domains. Past XPS studies with these wear resistant running films have shown peaks consistent with PTFE defluorination, conjugation, bonding of carbon radicals with environmental species and potentially, cross-linking [61]. Other investigators have found that such degraded forms of PTFE are brittle [69-79]. These surfaces can become so wear resistant that the mechanical energy absorbed by this interface initiates degradation of even highly chemically resistant materials like PTFE. During steady state, the dominant wear mechanism appears to be degradation, embrittlement and fracture of small portions of the running film.
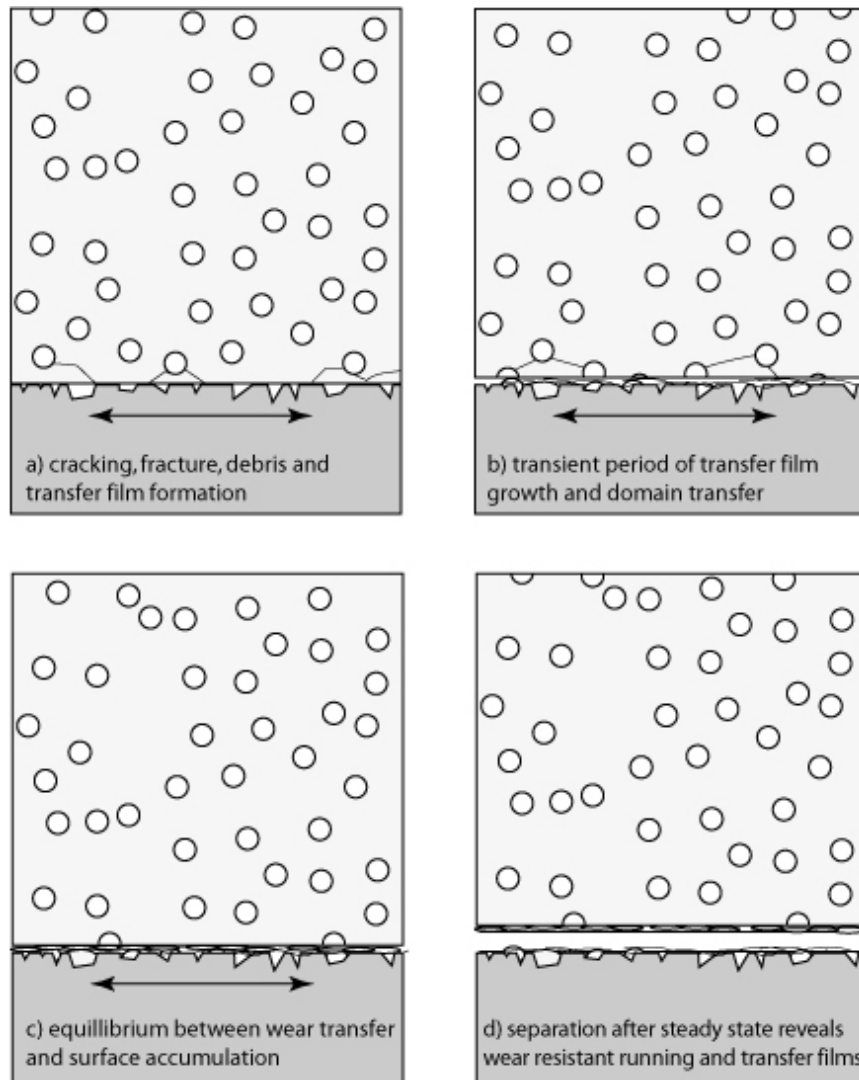
Figure 7-6. Hypothesized model of the wear of effective nanocomposites. a) Damage is localized around the asperity contact resulting in small debris size that facilitates transfer film formation. b) The transfer film continues to develop as the pin surface accumulates worn domains. c) The accumulation of domains at the surface initiates the formation of the fibrillated running film, and at steady state low wear results from interfacial sliding of protective transfer and running films. d) Following steady state sliding, separation reveals wear resistant films populated with alumina rich domains and degraded PTFE.

Closing Remarks

The wear resistance mechanisms of PTFE remain unclear. The matrix itself is complex and poorly understood, the dispersions are difficult to characterize, the nanoscale particles are inherently difficult to characterize, and tribology is itself one of the more complex sciences in

187

which to conduct fundamental studies. However, these studies have provided valuable insights into the validity of previous hypotheses regarding dispersion, filler material, matrix crystallinity and morphology, and toughness. A dominant wear resistance mechanism appears to be the compartmentalization of damage to small regions near the real area of contact. If this hypothesis is accepted as the primary wear reduction mechanism of these materials, two questions naturally come to mind: 1) by what mechanism is debris size regulated and 2) how do the nanoparticles initiate this mechanism. SEM observations have shown that cracks do not propagate through the alumina rich domains. The weak interface between the domains and the composite material likely initiates and deflects these cracks. The material science dictating the formation of these domains remains an open question. It is very interesting that of two phases of the same material, one promotes this mechanism while the other does not. The current hypothesis is that the nanoparticle surfaces may promote a finer lamellar structure that dominates the deformation mechanisms of the polymer crystals.

Perhaps most importantly, these studies have provided fruitful directions for future studies. Future studies must include nanoscale characterization and *in-situ* observation of the pin and the transfer film over time and over various length scales using electron and white-light optics, spectroscopy and interferometry. Tribometer designs for such studies are currently underway and should provide valuable insights into the nature of the transient wear process, the dominant factors determining the friction coefficients, the causes of counterface abrasion and transfer film formation, evolution and disruption.

CHAPTER 8
CONCLUSIONS

1. Nanoparticles were found to have dramatic effects on a number of physical properties of PTFE including, crystallinity, strength, elongation, toughness, wear resistance and friction coefficient. Crystallinity was increased by more than 50% with 12.5 wt% alumina nanoparticles. With 1 wt% alumina nanoparticles, ultimate strength was improved by nearly a factor of two and elongation to failure was improved by 100X. At 12.5 wt% the samples became very brittle and had lower strength and elongation than neat PTFE. Wear resistance at 2 wt% was improved by over 1,000X.

2. The changes in crystallinity and toughness did not correlate well with the wear resistance of the sample. A very brittle, high crystallinity 12.5 wt% sample had comparable wear performance to a very tough, low crystallinity 2 wt% sample.

3. Dispersion and agglomeration of the nanoparticles had little effect on the wear performance of the nanocomposites. The agglomerated hand-mixed samples had smaller, less severe wear transients but were more abrasive to the counterface and had higher steady-state wear rates by a factor of 2-4.

4. Alumina phase dominated the wear resistance of the nanocomposite. Dispersion, thermal and mechanical properties were similar, but wear rates were well over 100X higher for the round Δ:Γ alumina filled sample than for the irregular α phase alumina filled sample.

LIST OF REFERENCES

1.   Miyoshi, K. (1999), "Considerations in Vacuum Tribology (Adhesion, Friction, Wear, and Solid Lubrication in Vacuum)," *Tribology International*, **32,** 11, pp 605-616.

2.   Stachowiak, G. and Batchelor, A. (2001), *Engineering Tribology*. Butterworth-Heinemann.

3.   Schmitz, T., *et al.*(2005), "The Difficulty of Measuring Low Friction: Uncertainty Analysis for Friction Coefficient Measurements, "*Journal of Tribology-Transactions of the ASME*, **127,** 3, pp 673-678.

4.   Schmitz, T., *et al.*(2004), "Wear-Rate Uncertainty Analysis, "*Journal of Tribology-Transactions of the ASME*, **126,** 4, pp 802-808.

5.   Murari, A. and Barzon, A. (2003), "Comparison of New PEEK (R) Seals with Traditional Helicoflex for Ultra High Vacuum Applications," *Vacuum*, **72,** 3, pp 327-334.

6.   Murari, A., Vinante, C., and Monari, M. (2002), "Comparison of PEEK and Vespel (R) SP1 Characteristics as Vacuum Seals for Fusion Applications," *Vacuum*, **65,** 2, pp 137-145.

7.   Thomas, D. and Woolfenden, S. (2006), "Further Developments of Biaxially Oriented PTFE Gasket Materials," *Sealing Technology*, **2006,** 2, pp 11-13.

8.   Burris, D. and Sawyer, W. (2005), "Tribological Sensitivity of PTFE/Alumina Nanocomposites to a Range of Traditional Surface Finishes," *Tribology Transactions*, **48,** 2, pp 147-153.

9.   Burris, D. and Sawyer, W. (2006), "A Low Friction and Ultra Low Wear Rate PEEK/PTFE Composite," *Wear*, **261,** 3-4, pp 410-418.

10.   Chen, W., *et al.*(2003), "Tribological Behavior of Carbon-Nanotube-Filled PTFE Composites," *Tribology Letters*, **15,** 3, pp 275-278.

11.   Li, F., *et al.*(2001), "The Friction and Wear Characteristics of Nanometer ZnO Filled Polytetrafluoroethylene," *Wear*, **249,** 10-11, pp 877-882.

12.   Lu, Z. and Friedrich, K. (1995), "On Sliding Friction and Wear of PEEK and Its Composites," *Wear*, **181,** pp 624-631.

13.   Mccook, N., *et al.*(2005), "Wear Resistant Solid Lubricant Coating Made from PTFE and Epoxy," *Tribology Letters*, **18,** 1, pp 119-124.

14.   Menzel, B. and Blanchet, T. (2002), "Effect of Particle Size and Volume Fraction of Irradiated FEP Filler on the Transfer Wear of PTFE," *Lubrication Engineering*, **58,** 9, pp 29-35.

15.   Palabiyik, M. and Bahadur, S. (2000), "Mechanical and Tribological Properties of Polyamide 6 and High Density Polyethylene Polyblends with and without Compatibilizer," *Wear*, **246,** 1-2, pp 149-158.

16.   Sawyer, W., *et al.*(2003), "A Study on the Friction and Wear Behavior of PTFE Filled with Alumina Nanoparticles," *Wear*, **254,** 5-6, pp 573-580.

17.   Wang, Q., *et al.*(1996), "An Investigation of the Friction and Wear Properties of Nanometer Si^3N^4 Filled PEEK," *Wear*, **196,** 1-2, pp 82-86.

18.   Wang, Q., *et al.*(2000), "The Friction and Wear Characteristics of Nanometer Sic and Polytetrafluoroethylene Filled Polyetheretherketone," *Wear*, **243,** 1-2, pp 140-146.

19.   Burris, D. and Sawyer, W. (2006), "Improved Wear Resistance in Alumina-PTFE Nanocomposites with Irregular Shaped Nanoparticles," *Wear*, **260,** 7-8, pp 915-918.

20.   Bahadur, S. (2000), "The Development of Transfer Layers and Their Role in Polymer Tribology," *Wear*, **245,** 1-2, pp 92-99.

21.   Friedrich, K., Lu, Z., and Hager, A. (1995), "Recent Advances in Polymer Composites' Tribology," *Wear*, **190,** 2, pp 139-144.

22.   Zhang, S. (1998), "State-of-the-Art of Polymer Tribology," *Tribology International*, **31,** 1-3, pp 49-60.

23.   Siegel, R., *et al.*(2001), "Mechanical Behavior of Polymer and Ceramic Matrix Nanocomposites," *Scripta Materialia*, **44,** 8-9, pp 2061-2064.

24.   Ng, C., Schadler, L., and Siegel, R. (1999), "Synthesis and Mechanical Properties of Tio2-Epoxy Nanocomposites," *Nanostructured Materials*, **12,** 1-4, pp 507-510.

25.   Eitan, A., *et al.*(2006), "Reinforcement Mechanisms in MWCNT-Filled Polycarbonate," *Composites Science and Technology*, **66,** 9, pp 1162-1173.

26.   Agag, T., Koga, T., and Takeichi, T. (2001), "Studies on Thermal and Mechanical Properties of Polyimide-Clay Nanocomposites," *Polymer*, **42,** 8, pp 3399-3408.

27.   Ash, B., Schadler, L., and Siegel, R. (2002), "Glass Transition Behavior of Alumina/Polymethylmethacrylate Nanocomposites," *Materials Letters*, **55,** 1-2, pp 83-87.

28.   Ratna, D., *et al.* (2006), "Poly(Ethylene Oxide)/Clay Nanocomposite: Thermomechanical Properties and Morphology," *Polymer*, **47,** 11, pp 4068-4074.

29.   Yasmin, A., *et al.*(2006), "Mechanical and Thermal Behavior of Clay/Epoxy Nanocomposites," *Composites science and Technology*, **66,** pp 2415-2422.

30.   Bhimaraj, P., *et al.*(2005), "Effect of Matrix Morphology on the Wear and Friction Behavior of Alumina Nanoparticle/Poly(Ethylene) Terephthalate Composites," *Wear*, **258,** 9, pp 1437-1443.

31.   Schwartz, C. and Bahadur, S. (2000), "Studies on the Tribological Behavior and Transfer Film-Counterface Bond Strength for Polyphenylene Sulfide Filled with Nanoscale Alumina Particles," *Wear*, **237,** 2, pp 261-273.

32.   Wang, O., Xue, Q., and Shen, W. (1997), "The Friction and Wear Properties of Nanometre SiO_2 Filled Polyetheretherketone," *Tribology International*, **30,** 3, pp 193-197.

33.   Wang, Q., *et al.* (1996), "The Effect of Particle Size of Nanometer ZrO_2 on the Tribological Behaviour of PEEK," *Wear*, **198,** 1-2, pp 216-219.

34.   Xue, Q. and Wang, Q. (1997), "Wear Mechanisms of Polyetheretherketone Composites Filled with Various Kinds of SiC," *Wear*, **213,** 1-2, pp 54-58.

35.   McLaren, K. and Tabor, D. (1963), "Visco-Elastic Properties and Friction of Solids - Friction of Polymers - Influence of Speed and Temperature," *Nature*, **197,** 487, pp 856.

36.   Makinson, K. and Tabor, D. (1964), "Friction + Transfer of Polytetrafluoroethylene," *Nature*, **201,** 491, pp 464.

37.   Pooley, C. and Tabor, D. (1972), "Friction and Molecular Structure - Behavior of Some Thermoplastics," *Proceedings of the Royal Society of London Series A-Mathematical and Physical Sciences*, **329,** 1578, pp 251.

38.   Tanaka, K., Uchiyama, Y., and Toyooka, S. (1973), "Mechanism of Wear of Polytetrafluoroethylene," *Wear*, **23,** 2, pp 153-172.

39.   Blanchet, T. and Kennedy, F. (1992), "Sliding Wear Mechanism of Polytetrafluoroethylene (PTFE) and PTFE Composites," *Wear*, **153,** 1, pp 229-243.

40.   Suh, N. (1973), "Delamination Theory of Wear," *Wear*, **25,** 1, pp 111-124.

41.   Bahadur, S. and Gong, D. (1992), "The Action of Fillers in the Modification of the Tribological Behavior of Polymers," *Wear*, **158,** 1-2, pp 41-59.

42.   Burroughs, B., Kim, J., and Blanchet, T. (1999), "Boric Acid Self-Lubrication of B_2O_3-Filled Polymer Composites," *Tribology Transactions*, **42,** 3, pp 592-600.

43.   Li, F., *et al.*(2000), "The Tribological Behaviors of Copper-Coated Graphite Filled PTFE Composites," *Wear*, **237,** 1, pp 33-38.

44.   Lancaster.Jk (1972), "Polymer-Based Bearing Materials - Role of Fillers and Fiber Reinforcement in Wear," *Wear*, **22,** 3, pp 412.

45.   Sung, N. and Suh, N. (1979), "Effect of Fiber Orientation on Friction and Wear of Fiber Reinforced Polymeric Composites," *Wear*, **53,** 1, pp 129-141.

46.   Tanaka, K. and Kawakami, S. (1982), "Effect of Various Fillers on the Friction and Wear of Polytetrafluoroethylene-Based Composites," *Wear*, **79,** 2, pp 221-234.

47.   Briscoe, B., Pogosian, A., and Tabor, D. (1974), "Friction and Wear of High-Density Polythene - Action of Lead Oxide and Copper Oxide Fillers," *Wear*, **27,** 1, pp 19-34.

48.   Gong, D., Xue, Q., and Wang, H. (1991), "ESCA Study on Tribochemical Characteristics of Filled PTFE," *Wear*, **148,** 1, pp 161-169.

49.   Blanchet, T., Kennedy, F., and Jayne, D. (1993), "XPS Analysis of the Effect of Fillers on PTFE Transfer Film Development in Sliding Contacts," *Tribology Transactions*, **36,** 4, pp 535-544.

50.   Bahadur, S. and Tabor, D. (1984), "The Wear of Filled Polytetrafluoroethylene," *Wear*, **98,** 1-3, pp 1-13.

51.   Burris, D. (2006), "Wear Resistance Mechanisms in Polytetrafluoroethylene (PTFE) Based Tribological Nanocomposites," *Master's Thesis, University of Florida, Gainesville, Florida*,

52.   McElwain, S. (2006), "Wear Resistant PTFE Composites Via Nano-Scale Particles," *master's thesis, Rensselaer Polytechnic Institute, Troy, New York.*

53.   Reynaud, E., *et al.*(2001), "Nanofillers in Polymeric Matrix: A Study on Silica Reinforced PA6," *Polymer*, **42,** 21, pp 8759-8768.

54.   Sevostianov, I. and Kachanov, M. (2007), "Effect of Interphase Layers on the Overall Elastic and Conductive Properties of Matrix Composites. Applications to Nanosize Inclusion," *International Journal of Solids and Structures*, **44,** 3-4, pp 1304-1315.

55.   Wagner, D. and Vaia, R. (2004), "Nanocomposites: Issues at the Interface," *Materials Today*,   pp 38-42.

56.   Koerner, H., *et al.*(2005), "Deformation-Morphology Correlations in Electrically Conductive Carbon Nanotube Thermoplastic Polyurethane Nanocomposites," *Polymer*, **46,** 12, pp 4405-4420.

57.   He, P., *et al.*(2006), "Surface Modification and Ultrasonication Effect on the Mechanical Properties of Carbon Nanofiber/Polycarbonate Composites," *Composites Part A-Applied Science and Manufacturing*, **37,** 9, pp 1270-1275.

58.   Maiti, M. and Bhowmick, A. (2006), "New Insights into Rubber-Clay Nanocomposites by AFM Imaging," *Polymer*, **47,** 17, pp 6156-6166.

59.   Sternstein, S., *et al.*(2005), "Reinforcement and Nonlinear Viscoelasticity of Polymer Melts Containing Mixtures of Nanofillers," *Rubber Chemistry and Technology*, **78,** 2, pp 258-270.

60.   Zhu, A. and Sternstein, S. (2003), "Nonlinear Viscoelasticity of Nanofilled Polymers: Interfaces, Chain Statistics and Properties Recovery Kinetics," *Composites Science and Technology*, **63,** 8, pp 1113-1126.

61.   Burris, D.L., *et al*., *Polytetrafluoroethylene Matrix Nanocomposites for Tribological Applications*, in *Tribology of Polymeric Nanocomposites*, K. Friedrich, Editor. 2008.

62.   Beamson, G., *et al.*(1996), "Characterization of PTFE on Silicon Wafer Tribological Transfer Films by XPS, Imaging XPS and AFM," *Surface and Interface Analysis*, **24,** 3, pp 204.

63.   Breiby, D., *et al.*(2005), "Structural Surprises in Friction-Deposited Films of Poly(Tetrafluoroethylene)," *Macromolecules*, **38,** 6, pp 2383-2390.

64.   Wheeler, D. (1981), "The Transfer of Polytetrafluoroethylene Studied by X-Ray Photoelectron-Spectroscopy," *Wear*, **66,** 3, pp 355-365.

65.   Wittmann, J. and Smith, P. (1991), "Highly Oriented Thin-Films of Poly(Tetrafluoroethylene) as a Substrate for Oriented Growth of Materials," *Nature*, **352,** 6334, pp 414-417.

66.   Gong, D., *et al.*(1990), "Effect of Tribochemical Reaction of Polytetrafluoroethylene Transferred Film with Substrates on Its Wear Behavior," *Wear*, **137,** 2, pp 267-273.

67.   Blanchet, T. (1995), "A Model for Polymer Composite Wear Behavior Including Preferential Load Support and Surface Accumulation of Filler Particulates," *Tribology Transactions*, **38,** 4, pp 821-828.

68.   Han, S. and Blanchet, T. (1997), "Experimental Evaluation of a Steady-State Model for the Wear of Particle-Filled Polymer Composite Materials," *Journal of Tribology-Transactions of the ASME*, **119,** 4, pp 694-699.

69.   Abdou, S. and Mohamed, R. (2002), "Characterization of Structural Modifications in Poly-Tetra-Fluoroethylene Induced by Electron Beam Irradiation," *Journal of Physics and Chemistry of Solids*, **63,** 3, pp 393-398.

70.   Briscoe, B., Mahgerefteh, H., and Suga, S. (2003), "The Effect of Gamma Irradiation on the Pressure Dependence of the Room Temperature Transition in PTFE," *Polymer*, **44,** 3, pp 783-791.

71.   Fayolle, B., Audouin, L., and Verdu, J. (2003), "Radiation Induced Embrittlement of PTFE," *Polymer*, **44,** 9, pp 2773-2780.

72.   Harling, O., Kohse, G., and Riley, K. (2002), "Irradiation Performance of Polytetrafluoroethylene (Teflon ®) in a Mixed Fast Neutron and Gamma Radiation Field," *Journal of Nuclear Materials*, **304,** 1, pp 83-85.

73.   Zhao, X., *et al.*(2005), "An Experimental Study of Low Earth Orbit Atomic Oxygen and Ultraviolet Radiation Effects on a Spacecraft Material - Polytetrafluoroethylene," *Polymer Degradation and Stability*, **88,** 2, pp 275-285.

74.   Lappan, U., *et al.*(2002), "Number-Average Molecular Weight of Radiation-Degraded Poly(Tetrafluoroethylene). An End Group Analysis Based on Solid-State NMR and IR Spectroscopy," *Polymer*, **43,** 16, pp 4325-4330.

75.   Lappan, U., *et al.*(2001), "Radiation-Induced Branching and Crosslinking of Poly(Tetrafluoroethylene) (PTFE)," *Nuclear Instruments and Methods in Physics Research Section B-Beam Interactions with Materials and Atoms*, **185,** pp 178-183.

76.   Oshima, A., *et al.*(2001), "Chemical Structure and Physical Properties of Radiation-Induced Crosslinking of Polytetrafluoroethylene," *Radiation Physics and Chemistry*, **62,** 1, pp 39-45.

77.   Katoh, E., *et al.*(1999), "Evidence for Radiation Induced Crosslinking in Polytetrafluoroethylene by Means of High-Resolution Solid-State F-19 High-Speed MAS NMR," *Radiation Physics and Chemistry*, **54,** 2, pp 165-171.

78.   Fuchs, B. and Scheler, U. (2000), "Branching and Cross-Linking in Radiation-Modified Poly(Tetrafluoroethylene): A Solid-State NMR Investigation," *Macromolecules*, **33,** 1, pp 120-124.

79.   Blanchet, T. and Peng, Y. (1996), "Wear-Resistant Polytetrafluoroethylene Via Electron Irradiation," *Lubrication Engineering*, **52,** 6, pp 489-495.

80.   Blanchet, T. and Peng, Y. (1998), "Wear Resistant Irradiated FEP Unirradiated PTFE Composites," *Wear*, **214,** 2, pp 186-191.

81.   Yang, K., *et al.*(2006), "Morphology and Mechanical Properties of Polypropylene/Calcium Carbonate Nanocomposites," *Materials Letters*, **60,** 6, pp 805-809.

82.   Kojima, Y., *et al.*(1993), "Mechanical-Properties of Nylon 6-Clay Hybrid," *Journal of Materials Research*, **8,** 5, pp 1185-1189.

83.   Xiao, Z., *et al.*(2006), "Probing the Use of Small-Angle Light Scattering for Characterizing Structure of Titanium Dioxide/Low-Density Polyethylene Nanocomposites," *Journal of Polymer Science Part B-Polymer Physics*, **44,** 7, pp 1084-1095.

84.   Yang, H., *et al.*(2007), "Crystal Growth in Alumina/Poly(Ethylene Terephthalate) Nanocomposite Films," *Journal of Polymer Science, Part B: Polymer Physics*, **45,** 7, pp 747-757.

85.   Kuchta, F., *et al.*(1999), "Materials with Improved Properties from Polymer-Ceramic-Nanocomposites" *Mat Res Soc Symp Proc*, **576,** pp 363-368.

86.   Petrovicova, E., *et al.*(2000), "Nylon 11/Silica Nanocomposite Coatings Applied by the HVOF Process. I. Microstructure and Morphology," *Journal of Applied Polymer Science*, **77,** 8, pp 1684-1699.

87.   Bunn, C. and Howells, E. (1954), "Structures of Molecules and Crystals of Fluorocarbons," *Nature*, **174,** 4429, pp 549-551.

88.   Clark, E. (1999), "The Molecular Conformations of Polytetrafluoroethylene: Forms II and IV," *Polymer*, **40,** 16, pp 4659-4665.

89.   Farmer, B. and Eby, R. (1981), "Energy Calculations of the Crystal-Structure of the Low-Temperature Phase (II) of Polytetrafluoroethylene," *Polymer*, **22,** 11, pp 1487-1495.

90.   Rigby, H. and Bunn, C. (1949), "A Room-Temperature Transition in Polytetrafluoroethylene," *Nature*, **164,** 4170, pp 583-583.

91.   Weeks, J., Clark, E., and Eby, R. (1981), "Crystal-Structure of the Low-Temperature Phase(II) of Polytetrafluoroethylene," *Polymer*, **22,** 11, pp 1480-1486.

92.   Weeks, J., Eby, R., and Clark, E. (1981), "Disorder in the Crystal-Structures of Phase-1 and Phase-2 of Copolymers of Tetrafluoroethylene and Hexafluoropropylene," *Polymer*, **22,** 11, pp 1496-1499.

93.   Kimmig, M., Strobl, G., and Stuhn, B. (1994), "Chain Reorientation in Poly(Tetrafluoroethylene) by Mobile Twin-Helix Reversal Defects," *Macromolecules*, **27,** 9, pp 2481-2495.

94.   Tieyuan, F., *et al.*(1986), "Study of Factors Affecting Room Temperature Transition of Polytetrafluoroehtylene," *Chinese Journal of Polymer Science*, **2,** pp 170-179.

95.   Marega, C., *et al.*(2004), "Relationship between the Size of the Latex Beads and the Solid-Solid Phase Transitions in Emulsion Polymerized Poly(Tetrafluoroethylene)," *Macromolecules*, **37,** 15, pp 5630-5637.

96.   D'amore, M., *et al.*(2004), "Disordered Chain Conformations of Poly(Tetrafluoroethylene) in the High-Temperature Crystalline Form I," *Macromolecules*, **37,** 25, pp 9473-9480.

97.   Ting-Yung, H. and Eiss, N. (1983), "Effects of Molecular Weight and Crystallinity on Wear of Polytetrafluoroethylene," *Wear of Materials: International Conference on Wear of Materials*,   pp 636-642.

98.   Flom, D. and Porile, N. (1955), "Friction of Teflon Sliding on Teflon," *Journal of Applied Physics*, **26,** 9, pp 1088-1092.

99.   Steijn, R. (1968), "Sliding Experiments with Polytetrafluoroethylene," *ASLE Transactions*, **11,** 3, pp 235.

100.   Mccook, N., *et al.*(2005), "Cryogenic Friction Behavior of PTFE Based Solid Lubricant Composites," T*ribology Letters*, **20,** 2, pp 109-113.

101.   Burris, D.L., Perry, S.S., and Sawyer, W.G. (2007), "Macroscopic Evidence of Thermally Activated Friction with Polytetrafluoroethylene," *Tribology Letters*, **27,** 3, pp 323-328.

102.   Joyce, J. (2003), "Fracture Toughness Evaluation of Polytetrafluoroethylene," *Polymer Engineering and Science*, **43,** 10, pp 1702-1714.

103.   Brown, E. and Dattelbaum, D. (2005), "The Role of Crystalline Phase on Fracture and Microstructure Evolution of Polytetrafluoroethylene (PTFE)," *Polymer*, **46,** 9, pp 3056-3068.

104.   Brown, E., *et al.*(2006), "The Effect of Crystallinity on the Fracture of Polytetrafluoroethylene (PTFE)," *Materials Science and Engineering C-Biomimetic and Supramolecular Systems*, **26,** 8, pp 1338-1343.

105.   Rae, P. and Brown, E. (2005), "The Properties of Poly(Tetrafluoroethylene) (PTFE) in Tension," *Polymer*, **46,** 19, pp 8128-8140.

106.   Rae, P. and Dattelbaum, D. (2004), "The Properties of Poly (Tetrafluoroethylene) (PTFE) in Compression," *Polymer*, **45,** 22, pp 7615-7625.

107.   Pucciariello, R. and Villani, V. (2004), "Melting and Crystallization Behavior of Poly (Tetrafluoroethylene) by Temperature Modulated Calorimetry," *Polymer*, **45,** 6, pp 2031-2039.

108.   Pucciariello, R. and Villani, V. (2004), "Phase Behavior at Low Temperature of Poly(Tetrafluoroethylene) by Temperature-Modulated Calorimetry," *Journal of Fluorine Chemistry*, **125,** 2, pp 293-302.

109.   Huang, J. and Lee, W. (2001), "Sealing and Mechanical Behaviors of Expanded PTFE Gasket Sheets Characterized by Pvrc Room Temperature Tightness Tests," *Materials Chemistry and Physics*, **68,** 1-3, pp 180-196.

110.   Kurumada, K., *et al.*(1998), "Structure Generation in PTFE Porous Membranes Induced by the Uniaxial and Biaxial Stretching Operations," *Journal of Membrane Science*, **149,** 1, pp 51-57.

111.   Yang, J., *et al.*(2005), "Morphology Evolution in PTFE as a Function of Melt Time and Temperature - I. High Molecular Weight Single- and Multi-Molecule Folded Chain Single Crystals and Band Structures," *Chinese Journal of Polymer Science*, **23,** 2, pp 123-135.

112.   Yang, J., *et al.*(2005), "Morphology Evolution in Polytetrafluoroethylene as a Function of Melt Time and Temperature. Part III. Effect of Prior Deformation," *Polymer*, **46,** 20, pp 8723-8733.

113.   Lau, S.F., Suzuki, H., and Wunderlich, B. (1984), "The Thermodynamic Properties of Polytetrafluoroethylene," *Journal of Polymer Science Part B-Polymer Physics*, **22,** 3, pp 379-405.

114.   Jie, M., *et al.*(1998), "Damage Evolution and Energy Dissipation of Polymers with Crazes," *Theoretical and Applied Fracture Mechanics*, **28,** 3, pp 165-174.

115.   Kong, X., Chakravarthula, S.S., and Qiao, Y. (2006), "Evolution of Collective Damage in a Polyamide 6-Silicate Nanocomposite," *International Journal of Solids and Structures*, **43,** 20, pp 5969-5980.

116.   Marissen, R. (2000), "Craze Growth Mechanics," *Polymer*, **41,** 3, pp 1119-1129.

117.   Michler, G.H., Adhikari, R., and Henning, S. (2004), "Toughness Enhancement of Nanostructured Amorphous and Semicrystalline Polymers," *Macromolecular Symposia*, **214,** pp 47-71.

118.   Dennis, H.R., *et al* .(2001), "Effect of Melt Processing Conditions on the Extent of Exfoliation in Organoclay-Based Nanocomposites," *Polymer*, **42,** 23, pp 9513-9522.

119.   Fornes, T.D., *et al.*(2001), "Nylon 6 Nanocomposites: The Effect of Matrix Molecular Weight," *Polymer*, **42,** 25, pp 9929-9940.

120. Ma, D.L., *et al.*(2005), "Effect of Titania Nanoparticles on the Morphology of Low Density Polyethylene," *Journal of Polymer Science Part B-Polymer Physics*, **43,** 5, pp 488-497.

121. Burris, D.L., *et al.*(2007), "Polymeric Nanocomposites for Tribological Applications," *Macromolecular Materials and Engineering*, **292,** 4, pp 387-402.

122. Briscoe, B. (1981), "Wear of Polymers - an Essay on Fundamental-Aspects," *Tribology International*, **14,** 4, pp 231-243.

BIOGRAPHICAL SKETCH

David Burris graduated from Lemon Bay High School in Englewood, Florida, in June of 1998. He commenced his higher education at the University of Florida that summer. In the spring of 2002, he joined the Tribology Laboratory at the University of Florida where he began his studies of tribology. The following spring he received his bachelor's degree and began his graduate work studying the tribology of PTFE based solid lubricants. Upon receiving the degree of Doctor of Philosophy in mechanical engineering, David hopes to begin a research laboratory designed to study the underlying mechanisms of friction and wear at solid sliding interfaces.